Ph.D Thesis

Computational Study of Hydrogen Bonded Energetic Materials

Bokinala Moses Abraham

ACRHEM, School of Physics
University of Hyderabad
Hyderabad - 500 046
Telangana, India

Computational Study of Hydrogen Bonded Energetic Materials

A Thesis submitted to University of Hyderabad for the award of the degree of

Doctor of Philosophy

in Physics

by

Bokinala Moses Abraham
(15ACPA03)

ACRHEM, School of Physics
University of Hyderabad
Hyderabad-500 046
December 2019

Dedicated to

My Parents

Declaration

I, **Bokinala Moses Abraham** hereby declare that this thesis entitled ***Computational Study of Hydrogen Bonded Energetic Materials*** submitted by me under the supervision of Dr. G. S. Vaitheeswaran, ACRHEM, University of Hyderabad, Hyderabad, India, is a bonafide research work which is also free from plagiarism. I also declare that it has not been submitted previously in part or in full to this University or any other University or Institution for the award of any degree or diploma. I hereby agree that my thesis can be deposited in Shodhganga/INFLIBNET.

A report on plagiarism statistics from the University Librarian is enclosed.

Date

Bokinala Moses Abraham
Reg. No: 15ACPA03.

Dr. G. S. Vaitheeswaran,
Thesis Supervisor,
School of Physics,
University of Hyderabad.

Certificate

This is to certify that the thesis entitled ***Computational Study of Hydrogen Bonded Energetic Materials*** being submitted to the University of Hyderabad by **Bokinala Moses Abraham** (Reg. No. 15ACPA03), for the award of the degree of Doctor of Philosophy in Physics, is a record of *bonafide* work carried out by him under my supervision and is free of plagiarism. The matter embodied in this report has not been submitted to any other University or Institution for the award of any degree or diploma.

The student has passed the following courses towards the fulfilment of course work requirement for PhD.

S.No.	Course Code	Year	Name of the course	Credits	Pass/Fail
1	PY801	2015	Advanced Quantum Mechanics	04	Pass
2	PY804	2015	Advanced Electromagnetic Theory	04	Pass
3	PY801	2016	Research Methodology	04	Pass
4	PY804	2016	Advanced Mathematical Methods	04	Pass

Dr. G. S. Vaitheeswaran,
Thesis Supervisor,
School of Physics,
University of Hyderabad.

Director,
ACRHEM,
University of Hyderabad.

Dean,
School of Physics,
University of Hyderabad.

A word of Gratitude

Pursuing this doctoral research has been really a life changing experience and it would not have been possible without the time, support and encouragement that I received from many people.

First and foremost, I pay my obeisance to **GOD**, the almighty: without His will, I would have never found the right path. I thank Him for enlightening my soul with the respected love and compassion for the other humans and allowing me to enter a field where I could practice this desire. His grace and mercy was with me throughout my journey and evermore in this study.

It is a genuine pleasure to express my sincere and deepest gratitude to my supervisor **Dr. G. S. Vaitheeswaran**, School of Physics, University of Hyderabad for his motivation, creative suggestions, sustained enthusiasm and excellent guidance throughout the course of my doctoral research. His dedication and keen interest are solely and mainly responsible for the completion of my research work in time.

I owe my special thanks to doctoral committee members **Prof. Ashok Chatterjee** and **Dr. V. Ashoka**, School of Physics, University of Hyderabad for their suggestions and valuable feedback towards the completion of my doctoral research work. I extend my gratitude to **Dr. Vikas D. Ghule**, Department of Chemistry, NIT kurukshetra, India for his fruitful discussions and collaboration work. I also would like to thank the **anonymous reviewers** for reviewing my publications to improve the quality of the research work. My sincere thanks to **faculty members of ACRHEM** for teaching me the basic concepts of high energy materials and research methodology. A special thanks to **Prof. P. Prakash Babu**, former Pro Vice-Chancellor-2, University of Hyderabad for his constant support during critical situations. I am extremely thankful to **non-teaching staff of ACRHEM** as well as **School of Physics** for their help in office related work. I would like to thank **CMSD**, University of Hyderabad and **RSC-HPC System** at Novosibirsk, Russia for providing me the computational facilities.

I sincerely admire the contribution of all my group members **Dr. S. Appalakondaiah, Dr. N. Yedukondalu, Dr. E. Narsimha Rao, Dr. Athar Parveen, B. Adivaiah, J. Prathap Kumar and S. Mondal** for extending their sympathetic attitude, timely motivation, unstinted support and unfailing help during the course of entire study. I have to mention my special and sincere thanks to **M. V. Jyothirmai** and **Atiya Farheen** for their valuable discussions, suggestions, encouragement and moral support towards completion of my doctoral research work. I am extremely thankful to all my **ACRHEM**, **School of Physics friends**, **Sharonites**, **Noble mates**, **ANU and TMI friends** for their constant support whenever I needed. I would like to thank the organizing committees

of **Sorbonne-JNCASR School** on **Advanced Computational Material Science**, 2017 and **International Winter School** on **Frontiers in Materials Science**, JNCASR, 2018 for providing me the opportunity to participate in the international school's. I also would like to thank Science and Engineering Research Board, Government of India and Royal Society of Chemistry, United Kingdom for providing the International Travel Grants.

I would like to extend my sincere thanks to **Dr. G. M. Priscilla**, **Dr. D. Nalini**, **Dr. T. E. Divakar**, **Mr. B. G. Stephen** & **family members**, **Mrs. K. G. Karuna Sri** & **family members**, **Mr. P. S. Banerjee**, **Lt. Dr. M. J. Subhakar**, **Mr. T. Benjamin**, **Mr. M. Jashuva** & **family members**, **Dr. G. B. Anand Kumar** & **family members Mr. S. R. B. Chakravarthy**, **Dr. S. J. Earnest**, **Mrs. P. Santhi**, **Dr. T. Joseph**, Noble College, Machilipatnam, **Dr. Sandhya Cole**, Department of Physics, Acharya Nagarjuna University, Guntur.

My deepest gratitude goes to **Rev. Pulipaka Sudhakar** & **extended family members**, **Bishop Rt. Rev. Daniel Subhan** & **family members**, **B. Esrayelu** & **family members**, **K. Anil** & **family members (U.S.A.)**, **Nidhi Singh** and her husband **Sandeep Singh**, **Sarika Gupta** and her husband **Srikanth**, **Andy Baird** & **family members (U.S.A.)**, **Mr. T. B. R. Prasad** & **family members**, **Mr. Medanki Subbarao** & **family members**, **Mr. I. Satyaraju** and all family well-wishers for their invaluable support. I extend my gratitude to **Robert M. Bland (U.S.A.)**, Founder, Teen Missions International through **TMI India** for teaching me the crucial values about hard work and perseverance that seem to be severely lacking in our modern society. I also would like to thank the believers of **Good Shepherd Prayer Hall** for their constant prayers. Most importantly, none of this would have been possible without my family members, my dear lovable father **Rev. Bokinala Abraham**, mother **G. K. Karuna Kumari** and brother **B. Isac Maria Ben**, thank you all for your unflagging love, guidance and support even in the critical situations.

Last but not least, I would like to thank the Defence Research and Development Organization (DRDO), Ministry of Defence, Govt. of India through **ACRHEM** for their financial support. I also would like to acknowledge the director **Dr. V Kameswara Rao** and former director's of **ACRHEM**, Dean **Prof. V. Seshu Bai** and former deans of School of Physics for administrative support.

Bokinala Moses Abraham

Contents

List of Figures

List of Tables

Chapter 1

Introduction

Energetic Materials (EMs) cover a wide range of substances that can react to release a large amount of energy upon external stimulus such as heat, shock, impact, spark, etc. The development of EMs began around the thirteenth century with the formulation and use of gunpowder, which is also known as a black powder. EMs were initially used for fireworks (entertainment), but their power in the realm of armed conflict was also identified. Energetic materials include explosives, propellants and pyrotechnics that are widely used for a variety of civilian and military applications [1–3]. Explosives are further classified as primary and secondary explosives: the former are low-performing and highly sensitive compounds [4, 5], which leads to a very fast detonation to deflagration transition by producing a shock wave that is capable of initiating less sensitive and more powerful secondary explosive [6]. Primary explosives are used in blasting caps, primers, detonators and initiators, whereas the secondary explosives are used as projectiles in warheads. Secondary explosives are further divided into two categories: Low Performance Energetic Materials (LPEMs) and High Energy Density Materials (HEDMs). The purpose of LPEMs is to produce possible lowest sensitivity by sacrificing a small amount of performance, while the HEDMs are designed to produce relatively high performance. Propellants do not detonate but undergo rapid combustion leading to deflagration by releasing a significant volume of gas to generate relatively high pressure and temperatures, which are sufficient to raise, accelerate and move objects like missiles, projectiles, rockets, etc. [7–9]. Propellants are mainly divided into rocket and gun propellants: the former is either liquid or solid that acts as a propulsion system, whereas a gun propellant consists of both fuel and oxidizer. To further enhance the power of propellants, double

and triple based propellants containing one or more energetic components are developed based on nitroglycerin and nitroguanidine composition. Pyrotechnics undergo self-contained and self-sustained exothermic chemical reactions to generate defined visual and acoustic effects (fire, smoke, heat, light, sound, explosion or gas emission) [10–14]. Pyrotechnics are primarily classified into light-emitting, smoke generating and heat-generating pyrotechnics. The light-emitting pyrotechnics are used as fireworks, illumination (infrared and visible) and decoy flares. Smoke generating pyrotechnics are used for signaling and camouflage purposes. The heat-generating pyrotechnics are used as incendiary compositions, detonators and priming charges.

1.1 Energy – safety contradiction of EM's

In the field of EMs, energy may refer to multiple indices, such as power, detonation pressure, detonation velocity, reaction heat (heat of detonation or combustion) and so forth. The safety is generally evaluated by different kinds of sensitivities and is explained through the style of stimulation. The sensitivities are the degrees of an EM in response to different styles of external stimuli: higher sensitivity indicates lower safety [15, 16]. Therefore, both energy and safety are the most important parameters to tune the properties of EMs, as the energy refers to their performance and the safety assures their applicability. However, the controversial drama between energy and safety placed a great challenge on developing energetic materials with desired properties. It is generally known as energy-safety contradiction [17]. For example, CL-20 [18] and ONC [19] contains high performance than any other energetic materials, but the presence of more nitro groups and their sensitivity make the synthesis more expensive and strenuous. On the other hand, FOX-7 [20] is the best insensitive energetic material than the well-known TNT, but it possesses only 70% of the heat of detonation than the most widely used RDX and HMX [21]. Thus, an improved explosive should achieve an optimum balance between these two inherently contradicting objectives, implying a challenge to create highly energetic and low sensitive explosives. This is the major reason for less number of energetic materials in practical applications,

even though a large number of explosives are synthesized every year.

Typically, the response of an energetic material against an external stimulus can be referred to as low sensitivity and is governed by its physicochemical properties, multiscale structures, the live stimulation styles and the measurement conditions. Among these parameters, molecular and crystal structures (multiscale structures) are crucial in improving the safety of energetic materials from the point of view of the intrinsic qualities. At the level of molecule, the energy-safety contradiction is inherent; while, it can largely be alleviated at the higher level of crystal, i.e., to facilitate reduced sensitivity by improving crystal packing. In fact, it is essential to know what type of packing structure makes the ignition of energetic materials efficient or inefficient after impact. In other words, the energetic materials with a packing structure of ready shear sliding facilitate low impact sensitivity, in combination with high molecular stability. Generally, as shown in figure 1.1, the crystal packing is classified using four types of π - stacking: (1) face-to-face type: all molecular planes in crystal are parallel to one another, (2) crossing type and (3) wavelike type: All the molecular planes in crystal are either parallel or not parallel to two planes. If there is an inter-molecular crossing along these two planes, the crystal belongs to the crossing type; otherwise, it belongs to the wavelike type; and (4) mixing type: this type of stacking is different from the other three types of stacking. Among all the types, the perfect face-to-face crystal stacking, constructed with strong intra- and intermolecular hydrogen bonding, is highly desirable for impact insensitive EMs as it can efficiently buffer against external stimuli, facilitating low mechanical sensitivity. On the other hand, enhancing the detonation performance is still a primary challenge. Traditional explosives such as RDX, TNT and CL-20 gain their energy from the oxidation of a carbon backbone by oxidizing groups present in the same molecule. An explosive with a denser backbone generally tends to improve the density and detonation performance, while cleverly incorporating numerous explosophores (e.g., N_3, NO_2 and ONO_2) into the same energetic backbone also improves both. For instance, CL-20 possess highest energy than RDX and TNT since it contains dense strained backbone compared to the heterocyclic backbone of RDX and the benzene backbone of TNT. Meanwhile, the modern HEDMs derive most of their energy from

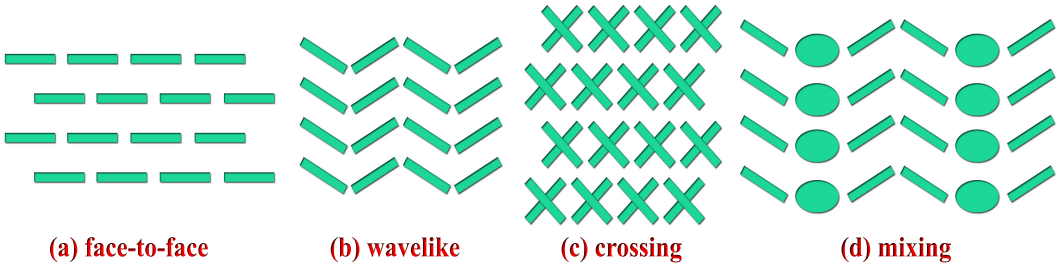

Figure 1.1: Four types of π-π stacking in energetic materials.

a combination of positive heats of formation rather than the oxidation of carbon backbone in traditional explosives. In recent years, fully nitrated heterocycles have shown enormous potential and emerged as eco-friendly EMs [22, 23]. The compatibility between backbones and explosophores has been thoroughly analyzed by studying the essential energetic features of the fully nitrated heterocycles [24, 25]. Specifically, five-membered azole moieties with high nitrogen content are widely used as energetic frameworks because of their decent balance between molecular stability and energetic performance, strikingly highlighting the uniqueness in the world of energetic materials [26, 27]. In addition, the introduction of oxygen atom on these fully nitrated heterocycles improves the oxygen balance and also enhances the density and balance the sensitivity [28, 29].

1.2 Role of hydrogen bonding in EM's

Most of the energetic solids are molecular crystals that are held together by intermolecular interactions, especially hydrogen bonding. The interactions between hydrogen and other atoms have found multiple applications in physical and chemical science [30, 31]. By smartly incorporating the energetic groups as proton acceptors, one can expect a strong hydrogen bonding networks that are crucial for the construction of high energy density materials [32–34]. The improved intra- and intermolecular interactions can tightly pack the crystal and thereby reducing the volume, which in turn enhances the density and stability of the EMs [35]. Therefore, multiple hydrogen bond interactions are highly efficient strategy to improve the performance and stability of explosives. For instance, the

density of 1,3,5-triamino-2,4,6-trinitrobenzene (TATB, 1.937 g cm^{-3}) is remarkably higher that of 1,3,5-trinitrobenzene (TAB, 1.676 g cm^{-3}) [36], which is primarily originating from additional amino-functionalization by virtue of strong hydrogen bonding interactions [37–39] (see figure 1.2).

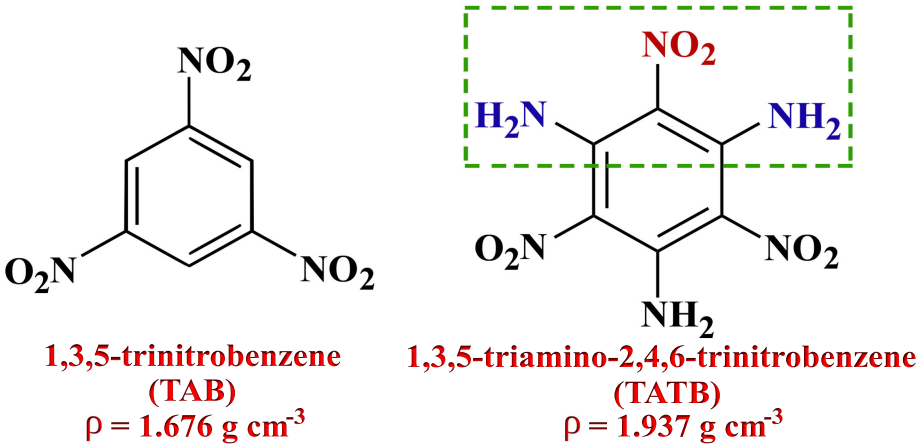

Figure 1.2: Molecular structures of 1,3,5-trinitrobenzene (TAB) and 1,3,5-triamino-2,4,6-trinitrobenzene (TATB).

In designing improved explosives, a key goal is to achieve an optimum balance between two inherently contradictory objectives: a high level of detonation performance and low sensitivity to accidental initiation of detonation. Apart from energetic co-crystals and metal-organic frameworks, another interesting approach to design powerful EMs is through the formulation of energetic ionic salts (EIS). The combination of their inherent individual explosive properties and unusual chemical structures yields a unique class of EIS with enhanced power due to distinct crystal packing and anion-cation interactions [40]. The principle parameter to design these EIS is to attain higher densities than their parent compounds. Typically, in metal salts, the nondirectional, soft and delocalized interactions allow the crystal to pack tightly, leading to greater densities [41, 42]. These intermolecular interactions between cation and anions play an important role in improving crystal packing efficiency, density and stability, which is revealed in several low sensitive HEDMs. Apart from their stability, such hydrogen bonding interactions can minimize their solubility and toxicity in most of

the common solvents. In addition, these materials possess advantages over parent nonionic molecules by exhibiting lower vapor pressures, which significantly reduces the risk of exposure via inhalation [43–45]. Recently, several EIS were derived from triazole, tetrazole and imidazole in which each cation or anion couple with its counterparts via protonation reactions that can overcome the associated adverse behavior. For example, 3,4-diamino-1,2,4-triazolium 5-nitrotetrazolate (1.739 gm cm^{-3}), 3,4-diamino-1,2,4-triazolium perchlorate (1.798 gm cm^{-3}) and 1-amino-1,2,3-triazolium 5-nitroiminotetrazolate (1.72 gm cm^{-3}), 1-amino-1,2,3-triazolium nitroformate (1.86 gm cm^{-3}) possess remarkably higher densities than their parent 3,4-diaminotriazole (1.552 gm cm^{-3}) [46] and 1-amino-1,2,3-triazole (1.423 gm cm^{-3}) [47] compounds, respectively. Hence, the dream of high performance with better sensitivities can be obtained through EIS.

1.3 High pressure research

The pressure is an important fundamental thermodynamic variable, which is defined as the force per unit area. The application of pressure on materials can be broadly categorized into two types: (i) electronic and (ii) lattice effects; in fact, these two effects are related to each other. In electronic effects, the function of pressure brings the ions closer, resulting in an outer electron orbitals overlap leading to semiconductor/insulator to metal transition or vice versa. In lattice effects, the inter-ionic distance decreases with increasing pressure, leading to hardening of phonon spectra and thereby changing the thermo-physical properties. In general, the pressure can be induced through experimentally or computationally. The former requires specialized techniques to impose high pressure on a sample. There are two major experimental techniques: static compression method and dynamic compression approach. In a static compression experiment, pressure cells are applied, namely diamond anvil cells [48–50]. shock-wave compression techniques [51, 52] are applied through strong shock to the sample and the propagation velocities of the shock wave within the sample are measured. From the computational point of view, the application of pressure is relatively straight forward within the framework of density functional theory: one simply calculates the applied

pressure either from the volume derivative of the calculated total energy or analytically from the self-consistent one-electron states. The former requires fitting an equation of state.

Materials could exhibit various properties and structures as a function of pressure, leaving us a huge space for producing new materials by tuning the pressure. Moreover, the effect of hydrostatic pressure can alter the molecular geometry, thereby tuning the molecular properties of EMs. In general, when an explosive detonates, the shock wave can produce a pressure of 500,000 times than the Earth's atmosphere and internal temperatures soar up to 3500 K [53, 54]. When shock propagates through an energetic solid, it suffers a sudden compression in volume by almost 30% and causes dramatic changes in the electronic properties. Moreover, polymorphism and phase transition in an EM play a crucial role in defining the performance of an explosive, which is mainly depending upon the type of polymorph that is used. Polymorphs with discrete crystal densities can change the detonation properties since detonation velocity is proportional to crystal density. Therefore, it is crucial to achieving a higher dense form of EMs in order to gain maximum detonation velocities. For instance, HMX can exist in four crystalline forms whose sensitivities are of order $\delta > \gamma > \alpha > \beta$, in which only β - HMX is widely used in energetic applications. However, the experimental determination of energetic materials to study the structure-properties under extreme conditions are impractical due to the unavailability of appropriate experimental techniques. Apart from the traditional experimental approaches, high-pressure technique using theoretical simulations is a modern weapon, especially in the field of EMs, which can change the intermolecular interactions, thereby inducing structural phase transition or even polymorphs.

Pressure on the scale of gigapascals can cause remarkable changes in the intermolecular interactions and reveals the hidden phenomena lying behind the extreme conditions [55–57]. Moreover, the influence of pressure on the crystal structure of energetic materials can facilitate efficient crystal packing and tune the non-covalent hydrogen bond interactions, thereby improving the detonation properties. These types of studies provide a better understanding of the nature of hydrogen bonding and structural stability of the energetic material under pres-

sure. Li et al.[58] carried out high pressure studies on energetic material acetamidinium nitrate ($C_2N_2H_7^+ \cdot NO_3^-$) using diamond anvil cell. Their results show a deviation in the ideal hydrogen bonded arrays along with a small slippage between adjacent ion pairs, which is responsible for the fabrication of new high density material with better detonation performance. The pressure induced rearrangement of hydrogen bonded networks causes a phase transition in carbohydrazide (CON_4H_6) energetic material [59]. The reported high pressure phase with space group P1 exhibits almost 23.1% higher density than the ambient structure ($P2_1/n$). However, the application of pressure can change the direction of atoms and molecules in hydrogen bonded structures, allowing the explosive properties (such as sensitivity) to be modified. Therefore, it is of great interest to study the behavior of hydrogen bonded systems under pressure for exploring high energy density materials.

1.4 Theory in energetic materials research

Theoretical simulations have become an indispensable tool in unraveling the intermolecular interactions within the crystal and are successful in accurately predicting the chemical and physical properties of a broad range of materials. Since, the experimentation with EMs requires sophisticated instruments, complicated procedures, time consuming and high maintenance costs, the implementation of quantum mechanical calculations have proven to be a cost- and time-effective strategy for understanding the behavior of EMs. Generally, most of the energetic solids contain molecules that are held together by van der Waals (vdW) interactions. Under external stimuli like hydrostatic pressure or a shock wave, the intermolecular interactions and the micro-structure may undergo significant changes, leading to a drastic variation in the mechanical, chemical and thermodynamic properties. Hence it is necessary to provide a clear picture of how the intermolecular interactions influence the macroscopic properties to enhance the energetic performance. However, the experimentally measured x-ray diffraction fails to locate the exact position of hydrogen atoms [60]; therefore, an effective density functional theory simulations [61] may help to study the atomic structure of

hydrogen containing materials, especially structures with intermolecular interactions. Moreover, due to the complexity of EMs, conventional electron exchange-correlation functionals fail to produce an accurate description of weak intermolecular interactions. This is clearly exemplified in various energetic crystals including RDX [62], FOX-7 [63, 64], CL-20 [65], TATB [66, 67], and HMX [68] and the results show that the generalized gradient approximation(GGA)/local density approximation (LDA) overestimate/underestimates the crystal volumes by nearly $\sim$30% when compared to experimental values. Therefore, to account for these long-range dispersive interactions quantitatively, a wide range of new functionals were developed to extend DFT and are continuously being improved.

1.5 Density functional theory

Advances in electronic structure calculations along with year-on-year enhancement in computational power enabled quantum mechanical calculations as accurate materials simulations and became as an integral tool in most of the materials investigations. Density functional theory (DFT) is one of the most successful and powerful quantum mechanical approaches, which is generally known as a mainstay of electronic structure calculations. From its origins in condensed matter physics, it has broadened into solid-state chemistry, high-pressure physics, materials science and more, powering entire theoretical sub-disciplines. DFT is neither just an approach of parameterizing empirical results nor simply another procedure of approaching the Schrödinger equation. It is a completely different method of solving *any* interacting problem, through mapping it *exactly* to a more simple-to-solve non-interacting problem. The theory originated in early thirties of the twentieth century from the pioneering work of Thomas [69] and Fermi [70] and further refined by Hartree [71], Dirac [72, 73], Fock [74] and Slater [75–77]. However, a solid foundation was given by Hohenberg, Kohn and Sham almost forty years after the work of Thomas and Fermi. In 1964, Hohenberg and Kohn proved that the ground state density uniquely determines the potential and thus, all properties of the system, including the many-body wave function. Almost exactly a year after the Hohenberg-Kohn theorems were published, Kohn and

Sham derived a set of self-consistent, iteratively solvable equations, which finally allowed us to do the actual computer simulations. For solving the Kohn–Sham equations, various efficient algorithms have been developed in increasingly sophisticated codes, which tremendously enhanced the application of DFT methods. In 1998, Kohn won the Nobel prize in chemistry for his development of the density-functional theory [78, 79].

1.6 Outline of the thesis

The primary objective of the thesis is to provide a clear picture of how the intermolecular interactions, especially hydrogen bonding, influence the macroscopic properties to enhance the energetic performance with reasonable sensitivity. Theoretical approach to demonstrate the structure - properties - performance interrelationship is shown in figure 1.3. Also, the effect of hydrostatic pressure was systematically investigated to understand the remarkable variations in the noncovalent interactions for the construction of high energy density materials. In order to conduct these studies, quantum mechanical calculations were performed using various density functional theory approaches. These computational studies are aimed to design models for accurate prediction of properties and performance of the existing as well as new EMs. In the present thesis, the physicochemical and detonation characteristics including structural, electronic, vibrational and performance parameters (heat of formation, detonation velocities and detonation pressures) for diammonium 5,5'-bistetrazole-1,1'-diolate (ABTOX), dimethylamine 5,5'-bistetrazole-1,1'-diolate (DMA-BTO), diuronium 1H,1'H-5,5'-bistetrazole-1,1'-diolate (DU-BTO), hydrazine 5,5'-bitetrazole-1,1'-diolate (HA-BTO), bis-2-methylimidazolium 1H,1H-5,5-bistetrazole-1,1'-diolate (M_2-BTO), dihydroxyl ammonium 5,5'-bistetrazole-1,1'-diolate (TKX-50), diammonium 3,3′-dinitro-5,5′-bis-1,2,4-triazole-1,1-diolate (DA-DNBTO) and dihydrazinium 3,3′-dinitro-5,5′-bis-1,2,4-triazole-1,1-diolate (DH-DNBTO) and 3,6-dihydrazino-s-tetrazine (DHT) were discussed in detail. Since the energetic solids contain molecules that are held together by van der Waals (vdW) interactions, we incorporated dispersion corrected DFT methods to capture these weak intermolecular interactions. In addition,

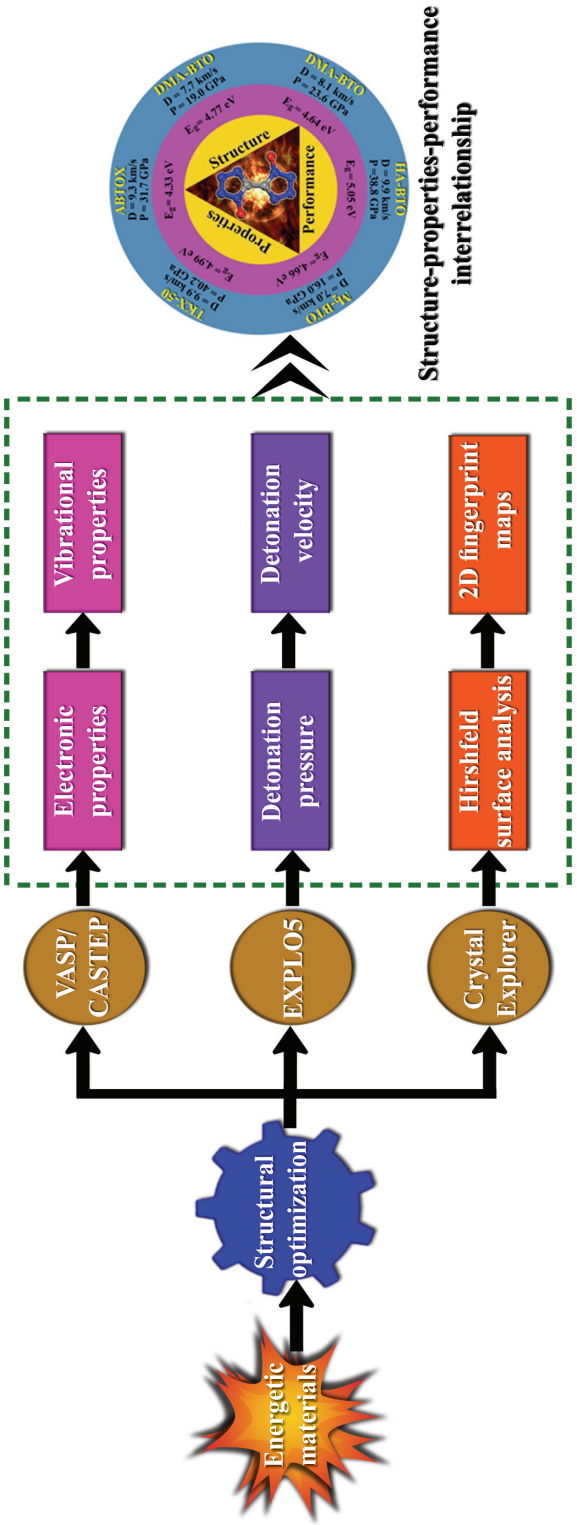

Figure 1.3: Theoretical approach to demonstrate the structure - properties - performance inter-relationship.

to predict reliable electronic band gaps, more accurate Heyd–Scuseria–Ernzerhof (HSE) hybrid functional obtained by mixing the PBE scheme with a certain quantity of non-local Hartree-Fock (HF) exchange energy has been implemented. The theory behind Hirshfeld surfaces and the associated 2D fingerprint plots for quantitative visualization of intermolecular interactions were also discussed.

Chapter 2 provides a short description of basic theoretical and mathematical background of the quantum mechanical calculations, which will help to understand the concepts of the DFT in more detail. It also includes various recently developed dispersion correction approaches for treating weak intermolecular interactions. In addition, the methodology of Heyd–Scuseria–Ernzerhof (HSE) hybrid functional for computing the electronic structure and optical properties were described in detail.

Chapter 3 presents the structure-property-performance interrelationship for a series of energetic ionic salts based on 5,5′-bitetrazole-1,1′-diolate (BTO). The physicochemical and detonation characteristics of these energetic salts including structural, electronic, vibrational and performance parameters (heat of formation, detonation velocities and detonation pressures) were discussed in detail. To predict the accurate energy band gap, electronic band structures for the studied energetic salts were calculated using HSE06 hybrid functional, which are found to be wide band gap insulator with a bandwidth ranging from 4.33-5.05 eV. The strong intermolecular hydrogen bonding environment between various cations and the BTO^{2-} anion are mainly responsible for enhanced molecular stability and prominent detonation performance. Such strong intermolecular hydrogen bonds are observed in hydroxylammonium and hydrazine cation compared to other cations. Careful inspection of various EIS revealed that the hydroxylammonium and hydrazine cations produce the highest density relative to other cations when combined with BTO anion. The detonation characteristics of BTO^{2-} are computed using EXPLO5 code [80]. In particular, TKX-50 and HA-BTO exhibit high detonation velocities (9.91 and 9.94 km/s) and detonation pressure (40.23 and 38.85 GPa), superior than the conventional nitrogen-rich explosive materials with moderate sensitivities. These results highlight the importance of hydrogen bonding interactions in designing energetic salts for next-generation explosives,

propellants and pyrotechnics.

In **chapter 4**, the quantum mechanical calculations and structure analysis were performed for similar energetic ionic salts (EIS) based on 3,3′-dinitro-5,5′-bis-1,2,4-triazole-1,1-diolate anion with ammonium (DA-DNBTO) and hydrazinium (DH-DNBTO) cations. The geometric optimization demonstrates the significance of van der Waals correction when studying the structure and properties of EIS, and highlights the importance of DFT-D2 method proposed by Grimme in reproducing the experimental crystal structures of energetic salts. The IR spectrum of DA-DNBTO contains a number of intense peaks in the high frequency range (above 2850 cm^{-1}) compared to DH-DNBTO. Especially, the electronic band gap of DNBTO salts obtained using the HSE06 hybrid functional is reduced to 50% when compared with that of BTO based energetic salts due to NO_2 group attached to the DNBTO anion. Besides, the O...O contacts that generally exist in most of the EMs do not show much impact on both the studied energetic salts. The strong intermolecular interactions of DA-DNBTO represents its inferiority in molecular stability, which is in good agreement with the experimentally measured impact sensitivity (>40 J) and friction sensitivity (360 N) values and also explains why it has the highest stability compared to DH-DNBTO. Our calculations re-verifies the importance of intermolecular hydrogen bonding in the construction of high performance and low sensitive energetic materials.

In **chapter 5**, the pressure dependent structural changes, IR spectra and the Hirshfeld surfaces of 3,6-dihydrazino-s-tetrazine (DHT) were reported in order to provide a detail description of hydrogen bonding interactions using dispersion corrected density functional theory (DFT). The strengthening of hydrogen bonding is observed by the pressure induced weakening of covalent N-H bonds, which is consistent with the red shift of NH/NH_2 stretching vibrational modes. The intermolecular interactions in DHT crystal lead to a more compact and stable structure that can increase the density but diminishes the heat of detonation, Q. The calculated detonation properties of DHT (D = 7.62 km/s, P = 25.19 GPa) are slightly smaller than the similar explosive 3,6-bis-nitroguanyl-1,2,4,5-tetrazine (BNT, D = 7.9 km/s, P = 27.36 GPa). Overall, the crystallographic and spectroscopic results along with Hirshfeld surface analysis as a function of pressure

reveal the presence of strong hydrogen bonding networks in the crystal structure of DHT.

In **chapter 6**, the potential crystal structures and properties of urea as a function of pressure were studied using ab-initio based electronic structure calculations. The enthalpy-pressure behavior shows that urea undergoes pressure induced structural phase transition from $P42_1m$ (phase I) $\rightarrow$ $P2_12_12_1$ (phase III) at 0.66 GPa with a volume collapse of 4.83%, driven by softening of acoustic mode along Γ-X direction. Another phase transition from $P2_12_12_1 \rightarrow P2_12_12$ structure is identified at 3.09 GPa. The softening of acoustic mode in U-R direction along with the violation of Born stability criteria in $P2_12_12_1$ structure is responsible for the pressure induced phase transition. Further, the adoption of pressure leads to breaking and formation of N-H...O bonds in the crystal structure of urea during phase transition, i.e., the H-acceptor capacitance of oxygen atom is varied between phase I/IV and -III. Band structure calculations were performed using hybrid functional (Heyd, Scuseria and Ernzerhof, HSE), which includes a part of exact Fock-exchange. The computed electronic band structure shows that the urea polymorphs are insulators with a direct band gap of 6.21, 6.85 and 6.99 eV for phase -I, -III and -IV, respectively, at selected pressures. We have also presented the dielectric functions (real ($\epsilon_1(\omega)$) and imaginary ($\epsilon_2(\omega)$) parts), refractive index and absorption coefficients to explore the optical characteristics of urea phases. The geometry interpretation of intermolecular interactions was quantitatively visualized using Hirshfeld surface analysis. Our results provide a complete picture on various properties of urea polymorphs that lay the foundation for further understanding of structures and their applications.

Finally, **chapter 7** summarizes the outcome of the entire thesis and also outlined some future research directions which have emerged naturally during the course of the current thesis work.

References

[1] D. Schmitt, P. Eyerer and P. Elsner, Propellants, Explos. Pyrotech., **22**, 109 (1997).

[2] M. B. Talawar, R. Sivabalan, T. Mukundan, H. Muthurajan, A. K. Sikder, B. R. Gandhe and A. S. Rao, J. Hazard. Mater., **161**, 589 (2009).

[3] D. M. Badgujar, M. B. Talawar, S. N. Asthana and P. P. J. Mahulikar, Hazard. Mater., **151**, 289 (2008).

[4] L. E. Fried and A. J. J. Ruggiero, Phys. Chem., **98**, 9786 (1994).

[5] M. B. Talawar, A. P. Agrawal, M. Anniyappan, D. S. Wani, M. K. Bansode and G. M. J. Gore, Hazard. Mater., **B137**, 1074 (2006).

[6] S. Meyers and E. S. J. Shanley, Hazard. Mater., **23**, 183 (1990).

[7] H. J. Maag and G. Klingenberg, Propellants, Explos. Pyrotech., **21**, 1 (1996).

[8] R. W. Millar, J. Hamid, R. Endsor, P. F. Swinton and J. Cooper, Propellants, Explos. Pyrotech., **33**, 66 (2008).

[9] J. Boehnlein-Mauss and H. Kroeber, Propellants, Explos. Pyrotech., **34**, 239 (2009).

[10] J. M. Welch, *Low Sensitivity Energetic Materials*, Ph.D. Thesis, Ludwig-Maximilians-Universität, München (2008).

[11] A. Ozretic, Can. Chem. News, **62**, 12 (2010).

[12] D. Spitzer, M. Comet, C. Baras, V. Pichot and N. Piazzon, J. Phys. Chem. Solids, **71**, 100 (2010).

[13] G. Steinhauser and T. M. Klapötke, Angew. Chem. Int. Ed., **47**, 3330 (2008).

[14] S. M. Danali, R. S. Palaiah and K. C. Raha, Def. Sci. J., **60**, 152 (2010).

[15] L. E. Fried, M. R. Manaa, P. F. Pagoria and R. L. Simpson, Annu. Rev. Mater. Res., **31**, 291 (2001).

[16] H. Dong and F. Zhou, *Properties of High Energetic Explosives and Relatives*, Science Press: Beijing (1989).

[17] C. Zhang, J. Energy Mater., **26**, 2 (2018).

[18] A. T. Nielsen, A. P. Chafin, S. L. Christian, D. W. Moore, M. P. Nadler, R. A. Nissan, D. J. Vanderah, R. D. Gilardi, C. F. George and J. L. Flippen-Anderson, Tetrahedron, **54**, 11793 (1998).

[19] M. X. Zhang, P. E. Eaton and R. Gilardi, Angew. Chemie Int. Ed., **39**, 401 (2000).

[20] A. K. Mandal, U. Thanigaivelan, R. K. Pandey, S. Asthana, R. B. Khomane and B. D. Kulkarni, Org. Process Res. Dev., **16**, 1711 (2012).

[21] R. Meyer, J. Kohler and A. Homburg, Explosives, *Wiley-VCH; Verlag GmbH, Weinheim*, (2007).

[22] Y. Liu, C. He, Y. Tang, G. H. Imler, D. A. Parrishc and J. M. Shreeve, Dalton Trans., **47**, 16558 (2018).

[23] R. W. Millar, S. P. Philbin, R. P. Claridge and J. Hamid, Propellants Explos. Pyrotech., **29**, 81 (2004).

[24] P. Yin, Q. Zhang and J. M. Shreeve, Acc. Chem. Res., **49**, 4 (2016).

[25] P. Yin, D. A. Parrish and J. M. Shreeve, Angew. Chem. Int. Ed., **53**, 12889 (2014).

[26] H. Wei, J. Zhang, C. He and J. M. Shreeve, Chem. Eur. J., **21**, 8607 (2015).

[27] J. Zhang, S. Dharavath, L. A. Mitchell, D. A. Parrish and J. M. Shreeve, J. Am. Chem. Soc., **138**, 7500 (2016).

[28] A. A. Dippold and T. M. Klapotke, J. Am. Chem. Soc., **135**, 9931 (2013).

[29] Y. Shang, B. Jin, R. Peng, Z. Guo, Q. Liu, J. Zhao and Q. Zhang, RSC Adv., **6**, 48590 (2016).

[30] N. U. Zhanpeisov and M. J. Anpo, Am. Chem. Soc., **126**, 9439 (2004).

[31] S. Grabowski, J. Chem. Rev., **111**, 2597 (2011).

[32] J. H. Joo and J. M. Shreeve, J. Am. Chem. Soc., **132**, 15081 (2010).

[33] A. K. S. Mehilal, R. K. Sinha and B. R. J. Gandhe, Hazard. Mater., **102**, 137 (2003).

[34] N. V. Latypov, J. Bergman, A. Langlet, U. Wellmar and U. Bemm, Tetrahedron, **54,** 11525 (1998).

[35] C. Ye and J. M. Shreeve, J. Phys. Chem. A, **111**, 1456 (2007).

[36] C. S. Choi and J. E. Abel, Acta Crystallogr., **B28**, 193 (1972).

[37] D. M. Hoffman and A. T. Fontes, Propellants, Explos. Pyrotech., **35**, 15 (2010).

[38] C. M. Tarver, J. Phys. Chem. A, **114**, 2727 (2010).

[39] H. H. Cady and A. C. Larson, Acta Crystallogr., **18**, 485 (1965).

[40] M. Armand, F. Endres, D. R. MacFarlane, H. Ohno and B. Scrosati, Nat. Mater., **8**, 621 (2009).

[41] C. F. J. Faul and M. Antonietti, Adv. Mater., **15**, 673 (2003).

[42] J. Perez and L. Riera, Chem. Commun., **0**, 533 (2008).

[43] R. P. Singh, R. D. Verma, D. T. Meshri and J. M. Shreeve, Angew. Chem., Int. Ed., **45**, 3584 (2006).

[44] H. X. Gao and J. M. Shreeve, Chem. Rev., **111**, 7377 (2011).

[45] R. Wang, Y. Guo, R. Sa and J. M. Shreeve, Chem. - A Eur. J., **16**, 8522 (2010).

[46] J. T. Wu, J. G. Zhang, X. Yin and K. Wu, Chem. - An Asian J., **10**, 1239 (2015).

[47] Q. H. Lin, Y. C. Li, Y. Y. Li, Z. Wang, W. Liu, C. Qi and S. P. Pang, J. Mater. Chem., **22**, 666 (2012).

[48] A. Jayaraman, Rev. Mod. Phys., **55**, 65 (1983).

[49] A. Jayaraman, Rev. Sci. Instrum., **57**, 103 (1986).

[50] A. L. Ruoff, *Recent Trends in High Pressure Research*, Oxford & IBH, New Delhi, p.769 (1992).

[51] H. Nagao, K. G. Nakamura, K. Kondo, N. Ozaki, K. Takamatsu, T. Ono, T. Shiota, D. Ichinose, K. A. Tanaka, K. Wakabayashi, K. Okada, M. Yoshida, M. Nakai, K. Nagai, K. Shigemori, T. Sakaiya and K. Otani, Phys. Plasma., **13**, 052705 (2006).

[52] J. H. Eggert, D. G. Hicks, P. M. Celliers, D. K. Bradley, R. S. McWilliams, R. Jeanloz, J. E. Miller, T. R. Boehly and G. W. Collins, Nat. Phys., **6**, 40 (2010).

[53] F. A. Fabbiani and C. R. Pulham, Chem. Soc. Rev., **35**, 932 (2006).

[54] C. Hejny and V. S. Minkov, IuCrJ, **2**, 281 (2015).

[55] T. T. Yan, S. R. Li, K. Wang, X. Tan, Z. M. Jiang, K. Yang, B. B. Liu, G. T. Zou and B. Zou, J. Phys. Chem. B, **116**, 9796 (2012).

[56] C. Q. Sun, X. Zhang and W. Zheng, Chem. Sci., **3**, 1455 (2012).

[57] K. Roszak and A. Katrusiak, J. Phys. Chem. C, **121**, 778 (2017).

[58] S. Li, Q. Li, R. Li, J. Liu, K. Yang, B. Liu and B. Zou, J. Phys. Chem. C, **118**, 23443 (2014).

[59] T. Yan, K. Wang, X. Tan, J. Liu, B. Liu and B. Zou, J. Phys. Chem. C, **118**, 22960 (2014).

[60] K. Fucke and J. Steed, Water, **2(3)**, 333 (2010).

[61] I. Ortega, R. Escribano, D. Fernandez, V. Herrero, B. Mate, A. Medialdea and M. Moreno, Chem. Phys. Lett., **378**, 218 (2003).

[62] M. S. Miao, Z. A. Dreger, J. M. Winey and Y. M. Gupta, J. Phys. Chem. A, **112**, 12228 (2008).

[63] J. J. Zhao and H. Liu, Comput. Mater. Sci., **42**, 698 (2008).

[64] S. Appalakondaiah, G. Vaitheeswaran and S. Lebegue, J. Chem. Phys., **140**, 014105 (2014).

[65] E. F. C. Byrd and B. M. Rice, J. Phys. Chem. C, **111**, 2787 (2007).

[66] H. Liu, J. J. Zhao, J. G. Du, Z. Z. Gong, G. F. Ji and D. Q. Wei, Phys. Lett. A, **367**, 383 (2007).

[67] S. Appalakondaiah, G. Vaitheeswaran and S. Lebegue, J. Phys. Chem. A, **119**, 6574 (2015).

[68] E. F. C. Byrd, G. E. Scuseria and C. F. Chabalowski, J. Phys. Chem. B, **108**, 13100 (2004).

[69] L. H. Thomas, Proc. Cambridge Phil. Soc., **23**, 542 (1926).

[70] E. Fermi, Z. Phys. **48**, 73 (1928).

[71] D. R. Hartree, Proc. Cambridge Phil. Soc., **24**, 89 (1928).

[72] P. A. M. Dirac, Proc. Royal Soc., (London)A, **123**, 714 (1929).

[73] P. A. M. Dirac, Proc. Cambridge Phil. Soc., **26**, 376 (1930).

[74] V. Fock, Z. Phys., 61, **126** (1930).

[75] J. C. Slater, Phys. Rev., **81**, 385 (1951).

[76] J. C. Slater, Phys. Rev., **82**, 538 (1951).

[77] J. C. Slater, Phys. Rev., **91**, 52 (1953).

[78] P. Hohenberg and W. Kohn, Physical Review, **136**, B864 (1964).

[79] W. Kohn, Reviews of Modern Physics, **71**, 1253 (1999).

[80] M. Suceska, Propellants Explos. Pyrotech., **24**, 280 (1999).

Chapter 2

Theoretical background

This chapter provides a quick pedagogical introduction to the basic theory essential for this thesis. Typically, to study various chemical and physical properties of materials, one needs to understand it from an atomistic view. Density functional theory (DFT) is an appropriate computational tool to deal with these kinds of problems. The fundamental concept behind this theory is, for any electronic system, the energy can be determined explicitly in terms of electron probability density [1]. For a more thorough introduction, refer theory books on electronic structure calculations [1–4] on which most of this introduction is based upon. In the following sections, the principles of DFT formalism and exchange-correlational functionals were discussed. Subsequently, the state-of-the-art dispersion correction methods are also discussed for describing long-range van der Waals (vdW) interactions. A brief description is given for Heyd-Scuseria-Ernzerhof (HSE) hybrid functional to predict reliable electronic and optical properties for the investigated compounds. Finally, the theory behind the Hirshfeld surface analysis was discussed in detail, which is used for quantitative visualization of intermolecular interactions.

2.1 The many-body Schrödinger equation

The most fundamental governing equation in a quantum mechanical description involves the computation of electronic wavefunctions by solving the time-independent Schrödinger equation for non-relativistic particle system:

$$\hat{H}|\psi> = E|\psi> \tag{2.1}$$

where E is the energy eigen value and $\hat{H}$ is the molecular electronic Hamiltonian operator which acts on the total wavefunction ψ.
The Hamiltonian operator for a system of atoms can be written as

$$\hat{H} = -\sum_{i=1}^{N_e} \frac{\hbar^2}{2m_i}\nabla_i^2 - \sum_{I=1}^{N_n} \frac{\hbar^2}{2M_I}\nabla_I^2 + \frac{e^2}{2}\sum_{I,J=1}^{N_n}\sum_{I\neq J}^{N_n} \frac{Z_I Z_J}{|R_I - R_J|} + \frac{e^2}{2}\sum_{i,j=1}^{N_e}\sum_{i\neq j}^{N_e} \frac{1}{|r_i - r_j|} - \frac{e^2}{2}\sum_{i=1}^{N_e}\sum_{I=1}^{N_n} \frac{Z_I}{|r_i - R_I|} \tag{2.2}$$

where $R = \{R_I/R_J, I/J = 1, 2, ...N_n\}$ is a set of N_n nuclear coordinates and $r = \{r_i/r_j, i/j = 1, 2, ...N_e\}$ is a set of N_e electronic coordinates. M_I (or M_J) and Z_I (or Z_J) are the nuclear masses and charges, respectively.
The above equation may be expressed more compactly as

$$\hat{H} = \hat{T}_e + \hat{T}_n + \hat{V}_{nn} + \hat{V}_{ee} + \hat{V}_{en} \tag{2.3}$$

Where $\hat{T}_e$ and $\hat{T}_n$ correspond to the kinetic energy operators for electrons and nuclei, whereas the $\hat{V}_{ee}$, $\hat{V}_{en}$ and $\hat{V}_{nn}$ terms represent electron-electron, electron-nucleus and nucleus-nucleus interactions, respectively. However, it is impossible to solve this equation exactly for any system more complex than a hydrogen atom. To turn the problem into a feasible enterprise, well-controlled and reasonable approximations are required.

2.1.1 The Born-Oppenheimer approximation

The first and fundamental approximation made in the electronic structure theory is the adiabatic or Born-Oppenheimer (BO) approximation, which leads to the decoupling of nuclear and electronic motions. As the electrons are lightest particles than the nuclei (the mass of the proton is approximately 2,000 times more than the electron), they react spontaneously to the displacements of nuclei due to their relatively low mass and thus, the motion of nuclei on any timescale is comparatively smaller than that of electrons. Therefore, it is convenient to describe the electronic states of a molecule by thinking that the nuclei are stationary and solve

the corresponding Schrödinger equation of a fixed molecular structure. The detail implications and a plausible derivation of the approximation can be found in Ref.[5, 6]. Following the approximation, we can come up with an electronic Hamiltonian by ignoring the nucleus-nucleus interaction and the kinetic energy term of the nucleus in equation 2.2:

$$\hat{H} = -\sum_{i=1}^{N_e} \frac{\hbar^2}{2m_i}\nabla_i^2 + \frac{e^2}{2}\sum_{i,j=1}^{N_e}\sum_{i\neq j}^{N_e} \frac{1}{|r_i - r_j|} - \frac{e^2}{2}\sum_{i=1}^{N_e}\sum_{I=1}^{N_n} \frac{Z_I}{|r_i - R_I|} \tag{2.4}$$

and can be simply expressed as

$$\hat{H} = \hat{T}_e + \hat{V}_{ee} + \hat{V}_{en} \tag{2.5}$$

Although this approximation significantly minimizes the complexity of handling the many-body Schrodinger equation; however, solving the electron-electron interaction in the above equation is still an extremely difficult task. In the light of the difficulties posed in finding solutions to the Schrödinger equation, many approximate electronic structure methods have been proposed from Hatree-Fock method to DFT approach to solve the so-called "Schrödinger-like" equations. As a result of rapid increase in the available of computational resources over the past 30 years, DFT has emerged as a most prominent and most extensively used first principles calculations, accounting for approximately 90% of all simulations today in the field of computational materials science. In the present thesis, the DFT approach was implemented, which is explained in the following sections.

2.2 Density functional theory

Based on the ideas of Thomas, Fermi, and many others, the DFT is made possible in 1964 with the formulation of Hohenberg and Kohn's fundamental theorems. The basic lemma of these theorems demonstrate that all the properties of a system can be uniquely determined by the ground state electron density. This statement is applicable to interacting particles of any system and the theorems are as follows:

2.2.1 The Hohenberg-Kohn theorems

Theorem-1: For interacting particles of any system in an external potential $V_{ext}(r)$, the ground-state particle density, $n_0(r)$ uniquely determines the potential $V_{ext}(r)$ (up to an additive constant).

This theorem enables us to establish a one-to-one unique correspondence between the ground-state density $n_0(r)$ and external potentia $V_{ext}(r)$, which in turn makes the energy and other physical observables only as a functional of the ground-state density $n_0(r)$ [4, 7, 8].

$$< \psi|A|\psi > = A[n_0(r)] \tag{2.6}$$

Theorem-2: The electron density $n(r)$ that minimises the energy E[n(r)] of the overall functional is the true electron density corresponding to the full solution of the Schrödinger equation.

$$E[n(r)] = F_{HK}[n(r)] + \int V_{ext}(r)n(r)dr \tag{2.7}$$

The functional F_{HK} is universal in the sense that it is independent of the external potential and the number of electrons. This is the most prominent interpretation of the Hohenberg and Kohn theorem; once approximations for the functional F_{HK} are known means we can apply it to all electronic systems. In the above equation, the exact ground-state total energy of the system E_0 is the global minimum value of the functional and the particle density that minimizes this functional is the exact ground-state density $n_0(r)$, *i.e.*,

$$\frac{\partial}{\partial n}E[n(r)]_{n=n_0} = 0, \textit{with } E_0 = E[n_0(r)] \tag{2.8}$$

However, the exact form of the electron density functional is not known. Through appropriate approximation, the framework of Hohenberg and Kohn provided an important method to recast the 3N-dimensional Schrödinger equation to a much simpler equation, which depends on just three spatial variables and may therefore be used to accurately calculate a wide range of ground state properties.

2.2.2 The Kohn-Sham equations

The framework of Hohenberg and Kohn used the ground state density to calculate properties of any system, but it does not provide a practical solution to find the ground state electronic density [9]. The possible way to determine the ground state electron density is given by Kohn-Sham (KS) equations. The basic idea is to replace the complicated many-body system by a corresponding fictitious system of non-interacting particles, each of which experiences the same external potential. Also, the exact ground state density can be written as the ground state density of a fictitious system of noninteracting particles. Within this assumption, the ground-state wave function of the system can be expressed using single-particle wavefunctions. The main advantage through this approach is to allow a straight forward determination of a large part of the kinetic energy in a simple way, i.e., the kinetic energy ($T[n]$) is decoupled into two parts as $T[n] = T_s[n] + T_c[n]$, where $T_c[n]$ represents the remainder and $T_s[n]$ is the kinetic energy of the non-interacting system, which can be expressed in terms of the single-particle orbitals, $\phi_i(r)$:

$$T_s[n] = -\frac{1}{2}\sum_{\sigma}\sum_{I=1}^{N}\int dr\phi_i^*(r)\nabla^2\phi_i(r). \tag{2.9}$$

Hence, an approximation to the kinetic energy may be computed using a manageable finite number of terms N and the mean density can be denoted in terms of the single particle wavefunctions. The density of the original many-body system containing an even number of spin-up and spin-down electrons can be expressed in terms of orbitals as

$$n(r) = \sum_{\sigma} n(r,\sigma) = \sum_{\sigma}\sum_{I=1}^{N}|\phi_i(r)|^2. \tag{2.10}$$

Thus, all $\phi_i(r)$ are functionals of n and the total number of electrons N is a simple functional of the density

$$N = \int n(r)dr \tag{2.11}$$

Coulomb (or Hartree) energy corresponding to the electron-electron interaction, equal to the classical electrostatic interaction potential U_H of the charge distribution $n(r)$, with the Hartree potential being

$$U_H[n] = \frac{1}{2}\int\int dr dr' \frac{n(r)n(r')}{|r-r'|} = \frac{1}{2}\int V_C(r)n(r)dr \tag{2.12}$$

where $V_C(r) = \int dr \frac{n(r)}{|r-r'|}$ and the external potential energy acting on the electrons can be written as

$$V_{ext}[n] = \int n(r)V_{ext}(r)dr \tag{2.13}$$

Returning to our energy functional with the interacting particle system, we introduce the exchange and correlation energy functional E_{xc} to relate the interacting particle system with the non-interacting one,

$$\begin{aligned} E_{KS}[n] &= T[n] + U[n] + V[n] \\ &= T_s[\phi_i[n]] + U_H[n] + E_{xc}[n] + V_{ext}[n] \\ &= T_s[n] + \int n(r)[V_{ext}(r) + \frac{1}{2}V_C(r)]dr + E_{xc}[n] \\ &= T_s[n] + V_{eff} \end{aligned} \tag{2.14}$$

where $V_{eff} = \int n(r)[V_{ext}(r) + \frac{1}{2}V_C(r)]dr + E_{xc}[n]$, the exchange-correlation energy E_{xc}[n] is defined as the difference between the true energy functional and the energy functional of the known components. One has to find a better approximation to E_{xc} in order to get good results for real materials. Kohn and Sham noticed that the total electron density of non-interacting particles moving in a potential called V_{KS} is identical to that of the real system of interacting electrons, which is given by

$$V_{KS}(r) = V_{ext}(r) + V_C(r) + V_{xc}(r) \tag{2.15}$$

with

$$V_{xc} = \frac{\delta E_{xc}}{\delta n} \tag{2.16}$$

is given as

$$H_{KS} = -\frac{1}{2}\nabla^2 + V_{KS}(r). \tag{2.17}$$

Therefore, Kohn-Sham Schrödinger-like equation can be written as

$$(H_{KS} - \varepsilon_i)\phi_i(r) = 0 \tag{2.18}$$

where ε_i are the eigenvalues of H_{KS} and the orbitals satisfying the above equation, ϕ_i, minimize the Kohn-Sham energy. This involves searching for the electron density that minimizes this functional, such that the solution of N single-particle equation determines the density and the ground-state energy of the system. Note that the independent particle equations with a potential V_{eff} is still a functional of the electron density and hence these equations must be solved iteratively. However, the Kohn-Sham equations are well defined with an accurate solution, but the exact form of the exchange-correlation energy is not known and the only solution is to find an approximation that gives an accurate result. In the next section, we will discuss about such functionals and their properties.

2.3 Exchange-correlation functionals

Finding an accurate approximations to the exchange correlation energy (E_{XC}) is the biggest challenge of Kohn-Sham DFT. Typically, the exchange interactions minimizes the total energy by reducing their Coulombic repulsion through the separation of electrons with the same spin; whereas, the correlation effects are the result of the collective nature of electrons to screen each other and decrease their overall Coulombic interaction. Moreover, exchange interactions can be calculated precisely for independent-particle methods such as Hartree-Fock, but not generally for KS methods; while, the correlation effects are more pronounced for

electrons with opposite spins as they are more likely to occupy nearby locations.

2.3.1 Exchange correlation energy

One can separate the exchange-correlation energy (E_{XC}) into a kinetic and potential energy term:

$$E_{xc}[n] = (T_e[n] - T_s[n]) + (E_{int}[n] - E_H[n]) = T_C[n] + V_{XC}[n] \tag{2.19}$$

Here T_C[n] is difference between a non-interacting, independent-particle system and the true multi body system due to correlation.

$$T_C[n] = T_e[n] - T_s[n] \tag{2.20}$$

While, V_{XC}[n] is difference between the true internal potential of an Coulombic, many body system and an independent particle approximation in which the internal interactions have been replaced by the classical self-interaction energy of a charge distribution E_H.

$$V_{XC}[n] = E_{int}[n] - E_H[n] \tag{2.21}$$

A large number of approximations to the exchange-correlation energy functional have been developed with the aim of accurately representing the true functional. This section presents a brief summary of the most popular approximation forms, namely the local density approximation (LDA) and the generalized gradient approximation (GGA).

2.3.2 Local density approximation

The local-density approximation (LDA) formulated by Kohn and Sham [9] assumed that the electron density can be treated locally as a uniform electron gas. The exchange correlation potential is local in the sense that it only depends on ρ(r) at the same position.

Within this approximation, the E_{xc} functional can be written as:

$$E_{xc}[n] = \int n(r)\epsilon_{xc}[n(r)]dr \tag{2.22}$$

Here, ϵ_{xc} is the exchange-correlation energy per particle for a homogeneous electron gas evaluated at the local density n(r). There are various LDA-based approximations to the exchange-correlation energy, but the most common one is derived from assuming the solid approaches the homogeneous electron gas limit. The functional ϵ_{xc} can be further split into exchange and correlation contributions,

$$\epsilon_{xc} = \epsilon_x + \epsilon_c \tag{2.23}$$

The exchange part, ϵ_x originally derived by Bloch [10] and Dirac [11] represents that the exchange energy of an electron in a uniform electron gas of a particular density.

$$\epsilon_x = -\frac{3}{4}\left(\frac{3n(r)}{\pi}\right)^{\frac{1}{3}} \tag{2.24}$$

The correlation energy (ϵ_c) is more complex and is not known except in the limits of infinitely-weak and infinitely-strong correlation case. However, the typical practice is to fit quantum Monte-Carlo simulation data for the correlation energy [12].

In principle, LDA is used to study the properties of slowly varying electron density systems, which demonstrates to some extent its better performance in explaining structural and elastic properties of both bulk solids and surfaces [13]. However, the LDA functional often leads to significant errors for the bonding of both molecules and solids. For instance, such calculations systematically overestimate molecular bond energies and the cohesive energy of solids. Therefore an accurate description of material properties requires functionals that go beyond LDA.

2.3.3 Generalized gradient approximation

Generalized gradient approximation (GGA) for the exchange-correlation energy improve upon the LDA description of atoms, molecules and solid by introducing one additional ingredient to the energy functional, the density gradient ∇n(r), accounting for "non-locality" in realistic systems. Thus, the generalized gradient approximation (GGA) E_{xc} is given by

$$E_{xc}{}^{GGA}[n] = \int f(n(r), \nabla n(r))dr \tag{2.25}$$

The idea is to use not only the information about the density n(r) at a particular point r, but also the gradient of the charge density, ∇n(r) in order to account for the non-homogeneity of the true electron density [14]. There are various parameterizations of GGA functionals which differ in the choice of the function $f(n(r), \nabla n(r))$. Typically, GGA functionals are more appropriate and accurate than LDA for molecular structures and other weakly bonded systems like hydrogen bonding. Nevertheless, it does not provide a consistent development over LDA for solids. However, it is highly difficult to satisfy every constraint simultaneously; hence the functional form has to be chosen according to the nature of the system under consideration.

2.4 Dispersion correction methods

Most of the energetic solids contain molecules that are held together by noncovalent interaction. However, due to the complexity of energetic materials, conventional electron exchange-correlation functionals fail to produce an accurate description of weak intermolecular interactions. This is clearly exemplified in various energetic crystals including RDX [15], FOX-7 [16, 17], CL-20 [18], TATB [19, 20] and HMX [21] and the results show that the generalized gradient approximation(GGA)/local density approximation (LDA) overestimate/underestimates the crystal volumes by nearly $\sim$30% when compared to experimental values. Since dispersion contributions to non-covalent interaction arise from correlated instantaneous electron dipole fluctuations, a proper theoretical approach of vdW

interactions poses severe computational challenges for molecular orbital methods.

In recent years, several dispersion correction approaches have been developed to improve the description of dispersion interactions in standard DFT. These approaches may be broadly divided into three main categories. (i) Pairwise additive dispersion-correction methods, which treat long-range interaction simply by adding dispersion correction energy to the internuclear energy term that strengthens the total energy coming from a standard DFT calculation. Grimme and co-workers introduced a series of empirical corrections collectively referred to as DFT-D or DFT + E_{disp} models. Particularly, the Tkatchenko and Scheffler (DFT-TS) [22] and Grimme (DFT-D2) [23] corrections to PBE are the most successful methods. (ii) Re-parametrization for the existing functionals, where the fitting data sets include noncovalent systems. Zhao and Truhlar developed hybrid meta-GGA functionals [24, 25], which belong to this category and are said to account for 'medium-range' electron correlation. (iii) The non-local correction methods, which use the electronic charge density as input and incorporates the non-local correlation contribution to the semi-local exchange functionals [26–30]. Langreth, Lundqvist, and co-workers developed a nonlocal vdW density functional (vdW-DF) in 2004 [28, 31] and its successor (vdW-DF2) in 2010 [32]. Since pair-wise additive corrections are one of the main methods used in this thesis, the intrinsic description of this approach will be presented in next the section.

2.4.1 Additive pair-wise correction methods

The semiempirical atom pair-wise interaction methods are largely successful in treating hydrogen bonding and other electrostatically dominated noncovalent interactions. In this approach, the total energy of a system is the sum of the Kohn-Sham energy E_{KS} and the dispersion correction E_{disp}

$$E_{DFT+D} = E_{KS} + E_{disp} \tag{2.26}$$

The total E_{disp} is the sum overall individual attractive atom pair contributions, which depends on the dispersion coefficients and the interatomic distance. The general formula for empirical dispersion corrections is thus given as

$$E_{disp} = -\sum_{AB} \sum_{n=6,8,10,\ldots} \frac{C_n^{AB}}{R_{AB}^n} f_{damp}(R_{AB}, A, B), \tag{2.27}$$

Here, the first sum is over all atom pairs in the system, C_n^{AB} represents the isotropic (averaged) n^{th}-order dispersion coefficient for atom pair AB and R_{AB} is their internuclear distance. The leading term of the expansion in the above equation with n = 6 ensures the correct asymptotic behavior of the potential, while the higher order terms influence its shape at shorter distances. In addition, a damping function f_{damp} is used to avoid singularities at short distances.

Various DFT+D approach has been proposed, differing in the way they define C_6 dispersion coefficients or the damping function. The most popular ones are those introduced by Tkatchenko and Scheffler (DFT-TS) and Grimme (DFT-D1, DFT-D2 and DFT-D3) [70,188,189].

2.4.1.1 DFT-TS method

The vdW-TS method of Tkatchenko and Scheffler [22] employs the electron density to evaluate system-dependent C_6 dispersion coefficients for atoms-in-materials. The fundamental idea of vdW-TS method is to determine the relative rather than absolute polarizability and C_6 dispersion coefficients of atoms inside a molecule (or a solid), referenced to highly accurate free-atom values. Moreover, this method is sensitive to the chemical environment of the atoms and corrects for long-range dispersion interactions by adding a correction of the form

$$E_{disp} = -\frac{1}{2} \sum_{A,B} \frac{C_{6AB}}{R_{AB}^6} f_{damp}(R_{AB}, R_{AB}^0), \tag{2.28}$$

Where R_A^0 and R_B^0 represents the vdW radii of atoms A and B, respectively. C_{6AB} is the corresponding C_6 coefficient and R_{AB} is the distance between atoms A and B.

In this method, C_{6AB} is obtained from the Casimir-Polder integral [33] which is given by

$$C_{6AB} = \frac{2C_{6AA}C_{6BB}}{\frac{\alpha_0^B}{\alpha_0^A}C_{6AA} + \frac{\alpha_0^A}{\alpha_0^B}C_{6BB}} \tag{2.29}$$

To eliminate spurious interactions at too short distances, a Fermi type damping function is used:

$$f_{damp} = \frac{1}{1 + e^{-d(R_{AB}/s_R R_{AB}^0 - 1)}} \tag{2.30}$$

where $R_{AB}^0 = R_A^0 + R_B^0$, s_R is free parameters and d adjusts the steepness of damping function. The free-atom reference values of α_0^A and C_{6AA} are taken from the self-interaction corrected Time Dependent (TD)-DFT calculations of Chu and Dalgarno [34]. They take advantage of the relationship between the polarizability and effective volume to calculate dispersion coefficients that depend on the chemical environment of the atom. DFT-TS method mainly relies on the Hirshfeld partitioning of the total electron density between the atoms to compute the dispersion coefficients. This effective density, and hence the volume, is compared to the density of the free-reference atom to obtain a scaling factor, which is used to define the response of the dispersion coefficients to chemical environment. However, TS method is less empirical than other approaches, with only a single adjustable parameter s_R that adapts the damping function to a particular XC functional. [35].

2.4.1.2 DFT-D2 method

In DFT-D2 method [23], the C_6 dispersion coefficients are calculated by making use of ionization potentials and static polarizabilities of isolated atoms as inputs. The corresponding empirical dispersion correction E_{disp} given by:

$$E_{disp} = -S_6 \sum_{i<j} \frac{C_6^{ij}}{R_{ij}^6} f_{damp}(R_{ij}) \tag{2.31}$$

where S_6 is global scaling factor that only depends on the density functional used and R_{ij} is an inter-atomic distance, C_6^{ij} denotes the dispersion coefficient for the pair of i^{th} and j^{th} atoms that depend on the chemical species. Careful testing of

systems showed that a geometric mean of the form

$$C_6^{ij} = \sqrt{C_6^i C_6^j}; C_6^i = 0.05 N I_p^i \alpha^i \tag{2.32}$$

yields much better results. Where I_P^i and α^i atomic ionization potentials and static dipole polarizabilities, respectively. In order to avoid near-singularities for small R, a damping function f_{damp} must be used, which is given by

$$f_{damp} = \frac{1}{1 + e^{-d(R_{ij}/R_r - 1)}} \tag{2.33}$$

here R_r is the sum of atomic vdW radii. A clear description regarding the implementation of the method can be found elsewhere [23].

2.5 Methodology

One of the major concerns in solid materials is the very peculiar nature of the wavefunction at various distances from the nuclei. However, the atomic wavefunctions are eigenstates of the atomic Hamiltonian and thus must be all mutually orthogonal. Since the core states are well localized around the nucleus, a large basis set would be required to accurately describe the oscillations in the core regions in order to maintain orthogonality between core and valence electrons. This leads to an all-electron plane-wave calculation which consumes a lot of computational cost. To alleviate this problem, the core and valence electrons must be treated in a different way for possible numerical advantages.

2.5.1 Pseudopotential method

The electronic states of an atom can be broadly categorized into: (1) core states, which are highly localized and do not contribute in chemical bonding, (2) semicore states, which are localized and polarizable but typically do not involve directly to chemical bonding and (3) valence states, which are extended and responsible for chemical bonding. In pseudopotential calculations, the description of

strong ionic potential in the core region is replaced by a weaker pseudopotential that incorporates the influence of the core electrons on the valence electrons. The corresponding set of all-electron wavefunctions and pseudo-wavefunctions are identical outside a chosen cutoff radius and thus possess similar scattering properties. However, inside the cutoff radius, the pseudo-wavefunctions do not exhibit the nodal structure that causes the oscillations, which means they can now be described with a reasonable number of plane-waves. A brief illustration of the concept behind the pseudopotential approach is shown in figure 2.1. The efforts of improving pseudopotential methods are based on following aims: (i) the number of plane waves to represent pseudo-eigenstates need to be as small as possible (ii) the valence charge density should be reproduced by the pseudo-charge density as precisely as possible and (iii) the potentiality for a certain atomic configuration should always produce accurate results in different solids. With this pseudopoten-

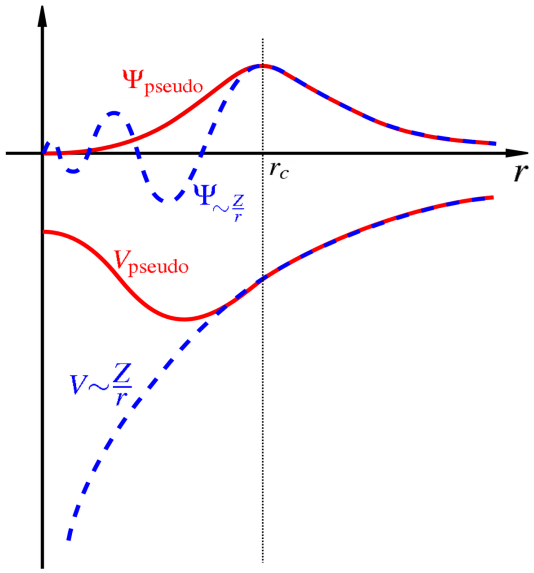

Figure 2.1: Schematic illustration of the concept behind the pseudopotential approach. The solid lines show the all-electron wavefunction and ionic potential; while the corresponding pseudo wavefunction given by the pseudopotential is plotted in dashed lines. All quantities are represented as a function of distance, r, from the atomic nucleus. The point beyond which the all-electron and pseudo-electron values become identical is designated as cutoff radius.

tial approach, the computational cost is significantly reduced, not only since the

number of orbitals are lowered, but mainly due to the employment of smaller basis sets. In the present thesis, various pseudopotential approaches are implemented as described below.

2.5.1.1 Norm-conserving pseudopotentials

The desired characteristic properties of pseudopotentials are generally referred to as softness, accuracy and transferability. The term ***soft*** indicates that the required number of plane waves to expand the pseudo wave functions must be as minimum as possible. The softer the pseudopotential is, the smoother will be the resulting pseudovalence orbitals. While, the pseudopotentials accuracy and transferability can be assessed by their ability to reproduce quantities from all electron calculations over a wide range of different chemical compounds. Both properties, softness and transferability, are related closely to the cutoff radius and compete with each other. Typically, the higher cuttoff makes the pseudopotentials softer; whereas, the low cutoffs give pseudopotentials with a very good transferability [36]. Nevertheless, the precise balance between the two requirements placed a great challenge in developing accurate pseudopotential methods. In order to ensure the optimum smoothness and transferability, Hamann and co-workers developed pseudopotentials which are known as norm-conserving pseudopotential (NCPP). In this approach, the pseudo and the all electron wave function inside the atomic sphere should possess the same norm to ensure similar electron densities for both wave functions in the outside region. This guarantees that the core region of the atom is not significantly affected by the surrounding environment and also assures the transferability. These type of pseudopotentials requires a comparatively huge number of plane waves for "semilocal" orbitals of elements because of their substantial fraction inside the core region and their importance to the bonding.

2.5.1.2 Ultra-soft pseudopotentials

The fundamental requirement of pseudopotentials is to create a smooth pseudized wave functions with reasonable accuracy. A much softer pseudo wave function

can be obtained when the number of Fourier components needed to describe it to a given accuracy is minimum. Unfortunately, norm-conserving pseudopotentials achieved reasonable accuracies at some sacrifice of smoothness, thus, requiring large cutoff energy that significantly enhanced the computational cost. To address this issue, Vanderbilt [37] proposed a new and radical modification for generating pseudopotentials by breaking the norm-conservation constraint and relaxing the condition that the psudo wave function inside the core region must have the same density as the all-electron wave function. Through this approach, a much softer pseudo wave function is obtained, which employs only fewer plane-waves for calculations with the same accuracy. For this reason, they are usually called as ultra-soft pseudopotentials. Moreover, the charge deficiency due to the relaxation of the norm-conservation conditions are equilibrated by the introduction of atom-centered augmentation charges to ensure the proper density and potential. In the present thesis, the ultra-soft and norm-conserving pseudopotential approaches are enabled through CAmbridge Series of Total Energy Package (CASTEP) [38].

2.5.2 Projector augmented wave method

Although there has been various pseudopotential approaches, the Projector Augmented Wave (PAW) method developed by Blöchl [39] is considered as one of the remarkably successful methods for treating the problem of highly oscillatory wavefunctions near the nuclei. It shares some features of Blöchl's earlier work on generalized separable potentials [40] and Vanderbilt's soft pseudopotential formalism [37]. One of the major advantages of the PAW approach over the other pseudopotential methods is a well controlled transformation between conveniently smooth pseudo wavefunctions and the all-electron wave functions. Additionally to the PAW transformation, the frozen core approximation [41] provides the possibility to use fixed core orbitals. As well as enabling 'softer' wavefunctions than norm-conserving pseudopotentials, and thus smaller basis sets. Crucially, this approach allows direct access to quantities whose evaluation requires values of densities, wavefunctions and electric fields in the immediate vicinity of the atomic nuclei [42], which is not possible with norm-conserving pseudopotentials.

All these advantage imply that PAW hould be ideal for tackling the significant challenges in plane-wave-based material calculations. The PAW method is incorporated through Vienna Ab-initio Simulation Package (VASP) [43].

2.6 Density functional perturbation theory

Born and Oppenheimer (BO) proposed adiabatic approximation which allows one to decouple the vibrational from the electronic degrees of freedom in a solid [5]. According to this approach, the lattice-dynamical properties of a solid system can be obtained by solving the energy eigenvalues and eigenfunctions. The BO approximation simplified many body Hamiltonian and the resultant equation is:

$$\hat{H}_{BO}(R) = \hat{T}_e + \hat{V}_{ee} + \hat{V}_{en} + \hat{V}_{nn} \tag{2.34}$$

In above equation, the kinetic energy operator of electrons is represented by $\hat{T}_e$; while, nuclei-nuclei, electron-nuclei and electron-election electrostatic interactions are denoted by $\hat{V}_{nn}$, $\hat{V}_{en}$ and $\hat{V}_{ee}$ respectively. The equilibrium geometry of the solid can be obtained by equating the inter atomic forces (first derivative of Born-Oppenheimer energy surface) to zero

$$F_I \equiv -\frac{\partial E(R)}{\partial R_I} = 0 \tag{2.35}$$

whereas the vibrational frequencies, ω, are determined by the eigenvalues of the Hessian of the Born-Oppenheimer energy, scaled by the nuclear masses:

$$det|\frac{1}{\sqrt{M_I M_J}}\frac{\partial^2 E(R)}{\partial R_I \partial R_J} - \omega^2| = 0 \tag{2.36}$$

The basic tool for computing the first and second derivatives of its BO energy surface is the Hellmann-Feynman theorem. According to this, the first derivative of the eigenvalues of a Hamiltonian, that depends on a parameter λ is given by the expectation value of the derivative of the Hamiltonian:

$$\frac{\partial E_\lambda}{\lambda} =< \psi_\lambda | \frac{\partial H_\lambda}{\lambda} | \psi\lambda > \tag{2.37}$$

Here ψ_λ and E_λ represents eigenfunction and eigenvalue, respectively. The forces $\mathbf{F}_I$ can be calculated by applying the Hellman-Feynman theorem to the BO Hamiltonian:

$$F_I \equiv -\frac{\partial E(R)}{\partial R_I} = - < \psi(R) | \frac{\partial H_B O(R)}{\partial R_I} | \psi(R) > \tag{2.38}$$

$$F_I \equiv -\int n_R(r) \frac{\partial V_R(r)}{\partial R_I} - \frac{\partial E_N(R)}{\partial R_I} \tag{2.39}$$

Here $n_R(r)$, V_R (r) and $E_N(R)$ represents electron charge density, electron-nucleus interaction potential and electrostatic interaction between different nuclei, respectively. Finally, the Hessian of the BO energy surface is determined by differentiating the Hellmann-Feynman forces with respect to nuclear coordinates:

$$\frac{\partial^2 E(R)}{\partial R_I \partial R_J} = \int \frac{\partial n_R(r)}{\partial R_J} \frac{\partial V_{en}(R)}{\partial R_I} dr + \int n_R(r) \frac{\partial^2 V_{en}(R)}{\partial R_I \partial R_J} dr + \frac{\partial^2 V_{nn}(R)}{\partial R_I \partial R_J} \tag{2.40}$$

The ground-state electron charge density, $n_R(r)$ and its linear response to a distortion of the nuclear geometry, $\frac{\partial n_R(r)}{\partial R_I}$ are required to solve the inter-atomic force constants (IFC) matrix (Hessian matrix) [44]. Once IFC is known, the Fourier transform of IFC resulting in the dynamical matrix in reciprocal space. Therefore, density functional perturbation theory is an accurate and efficient tool to calculate the lattice dynamics. [45].

2.7 Heyd-Scuseria-Ernzerhof (HSE) hybrid functional

Typically, the standard DFT formalism is insufficient to produce an accurate description of electronic structures: the PBE functional is a reasonable representation of total energies for a variety of stoichiometries, but the unphysical

self-interactions in d-electron systems can cause a huge amount of error due to the local mean-field treatment. Further developments were aimed to reduce self-interaction errors present in (semi-)local functionals by adding "nonlocal" terms into the XC energy. This description was explicitly implemented in hybrid functionals that mix a semi/local GGA/LDA exchange potential with an additional amount of non-local exact Hartree-Fock (HF) exchange energy, which has been considered as the best approach due to its relatively accurate band gap and semi-core *d* states [46–49]. A general hybrid exchange-correlation energy functional $E_{XC}^{hybrid}[n]$ is defined as:

$$E_{XC}^{hybrid}[n] = \alpha E_X^{HF}(w) + E_C^{GGA} - (\alpha - 1)E_X^{GGA} \tag{2.41}$$

where E_X^{HF} is the exact non-local Hartree-Fock exchange energy, E_X^{GGA} and E_C^{GGA} are the semilocal GGA exchange and correlation functionals, respectively. The coefficient α reflects the mixing parameter and ω is an adjustable parameter.

Although this approach show improvement over standard DFT formalism, but still the Hartree-Fock exchange in hybrid DFT approach is much less tractable in large systems, where the linear scaling Hartree-Fock simulations depend on the natural decay of the Hartree-Fock exchange interactions over distance. In order to avoid slowly decaying exchange interaction, Screened Coulomb potential is introduced. Thus, the exchange part is separated into Short Range (SR) and Long Range (LR) through coulomb kernel:

$$\frac{1}{r} = S_{\mu}(r) + L_{\mu}(r) = \frac{1 - erf(\mu r)}{r} + \frac{erf(\mu r)}{r} \tag{2.42}$$

Here, the range separation is defined by Screening parameter, μ. Thus, the expression for HSE screened hybrid functional is given by:

$$E_{XC}^{HSE} = \frac{1}{4}E_X^{HF,SR}(\mu) + \frac{3}{4}E_X^{PBE,SR}(\mu) + \frac{3}{4}E_X^{PBE,LR}(\mu) + E_C^{PBE} \tag{2.43}$$

where $E_X^{HF,SR}(\mu)$ is the short range HF exchange. $E_X^{PBE,SR}(\mu)$ and $E_X^{PBE,LR}(\mu)$ are the SR and LR components of the PBE exchange functional. The proposed 25% of the mixing parameter is to be adjusted to suit the type of system being investi-

gated. Overall, this functional provides better numbers for semiconductors and insulators, particularly for the calculations of reliable band gaps [50, 51]. A more detailed description about the implementation of individual terms and parameters of HSE can be found in Refs. [52] and [53].

2.8 Hirshfeld surface analysis

The quantitative description of a molecule in condensed phase is a challenging task; however, it continues to attract wide attention since the recognition of distinct entities in molecular crystals. Various approaches were generalized to extract continuous molecular fragments from electron density distributions; among them, Hirshfeld surface analysis is a most effective method based on Hirshfeld's "stockholder partitioning" concept [54] for defining atoms in molecules. This approach is used to analyze the information about crystal structure and its molecular interactions for exploring crystal packing and the associated intermolecular interactions, which seems to be important in the crystal engineering point of view.

The Hirshfeld surfaces are constructed by screening space in the crystal into sections where the electron distribution of a sum of sphere-shaped atoms for the molecule (i.e.the pro-molecule) dominates the corresponding sum over the crystal (i.e. the pro-crystal). This method was developed for partitioning the crystal electron density into molecular fragments by defining a molecular weight function:

$$w(r) = \frac{\sum\limits_{a \in molecule} \rho_a(r)}{\sum\limits_{a \in crystal} \rho_a(r)} = \frac{\rho_{promolecue}(r)}{\rho_{procrystal}(r)} \tag{2.44}$$

Here, $\rho_a(r)$ is a spherically average atomic electron density function centred on nucleus a [55]. Hirshfeld surfaces are produced through the partitioning of space within a crystal where the ratio of pro-molecule to pro-crystal electron densities is equal to 0.5, resulting in continuous non-overlapping surfaces [56, 57].

The strength of the interactions can be described by d_{norm} (normalised contact distance):

$$d_{norm} = \frac{(d_i - r_i^{vdw})}{r_i^{vdw}} + \frac{(d_e - r_e^{vdw})}{r_e} \tag{2.45}$$

Where r_i and r_e denote the vdW radii of two atoms inside and outside to the Hirshfeld surfaces, d_i and d_e represent the internal and external separations from the nearest atoms, respectively. The 3D d_{norm} surface is used to identify close intermolecular contacts, in which the positive and negative values denote the intermolecular contacts that are longer and shorter than the vdW separations, respectively. The graphical plots are mapped onto the Hirshfeld surfaces with d_{norm} using blue (longer intermolecular contacts), white (contacts around the vdW separation) and red (shorter intermolecular contacts) colours [58]. In addition, the overall summary of intermolecular interaction in the molecule is provided by the associated 2D fingerprint plots. The Hirshfeld surfaces are calculated in the user-friendly program CrystalExplorer [59], which requires only Crystallographic Information Files (CIFs) as an input.

References

[1] P. W. Atkins and R. S. Friedman, *Molecular Quantum Mechanics*, Oxford University Press, Oxford (1997).

[2] F. Jensen, *Introduction to Computational Chemistry*, Wiley, Chichester (1999).

[3] T. Helgaker, P. Jørgensen and J. Olsen, *Molecular Electronic–Structure Theory*, Wiley, Chichester (2000).

[4] W. Koch and M. C. Holthausen, *A Chemists's Guide to Density Functional Theory*, Wiley-VCH (2001).

[5] M. Born and J. R. Oppenheimer, Am. J. Phys., **84**, 451 (1927).

[6] M. Born and R. Oppenheimer, Annalen der Physik, **20**, 457 (1927).

[7] P. Hohenberg and W. Kohn, Phys. Rev., **136**, B864 (1964).

[8] W. Kohn. Rev. Mod. Phys., **71**, 1253 (1999).

[9] W. Kohn and L. Sham, Phys. Rev., **140**, A1133 (1965).

[10] F. Bloch, Z. Physik, **57**, 545 (1929).

[11] P. A. M. Dirac, Proc. Roy. Soc. Lond. A, **123**, 714 (1929).

[12] D. M. Ceperley and B. J. Alder, Phys. Rev. Lett., **45**, 566 (1980).

[13] R. O. Jones and O. Gunnarsson, Rev. Mod. Phys. **61**, 689 (1989).

[14] J. P. Perdew, M. Ernzerhof and K. Burke, J. Chem. Phys., **105**, 9982 (1999).

[15] M. S. Miao, Z. A. Dreger, J. M. Winey and Y. M. Gupta, J. Phys. Chem. A, **112**, 12228 (2008).

[16] J. J. Zhao and H. Liu, Comput. Mater. Sci., **42**, 698 (2008).

[17] S. Appalakondaiah, G. Vaitheeswaran and S. Lebegue, J. Chem. Phys., **140**, 014105 (2014).

[18] E. F. C. Byrd and B. M. Rice, J. Phys. Chem. C, **111**, 2787 (2007).

[19] H. Liu, J. J. Zhao, J. G. Du, Z. Z. Gong, G. F. Ji and D. Q. Wei, Phys. Lett. A, **367**, 383 (2007).

[20] S. Appalakondaiah, G. Vaitheeswaran and S. Lebegue, J. Phys. Chem. A, **119**, 6574 (2015).

[21] E. F. C. Byrd, G. E. Scuseria and C. F. Chabalowski, J. Phys. Chem. B, **108**, 13100 (2004).

[22] A. Tkatchenko and M. Scheffler, Phy. Rev. Lett., **102**, 073005 (2009).

[23] S. Grimme, J. Compu. Chem., **27**, 1787 (2006).

[24] Y. Zhao, N. E. Schultz and D. G. Truhlar, J. Chem. Theory Comput., **2**, 364 (2006).

[25] Y. Zhao and D. G. Truhlar, Theor. Chem. Acc., **120**, 215 (2008).

[26] A. Hesselmann, G. Jansen and M. Schutz, J. Chem.Phys., **122**, 014103 (2005).

[27] O. A. Lilienfeld, I. Tavernelli, U. Roethlisberger and D. Sebastiani, Phys. Rev. Lett., **93**, 153004 (2004).

[28] M. Dion, H. Rydberg, E. Schroder, D. C. Langreth and B. I. Lundqvist, Phys. Rev. Lett., **92**, 246401 (2004).

[29] O. A. Vydrov and T. V. Voorhis, Phys. Rev. Lett., **103**, 063004 (2009).

[30] O. A. Vydrov and T. Van Voorhis, J. Chem. Phys., **133**, 244103 (2010).

[31] M. Dion, H. Rydberg, E. Schroder, D. C. Langreth and B. I. Lundqvist, Phys. Rev. Lett., **95**, 109902 (2005).

[32] K. Lee, E. D. Murray, L. Kong, B. I. Lundqvist and D. C. Langreth, Phys. Rev. B:Condens. Matter Mater. Phys., **82**, 081101 (2010).

[33] H. B. G. Casimir and B. Polder, Phys. Rev., **73**, 360 (1948).

[34] X. Chu and A. Dalgarno, J. Chem. Phys., **121**, 4083 (2004).

[35] A. Tkatchenko, R. A. DiStasio, R. Car and M. Scheffler, Phy. Rev. Lett., **108**, 236402 (2012).

[36] S. Goedecker and K. Maschke, Phys. Rev. A **45**, 88 (1992).

[37] D. Vanderbilt, Phys. Rev. B, **41**, 7892 (1990).

[38] M. C. Payne, M. P. Teter, D. C. Allen, T. A. Arias and J. D. Joannopoulos, Rev. Mod. Phys., **64**, 1045 (1992).

[39] P. E. Blöchl, Phys. Rev. B, **50**, 17953 (1994).

[40] P. E. Blöchl, Phys. Rev. B: Condens. Matter Mater. Phys., **41**, 5414 (1990).

[41] J. Lehtomäki, I. Makkonen, M. A. Caro and A Harju, J. Chem. Phys., **141**, 234102 (2014).

[42] N. D. M. Hine, J. Phys.: Condens. Matter, **29**, 024001 (2017).

[43] G. Kresse and D. Joubert, Phys. Rev. B, **54**, 11169 (1996).

[44] S. Baroni, S. D. Gironcoli, A. D. Corso and P. Giannozzi, Rev. Mod. Phys., **73**, 515 (2001).

[45] M. J. Verstraete and Z. Zanolli, Lecture Notes of the 45^{th} IFF Spring School, *Computing Solids- Models, ab Initio Methods and Supercomputing*, Forschungszentrum Jülich (2014).

[46] J. Heyd and G. E. Scuseria, J. Chem. Phys., **121**, 1187 (2004).

[47] J. Heyd, J. E. Peralta, G. E. Scuseria and R. L. Martin, J. Chem. Phys., **123**, 174101 (2005).

[48] J. Heyd, G. E. Scuseria and M. Ernzerhof, J. Chem. Phys., **124**, 219906 (2006).

[49] A. V. Krukau, O. A. Vydrov, A. F. Izmaylov and G. E. Scuseria, J. Chem. Phys., **125**, 224106 (2006).

[50] J. E. Moussa, P. A. Schultz and J. R. Chelikowsky, J. Chem. Phys., **136**, 204117 (2012).

[51] M. A. L. Marques, J. Vidal, M. J. T. Oliveira, L. Reining and S. Botti, Phys. Rev. B: Condens. Matter Mater. Phys., **83**, 035119 (2011).

[52] J. Heyd, G. E. Scuseria and M. Ernzerhof, J. Chem. Phys., **118**, 8207 (2003).

[53] J. Heyd and G. E. Scuseria, J. Chem. Phys, **120**, 7274 (2004).

[54] F. L. Hirshfeld, Theoretica Chimica Acta, **44**, 129 (1977).

[55] E. Clementi and C. Roetti, Atomic Data and Nuclear Data Tables, **14**, 177 (1974).

[56] M. A. Spackman and P. G. Byrom, Chemical Physics Letters, **267**, 215 (1997).

[57] J. J. McKinnon, M. A. Spackman and A. S. Mitchell, Acta Crystallographica Section B-Structural Science, **60**, 627 (2004).

[58] M. A. Spackman and J. J. McKinnon, Crystengcomm, **4**, 378 (2002).

[59] S. K. Wolff, D. J. Grimwood, J. J. McKinnon, M. J. Turner, D. Jayatilaka and M. A. Spackman, *CrystalExplorer 3.1*, University of Western Australia, Australia (2012).

Chapter 3

Structure-property-performance interrelationship of 5,5′-bitetrazole-1,1′-diolate based energetic ionic salts

This chapter presents a comparative study on physicochemical and detonation characteristics of 5,5′-bitetrazole-1,1′-diolate based energetic ionic salts including structural, electronic, vibrational and performance parameters (heat of formation, detonation pressures, and detonation velocities). The geometry interpretation of intermolecular interactions were quantitatively visualized using the Hirshfeld surface analysis. In the simplest possible scenario, this chapter explores the structure-property-performance inter-relationship to highlight the importance of hydrogen bonding interactions in designing energetic salts for next-generation explosives, propellants and pyrotechnics.

B. Moses Abraham, Vikas D. Ghule and G. Vaitheeswaran, "A comparative study of the structure, stability and energetic performance of 5,5′-bitetrazole-1,1′-diolate based energetic ionic salts: future high energy density materials", **Phys. Chem. Chem. Phys.**, 20, 29693 (2018).

3.1 Introduction

From gunpowder to modern energetic materials, the so-called age of explosives improved the potential to develop a variety of energetic materials that are extensively used in both civilian and military applications, such as mining engineering, weapons research and aerospace science. With the continuing demand for the search of advanced energetic materials, researchers are fascinated towards developing and designing materials with high power, better safety levels and good environmental compatibility. Nevertheless, till date, the controversial drama between performance and sensitivity placed a serious challenge to design explosives with desired applications. For example, CL-20 [1] and ONC [2] contains high performance than any other energetic materials, but the presence of more nitro groups and their sensitivity make the synthesis more expensive and strenuous. On the other hand, FOX-7 [3] is the best insensitive energetic material than the well-known TNT, but it possesses only 70% of the heat of detonation than the most widely used RDX and HMX [4]. Therefore, the future high energy density materials (HEDMs) have to be developed with creative strategies by concentrating on the combination of physics, crystallography and chemistry.

Apart from energetic co-crystals and metal-organic frameworks, another interesting approach to design powerful energetic materials is through the formulation of energetic ionic salts (EIS). The combination of their inherent individual explosive properties and unusual chemical structures yields a unique class of EIS with enhanced power due to distinct crystal packing and anion-cation interactions [5]. The principle parameter to design these EIS is to attain higher densities than their parent compounds. Typically, in metal salts, the nondirectional, soft and delocalized interactions allow the crystal to pack tightly, leading to greater densities [6, 7]. However, when organic anion and non-metal cation form together, the driving forces are weak interactions [8, 9]. These intermolecular interactions, especially hydrogen bonding between cation and anions play an important role

in improving crystal packing efficiency, density and stability, which is revealed in several low sensitive HEDMs. Apart from their stability, the non-covalent interactions, such as hydrogen bonding can minimize their solubility and toxicity in most of the common solvents. In addition, the EIS may contain lower vapor pressure than their parent nonionic molecules and thus, significantly reduces the risk of exposure via inhalation [10–12]. Recently, several EIS were derived from triazole, tetrazole and imidazole in which each cation or anion couple with its counterparts via protonation reactions that can overcome the associated adverse behavior. For example, 3,4-diamino-1,2,4-triazolium 5-nitrotetrazolate (1.739 gm cm^{-3}), 3,4-diamino-1,2,4-triazolium perchlorate (1.798 gm cm^{-3}) and 1-amino-1,2,3-triazolium 5-nitroiminotetrazolate (1.72 gm cm^{-3}), 1-amino-1,2,3-triazolium nitroformate (1.86 gm cm^{-3}) possess remarkably higher densities than their parent 3,4-diaminotriazole (1.552 gm cm^{-3}) [14] and 1-amino-1,2,3-triazole (1.423 gm cm^{-3}) [13] compounds, respectively. Hence, the dream of high performance with better sensitivities can be obtained through EIS.

Tetrazole is an extremely significant precursor towards developing various energetic salts ranging from insensitive secondary explosives to sensitive primary explosives. It is a five-membered heterocyclic structure with four N atoms in the ring. The introduction of single oxygen atom into tetrazole ring structure makes them interesting materials with desired properties for future applications: i) owing to its high crystal density, the explosive power will be increased significantly; ii) the enhanced oxygen balance results in maximum energy output on decomposition/explosion; iii) the enhanced intermolecular interactions and the reduced heat of formation (HOF) will ensure low sensitivity towards mechanical stimuli. Therefore, by introducing these ideas together, Tselinskii designed an innovative tetrazole derivative 5,5′-bistetrazole-1,1′-diolate (BTO) in 2001 [15]. The bi-tetrazole rings and two hydroxyl groups of BTO molecules are joined together by N-O bonds with enhanced structure-property characteristics, which is suitable for the design of new EIS. Moreover, the strongly acidic dihydroxylated

bitetrazole can readily be abstracted by nitrogen-rich bases such as ammonia, urea, guanidine, hydrazine or even other tetrazole derivatives. For example, the future high energy material TKX-50 contains remarkably high density (1.877 g cm^{-3}) [16] when compared to their pure hydroxylammonium (1.67 g cm^{-3}) compound. The impact and friction sensitivities of TKX-50 (20 J and 120 N) are smaller than that of β-HMX (7 J and 112 N) and ϵ-CL-20 (4 J and 48 N). The remarkable mechanical stability of TKX-50 can be ascribed to several factors: i) the strong intra and weak interlayer bonding interactions can promote dissipation of mechanical energy through interlayer sliding and ii) the presence of face-to-face $\boldsymbol{\pi}...\boldsymbol{\pi}$ stacking in the crystal can reasonably transform the external mechanical energy into intermolecular interaction energy. Based on the exceptional performance of TKX-50, various novel energetic salts of BTO families were synthesized and are found to perform significantly well when compared with the traditional explosives. The recently synthesized HA-BTO [17] possess higher crystal density (1.912 g cm^{-3}) and good impact and friction sensitivities (28 J and 120 N) than those of TKX-50. The heat of formation of HA-BTO (425.6 kJ mol^{-1}) is four times superior to RDX and equal to that of TKX-50. The detonation velocity (8931 m s^{-1}) and detonation pressure (36.1 GPa) are also greater than that of RDX [17]. Therefore, in this chapter, we tried to understand the structure-property-performance interrelationship of 5,5′-bistetrazole-1,1′-diolate skeleton when combined with various cations (see figure 3.1) to enhance the performance of EIS.

3.2 Theoretical methodology

Geometry optimizations were carried out using density functional theory (DFT) with a plane wave basis set via Vienna ab initio Simulation Package (VASP) [18, 19]. The exchange and correlation energy is characterized by projector augmented wave (PAW) [20] method, employing the Perdew-Burke-Ernzerhof (PBE) [21] generalized gradient approximation (GGA). The conjugate gradient minimiza-

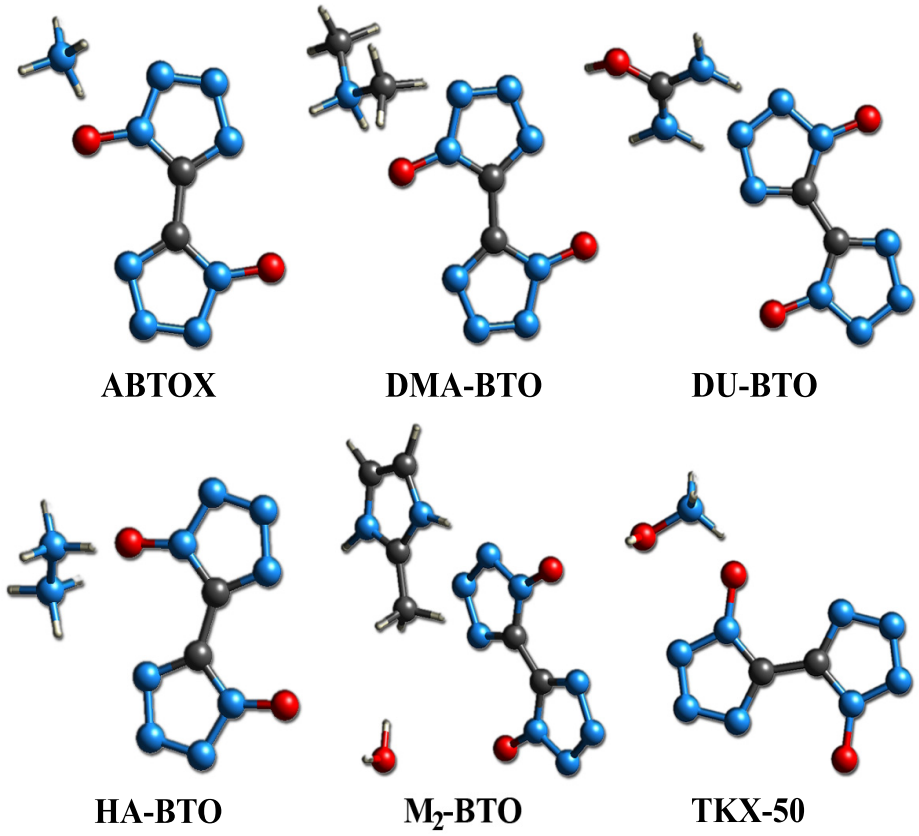

Figure 3.1: The crystal structures of 5,5′-bitetrazole-1,1′-diolate based energetic salts

tion scheme is used to relax the coordinates of all structures until the maximum force on each atom is less than 0.01 eV/Å. The optimization of geometries was based on convergence thresholds for the displacement and total energy as 5×10^{-4} Å and 5×10^{-6} eV/atom, respectively. For the Brillouin zone integrations, a Monkhorst-Pack grid [22] of most suitable mesh is used for each structure. The accurate description of any material mainly depends on the exchange-correlation functional that is employed. Fortunately, the ability of electronic structure methods to balance computational efficiency and accuracy has led to its widespread usage in a variety of molecular systems. However, the conventional DFT functionals (LDA and GGA) fail to describe long-range interactions [27–32] that orig-

inate from non-local electron correlation. In order to capture these non-bonding interactions within the energetic salts, we incorporated the van der Waals (vdW) correction approach developed by Grimme and co-workers. The obtained total energy after incorporating dispersion correction is given by:

$$E_{DFT+D} = E_{DFT} + E_{disp}, \tag{3.1}$$

The empirical dispersion correction energy (E_{disp}) is attractive for any distance and thus stabilizes the system with respect to their constituting atoms.

$$E_{disp} = -s_6 \sum_{i<j} \frac{C_{ij}}{R_{ij}^6} f_{damp}(R_{ij}), \tag{3.2}$$

Here, S_6 is a global scaling factor, C_{ij} represents the dispersion coefficient for atom pair ij, which can refer to atoms as well as complete crystal as it is obtained from a centered multipole expansion. The damping function f_{damp} must be used to avoid near-singularities for small R_{ij}, which is given by:

$$f_{damp} = \frac{1}{1+e^{-d(R_{ij}/R_0-1)}}$$

where R_0 is the sum of atomic vdW radii. The inclusion of these London dispersion forces is indispensable in theoretical calculations in order to reach chemical accuracy ($\sim$1 kcal/mol).

Usually, the standard DFT formalism is insufficient to produce an accurate description of electronic structures: The PBE functional is a reasonable representation of total energies for a variety of stoichiometries, but the unphysical self-interactions in d-electron systems can cause a huge amount of error due to the local mean-field treatment. Comparatively, Hubbard U (PBE+U) correction can reduce the problem to some extent, but it introduces different set of complications. On the other hand, modified Becke–Johnson (mBJ), a meta-GGA functional [33–40] is the most sophisticated semilocal approximation that balances the non-locality contributions to the exchange and correlation energy. Even though

mBJ shows some underestimation of the band gaps, it qualitatively minimizes the error compared to conventional DFT functionals. Unfortunately, the total energy cannot be calculated through mBJ, since it is an empirical potential not being a derivative of exchange and correlation energy. The Heyd-Scuseria-Ernzerhof (HSE) hybrid functional that screens the Coulomb potential for the Hartree-Fock (HF) exchange has been considered as the best approach for its relatively accurate band gap and semi core d states. However, HSE calculations are highly expensive because of shear size of the system as well as the complexity of the method. As a consequence, the clear description of electronic structures using hybrid functionals for most of the energetic materials are absent in the literature. Therefore, to reduce self-interaction error of DFT in electronic structure calculations, we have incorporated HSE06 functional approach. The complete description and implementation of HSE methodology can be found in Ref [41] and [42].

The density functional perturbation theory (DFPT) simulations were carried out through CASTEP package [43] via plane wave pseudo-potential approach. The norm-conserving [44] pseudopotentials [45] were adopted for calculating zone center IR spectra. The Monkhorst-Pack k-point grid separation of $2\pi \times 0.04$ Å^{-1} and a kinetic energy cutoff of 950 eV were used in the calculations. Upon relaxation, the atomic forces in the relaxed systems were smaller than 0.01 eV/Å. The total energy convergence is obtained when the energy difference between successive self-consistent iterations were 5.0×10^{-6} eV/atom. The CrystalExplorer 3.1 [46] software is used for qualitative analysis of Hirshfeld surfaces [47] and related 2D fingerprint maps [48]. For evaluating the energetic performance, the detonation pressure and detonation velocities were calculated using EXPLO5 [49] program.

3.3 Results and discussion

As mentioned earlier, performance and sensitivity are the two major concerns of explosive materials. Various articles reported several factors influencing them, including crystal packing, density, decomposition, initiation, oxygen balance, dislocations, voids, energy localization, defects, energy dissipation mechanisms, intermolecular hydrogen bonding, short- and long-range interactions in molecular crystals and many more. In the present chapter, we attempt to understand the results in four sections: The molecular structure, vibrational and electronic properties, Hirshfeld surface analysis and detonation performance. Comparing these properties of EIS, we can quantitatively analyze their difference in power and sensitivity.

3.3.1 Molecular structure and ground state properties

The crystallographic data of BTO energetic salts are shown in Table 3.1. The DMA-BTO [24], HA-BTO [17] and M_2-BTO [26] crystallizes in same triclinic structure with space group P-1. Whereas, ABTOX [23], DU-BTO [25] and TKX-50 [16] possesses monoclinic structure with space group P21/c, P21/n and P21/c, respectively. Dreger et. al., [50] studied the structural and vibrational properties of TKX-50 using DFT standard functionals LDA (CA-PZ), GGA (PW91) and GGA (PBE) and their improved versions (PBE-TS, PW901-OBS and PBE-D2). The errors in their calculated volumes are -7.8, 13.0, 13.3, 5.8, -1.3 and 0.02% for CZ-PZ, PW91, PBE, TS, OBS and D2, respectively. These values represent that the DFT-D2 method reproduces the experimental results more accurately. Subsequently, similar articles were reported on TKX-50 using D2 Grimme method to understand various energetic properties [51, 52]. Even our earlier experience also demonstrates that the DFT-D2 method can quantitatively reproduce the structural properties of explosive materials [53]. Therefore, in the present chapter, we optimize the geometry of EIS salts using a DFT-D2 approach by full relaxation

Table 3.1: Computed lattice constants (a, b, c), angle (α, β, γ) and volume (V) of ABTOX, DMA-BTO, DU-BTO, HA-BTO, M_2BTO and TKX-50 crystals using DFT-D2 method along with experimental values in brackets.

	ABTOX [23]	DMA-BTO [24]	DU-BTO [25]	HA-BTO [17]	M_2-BTO [26]	TKX-50 [16]
Formula	$C_2H_8N_{10}O_2$	$C_6H_{16}N_{10}O_2$	$C_4H_{10}N_12O_4$	$C_2H_6N_{10}O_2$	$C_{10}H18N_{12}O_4$	$C_2H_8N_{10}O_4$
CCDC	1057866	1447137	1487783	1479231	1435485	872232
Crystal system	Monoclinic	Triclinic	Monoclinic	Triclinic	Triclinic	Monoclinic
Space group	P21/c	P-1	P21/n	P-1	P-1	P21/c
a [Å]	3.582 (3.678)	5.417 (5.571)	3.611 (3.680)	4.796 (4.751)	5.280 (5.386)	5.555 (5.440)
b [Å]	14.449 (14.506)	7.091 (7.293)	17.615 (17.688)	5.967 (5.910)	7.169 (7.267)	11.489 (11.751)
c [Å]	7.410 (7.345)	8.454 (8.500)	8.831 (8.780)	6.877 (6.702)	11.182 (11.149)	6.446 (6.561)
α [^{o}]	90	108.29 (109.86)	90	98.80 (98.68)	106.40 (106.36)	90
β [^{o}]	101.96 (101.37)	101.85 (102.04)	96.01 (95.75)	94.13 (90.70)	93.06 (92.34)	96.14 (95.07)
γ [^{o}]	90	100.89 (101.23)	90	108.81 (109.07)	103.36 (104.61)	90
Z	2	1	2	1	1	2
V [Å^3]	375.30 (384.29)	290.34 (304.1)	558.78 (568.7)	182.56 (175.44)	391.88 (400.0)	409.11 (417.86)
$\rho[gcm^{-3}]$	1.790 (1.765)	1.488 (1.421)	1.724 (1.695)	1.838 (1.913)	1.569 (1.534)	1.91 (1.87)

of all atoms and cell parameters and also to assert the reliability of the employed method. As is depicted in Table 3.1, our optimized lattice parameters show good agreement with the experimental values, confirming the reliability.

Under ambient conditions, the average N-N and C-N bond lengths of the tetrazole rings range from 1.374 Å for N1-N2 to 1.337 Å for N2=N3 and 1.371 Å for C1-N1 to 1.349 Å for C1=N4, which is normally longer than the N=N (1.245 Å) and C=N (1.27 Å), and shorter than the N-N (1.454 Å) and C-N (1.47 Å) bond lengths [54, 55]. It is noteworthy to mention that the each cation is surrounded by a large number of BTO^{2-} anions through strong HBs towards the O and N atoms of tetrazole rings. Moreover, all possible 2,3,4-N and O atoms of BTO^{2-} anions act as HB acceptors. The hydroxylammonium, 2-methylimidazolium and uronium cations act as both HB acceptor and donor due to the presence of both O and H atoms. These HBs are due to the interaction between donors (O-H and N-H) of various cations and proton acceptors (O and N atoms) of BTO^{2-} anions. Among them, (cation) D-H...O (BTO^{2-}) bonds contain strongest HBs due to high electronegative value of O atom than the N atom in BTO^{2-}. On the other hand, the methyl groups in DMA-BTO and M_2-BTO cations do not contribute to the hydrogen bonds. The intermolecular interactions in cations play a significant role in closely packing the adjacent BTO layers. Hence, the H...A distance of the HB's in cations can significantly demonstrate how close the interactions between cations and BTO's are. Further, D–H...A length (1.492 Å) for the uronium cation to the oxygen of the BTO anion is shorter than the usual cation-HBs (1.893 Å) for explosives [56]. Figure 3.2 displays the intermolecular interactions around various cations in which the H...A distance (1.573 Å) for hydroxylammonium cation in TKX-50 is the next shortest among the studied energetic salts. The H...A lengths for various cations are in the following ranges: hydroxylammonium: 1.573-2.471 Å, 2-methylimidazolium: 1.722-2.467 Å, hydrazine: 1.630-2.376 Å, uronium: 1.492-2.418 Å, methylamine: 1.724-2.381 Å, ammonium: 1.883-1.954 Å. The extensive intermolecular hydrogen bonding

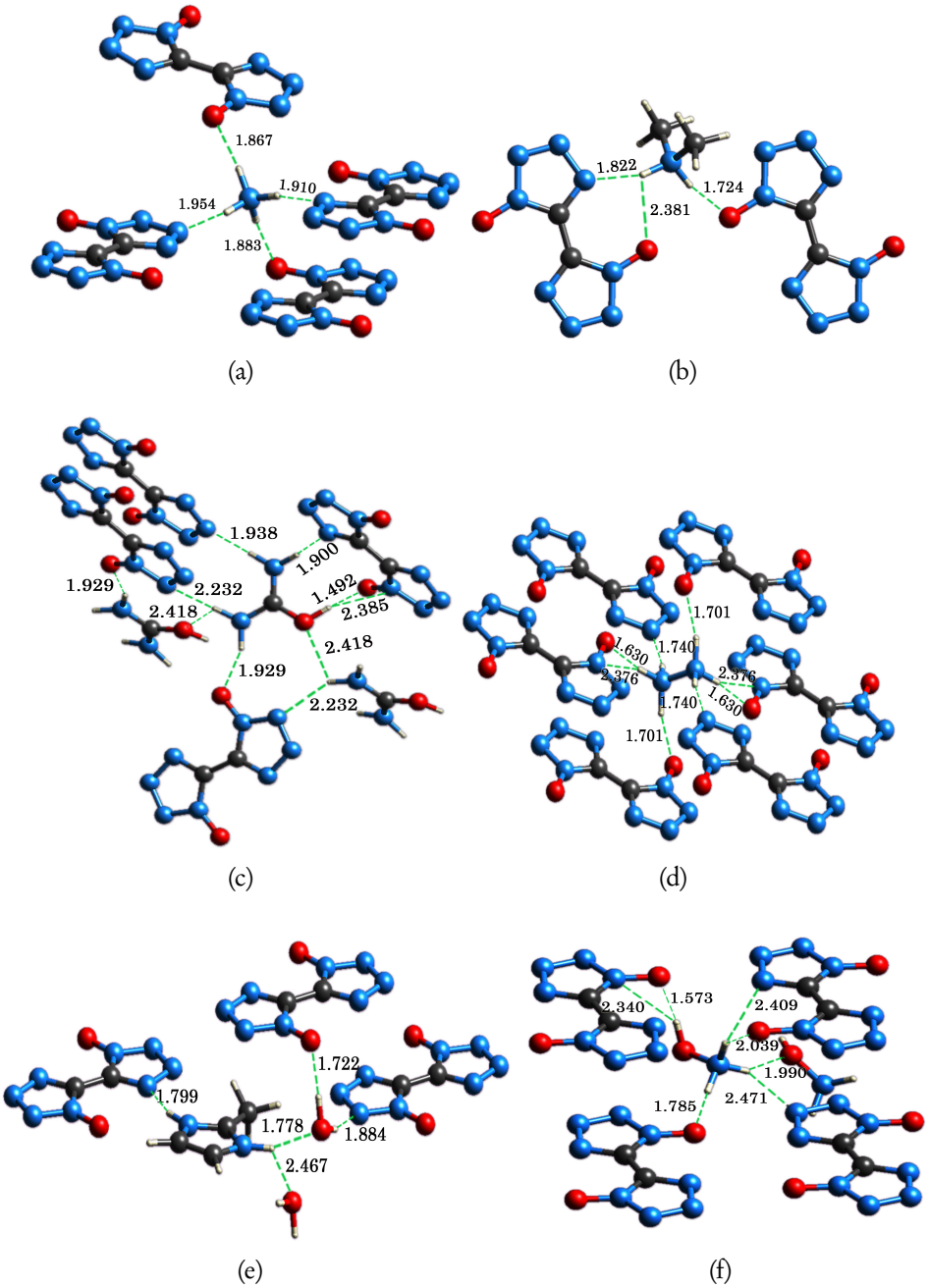

Figure 3.2: Intermolecular HBs around various cations, represented by green dash. (a) ABTOX, (b) DMA-BTO, (c) DU-BTO, (d) HA-BTO, (e) M_2BTO and (f) TKX-50.

between BTO anion and cations not only enhances the detonation properties but also increases the thermal stability and allows the molecule to possess low sensitivity by providing improved safety in storage and transportation.

The strength of the intermolecular interactions can be understood by measuring D...A distance. As demonstrated in figure 3.2, the O...O, N...O, N...N contacts range within 2.52-2.71, 2.69-3.36, 2.77-3.38 Å. According to bond radii criteria of O (1.52 Å) and N(1.55 Å), the above contact distances can be transformed as the ratios to the related sum of vdW radii (R_1) of 3.04 (O+O), 3.07 (N+O) and 3.1 (N+N) Å, respectively. These are 0.83-0.89, 0.88-1.09 and 0.89-1.09 for O...O, N...O and N...N contacts, respectively. Hence, R_1 decreases in the order: O...O < N...O < N...N, showing an increase in intermolecular interactions in the same order. More interestingly, the average R_1 values of the D...A contacts for HA-BTO are evidently shorter than other cations, suggesting an increase in the intermolecular interactions among the studied energetic salts. The strongest intermolecular interactions in this material is mainly responsible for its high molecular stability and also contains smaller IS than other cations. The next strong intermolecular interactions are observed in M_2BTO. The average R_1 values for various EIS are in the following range: TKX-50: 0.90-1.01, M_2BTO: 0.90-0.99, HA-BTO: 0.885-0.99, DU-BTO: 0.90-1.045, DMA-BTO: 0.91-0.95, ABTOX: 0.945-0.96.

3.3.2 Zone center phonon frequencies

The energetic salts are strongly bounded by weak intermolecular interactions, usually vdW forces and/or hydrogen bonds. Especially in complex molecular crystals, the signature of the corresponding strong hydrogen bonding environments are difficult to capture via x-ray diffraction because of very low intensity. However, the distribution of various hydrogen bonding networks and the presence of vibrational delocalization due to intermolecular vibrational coupling leads to strong congested spectra, which are challenging as well as difficult to elucidate. A widespread analysis, incorporating group theoretical methods and DFPT, can

overcome the scepticism of interpreting complementary structural information involving strong hydrogen bonding networks. Recently, Dreger et. al., [50] studied the Raman spectroscopic measurements and DFT method through CASTEP program to understand the structural and vibrational behavior of TKX-50 and observed that the presence of strong intermolecular interactions and the coupling of vibrational modes might strongly contribute to the shock insensitivity of TKX-50. Nevertheless, the detail investigations related to the vibrational description of the studied energetic salts are not yet reported. Therefore, the fundamental vibrational frequencies along with their corresponding intensities of the IR spectrum were extensively investigated for the studied energetic salts.

According to the crystal information of ABTOX, the monoclinic (P21/c) structure with 44 atoms of unit cell gives rise to 3 acoustic and 129 optical phonon modes at Brillouin zone Γ-point. The optical vibrational modes of the studied energetic salts in the centre of the Brillouin zone are classified with the irreducible representations as:

$$\Gamma_{optical}(\text{ABTOX}) = 32A_u(\text{IR})\oplus 31B_u(\text{IR})\oplus 33A_g(\text{Raman})\oplus 33B_g\ (\text{Raman})$$

$$\Gamma_{optical}(\text{DMA-BTO}) = 48A_u\ (\text{IR})\oplus 51A_g\ (\text{Raman})$$

$$\Gamma_{optical}(\text{DU-BTO}) = 44A_u(\text{IR})\oplus 43B_u(\text{IR})\oplus 45A_g\ (\text{Raman})\oplus 45B_g\ (\text{Raman})$$

$$\Gamma_{optical}(\text{HA-BTO}) = 27A_u\ (\text{IR})\oplus 30A_g\ (\text{Raman})$$

$$\Gamma_{optical}(M_2\text{-BTO}) = 63A_u\ (\text{IR})\oplus 66A_g\ (\text{Raman})$$

$$\Gamma_{optical}(\text{TKX-BTO}) = 35A_u\ (\text{IR})\oplus 34B_u\ (\text{IR})\oplus 36A_g\ (\text{Raman})\oplus 36B_g\ (\text{Raman})$$

From the vibrational assignments presented in Table 3.2, it immediately reflects that very less number of modes appear as "pure" vibrations of particular functional groups and most of them are contributions from the vibrations of various functional groups, as is often in most of the energetic materials. For all the energetic salts, the low frequency modes up to nearly 250 cm^{-1} are because of lattice vibrations (rotational and/or translational) or their combination with low-frequency molecular motions of both cation and anion vibrations. In the

Table 3.2: Calculated infrared active modes and their assignments for six EIS at DFT-D2 equilibrium volume using NCP approach

Modes	Frequency (cm^{-1})	Assignment	Modes	Frequency (cm^{-1})	Assignment
	ABTOX			DMA-BTO	
M04-M30	45-242	lattice modes	M04-M19	198	lattice modes
M31,M32	275,278	anion twist	M20-M24	233-286	θCH_3
M33,M34	303,317	ring rock	M25	302	$\theta CH_3 + \rho H_2 + \rho N{=}O$
M35,M36	357,361	anion wag + cation rot	M26,M27	329,331	$\theta CH_3 + \rho NH_2$
M37,M38	398,405	cation rot + ring in-plane- shifting	M28	336	$\theta CH_3 + \rho NH_2$ + anion wag
M39,M40	423,428	anion wag	M29	399	ring in-plane shift
M41-M44	477-492	ρNH_3	M30	412	ρCH_2
M45,M46	500,511	cation rot	M31,M32	415,421	$\omega CH_3 + \tau$C-C
M47,M48	524,526	ρNH_3	M33,M34	497,597	ring rot + $\rho N{=}O$
M49-M54	532-552	cation rot	M35,M36	641,659	ring out-of-plane bend
M55	610	ring rot + $\tau N{=}O$ + cation rot	M37	675	ωC-C + τN-N
M56	618	ring rot + $\tau N{=}O + \rho NH_3$	M38	707	τC-C + τN-N
M57-M60	647-662	ring out-of-plane bend	M39,M40	718,766	ring str + $\nu N{=}O$
M61,M62	680	ωC-C + τN-N	M41,M42	885,886	ωCH + νNH
M63,M64	712	τC-C + τN-N	M43,M44	913,921	$\rho CH_2 + \rho NH_2$
M65,M66	726	$\nu N{=}O$	M45	942	$\nu_a N{=}N{-}N + \sigma C{=}N{-}N$
M67,M68	774-775	$\nu N{=}O$ + ring str	M46	964	$\omega CH_3 + \rho NH_2 + \nu$C-N + $\sigma N{=}N{-}N$
M69,M70	962	$\sigma N{=}N{-}N$	M47	1004	ring str
M71,M72	967	ρC-C + νC-N + $\sigma N{=}N{-}N$	M48	1015	$\omega CH_3 + \nu$CH
M73	1020	νC-N + $\sigma N{=}N{-}N$	M49	1016	ωCH_3
M74	1020	νN-N + ν_sC-N-N	M50	1030	$\rho CH_2 + \tau NH_2 + \nu_a N{=}N{-}N$

Continued on next page

Table 3.2 – Continued from previous page

Modes	Frequency (cm^{-1})	Assignment	Modes	Frequency (cm^{-1})	Assignment
M75,M76	1065,1066	νN-N + ν_aN=N-N	M51,M52	1039,1045	ωCH_3 + τNH_2
M77,M78	1098,1099	νN-N + τN=N	M53,M54	1076,1078	ωCH_3 + ωNH_2
M79,M80	1113,1114	νN-N	M55	1082	ωCH_3 + ωNH_2 + νN-N + τN=N
M81,M82	1127,1130	νC-N + ν_aN=N-N	M56	1108	νN-N
M83,M84	1202,1204	ν_sN=N-N	M57	1115	ν_aN=N-N + νC-N + C-C in-plane shift
M85,M86	1207,1208	νN=N + ν_aN=C-N + νN=O	M58	1184	ν_sN=N-N
M87,M88	1268,1271	ρC-C + νC=N + νN=O	M59	1197	νC=N + ν_aN=N-N
M89	1315	νC=N + τC-N	M60,M61	1211,1213	ωCH_3
M90	1316	ωNH_3 + νC=N + τC-N	M62	1263	ωCH_3 + ρNH_2 + ρC-C + νN=O
M91,M92	1385,1397	ωNH_3 + ρC-N + νC-N + νN=O	M63	1264	ωCH_3 + ρNH_2 + νC=N
M93,M94	1420,1421	ωNH_3 + ρC-N + νC-N	M64	1275	ωCH_3 + ρNH_2 + ρC-C + νC=N
M95-M97	1429-1438	ωNH_4	M65	1316	νC=N + τC-N
M98-M106	1441-1470	ωNH_3 + ρNH	M66,M67	1382,1384	ωCH_3
M107	1560	σNH_4	M68	1388	ωCH_3 + νC-N
M108	1560	νC-C	M69,M70	1409,1413	ωCH_3
M109-M116	1695-1729	σNH_4	M71	1427	σCH_2 + ρCH + ρNH
M117,M118	2965,2966	$\nu_s NH_2$	M72	1431	τNH_2 + σCH_2 + ρCH
M119,M120	2969,2972	$\nu_s NH_4$	M73	1431	τNH_2 + σCH_2 + ρCH + τC-C + νN-O
M121	2990	$\nu_a NH_2$	M74	1441	τNH_2 + σCH_2 + ρC-C
M122-M124	2933-3008	$\nu_a NH_4$	M75,M76	1443,1447	ωNH_2 + σCH_2 + ρCH
M125-M127	3025-3047	$\nu_s NH_2$	M77-M81	1457-1476	τNH_2 + σCH_2 + ρCH
M128-M131	3052	$\nu_a NH_2$	M82,M83	1483-1488	ωNH_2 + σCH_2 + ρCH
M132	3080	$\nu_a NH_4$	M84	1557	σNH_2 + νC-C

Continued on next page

Table 3.2 – Continued from previous page

Modes	Frequency (cm^{-1})	Assignment	Modes	Frequency (cm^{-1})	Assignment
	DU-BTO		M85,M86	1593,1604	σNH_2
M04-M34	45-187	lattice modes	M87,M88	2817,2820	ν_a
NH_2 M35-M37	195-210	ρ(C-NH_2)	M89,M90	2852,2859	$\nu_s NH_2$
M38	218	(C-NH_2) trans	M91-M94	2961-2965	$\nu_s CH_3$
M39-M42	247-254	cation rot, ring rock	M95,M96	3065	$\nu_s CH_2$ + νCH
M43,M44	268,270	ρN=O + τC-C	M97,M98	3068	$\nu_a CH_2$
M45,M46	318,319	cation rot + ring out-of-plane bend	M99,M100	3073,3075	$\nu_s CH_2$ + νCH
M47,M48	388,390	ρOH + anion wag	M101,M102	3079	$\nu_s CH_2$
M49,M50	402	νC-C + ring-in-plane shift		HA-BTO	
M51,M52	432,433	ρOH + τN=O + ring out-of-plane bend	M04-M16	74-353	lattice modes
M53-M58	475-504	ωNH_2	M17	367	ρNH_3 + ring out-of-plane bend
M59-M62	535-543	ρHN_2	M18	405	νC-C + ring in-plane shift
M63-M66	590-595	ρC-O-H + ρ(CNH_2) + νC=N	M19	433	ρNH_3 + ring out-of-plane bend
M67,M68	598,605	ρC-O-H + ρ(CNH_2) + ring rot	M20	509	ρNH_3 + anion rot + ρN=O
M69-M72	634-637	τNH_2 + ρNH	M21	602	ρNH_3 + anion rot
M73	639	ωNH_2 + ρOH + ring out-of-plane bend	M22	635	ρNH_3 + ring out-of-plane bend
M74-M77	640-648	τNH_2 + ρNH	M23	653	ρNH_3
M78,M79	651,661	ωNH_2 + ρOH + ring out-of-plane bend	M24	681	ωC-C + τN-N
M80,M81	661,680	ρNH + ωC-C + τN-N	M25,M26	684,701	ρNH_3
M82,M83	681,714	τC-C + τN-N	M27	716	τC-C + τN-N
M84,M85	714,725	ω(CNH_2) + ring str	M28	732	ρNH_3 + νN=O

Continued on next page

Table 3.2 – Continued from previous page

Modes	Frequency (cm^{-1})	Assignment	Modes	Frequency (cm^{-1})	Assignment
M86-M90	725-731	$\omega(CNH_2)$	M29	772	ρNH_3 + νN=O + ring str
M91,M92	773	ρOH + ring str	M30	960	σN=N-N + νN-N
M93-M96	810-811	τNH_2	M31	963	σN=N-N + νC-N
M97	962	ρOH +νN-N + σC=N-N	M32	1005	cation str
M98	962	ρOH + σN=N-N	M33	1012	ring str + NH wag
M99,M100	966,967	ρC-C + νC-N + σN=N-N	M34	1084	ν_aN=N-N
M101-M104	1003-1008	cation str	M35	1098	ρNH_2 + νN-N + τN=N
M105	1018	ρOH + ν_sC-N-N + νN-N	M36	1116	νN-N + τN=N
M106	1019	ρOH + ring str	M37	1121	ρNH_2 + ν_aN=N-N
M107,M108	1043,1047	ρNH_2 + ρOH	M38,M39	1130,1173	ωNH_3
M109,M110	1052,1054	ρOH	M40	1205	ωNH_3 + ring str
M111	1073	ρNH_2 + ρOH + ν_aN=N-N	M41	1205	ν_sN-N=N
M112	1074	ρOH + ν_aN=N-N	M42	1262	σNH_2 + νC=N + νN=O
M113,M114	1076,1082	ρNH_2	M43	1320	ωNH_2 + νC=N + νN=O
M115,M116	1087,1088	ρNH_2 + ρOH	M44	1326	cation rot
M117,M118	1099,1102	ρNH_2 + νN-N	M45	1386	ωNH_2 + νC-N
M119	1111	νN-N + τN=N	M46	1396	ρNH_2
M120-M121	1112-1128	ρNH_2 + νN=N + νC-N	M47	1432	ωNH_3 + νC-N
M123-M126	1167-1174	ρNH_2	M48	1507	ωNH_3
M127	1202	ρNH_2 + ρOH + νN=N-N	M49	1546	ωNH_3 + νC-C
M128	1203	ρNH2 + νN=N	M50	1552	σNH_2 + ρNH
M129-M130	1204-1207	ρOH + νN=N + νC=N + νN=O	M51	1567	ωNH_3 + νC-C
M131	1260	ρOH + ρC-C + νN=O + νC=N	M52-M54	1621-1659	σNH_2 + ρNH
M132	1261	ρOH + ρC-C + νN=O	M55,M56	2545,2557	$\nu_a NH_2$
M133-M134	1318-1320	ρOH + νC=N + νN=O	M57,M58	2593,2664	$\nu_s NH_2$ + νNH

Continued on next page

Table 3.2 – Continued from previous page

Modes	Frequency (cm^{-1})	Assignment	Modes	Frequency (cm^{-1})	Assignment
M135-M136	1366	ρOH	M59	2777	$\nu_s NH_2$
M137	1370	ρOH + νC-N	M60	2840	$\nu_s NH_3$
M138	1387	ρOH		TKX-50	
M139	1400	ρOH + νN=O	M04-M33	23-240	lattice modes
M140	1412	ρOH	M34	247	θNH_3
M141-M142	1427-1430	ρC-O + ρC-C + νN=O	M35	264	ring twist, cation rock
M143-M145	1528-1541	σNH_2 + νC-O	M36	278	ring twist, θNH_3
M146-147	1562	σNH_2 + νC-C	M37	285	cation rock
M149-M152	1574-1583	σNH_2 + ρOH	M38	298	ρN=O, cation rock
M153-M157	1641-1663	σNH_2	M39-M40	306-311	cation rock
M157-160	1678-1707	σNH_2 + ρOH + νC=N	M41	325	θNH_3
M161-M164	2422-2455	νOH	M42	340	ring rock, ρN=O, θNH_3
M165-M168	3078-3109	$\nu_s NH_2$	M43-M47	352-380	θNH_3
M169-M172	3181-3200	$\nu_a NH_2$	M48-M49	391-404	ring out-of-plane bend, ring rot, τN=O, θNH_3, ρOH
M173-M176	3240-3256	$\nu_s NH_2$	M50	405	νC-C, ring in-plane shift
M177-M180	3424-3440	$\nu_a NH_2$	M51	421	ring rot
	M_2-BTO		M52-M53	426-493	ring out-of-plane bend, ring rot, τN=O, θNH_3, ρOH
M04-M28	55-232	lattice modes	M54	494	ring rot, τN=O, θNH_3, ρOH
M29-M31	240-265	ωcation	M55-M56	595	ring rot, τN=O, ρOH
M32	272	ρN=O + τ anion C-C	M57-M59	633-663	ring out-of-plane bending
M33,M34	311,358	ωCH_3 + anion ring out-of-plane bend	M60	664	ωOH
M35,M36	363,367	ωCH_3 + cation ring rot	M61-M62	683-684	ωC-C + τN-N

Continued on next page

Table 3.2 – Continued from previous page

Modes	Frequency (cm^{-1})	Assignment	Modes	Frequency (cm^{-1})	Assignment
M37	413	ν anion C-C + anion ring in-plane shift	M63-M64	708	νN=O + ωOH
M38	416	anion ring out-of-plane + τN=O	M65-M69	715	τC-C + τN-N
M39	480	anion ring rot + τN=O + τOH_2	M67-M68	754	νring + ωOH
M40,M41	566,577	ρOH_2 + ρNH	M69-M72	859-866	ωOH
M42	589	anion ring rot + τN=O + ρNH	M73	954	νring + ωOH
M43-M45	611-637	ρ(HC=CH)	M74	955	ρC-C + νC-N + σN=N-N + ωOH
M46	643	ring out-of-plane bend	M75-76	961-963	ρC-C + νC-N + σN=N-N
M47	644	ωCH_3 + ω(HC=CH) + τ cation C=N	M77-M79	1008-1009	νN-O + ωOH + ωNH_2
M48	655	ρNH + ρOH_2 + τ anion C-C + τN-N	M80-M81	1010-1011	νN-O + ν_sC-N-N + νN-N
M49,M50	658,663	ν cation C-C + ρOH + σC-N-C	M82	1012	νN-O
M51	674	τN-N + ωOH	M83-M88	1066-1095	νN-N + τ N=N
M52	708	τ anion C-C + τN-N	M89-M90	1121	ρNH_2 + ρOH + νN=O + ν_aN=N-N
M53	709	τOH_2 + ρOH + νN=O	M91-M94	1153-1163	ωNH_3
M54	725	τOH_2 + ω(HC=CH)	M95-97	1514-1693	ωNH_3 + ρOH + νC=N + ν_sN=N-N
M55-M57	737-750	ωOH + ω(HC=CH)	M98	1208	ωNH_3 + ρOH + νC=N + νN=N
M58	774	ωOH + ν anion ring str	M99-M102	1212-1222	ωNH_3
M59	826	ωOH_3 + τ(HC=CH)	M103	1249	ν_sN=O + ρ C-C + ρNH + ρOH
M60	830	ωOH_2 + ρNH + ρCH	M104	1256	ν_aN=O + ρNH_2
M61,M62	847,852	ωOH_2 + τ(HC=CH)	M105-M106	1317-1318	νC=N + νN-N + ρOH
M63,M64	901,902	σN-C=C + σC-N-N + ρOH	M107-M08	1384-1386	νC-N + ρNH + ρOH

Continued on next page

Table 3.2 – Continued from previous page

Modes	Frequency (cm^{-1})	Assignment	Modes	Frequency (cm^{-1})	Assignment
M65	938	ωNH_3 + ρCH + ρNH + anion ring str	M109-M110	1423-1429	ρC-C + σC-N-N + ρOH
M66,M67	951,962	ωCH_3 + ρCH + ρNH	M111-M115	1502-1545	ωNH_3 + ωOH
M68	968	ωCH_3 + ρNH + τ anion C-C + ν_aC-N-N	M116	1550	σNH_2 + ρNH + ρOH
M69-M71	969-978	ωNH + ωCH_3 + ωCH	M117	1556	ρNH + ρOH
M72-M74	982-1001	ωNH + ωCH_3	M118	1557	σNH_2 + ρNH + ρOH
M75	1020	νN-N + ν cation C-N	M119	1567	σNH_2 + ρNH
M76,M77	1030	ωNH + ωCH_3	M120-M122	1569-1571	σNH_2 + ρNH + νC-C
M78	1047	νN-N + τN=N	M123-M124	1579-1580	σNH_2 + ρNH + ρOH
M79	1081	ρ(HC=CH) + ρNH	M125-M126	1585-1586	σNH_2 + ρNH
M80	1086	σ(HN-CH)	M127-M128	1514-1693	σNH_2 + ρNH, ρOH
M81	1091	νN-N + τN=N	M129-M32	2654-2671	ν_aNH + ν_aOH
M82,M83	1102,1109	ρNH + σ(HC=CH)	M133-M136	2911-2921	ν_sNH + ν_sOH
M84	1116	σ(HC=CH) + ρNH + νN-N	M137-M140	3108-3118	$\nu_s NH_2$
M85	1128	σ(HN-CH)	M141-M144	3186-3200	$\nu_a NH_2$
M86	1135	σ(HN-CH) + νanion N-C + ν_aN=N-N		Symbol	Description
M87	1144	σ(HN-CH)		ν_s	symmetric stretching
M88	1202	νN=N		ν_a	asymmetric stretching
M89	1207	ρCH + νN=N + νC=N		β	bending
M90	1273	ωCH_3 + ρNH + ν anion C=N + νN=O		ρ	rocking
M91	1292	ωCH_2 + ρNH + ρCH + νcation C-N + ν cation C=N		ω	wagging

Continued on next page

Table 3.2 – Continued from previous page

Modes	Frequency (cm^{-1})	Assignment	Modes	Frequency (cm^{-1})	Assignment
M92	1300	ωCH_2 + ρCH + ν cation C=N		τ	twisting
M93-M95	1301-1326	ωCH_3 + ρNH + ρCH + ν anion C=N + ν cation C-N		σ	scissoring
M96	1356	ωCH_3 + ρNH + ν cation C-C + ν cation, anion C-N		ν	stretching
M97	1364	ωCH_3 + ρNH		δ	deformation
M98	1392	σCH_2 + ρNH + νN=O + ν anion N-C		ρ	rocking
M99,M100	1408,1411	ρCH + σCH_2 + ν_a cation N=C-N		ω	wagging
M101	1420	ρNH + ρCH + σCH_2 + ν_a cation, anion N-C=N		ν	stretching
M102	1424	ρNH + σCH_2 + τC=C + ν cation N-C + τ anion C-C + ν cation N-C + νN=O		θ	rotation
M103	1424	ρNH + ρCH + σCH_2			
M104	1440	ρNH + σCH_2 + νN=C, τ cation C=C + τ anion C-C			
M105	1444	ρNH + σCH_2 + νN=C + τ cation C=C			
M106,M107	1484,1486	ρNH + ρCH + ν cation C-C + νC=C			
M108,M109	1493,1495	ρNH + ρCH + σCH_2 + νN=C + ν cation C=C			
M110	1556	ρNH + νC-C			

Continued on next page

Table 3.2 – Continued from previous page

Modes	Frequency (cm^{-1})	Assignment	Modes	Frequency (cm^{-1})	Assignment
M11,M112	1599,1602	ρNH + ρCH + ν cation C-C + νC=C			
M113,M114	1646,1651	σOH_2			
M115	2862	νNH			
M116	2869	νNH + $\nu_s OH_2$			
M117-M119	2955-2962	νNH + $\nu_s CH_3$ + $\nu_s OH_2$			
M120	2972	νNH + $\nu_s CH_3$			
M121,M122	3036,3037	$\nu_a CH_3$			
M123,M124	3078,3079	$\nu_a CH_2$			
M125-M127	3182-3188	νOH + ring CH			
M128	3201	νOH + ring CH + νNH			
M129,M130	3218,3219	ν ring CH			
M131,M132	3338,3346	νOH			

frequency range of 500-900 cm^{-1}, DU-BTO crystal contains more number of peaks than other energetic salts with a sharp intense peak at 647 cm^{-1}, which belongs to NH rocking and NH_2 wagging vibrations of uronium cation. The DMA-BTO structure contains only one intense peak in this region (913 cm^{-1}) with NH_2 and CH_2 rocking vibrations of methylamine cation. Further, the peak of M_2-BTO located at 826 cm^{-1} is assigned to HC=CH twisting and OH_3 wagging of methylimidazolium cation, whereas the peak located at 859 cm^{-1} of TKX-50 belongs to OH wagging of hydroxylammonium. Contrarily, ABTOX does not show any major peak in this region. The most of in-plane bending vibrations are described as ring C-C stretching modes, whereas out-of-plane bending modes are generalized as ring C-C deformations with pure or mixed vibrations. For all the energetic salts, the anionic ring out-of-plane bending modes are located in the range of 633-663 cm^{-1}. Figure 3.3c contains a maximum number of peaks throughout the spectrum except for DMA-BTO and ABTOX salts and are barely assigned to the modes of BTO aromatic ring system. In all cases, the distinct sharp peak is observed at $\sim$1205 cm^{-1}, which corresponds to the vibrations of BTO ring structure (νN=N + νN=N + ν_aN=C-N + ν_aN-N=N + νN=O). The mixed cation and anion vibrations are observed in figure 3.3d. The OH rocking motion of uronium cation and ring C-N stretching of BTO anion located at 1366 cm^{-1} is the strongest peak in this region.

Figure 3.3e and f corresponds to symmetric/asymmetric stretching frequencies of CH_2, CH_3, NH_2, NH_3, NH_4, OH and OH_2 modes. These vibrational frequencies for various cations are in the following range: uronium: 3078-3440 cm^{-1} Å [ν_s(OH,NH_2), ν_a(NH_2)], ammonium: 2965-3080 cm^{-1} Å [ν_s/ν_a(NH_2,NH_4)], hydroxylammonium: 2654-3200 cm^{-1} Å [ν_s(OH,NH,NH_2), ν_a(OH,NH,NH_2)], methylamine: 2817-3079 cm^{-1} Å [ν_s(NH_2,CH,CH_2,CH_3), ν_a(NH_2,CH_2)], 2-me thylimidzaolium: 2862-3346 cm^{-1} Å [ν_s(NH,OH,OH_2,CH_3), ν_a(CH_2,CH_3)], hydrazine: 2545-2840 cm^{-1} Å [ν_s(NH,NH_2,NH_3), ν_a(NH_2)] and their corresponding sharp intense bands are located at 3200, 3052, 2671, 2820, 2862, 2546 cm^{-1},

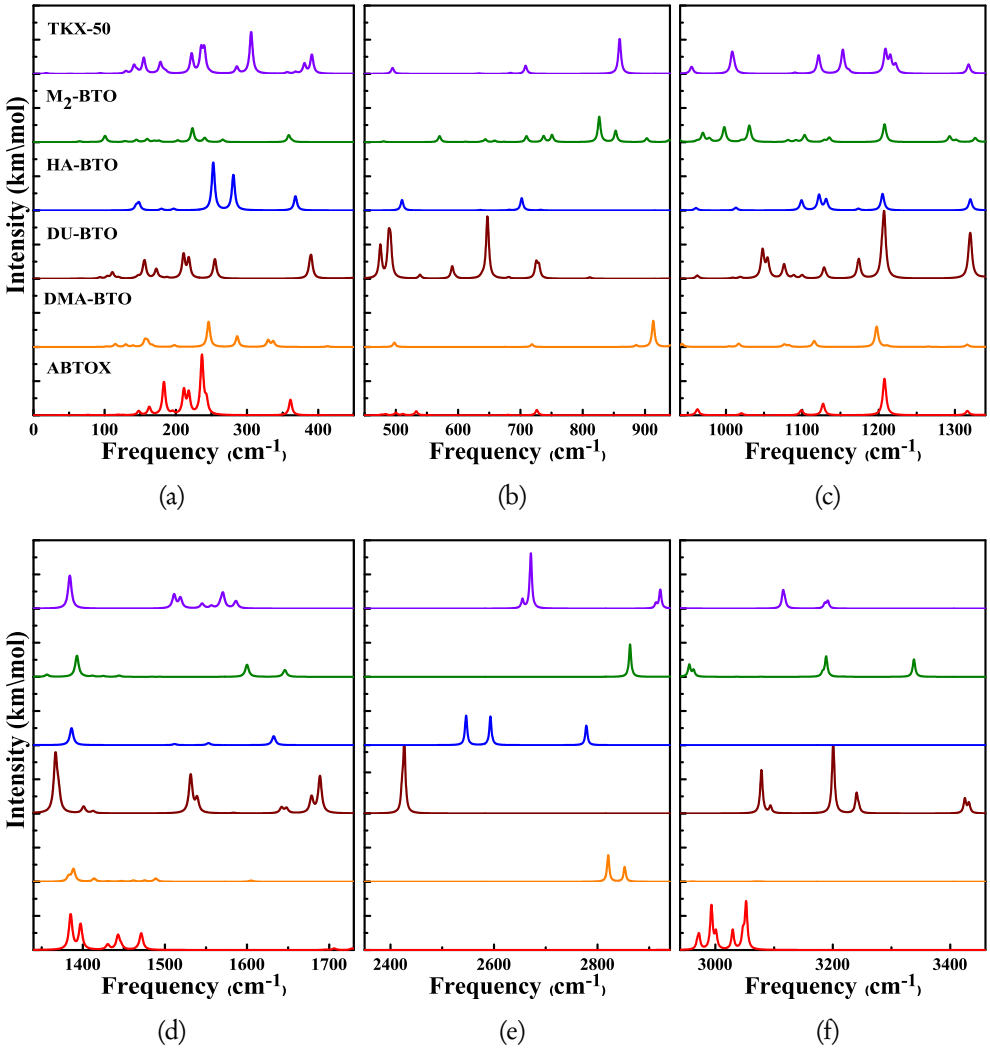

Figure 3.3: Calculated IR spectra of various EIS in the frequency range (a) 0-450 cm^{-1}, (b) 450-940 cm^{-1}, (c) 940-1340 cm^{-1} (d) 1340-1739 cm^{-1}, (e)2350-2940 cm^{-1} (f) 2940-3460 cm^{-1}

respectively. Typically, the IR stretching vibrations in the region of 1600 - 3200 cm^{-1} are related to strong HBs, whereas the weak HBs usually occur at 3200-3700 cm^{-1}. Further, the strength of D-H..A hydrogen bond can be expressed as the separation between donor and the acceptor atoms ($R_{D...O}$): A distance in the range 2.5-2.7 Å is considered as strong hydrogen bond, whereas, a separation greater than 2.7 Å is characterized by weak hydrogen bond [57]. Therefore, the correlation between stretching frequencies and $R_{D...O}$ can be used to demonstrate and characterize hydrogen bond strength [58]. From figure 3.3e and f, the IR spectra corresponding to D-H stretching vibrations in the crystal structure of HA-BTO are located at much lower frequency and the next lowest is observed in TKX-50 compared to other cations, representing the existence of strong hydrogen bonding environment in the crystal structure of HA-BTO.

3.3.3 Electronic band structure and density of states

The electronic structure of explosive materials are highly sensitive even to a small variation in their crystal system as the hybridization of electronic states mainly rely on the lattice structure, bond lengths and bond angles etc. In addition, the energy band gap can also be correlated with the sensitivity of energetic materials based on the principle of easiest transition [59]: lower the band gap, higher the probability of electron transition from valence band to conduction band and thus leads to higher sensitivity. In this context, a reliable theoretical approach based on quantum mechanical calculations is required to accurately predict the electronic band structure of complex explosive materials. The Heyd-Scuseria-Ernzerhof method has been proven as the state of the art in quantitatively predicting and screening the electronic structures of existing as well as new materials. Therefore, we employed the HSE06 approach to investigate the electronic properties of these EIS. The calculated electronic band structure for the studied EIS using HSE functional along specific high symmetry directions were displayed in figure 3.4. The maximum and minimum of the valence and conduction bands for

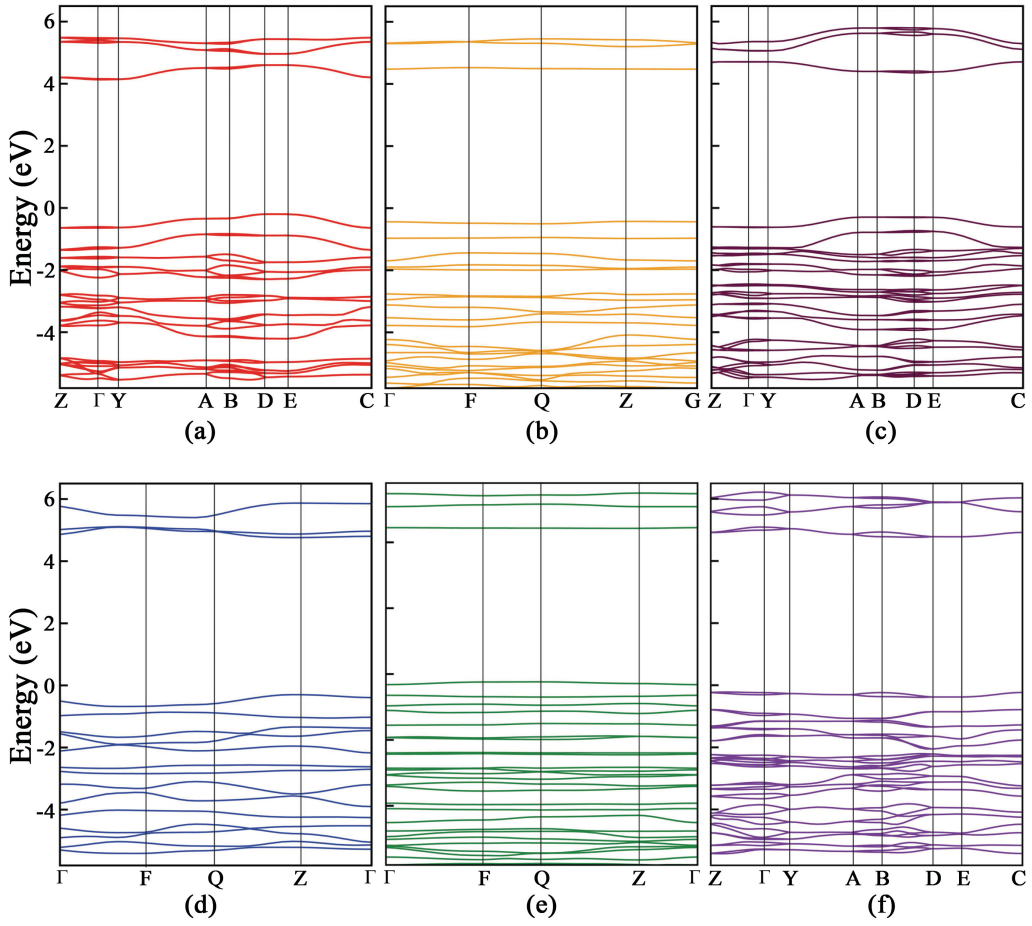

Figure 3.4: The calculated band structure of (a)ABTOX, (b)DMA-BTO, (c) DU-BTO, (d)HA-BTO, (e) M_2BTO and (f) TKX-50 crystals using HSE functional.

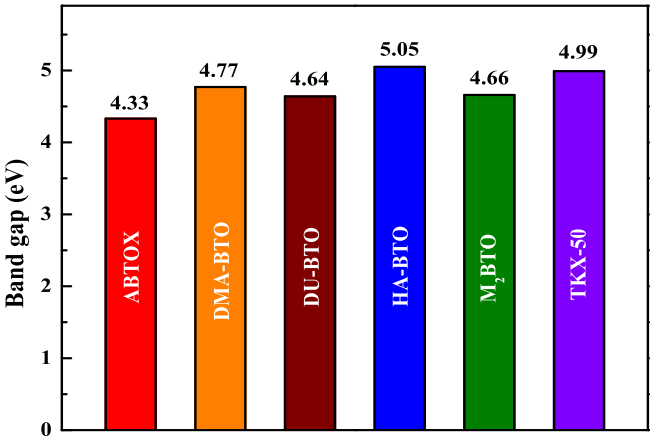

Figure 3.5: The calculated band gaps for ABTOX, DMA-BTO, DU-BTO, HA-BTO, M_2BTO and TKX-50 crystals using HSE functional at optimized parameters.

HA-BTO, DU-BTO and DMA-BTO are situated along the same -Z, -D and -Γ directions, representing the direct band gap with a width of 5.05, 4.64 and 4.77 eV, respectively. Whereas, for M_2-BTO, ABTOX and TKX-50, the energy band get the maximum at point -Q, -D and -C in the valence band and the minimum at point -Z, -Z and -B in the conduction band, indicating the indirect band gap with a width of 4.66, 4.33 and 4.99 eV, respectively. Overall, the maximum band gap corresponds to HA-BTO, whereas the minimum one is for ABTOX (see figure 3.5). As mentioned earlier, the explosive materials with smaller band gaps were expected to possess lower stability and higher reactivity in the photochemical process that may lead to possible electron transfer; it might be inferred that the HA-BTO has the lowest reactivity among the studied energetic salts followed by TKX-50. The observed criteria is also consistent with the impact sensitivity measured through standard BAM [60] method, where HA-BTO (28 J) possesses a lower impact sensitive compared to TKX-50 (20 J) [17].

The calculated total densities of states (DOS) along with cationic and anionic partial DOS for the studied energetic salts are presented in figure 3.6. The valence band maximum (VBM) and conduction band minimum (CBM) for ABTOX, HA-

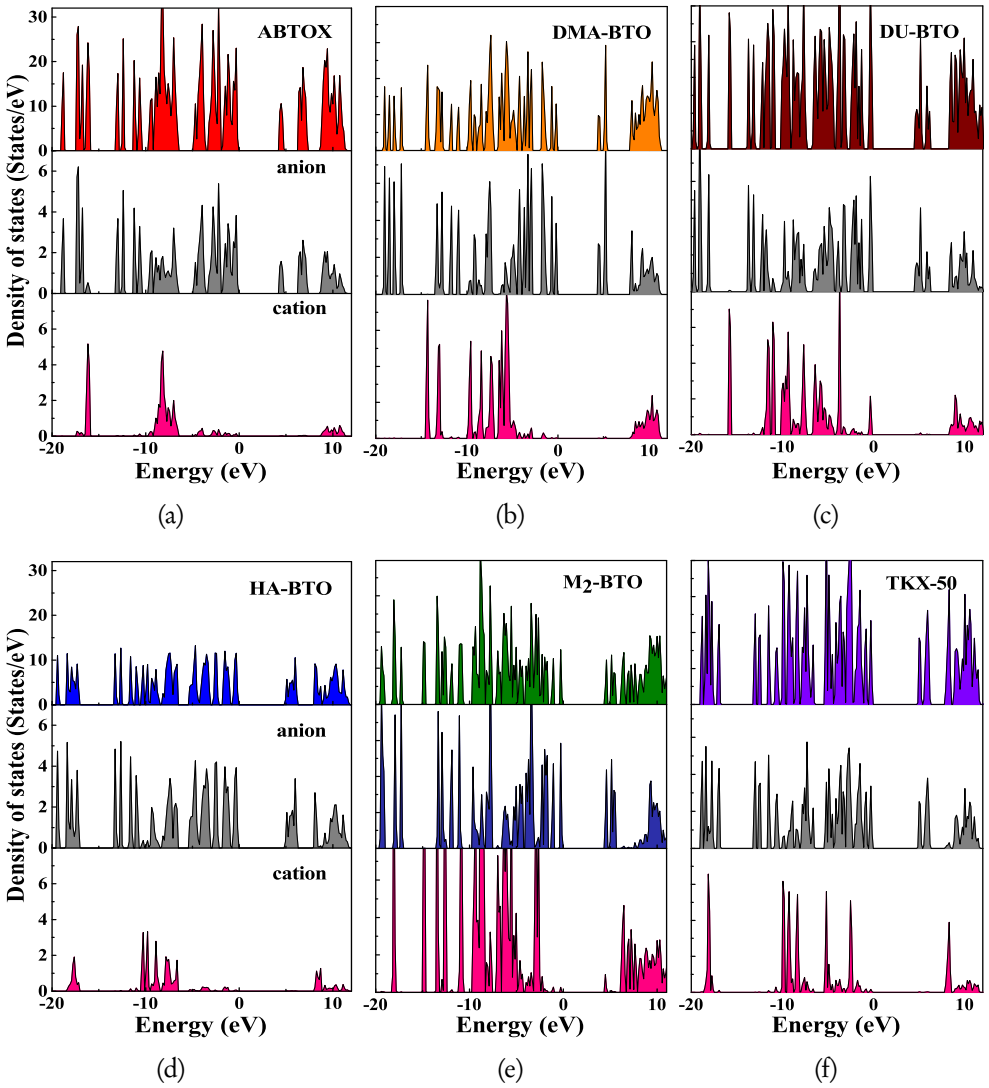

Figure 3.6: The calculated Total, anionic and cationic DOSs (a) ABTOX, (b) DMA-BTO, (c) DU-BTO, (d) HA-BTO, (e) M_2BTO and (f) TKX-50 crystals using HSE functional.

BTO, DMA-BTO, and TKX-50 are of anionic behavior. In the case of DU-BTO, the upper occupied states show a mixed nature, whereas the peak at 3.4 eV corresponds to the anionic nature. In contrast to the DU-BTO, the CBM of M_2-BTO is determined by the anion-cation hybridization, while the VBM show pure anionic behavior. For the valence band of the ABTOX spectrum, the bands at energies of -18.7 eV, -17.18 eV, -12.3 eV, -11.2 eV, -10.6 eV, -7.0 eV, -3.9 eV and -2.7 eV mainly correspond to the anionic states. On the other hand, the bands at -16.1 eV and -8.3 eV are due to the cationic states.

3.3.4 Hirshfeld surface and 2D fingerprint plots

The visualization and analysis of molecular structure using Hirshfeld surfaces can offer an effective way to explore the crystal packing and the associated intermolecular interactions. The majority contacts of Hirshfeld surfaces for all the BTO salts are mainly due to N...H/ H...N contacts, ranging from 35 to 50%. The O...H/H...O interactions occupy the next highest contribution with the proportion varying from 16 - 27%, which is notably lower/higher in DAM-BTO/HA-BTO, respectively. These contacts are the shortest interactions in all molecules, which can be identified as large red spots on the d_{norm} surfaces and appear as a pair of spikes at the bottom of each fingerprint plot (see figure 3.7). Further, the shorter distance of the spikes to the original point (0.68-1.05 Å , the sum values of horizontal and vertical coordinates) represent the strong hydrogen bonding networks in these crystals. In addition,Jeffery et. al. [61] classified these spikes as moderate and strong hydrogen bonds. The N...N interactions show a much larger contribution in HA-BTO than in the other structures with a proportion of 18.3%. The "wings" seen in the plots of M_2-BTO and DMA-BTO belong to signature C...H/H...C interactions with the proportion of 5.2 and 5.6%, while HA-BTO does not produce any contribution. One of the prominent short contacts is found in DU-BTO and is due to the close approach of BTO oxygen to the uronium proton i.e., a significant O-H...O interaction. Another short inter-

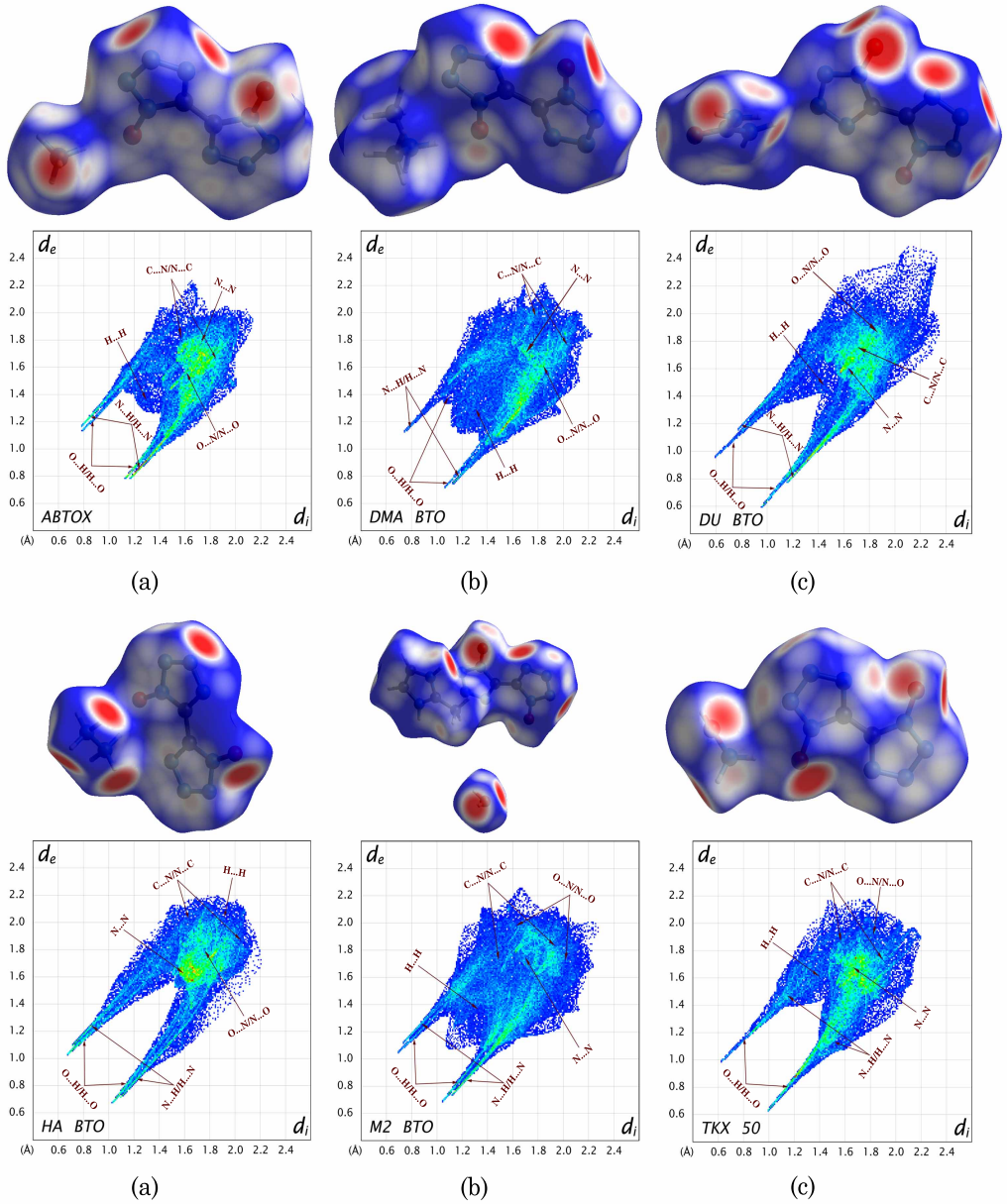

Figure 3.7: (Hirshfeld surface and corresponding 2D fingerprint plots of (a) ABTOX, (b) DMA-BTO, (c) DU-BTO, (d) HA-BTO, (e) M_2BTO and (f) TKX-50 crystals.

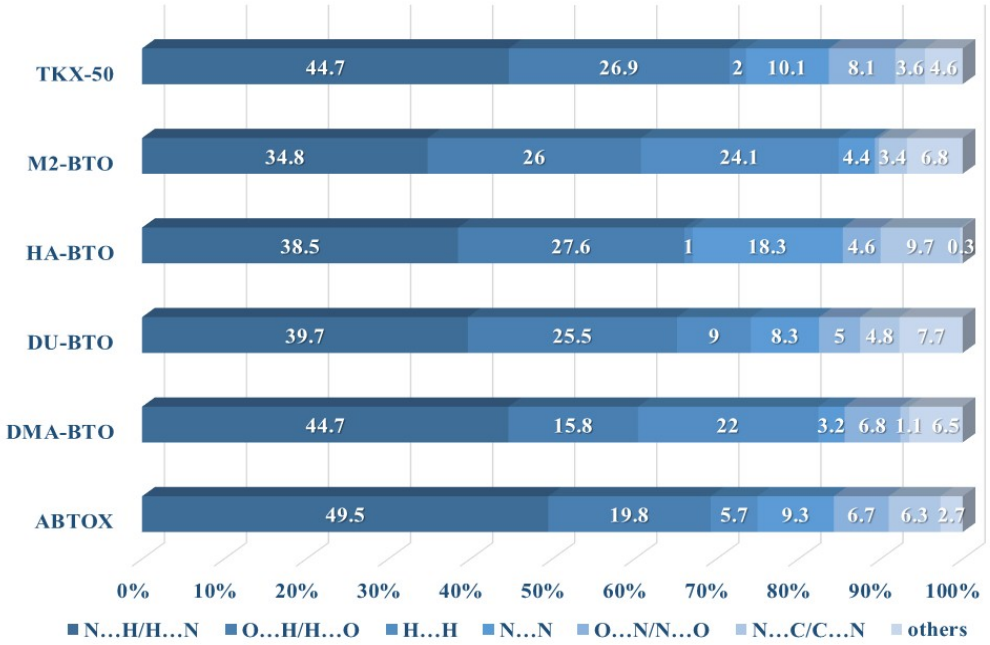

Figure 3.8: Populations of close contacts of 6 EIS molecules in crystal stacking.

action observed in TKX-50, where the HA cation interacts with oxygen from BTO groups. By analyzing $d_i + d_e$ of these energetic salts, we found that HA-BTO, TKX-50 and DU-BTO possess stronger hydrogen bonds compared to the remaining molecules. The H...H contacts in HA-BTO feature lowest proportion than the other molecules, making up only 1% of the surface. Whereas, DMA-BTO and M_2-BTO show significantly more H...H contacts (23%) with almost 15% higher contribution than any of the energetic salts and fewer N...N (4%) interactions, compared to 9-18% for the other salts. This huge variation in these interactions can be attributed to the presence of more hydrogen atoms: M_2-BTO possesses highest number of hydrogen atoms, while HA-BTO contains less number compared to other molecules. Despite the high contribution of H...H contacts in M_2-BTO, its role in the stabilization of the molecule is typically less in magnitude, as these interactions are among the same species (see figure 3.8).

Table 3.3: Energetic properties of the BTO salts along with experimental values in brackets.

Salt	OB (%)	HOF_{cation} (kJ/mol)	HOF_{anion} (kJ/mol)	HOF_{salt} (kJ/mol)	Density (g/cm^3)	VOD (km/s)	DP (GPa)
ABTOX	-47.1	635	583	300	1.765[23]	9.30 (8.76)[23]	31.74
DMA-BTO	-110.8	586	583	447	1.421[24]	7.73	19.08
DU-BTO	-49.7	428	583 (587.7)[25]	97	1.695[25]	8.11 (8.26)[25]	23.69 (29.15)[25]
HA-BTO	-39.6	2084	583	463 (425.6)[17]	1.913[17]	9.94 (8.93)[17]	38.85 (36.1)[17]
M_2-BTO	-119.8	659	583	675 (662.4)[26]	1.534 [26]	7.00 (7.10)[26]	16.01 (20.23)[26]
TKX-50	-27.1	677	583	432 (446.6)[16] (426.4)[17]	1.877[16]	9.91 (9.69)[16] (9.16)[17]	40.23 (42.4)[16] (38.1)[17]

HOF_{cation}, HOF_{anion}, and HOF_{salt} are the heats of formation of cation, anion and salt, respectively.

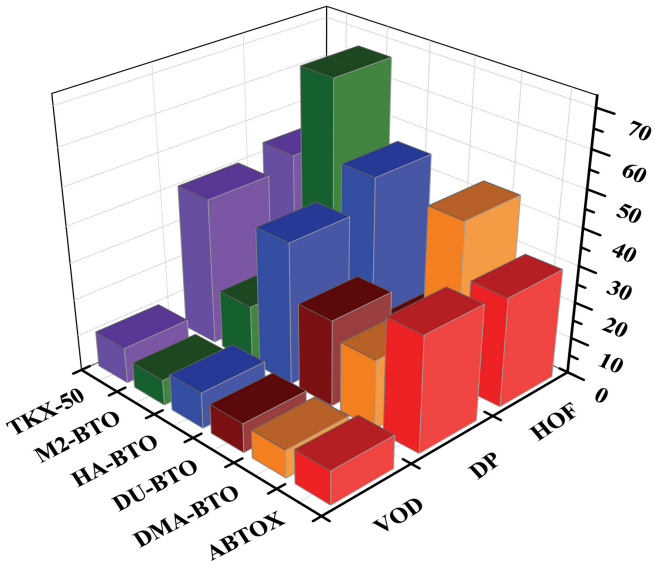

Figure 3.9: The energetic performance of BTO based energetic salts. HOF values are in $\times 10^1$ order.

3.3.5 Detonation properties

Detonation pressure (P) and velocity (D) are prime indicators for the performance of energetic materials. Based on computed densities and heat of formation, P and D were predicted using the EXPLO5 code (see Table 3.3). The BTO energetic salts show positive heats of formation (HOF) and except urea salt (DU-BTO), all other salts have HOF above 300 kJ/mol. The densities of these energetic salts fall in the range of 1.49–1.91 g/cm^3, in which HA-BTO and TKX-50 show greater densities. It is also noteworthy that the presence of heterocyclic cations (in M_2-BTO) helps to achieve high positive HOFs due to their high energy contribution. The oxygen balance (OB) for the six molecules ranges from -119 to -27 % in which TKX-50 show better OB. It is acclaimed that the positive HOFs and high densities are favorable to achieve superior detonation performance. HA-BTO and TKX-50 salts having relatively high HOF ($>$ 400 kJ/mol) and high densities ($>$ 1.84 g/cm^3), resulted in superior detonation pressures (above 38 GPa) and detonation velocities (above 9.9 km/s), making them potential explosive materials (see fig-

ure 3.9). However, DU-BTO and ABTOX show higher performance than TNT (P = 22.0 GPa, D = 6.94 km/s) while M_2-BTO and DMA-BTO indicate the poor performance due to their lower densities.

3.4 Conclusions

In summary, first-principles calculations were carried out on a series of 5,5′-bitetrazole-1,1′-diolate based EIS to understand the structure-property-performance interrelationship. The D-H stretching vibrational modes of hydrazine cations are found at much lower frequency followed by hydroxylammonium and the corresponding shorter D...A contact distance demonstrates the presence of strong hydrogen bonding environment in HA-BTO and TKX-50. The electronic band structure using HSE functional predict these energetic salts as wide band gap insulators with a bandwidth ranging from 4.33-5.05 eV. The 2D fingerprint maps reveal that these energetic salts are mainly governed by N..H/H..N interactions with 35 to 50% of contributions to the total Hirshfeld surfaces. These strong intermolecular interactions, especially in TKX-50 and HA-BTO are mainly responsible for its superior molecular stability when compared to other EIS. The calculated detonation properties demonstrate these energetic salts as potential explosive candidates, especially, HA-BTO and TKX-50 provide superior detonation velocities (9.94 and 9.91 km/s) and detonation pressure (38.85 and 40.23 GPa) owing to their high positive HOFs and densities. These results highlight favorable properties and provide theoretical guidance for understanding structure-property-performance interrelationship of energetic salts.

References

[1] A. T. Nielsen, A. P. Chafin, S. L. Christian, D. W. Moore, M. P. Nadler, R. A. Nissan, D. J. Vanderah, R. D. Gilardi, C. F. George and J. L. Flippen-Anderson, Tetrahedron, **54**, 11793 (1998).

[2] M.-X. Zhang, P. E. Eaton and R. Gilardi, Angew. Chemie Int. Ed., **39**, 401 (2000).

[3] A. K. Mandal, U. Thanigaivelan, R. K. Pandey, S. Asthana, R. B. Khomane and B. D. Kulkarni, Org. Process Res. Dev., **16**, 1711 (2012).

[4] R. Meyer, J. Kohler and A. Homburg, Explosives, *Wiley-VCH; Verlag GmbH, Weinheim* (2007).

[5] M. Armand, F. Endres, D. R. MacFarlane, H. Ohno and B. Scrosati, Nat. Mater., **8**, 621 (2009).

[6] C. F. J. Faul and M. Antonietti, Adv. Mater., **15**, 673 (2003).

[7] J. Perez and L. Riera, Chem. Commun., **0**, 533 (2008).

[8] D. R. Turner, A. J. Edwards and R. O. Piltz, CrystEngComm, **14**, 6447 (2012).

[9] Y. V. Nelyubina, M. Y. Antipin and K. A. Lyssenko, Russ. Chem. Rev., **79**, 167 (2010).

[10] R. P. Singh, R. D. Verma, D. T. Meshri, J. M. Shreeve and J. M. Shreeve, Angew. Chem., Int. Ed., **45**, 3584 (2006).

[11] H. X. Gao and J. M. Shreeve, Chem. Rev., **111**, 7377 (2011).

[12] R. Wang, Y. Guo, R. Sa and J. M. Shreeve, Chem. - A Eur. J., **16**, 8522 (2010).

[13] Q. H. Lin, Y. C. Li, Y. Y. Li, Z. Wang, W. Liu, C. Qi and S. P. Pang, J. Mater. Chem., **22**, 666 (2012).

[14] J. T. Wu, J. G. Zhang, X. Yin and K. Wu, Chem. - An Asian J., **10**, 1239 (2015).

[15] I. V. Tselinskii, S. F. Mel'nikova and T. V. Romanova, Russ. J. Org. Chem., **37**, 430 (2001).

[16] N. Fischer, D. Fischer, T. M. Klapotke and D. G. Piercey, J. Mater. Chem., **22**, 20418 (2012).

[17] Z. B. Zhang, C. X. Xu, X. Yin and J. G. Zhang, Dalt. Trans., **45**, 19045 (2016).

[18] G. Kresse and J. Furthmuller, Phys. Rev. B, **54**, 11169 (1996).

[19] G. Kresse and J. Hafner, Phys. Rev. B, **48**, 13115 (1993).

[20] G. Kresse and D. Joubert, Phys. Rev. B, **59**, 1758 (1999).

[21] J. P. Perdew, K. Burke and M. Ernzerhof, Phys. Rev. Lett., **77**, 3865 (1996).

[22] H. J. Monkhorst and J. D. Pack, Phys. Rev. B, **13**, 5188 (1976).

[23] X. Wang, S. Jin, C. Zhang, L. Li, S. Chen and Q. Shu, Chinese J. Chem., **33**, 1229 (2015).

[24] Y. Yu, S. Chen, X. Li, S. Jin, L. Li, G. Zhang, X. Ma and Q. Shu, RSC Adv., **7**, 18523 (2017).

[25] Y. Shang, B. Jin, Q. Liu, R. Peng, Z. Guo and Q. Zhang, J. Mol. Struct., **1133**, 519 (2017).

[26] S. Yu, J. Bo, P. Fang, L. Q. Qiang, G. Zhicheng, Z. Jun, Z. Q. Chun and C. S. Jin, Chinese Journal of Explosives and Propellants, **39**, 104 (2016).

[27] S. Grimme, Rev. Comput. Mol. Sci., **1**, 211 (2011).

[28] K. Berland and P. Hyldgaard, Phys. Rev. B, **89**, 035412 (2014).

[29] E. R. Johnson, I. D. Mackie and G. A. DiLabio, J. Phys. Org. Chem, **22**, 1127 (2009).

[30] S. Kummel and L. Kronik, Rev. Mod. Phys., **80**, 3 (2008).

[31] J. Klimes and A. Michaelides, J. Chem. Phys., **137**, 120901 (2012).

[32] A. Tkatchenko, L. Romaner, O. T. Hofmann, E. Zojer, C. Ambrosch-Draxl and M. Scheffler, MRS Bull., **35**, 435 (2010).

[33] J. M. Campo, J. L. Gazquez, S. B. Trickey and A. Vela, Chem. Phys. Lett., **543**, 179 (2012).

[34] J. P. Perdew, S. Kurth, A. Zupan and P. Blaha, Phys. Rev. Lett., **82**, 2544 (1999).

[35] R. Peverati and D. G. Truhlar, J. Phys. Chem. Lett., **3**, 117 (2012).

[36] J. P. Perdew, A. Ruzsinszky, G. I. Csonka, L. A. Constantin and J. Sun, Phys. Rev. Lett., **103**, 026403 (2009).

[37] J. Sun, B. Xiao and A. Ruzsinszky, J. Chem. Phys., **137**, 051101 (2012).

[38] J. Tao, J. P. Perdew, V. N. Staroverov and G. E. Scuseria, Phys. Rev. Lett., **91**, 146401 (2003).

[39] Y. Zhao and D. G. Truhlar, Theor. Chem. Acc., **120**, 215 (2008).

[40] A. Ruzsinszky, J. Sun, B. Xiao and G. I. Csonka, J. Chem. Theory Comput., **8**, 2078 (2012).

[41] J. Heyd and G. E. Scuseria, J. Chem. Phys, **120**, 7274 (2004).

[42] J. Heyd, G. E. Scuseria and M. Ernzerhof, J. Chem. Phys., **118**, 8207 (2003).

[43] M. C. Payne, M. P. Teter, D. C. Allan, T. A. Arias and J. D. Joannopoulos, Rev. Mod. Phys., **64**, 1045 (1992).

[44] N. Troullier and J. L. Martins, Phys. Rev. B, **43**, 1993 (1991).

[45] D. Vanderbilt, Phys. Rev. B, **41**, 7892 (1990).

[46] S. K. Wolff, D. J. Grimwood, J. J. McKinnon, D. Jayatilaka and M. A. Spackman, *CrystalExplorer University of Western Australia* (2005).

[47] J. J. McKinnon, M. A. Spackman and A. S. Mitchell, Acta Crystallogr. Sect. B Struct. Sci., **60**, 627 (2004).

[48] M. A. Spackman and J. J. McKinnon, CrystEngComm, **4**, 378 (2002).

[49] M. Suceska, Propellants Explos. Pyrotech., **24**, 280 (1999).

[50] Z. A. Dreger, Y. Tao, B. B. Averkiev, Y. M. Gupta and T. M. Klapotke, J. Phys. Chem. B, **119**, 6836 (2015).

[51] Z. A. Dreger, A. I. Stash, Z. G. Yu, Y. S. Chen and Y. Tao, J. Phys. Chem. C, **121**, 5761 (2017).

[52] L. Meng, Z. Lu, X. Wei, X. Xue, Y. Ma, Q. Zeng, G. Fan, F. Nie and C. Zhang, CrystEngComm, **18**, 2258 (2016).

[53] N. Yedukondalu, V. D. Ghule and G. Vaitheeswaran, J. Chem. Phys., **145**, 064706 (2016).

[54] Z. B. Zhang, C. X. Xu, L. Yin, Z. Wang, X. Yin and J. G. Zhang, RSC Adv., **6**, 73551 (2016).

[55] Z. B. Zhang, T. Li, L. Yin, X. Yin and J. G. Zhang, RSC Adv., **6**, 76075 (2016).

[56] F. H. Allen, Acta Crystallogr. B., **58**, 380 (2002).

[57] J. Emsley, Chem. Soc. Rev., **9**, 91 (1980).

[58] A. Novak, *Springer Berlin Heidelberg, Berlin, Heidelberg*, **18**, 177 (1974).

[59] W. Zhu and H. Xiao, Struct. Chem., **21**, 847 (2010).

[60] *NATO standardization Agreement (STANAG) on Explosives, Impact-Sensitivity Tests, no. 4489*, 1st ed., September 17 (1999).

[61] G. A. Jeffrey, *Oxford University Press: Oxford* (1997).

Chapter 4

A comparative study of 3,3′-dinitro-5,5′-bis-1,2,4-triazole-1,1′-diolate derivatives

As a continuation of previous chapter, the structural, electronic and vibrational properties of another similar energetic ionic salts (EIS) based on 3,3′-dinitro-5,5′-bis-1,2,4-triazole-1,1-diolate anion with ammonium (DA-DNBTO) and hydrazinium (DH-DNBTO) cations were discussed in detail. The Hirshfeld surface analysis and the related 2D fingerprint plots were quantitatively analysed to understand the importance of intermolecular interactions present in the molecule. Further, the influence of intermolecular interactions on performance and sensitivity of these energetic salts were discussed in detail.

B. Moses Abraham and G. Vaitheeswaran, "From van der Waals Interactions to Structures and Properties of 3,3′-Dinitro-5,5′-Bis-1,2,4-Triazole-1,1′-Diolate Based Energetic Materials" **Mat. Chem. Phys.**, **240**, 122175 (2020).

4.1 Introduction

For centuries, researchers have tapped the incredible energy stored in the molecules of explosive materials. Nevertheless, the science of energetic materials face tremendous challenges in predicting the precise correlation between performance and sensitivity characteristics with high fidelity. For instance, in most cases, the performance of an explosive can be enhanced at the cost of lower safety [1]. On the other hand, there is an exponential increase in the demand for national defense and the economy. Therefore, it is of great interest to design and develop energetic materials with superior energetic output along with reasonable safety over the currently used traditional explosives. In recent years, fully nitrated heterocycles have shown enormous potential and emerged as eco-friendly energetic materials [2, 3]. The compatibility between backbones and explosophores has been thoroughly analyzed by studying the essential energetic features of the fully nitrated heterocycles [4, 5]. Specifically, five-membered azole moieties with high nitrogen content are widely used as energetic frameworks because of their decent balance between molecular stability and energetic performance, strikingly highlighting the uniqueness in the world of energetic materials [6, 7]. In addition, the introduction of oxygen atom on these fully nitrated heterocycles improve the oxygen balance and also enhance the density and balance the sensitivity [8, 9]. Moreover, combining azoles with a cation to form energetic ionic salts (EIS) was found to be an effective strategy for the construction of high energy density materials [10, 11]. Typical, the combination of high nitrogen anions and cations in EIS with a large number of energetic C-N and N-N bonds can boost the performance of an explosive. They can also possess higher heat of formation, lower vapor pressures, high stability and a higher level of environmental compatibility compared to that of their non-ionic analogues. In general, the performance and properties of most existing EIS lie in between their parent components. However, there are few exceptions in which EIS outperforms some key energetic properties

than their parent components, such as density, detonation power and sensitivity. For instance, the hydrazine 5,5′-bitetrazole-1,1′-diolate [12] (HA-BTO) possesses remarkably higher density (1.912 g/cm^3) than its parent hydrazine (1.02 g/cm^3) compound (see figure 4.1). The detonation performance of HA-BTO (D = 8931 m s^{-1}, P = 36.1 GPa) is much higher than 1,3,5-trinitro-1,3,5-triazinane (RDX, D = 8512 m s^{-1}, P = 31.2 GPa) and the impact sensitivity (28 J) is better than 1-methyl-2,4,6-trinitrobenzene (TNT, 15J) [12]. Recently, a series of different organic linked energetic salts (-CH_2-O-CH_2-, -CH_2-CH_2-, -CH=CH-) were synthesized to decrease the sensitivity and enhance the thermal stability of energetic salts [13–16]. These exceptional features of EIS may facilitate potential applications to promote energetic materials evolution.

Generally, most of the energetic solids contain molecules that are held together by van der Waals (vdW) interactions. Under external stimuli like hydrostatic pressure or a shock wave, the intermolecular interactions and the micro-structure may undergo significant changes, leading to a drastic variation in the mechanical, chemical and thermodynamic properties. The Zeldovich-von Neumam Doering model [17–19] suggest that the detonation performance differs based on the variation in these properties. Hence it is necessary to provide a clear picture of how the intermolecular interactions influence the macroscopic properties to enhance the energetic performance. However, the experimentally measured x-ray diffraction fail to locate the exact position of hydrogen atoms [20]. Therefore effective methods based on theoretical simulations [21] or neutron diffraction measurements [22] are required to study the atomic structure of hydrogen containing materials, especially structures with intermolecular interactions. The first principles calculations have become an indispensable tool in unravelling the intermolecular interactions within the crystal and are successful in accurately predicting the chemical and physical properties of a broad range of materials [23]. However, due to the complexity of energetic materials, conventional electron exchange-correlation functionals fail to produce an accurate description of weak intermolecular inter-

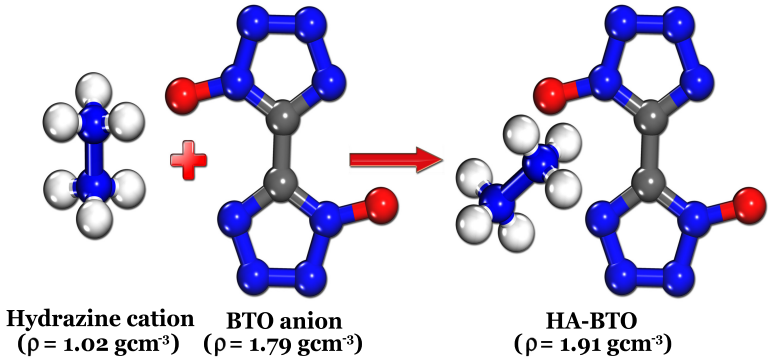

Figure 4.1: The combination of hydrazine (HA) cation and 5,5′-bitetrazole-1,1′-diolate (BTO) anion to form HA-BTO energetic ionic salt. Grey, white, blue, and red balls represent carbon, hydrogen, nitrogen, and oxygen atoms, respectively.

actions. This is clearly exemplified in various energetic crystals including RDX [24], FOX-7 [25, 26], CL-20 [27], TATB [28, 29] and HMX [30] and the results show that the generalized gradient approximation(GGA)/local density approximation (LDA) overestimate/underestimates the crystal volumes by nearly ∼30% when compared to experimental values. Therefore, to account for these long-range dispersive interactions quantitatively, a wide range of new functionals were developed to extent DFT and are continuously being improved. Among the most successful ones are the class of dispersion-corrected functionals such as those of Tkatchenko and Scheffler [31] (TS) and Grimme [32] (D2), and the Langreth-Lundqvist density functionals of the vdW-DF family [33]. Most of the theoretical calculations study the vdW interactions using Atoms in Molecules (AIM), Natural Bond Orbital (NBO), density functional theory to understand the band structure, binding energy, Hirshfeld surface, charge density, etc., However, there is a huge lack in the engineering of new and enhanced research on the inter-relationship between van der Waals interactions and macro properties of energetic solids.

In our previous chapter [34], we systematically investigated the structure - property - performance interrelationship of 5,5′-bitetrazole-1,1′-diolate (BTO) based energetic ionic salts. Here, we selected similar energetic salts based on 3,3′-dinitro-

5,5′-bis-1,2,4-triazole-1,1-diolate anion with ammonium (DA-DNBTO) and hydrazinium (DH-DNBTO) cations. The first principles calculations were performed to study the structural, electronic and vibrational properties of DNBTO salts. The Hirshfeld surface analysis and the related 2D fingerprint plots were quantitatively analyzed to understand the importance of intermolecular interactions present in the molecule. The strongest intermolecular interactions of DA-DNBTO indicates its inferiority in molecular stability, which is in good agreement with the experimentally measured impact sensitivity (>40 J) and friction sensitivity (360 N) values [8] and also explains why it has the highest stability compared to DH-DNBTO. In view of these observations, it was adorable to construct energetic salts with intermolecular hydrogen bonding as the future generation high energy density materials.

4.2 Computational methods

The DNBTO based energetic ionic salts were studied using two distinct approaches within the framework of density functional theory. Initially, CAmbridge series of total energy package (CASTEP) [35] based on plane-wave pseudopotential (PW-PP) approach is used to simulate vibrational and associated properties, where the density functional perturbation theory (also known as linear response method) is implemented. The structural relaxation was carried out through Broyden-Fletcher-Goldfarb-Shanno (BFGS) [36] scheme. The electron-ion interactions were treated using Vanderbilt-type ultrasoft pseudopotentials (USPP) [37] to perform geometric optimization, while dynamical properties were calculated through norm-conserving pseudopotentials (NCPP) [38]. The electron-electron interactions were included via generalized gradient approximation (GGA) with Perdew-Burke- Ernzerhof (PBE) [39] parameterization. The kinetic energy cut-off of 600 eV for USPP, 950 eV for NCPP and k-point grid of 4x4x3 for DA-DNBTO and 7x3x3 for DH-DNBTO were used according to Monkhorst-Pack [40] grid scheme. The self-

consistent energy convergence, stress and maximum displacement were set to be 1.0×10^{-5} eV/atom, 0.05 GPa and 1×10^{-3} Å, respectively.

The non bonding vdW interactions are essential for describing the intermolecular interactions in various energetic materials, were accounted for in our calculations using Grimme's semiempirical dispersion correlation, known as the DFT-D2 [32] approach. We have used this method to maintain consistency with earlier studies and to ensure that precise correlation could be made with our previous work [34]. However, as mentioned in the text, we also used TS method [31], but no prominent difference was observed. In these methods, the total energy of the system after the inclusion of semiempirical correlation (E_{disp} is given by:

$$E_{DFT+D} = E_{KS-DFT} + E_{disp}$$

Where E_{KS-DFT} is the self-consistent Kohn-Sham energy and the dispersion energy for periodic systems is given by

$$E_{disp} = -s_6 \sum_{i<j} \frac{C_{ij}}{R_{ij}^6} f_{damp}(R_{ij}),$$

Where S_6 and C_{ij} represents the scaling factor and dispersion coefficient, respectively. R_{ij} is the interatomic distance for atom pair ij and f_{damp} is the damping function, which is required to control singularities at small distances.

As a next step, we implemented the projector augmented wave (PAW) method through Vienna ab initio simulation package (VASP) to study the electronic properties. Typically, the LDA (local)/GGA (semi-local) functionals underestimate the energy band gap values, which can be overcome by mixing the PBE scheme with a certain quantity of non-local Hartree-Fock (HF) exchange energy, the so-called HSE functional. This description has proven to improve the energy band gap of electronic structure. Thus, in the calculations of electronic properties, the standard HSE06 approach was adopted, namely, the Hartree-Fock mixing parameter $\alpha = 25\%$ and the screening parameter $\nu = 0.2$ Å^{-1}. The Hirshfeld surfaces and

Table 4.1: The calculated lattice parameters, crystallographic angles and volume of DA-DNBTO and DH-DNBTO using various DFT dispersion corrections.

		PBE	TS	D2	Expt [Ref.[8]]
DA-DNBTO	a [Å]	6.969 (+8.13%)	6.575 (+2.01%)	6.430 (-0.23%)	6.445
	b [Å]	6.848 (+2.69%)	6.692 (+0.35%)	6.714 (+0.68%)	6.668
	c [Å]	8.354 (-0.01%)	8.351 (-0.04%)	8.329 (-0.31%)	8.355
	α [^{o}]	69.83 (-0.75%)	69.79 (-0.81%)	69.63 (-1.03%)	70.36
	β [^{o}]	83.06 (-1.21%)	83.38 (-0.83%)	83.44 (-0.76%)	84.08
	γ [^{o}]	71.01 (-1.11%)	72.29 (+0.68%)	71.73 (-0.09%)	71.80
	V [Å^3]	353.9 (+10.18%)	328.5 (+2.27%)	320.1 (-0.34%)	321.2
DH-DNBTO	a [Å]	3.818 (+2.22%)	3.667 (-1.82%)	3.622 (-3.02%)	3.735
	b [Å]	8.256 (+3.00%)	8.048 (+0.41%)	7.969 (-0.57%)	8.015
	c [Å]	11.33 (+9.89%)	10.65 (+3.29%)	10.48 (+1.64%)	10.31
	α [^{o}]	73.41 (+3.78%)	71.25 (+0.73%)	71.28 (+0.77%)	70.73
	β [^{o}]	79.59 (-10.78%)	87.07 (-2.39%)	88.83 (-0.42%)	89.21
	γ [^{o}]	93.14 (+8.31%)	86.83 (+0.97%)	87.36 (+1.59%)	85.99
	V [Å^3]	334.7 (+15.17%)	297.0 (+2.20%)	286.3 (-1.47%)	290.6

the associated 2D fingerprint plots were analyzed using CrystalEXplorer 3.1 [41]. The stockholder concept is used in Hirshfeld surface to divide the molecule's electron density into atomic fragments. By defining a molecular weight function, we can extract molecular fragments in crystals:

$$w(r) = \rho_{promolecule(r)} / \rho_{procystal(r)}$$

Where promolecule and procrystal are sum over the well-defined contributions of atoms belonging to a single molecule and the crystal, respectively.

4.3 Results and discussion

4.3.1 Structural properties of DNBTO salts

The energetic salts diammonium 3,3′-dinitro-5,5′-bis-1,2,4-triazole-1,1-diolate (DA-DNBTO) and dihydrazinium 3,3′-dinitro-5,5′-bis-1,2,4-triazole-1,1-diolate (DH-DNBTO) [8] crystallizes in the triclinic structure (space group P-1) with one formula unit per unit cell. Initially, the lattice parameters and ionic positions were fully relaxed using PBE-GGA functional and the obtained volumes are found to be overestimated by 10.18% and 15.17% for DA-DNBTO and DH-DNBTO, respectively. This clearly demonstrate the inadequacy of standard exchange - correlation potentials in treating the weak dispersive interactions. Our previous articles [26, 29, 42] also reported the inability of LDA/GGA functionals in treating these long range interactions in molecular crystalline solids. In order to capture these missing vdW interactions, the semiempirical approaches (TS and D2) were incorporated into our calculations. The TS scheme overestimated the volume of DA-DNBTO by 2.27%, whereas D2 method provides comparable volume (320.1 Å^3) to the experiment (321.2 Å^3) with an error of -0.34%. The corresponding deviations using D2 scheme in cell parameters **a, b, and c**, are -0.23%, +0.68% and -0.31%, respectively. The calculated lattice constants, angles and volumes of DA-DNBTO and DH-DNBTO structures using various methods were presented in

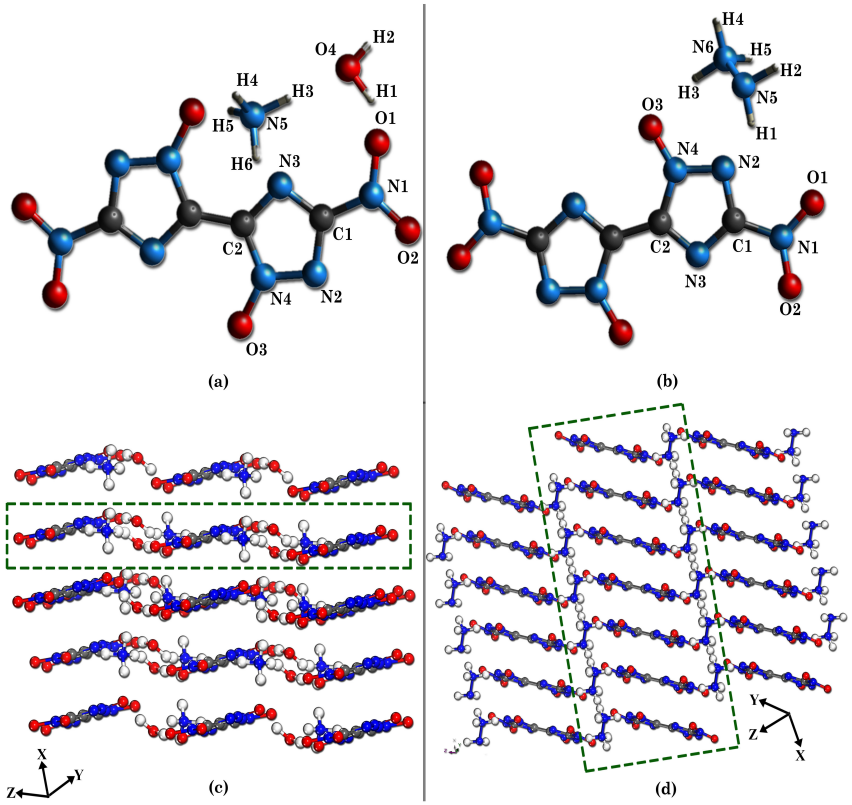

Figure 4.2: The ball-and-stick image depicting the molecular structure of (a) DA-DNBTO and (b) DH-DNBTO. The packing diagram of (c) DA-DNBTO and (d) DH-DNBTO. The layer motif is highlighted with green rectangular box. The gray, white, red and blue colors represent C, H, O and N atoms, respectively.

Table 4.1. For DH-DNBTO, the calculated volumes are overestimated by 2.20% and underestimated by 1.47% using DFT-TS and DFT-D2 methods, respectively. Among the two DFT-D methods, the DFT-D2 method proposed by Grimme works well for the studied energetic salts, with minor discrepancies between experimental values and theoretically predicted data at 0 K.

The molecular structure of (a) DA-DNBTO and (b) DH-DNBTO are shown in figure 4.2a and b. The main body of DNBTO anion is constructed by triazole ring and carbon-carbon double bonds. All C-atoms and N-atoms of the triazole ring are in the same plane and the bond length of C=C is much longer than that

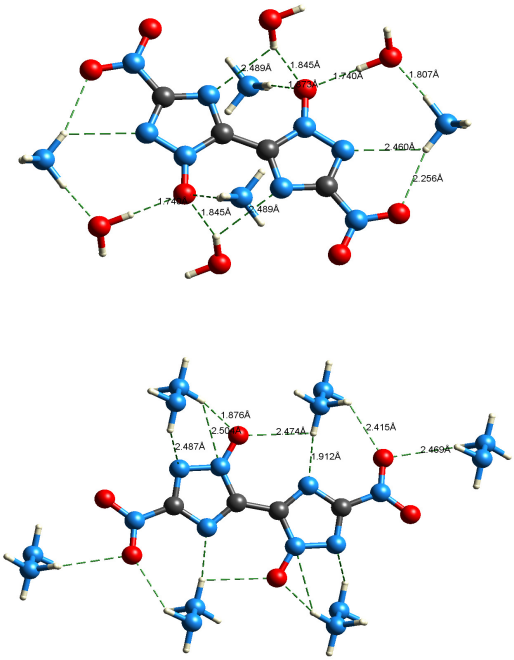

Figure 4.3: The hydrogen bonds in the energetic salts (a) DA-DNBTO and (b) DH-DNBTO

of N=N bond due to diverse electronegativity. The average C-N bonds of the triazole rings were 1.34 Å for C1-N3, 1.39 Å for C2-N4, 1.34 Å for C1=N2, which were longer than the general C=N bond length (1.27 Å) and shorter than the general C-N bond (1.47 Å) [43]. Further, DA-DNBTO and DH-DNBTO cations bridge the anions by strong van der Waals and electrostatic attractions, generally of hydrogen bonds. This behavior is not found in traditional energetic crystals made of homogenous neutral molecules, since the vdW attractions are the intermolecular interactions that govern the crystals. The packing diagram of DA-DNBTO and DH-DNBTO are shown in figure 4.2c and d. In case of DA-DNBTO, the water molecules are hydrogen bonded with one nitrogen atom of the triazole (N3) and two oxygen O3 of the N-oxide. Further, the ammonium molecule forms four distinct hydrogen bonds with oxygen atoms (O2) of the nitro group, N-oxide, water molecule and nitrogen atom of the triazole (N2).

Such crystal units are repeated to have wave-like stacking, similar to FOX-7 [44]. The unique structure with large number of hydrogen bonds not only play a key role in forming an interesting structure, but also decreases the sensitivity and enhances the thermal stability of the salt [45]. In DH-DNBTO, the nitrogen and oxygen atoms of $DNBTO^{2-}$ anion and hydrogen atoms in cations are connected to form a structure like ladder, where the hydrazinium cations and $DNBTO^{2-}$ anions behave like strand and rung of the ladder, respectively. Typically, this hydrogen...acceptor (H...A) distance can quantitatively illustrate how close the interactions between anions and cation are. It is noteworthy that the D-H...A (1.740 Å) distance between hydrogen atom of the water molecule and oxygen O3 atom of the N-oxide in DA-DNBTO is the shortest hydrogen bond in the crystal. In case of DH-DNBTO, the distance between hydrogen atom of the hydrazinium cation and the oxygen O3 atom of the N-oxide (1.876 Å) is the shortest hydrogen bond in the system. Moreover, the H...A lengths are in the range of 1.845-2.489 Å for DA-DNBTO and 1.876-2.504 Å for DH-DNBTO, respectively (see figure 4.3). These hydrogen bonding interactions between DNBTO anion and various cations not only helps to increase density but also enhances the detonation performance and thermal stability of the studied EIS.

4.3.2 Vibrational properties

DA-DNBTO and DH-DNBTO crystallize in the triclinic structure (space group P-1) with 34 and 32 atoms per unit cell resulting in 102 (3 acoustic + 99 optical) and 96 (3 acoustic + 93 optical) vibrational modes. According to group theory analysis, the irreducible representations of the modes are Γ_{tot} = 51 Au $\oplus$ 51 Ag ($\Gamma_{acoustic}$ = 3 Au; Γ_{optic} = 48 Au $\oplus$ 51 Ag) and Γ_{tot} = 48 Au $\oplus$ 48 Ag ($\Gamma_{acoustic}$ = 3 Au; Γ_{optic} = 45 Au $\oplus$ 51
48 Ag) for DA-DNBTO and DH-DNBTO, respectively. The Au modes are IR active and Ag modes are Raman active. The calculated IR spectra of both the studied compounds are shown in figure 4.4. The horizontal and vertical axes

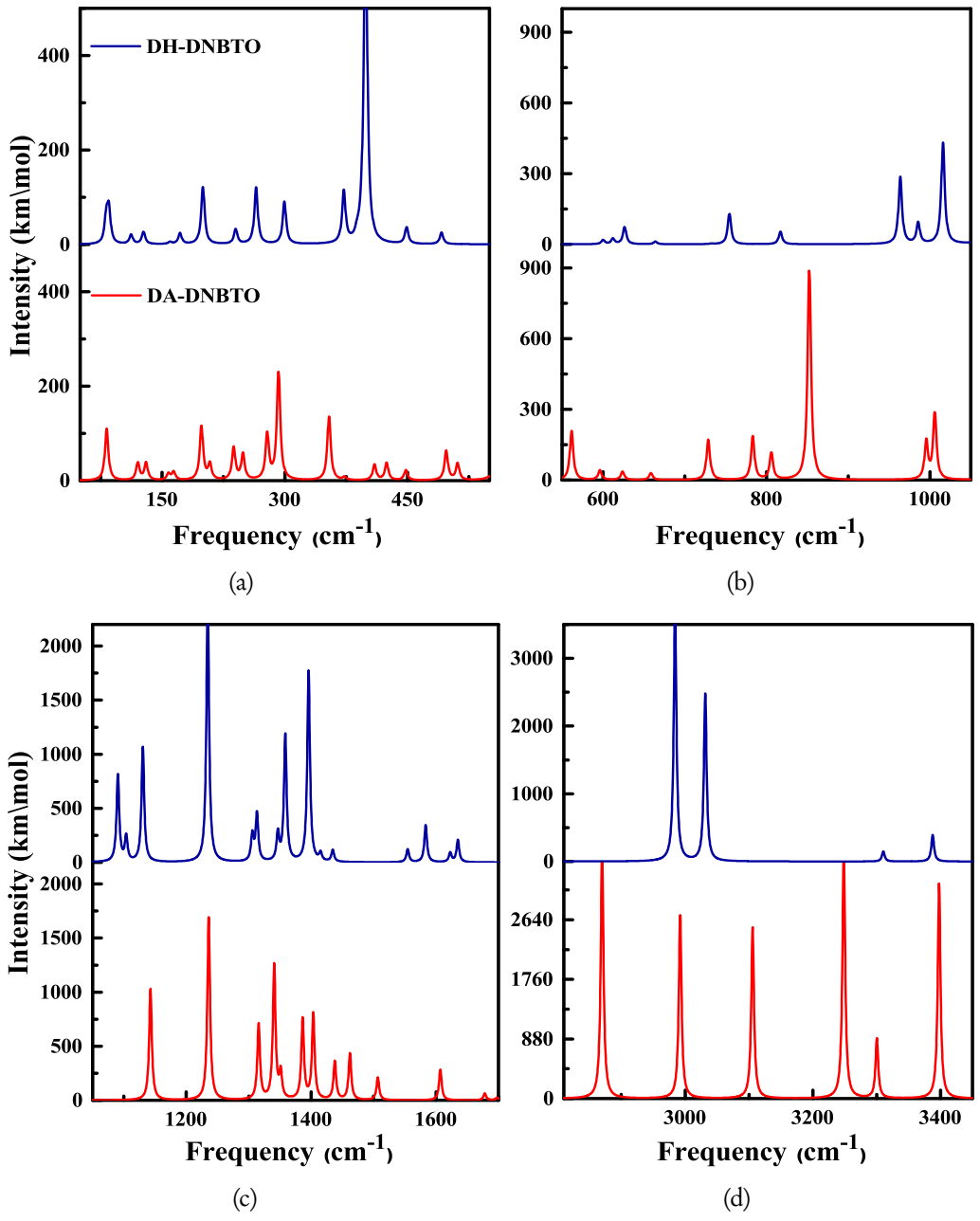

Figure 4.4: Calculated infrared spectra of (a) DA-DNBTO and (b) DH-DNBTO crystals at the optimized lattice constants.

represent frequency and intensity, respectively. To provide a clear picture of different intensities, the spectrum is divided into four parts. In both the structures, the strongest peak is absorbed in the high frequency range, whereas the low frequency region is composed of low intensity peaks. The frequencies of IR peaks for both the spectra are listed in Table 4.2 along with their corresponding vibrational assignments. In case of DA-DNBTO, the low frequency vibrations between 82 to 198 cm^{-1} are due to translational and/or rotational motion of both cation and anions. The H_2O, NH_4, N=O, NO_2 rocking (292, 497 and 728 cm^{-1}), NH_4 wagging (1386 and 1403 cm^{-1}) and H_2O, NH_4 twisting (409, 424 and 783 cm^{-1}) modes were observed in the system. Moreover, the difference in calculated spectra for the range of 1100-1500 cm^{-1} is relatively small, as the corresponding vibrations are dominated by the intramolecular stretching modes. The vibrations in the high frequency range (above 2870 cm^{-1}) originates from either H_2O or NH_4 stretching frequencies: The peaks at 3397 and 3248 cm^{-1} corresponds to H_2O asymmetric stretching vibrations, whereas, the modes at 3300 and 3105 cm^{-1} belongs to NH_4 asymmetric stretching vibrations. Two other modes located at 2992 and 2869 cm^{-1} represents NH_4 symmetric stretching vibrations.

For DH-DNBTO structure, the lattice modes located in the range 47 to 159 cm^{-1} belong to rotational and/or translational motion of both DNBTO anion and hydrazinium cation. The vibrational modes ranging from 264 to 398 cm^{-1} are assigned to rotational motion of hydrazinum cation. The wagging (1090 and 1103 cm^{-1}), twisting (1130 cm^{-1}) and scissoring (1305, 1313, 1554, 1583 and 1635 cm^{-1}) modes belong to hydrazinum cation. The C-N bending, C=N-C, N=C-N, C-N-O twisting and N-O rocking modes were observed at 626, 754, 1016, 1234 and 1395 cm^{-1}, respectively. Further, the bands at 2589, 2984, 3031 and 3387 cm^{-1} correspond to asymmetric stretching vibrations of H3, H4, H5 and (H1 and H2) of hydrazinum cation. Few simulated IR modes of DA-DNBTO and DH-DNBTO energetic salts were shown in figure 4.5. It is noteworthy that the spectrum of DA-DNBTO contains more number of peaks in the high frequency

Table 4.2: Calculated infrared active modes and their assignments for DA-DNBTO and DH-DNBTO energetic salts at DFT-D2 equilibrium volume using NCP approach.

Modes	Frequency (cm^{-1})	Assignment	Modes	Frequency (cm^{-1})	Assignment
		DA-DNBTO			**DH-DNBTO**
M04-M26	86-298	lattice modes	M04-M26	41-334	lattice modes
M27	311	H_2O trans. + NH_4 trans. + ring out-of-plane bend.	M27,M28	369,378	ωNH_3 + ωNH_2
M28	337	H_2O trans. + NH_4 trans. + $\rho N=O$	M29	388	ρNH_2 + anion ring out-of-plane bend.
M29,M30	354,361	H_2O trans. + NH_4 trans.	M30,M31	396,397	ρNH_2
M31	372	ρHO + ρNH_4 + anion wag.	M32	449	anion str.
M32	409	ρNH_4	M33,M34	468,483	anion ring out-of-plane bend.
M33	411	ρH_2O + ρNH_3 + anion wag.	M35	491	θNH_3 + $\omega N=O$ + $\omega O\text{-}N=O$
M34	424	ρNH_4 + anion str.	M36	552	θNH_3 + anion ring in-plane shift
M35	442	ρH_2O + ρNH_4 + anion wag.	M37	600	θNH_3 + anion ring rot. + $\omega N=O$
M36	444	ρH_2O + ρNH_4	M38,M39	612,618	θNH_3
M37	447	ρH_2O + ρNH_3	M40	626	anion ring out-of-plane bend.
M38	458	ρNH_3 + anion ring out-of-plane bend.	M41	629	$\omega O\text{-}N=O$ + $\omega N=C\text{-}N$ + θNH_3
M39	478	ρH_2O + ρNH_4	M42	664	$\omega N=C\text{-}N$
M40	497	ρH_2O + ρNH_3 + $\rho N=O$	M43	696	$\tau C\text{-}C$ + $\tau C\text{-}N$ + $\tau C=N$
M41	511	ρH_2O + ρNH_3	M44	709	anion ring rot. + $\omega N=O$
M42,M43	543,560	ρH_2O + ρNH_4	M45,M46	732,733	$\tau C\text{-}N$
M44	565	ρH_2O + ρNH_3	M47,M48	754,784	$\sigma O\text{-}N=O$ + $\nu N=O$
M45	596	ρH_2O + ring rot. + ρNH_3	M49,M50	817,859	$\sigma O\text{-}N=O$ + $\sigma N=C\text{-}N$ + $\nu N=O$
M46	624	$\tau N\text{-}N$ + $\omega N\text{-}C$ + $\omega C=N\text{-}N$	M51,M52	961,964	$\nu N\text{-}N$ + ωNH_3
M47	630	$\tau N\text{-}N$ + $\omega N\text{-}C$ + $\omega N\text{-}C=N$	M53	985	$\nu_s C\text{-}N\text{-}N$

Continued on next page

Table 4.2 – Continued from previous page

Modes	Frequency (cm^{-1})	Assignment	Modes	Frequency (cm^{-1})	Assignment
M48	658	ωC-C + ωN-C=N	M54	1006	ν_sO-N=O + ν_sN=C-N + τC-C
M49	690	ωH_2O + ring rot. + ρN=O	M55	1016	ν_sO-N=O + ν_sN=C-N + νN-N
M50	701	τC-C + ρOH + ωN-C=N	M56	1073	ρNH_2 +ωNH + νN-N
M51	728	τH_2O + σN-C=N + σO-N=O	M57,M58	1084,1095	ωNH_3 + ωNH_2
M52	732	τC-N + τO-N=O	M59	1102	ρNH_2 + ωNH + νN-N + νC-N
M53	734	τC-N + ωHO	M60	1114	ρNH_2 + ωNH + νN-N
M54	762	τH_2O + σO=N-O + νN=O	M61	1130	ρNH_2 + νC-N + ν_aN=C-N
M55,M56	783,787	τH_2O + ρNH_3	M62	1234	ν_sO-N=O + νN-N + τC-N + σNH_2
M57	806	ωHO + σO=N-O + σC=N-C	M63	1239	νN=O + νC-N + τC-C
M58	824	ωH_2O + τC-C + σO=N-O	M64	1266	ν_sO-N=O + ν_sN=C-N
M59	849	ωH_2O + σN-C=N	M65	1305	ωNH_3 + ωNH_2 + νC-N
M60	852	ωH_2O	M66	1308	ωNH_3 + ωNH_2
M61	986	σN-C=N + ν_aO=N-O	M67	1313	ωNH_3 + ωNH_2 + νC-N + τC=N
M62	995	σN-C=N	M68	1344	νC-N + νN-N + τC-C
M63	1005	ν_sN-N-C + σC=N-C	M69	1346	νN=O + νC-N + νC=N
M64	1104	νN-C + νN-N	M70	1358	νN=O + νC-N + νC=N + ωNH_3
M65	1142	νN-C + ν_aN-N-C + ν_aN-C=N	M71	1395	ν_aO-N=O + ν_aN=C-N + νN=O
M66	1219	ν_sO=N-O + τC-C + ν_aN-C=N + ν_aO=N-N	M72	1402	τN_2H_4 + ωNH + ν_aO-N=O + ν_aN=C-N
M67	1235	ν_sO=N-O + ν_sN=C-N + νN-N	M73	1414	τN_2H_4 + ωNH
M68	1246	ν_sO=N-O + νN=O + τC-C	M74	1415	τN_2H_4 + ωNH + νN=O + νC-C
M69	1315	νC-N + ν_aN-C-N	M75	1420	τN_2H_4 + ωNH + νN=O
M70	1318	τC-C + νC-N + νN-N	M76	1434	ν_aO-N=O + ν_aN=C-N
M71	1340	ωNH_3 + νN=O + νN=C	M77	1454	τNH_2 + ωNH_3 + τC-N + ν_aO-N=O

Continued on next page

Table 4.2 – Continued from previous page

Modes	Frequency (cm^{-1})	Assignment
M72	1351	νC=N + νC-N
M73	1373	ωNH_4 + νN=O + τN-N + τN-N
M74	1385	ωNH_4 + ν_aN=C-N + τN-N
M75	1391	ωNH_4 + νN=O + ν_aN=C-N
M76	1403	ωNH_3 + ρNH + ν_aN=C-N
M77	1405	νN=O + τC-C + ν_aN=C-N
M78	1437	νN-O + τC-N + ν_aN=C-N
M79	1445	ωNH_4 + νN-O + τC-N
M80	1461	ωNH_4
M81	1477	ωNH_3 + $\nu_a NO_2$
M82	1506	ωNH_3
M83	1508	ωNH_4
M84	1567	σH_2O + νC-C
M85,M86	1606,1628	σH_2O
M87	1678	σNH_4
M88	1690	σH_2O + σNH_4
M89	1697	σNH_4
M90	1713	σH_2O + σNH_4
M91	2849	$\nu_s H_2O$ + $\nu_a NH_2$
M92-M95	2869-3103	$\nu_s H_2O$ + $\nu_s NH_4$
M96	3105	$\nu_s NH_2$
M97,M98	3235,3248	$\nu_a H_2O$ + $\nu_a NH_4$
M99,M100	3300,3301	$\nu_a NH_4$
M101,M102	3393,3397	$\nu_a H_2O$
M78	1546	ωNH_3 + σNH_2 + νC-C
M79	1549	ωNH_3 + σNH_2
M80	1558	ωNH_3 + νC-C
M81-M84	1579-1622	σNH_4 + ωNH
M85	1628	σNH_2 + ωNH
M86	1634	σNH_4 + ωNH
M87-M92	2587-3030	νNH
M593,M94	3309,3310	$\nu_s NH_2$
M95,M96	3387,3390	$\nu_a NH_2$

Symbol	Description
ν_s	symmetric stretching
ν_a	asymmetric stretching
β	bending
ρ	rocking
ω	wagging
τ	twisting
σ	scissoring
ν	stretching
δ	deformation
θ	rotation

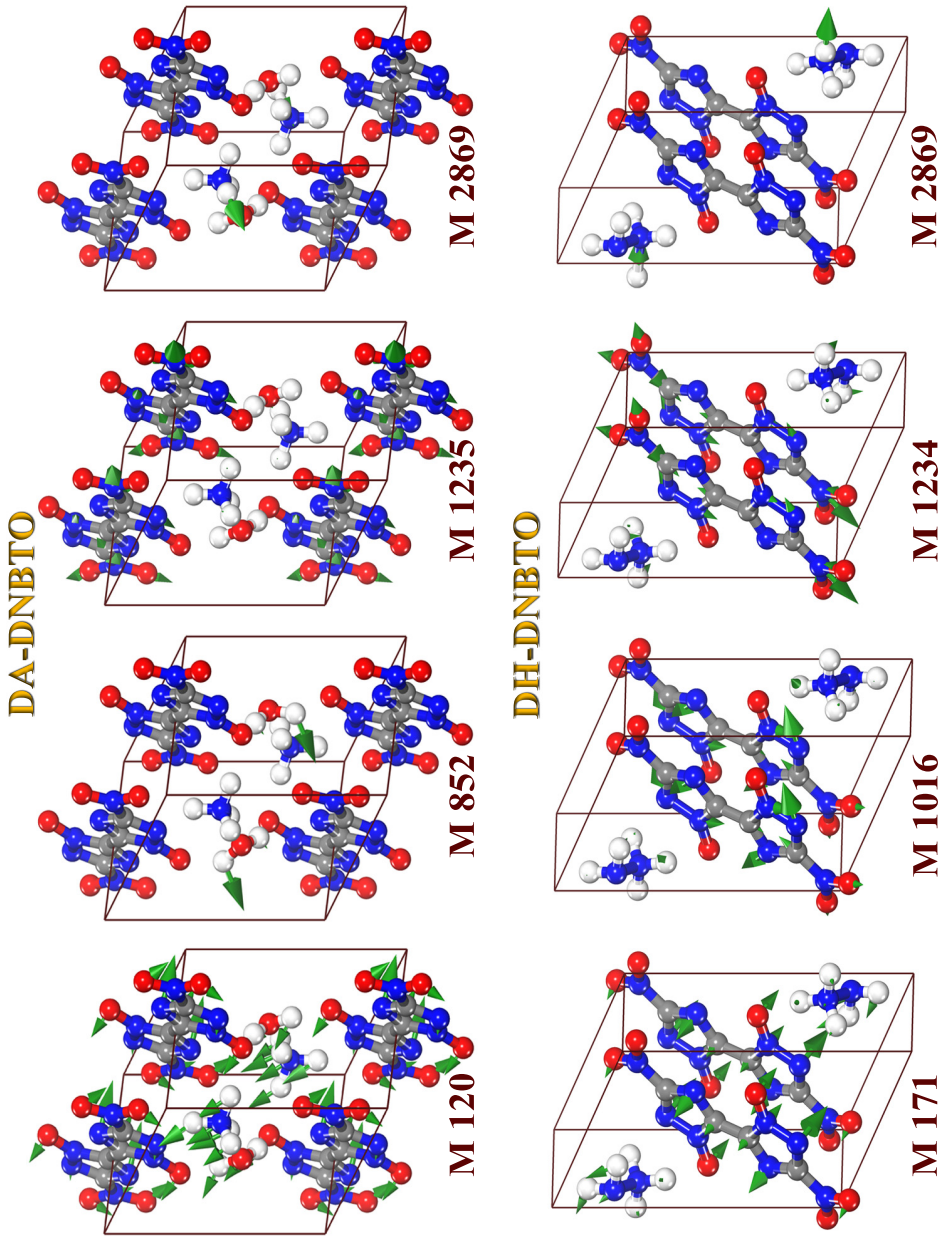

Figure 4.5: Few simulated IR modes of DA-DNBTO and DH-DNBTO salts

range (above 2850 cm^{-1}) compared to DH-DNBTO. Typically, the strength of the hydrogen bonds depends on the increasing integrated intensity and decreasing wavenumber of the stretching vibrations [46]. The former is a function of O...H bond strength and the latter is a repeated combination of low-frequency breathing vibrations (σ) with the stretching modes of the hydrogen bond. In the simplest possible scenario, the presence of intense spectra along with a large number of peaks in the high frequency range of DA-DNBTO spectrum represents the existence of strong hydrogen bonds compared to DH-DNBTO.

4.3.3 Electronic structure and chemical bonding

The electronic structure of energetic materials provide significant information regarding the stability as well as the initiation and decomposition mechanism of explosive materials. Especially, the electronic band gap can be used as an important criterion to predict the impact sensitivity of energetic materials. Zhang et. al.[47] established the correlation between impact sensitivity, band gap and bond dissociation energy for nitro-aromatic explosive materials and found that the intermolecular interactions are the deciding factor for band gap of crystals. The later work by Zhu and Xia [48] also emphasized the correlation between sensitivity and band gap of crystalline 1H′-tetrazole and its derivatives. Their results suggest that the smaller band gap can easily transfer the electron from valence to conduction band, which leads to the decomposition followed by an explosion of the crystal. Our recent work using DFT approach [34] also showed that the band gap could be used to correlate the impact sensitivity of various energetic ionic salts of similar structures. Hence, the prediction of an accurate band gap for the studied EIS is necessary in this context. However, as discussed earlier, the standard DFT formalism (LDA/GGA) fail to predict the accurate band gap values (generally underestimates the band gap by 30% when compared with experiments). In order to overcome this problem, we have used HSE functional to calculate the electronic properties of the studied EIS. The calculated band gaps

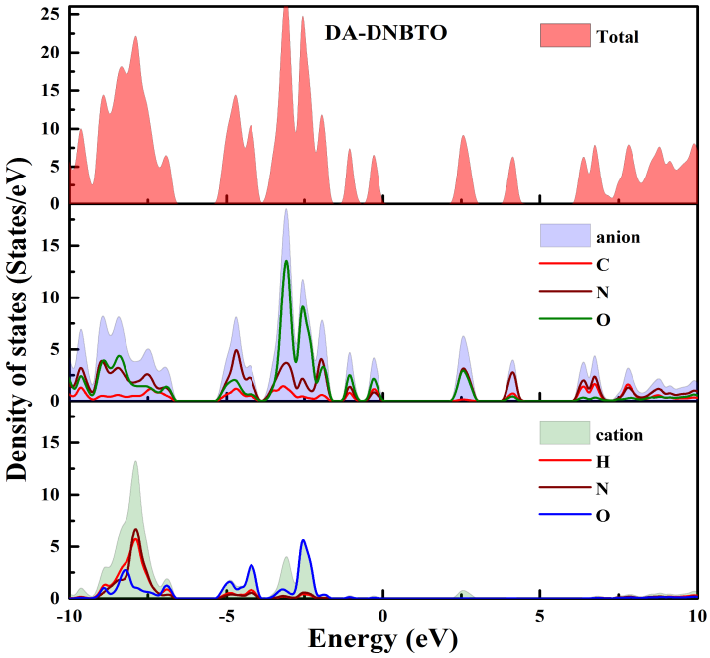

(a)

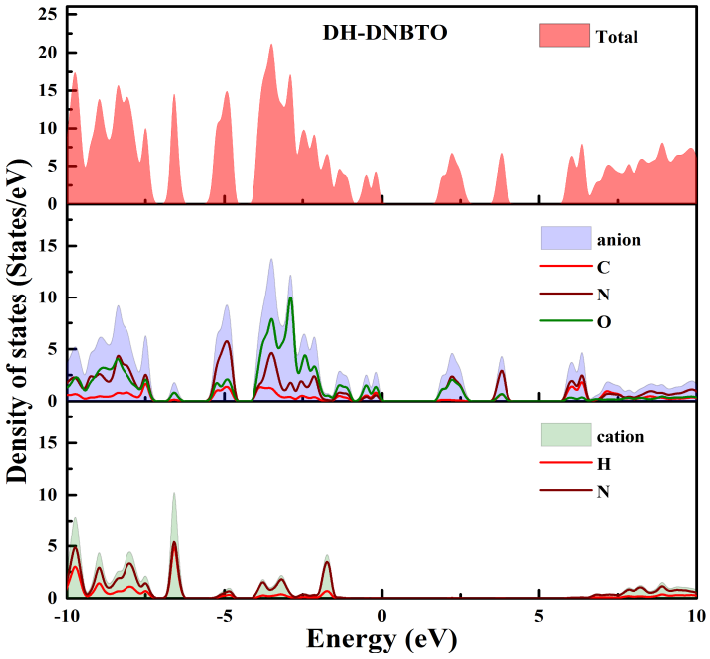

(b)

Figure 4.6: Calculated total and partial density of states (TDOS/PDOS) of (a) DA-DNBTO and (b) DH-DNBTO energetic salts using the HSE functional.

for DA-DNBTO and DH-DNBTO using HSE functional is found to be 2.25 and 1.78 eV, respectively, These values are reduced to 50% when compared with the band gap values of BTO based EIS. The reason behind the band gap reduction for DNBTO energetic salts are clearly illustrated in the following section.

The total and partial density of states along with cationic and anionic contribution obtained with HSE functional is shown in figure 4.6. In both the structures, the valance band maximum (VBM) is mostly composed of C, N and O atoms of DNBTO anion, whereas the dominant components for conduction band minimum (CBM) are N and O atoms of DNBTO anion. The significantly less contribution of cation near the Fermi level represents a degree of ionic (nondirectional) bonding between DNBTO anion and cations. There is a strong overlap between C, N and O atoms of DNBTO anion in the energy range from -10 to -7 eV. Similarly, the states of H, N and O atoms show considerable overlap in the energy range from -9 to -7 eV. This overlap suggest strong hybridization between corresponding atoms in cation and anion, representing covalent (directional) bonding. Further, when compared with the DOS of BTO based EIS, an extra peak is appeared in the Fermi region of DNBTO energetic salts due to the contribution of NO_2 group attached to the cation, which indicates that the NO_2 group might be responsible for initiation of the decomposition process in DNBTO based EIS.

4.3.4 Sensitivity analysis

Analyzing the variations of sensitivity by understanding the chemical nature of energetic materials through theoretical simulations can develop new materials with high performance and desirable impact sensitivity. However, due to the complexity in the environment of energetic crystals, it is difficult to know which material properties drive the impact-induced initiation and what physical mechanism enable reactions are not completely understood at the basic level. Many questions still revolve around the mind regarding the physical mechanism behind the bond breaking, which chemical bonds will break first, the influence

of crystal structure, the time scale of reaction and the microscopic/macroscopic variables that are involved in controlling the reaction process. According to the molecular factors, several articles proposed that the key step for initiation of detonation might be the breaking of weakest N-NO_2/C-NO_2 bonds in the molecules [49, 50]. For instance, the breaking of N-NO_2 linkage in methylenetetranitramine (HMX) and cyclotrimethylenetrinitramine (RDX) leads to weakening of next nearest neighbor bonds, which induces the entire decomposition of molecules [51]. Zhang et. al.[52, 53] predicted a correlation between electronic structure and sensitivity of 38 nitroaromatic explosives through BLYP/DNP method and by calculating the Mulliken charges of the nitro groups. It is noteworthy to mention that the obtained band gap values for the studied DNBTO based energetic salts are much lower when compared with our previously reported BTO based EIS (see Fig. 5 in ref [34]). Based on the Principle of Easiest Transition criteria, DA-DNBTO and DH-DNBTO should be more sensitivity than BTO based energetic salts, but the experimentally measured impact sensitivity value reveals that DA-DNBTO (>40 J) is less sensitive, while DH-DNBTO (15 J) is sensitive in nature. This clearly represents the violation of impact sensitivity and band gap criteria and it is of great importance to unravel the hidden physical and chemical phenomenon for a better understanding of electronic structure-sensitivity correlation.

As mentioned in the earlier section, the states in the energy range of 2.5 eV is mainly due to the contribution of N and O atoms of NO_2 from DNBTO anion. These peaks are absent in BTO based energetic salts (See figure 3.6 of Chapter 3) and are mainly responsible for deciding the sensitivity in the studied DNBTO salts. It is expected that the explosive molecules containing trigger bonds (C-NO_2/NO_2) are lesser stable: larger the trigger bond length in the molecules, easier the breakdown or dissociation and hence the molecule will be less stable. However, one can enhance the stability of C-NO_2 bonds by introducing hydrogen bonding. For example, by increasing the number of NH_2 from 0, 1, 2, to 3,

the weakest C-NO_2 bond strength of TNB, TNA, DATB and TATB is increased from 67.7, 71.6, 74.6 to 77.2, respectively [54]. Therefore, we can conclude that the high stability of DA-DNBTO is mainly due to the presence of strong hydrogen bonding between NO_2 and NH_4.

4.3.5 Hirshfeld surface analysis

The presence of non-covalent interactions can greatly influence the impact sensitivity [55, 56]: higher the strength of intermolecular interactions, lower will be the impact sensitivity. Typically, these non-covalent interactions are weaker than the covalent bonding, thus the former will break first under external stimuli followed by the breaking of covalent bonding. Moreover, these non-covalent interactions strongly influence the crystal packing structure and thereby tailoring the impact sensitivity and mechanical properties [55–58]. Hirshfeld surface analysis and the breakdown of associated 2D fingerprint plots have gained much attention in describing the intermolecular interactions within a crystal and helps to explore vital information about both close interactions as well as the distant contacts where the interactions are weak. The 3D d_{norm} surfaces of the studied compounds were generated using standard surface resolution mapped over a fixed colour scale of 1.5 Å (blue) to -1.5 Å (red). The molecular Hirshfeld surfaces and 2D fingerprint plots of DA-DNBTO and DH-DNBTO are shown in figure 4.7. In DA-DNBTO, the several bright red spots denote the strong hydrogen bonds of N-O...H, O-H...N, O-H...O and N-H...O interactions. The distribution of these red spots demonstrates the correlation between the sliding characteristics and the Hirshfeld surface [59]: larger the red spots (strong intermolecular interactions) on the surface edges, greater will be the tendency of a crystal to slide readily along the blocks. Since most of the red spots are located along the edges of the Hirshfeld surfaces, the sliding occurs more easily along molecular plane and thus withholds the maximum external stimuli. The two sharp spikes at the bottom left of the fingerprint spectra represent O...H/H...N interactions. Ac-

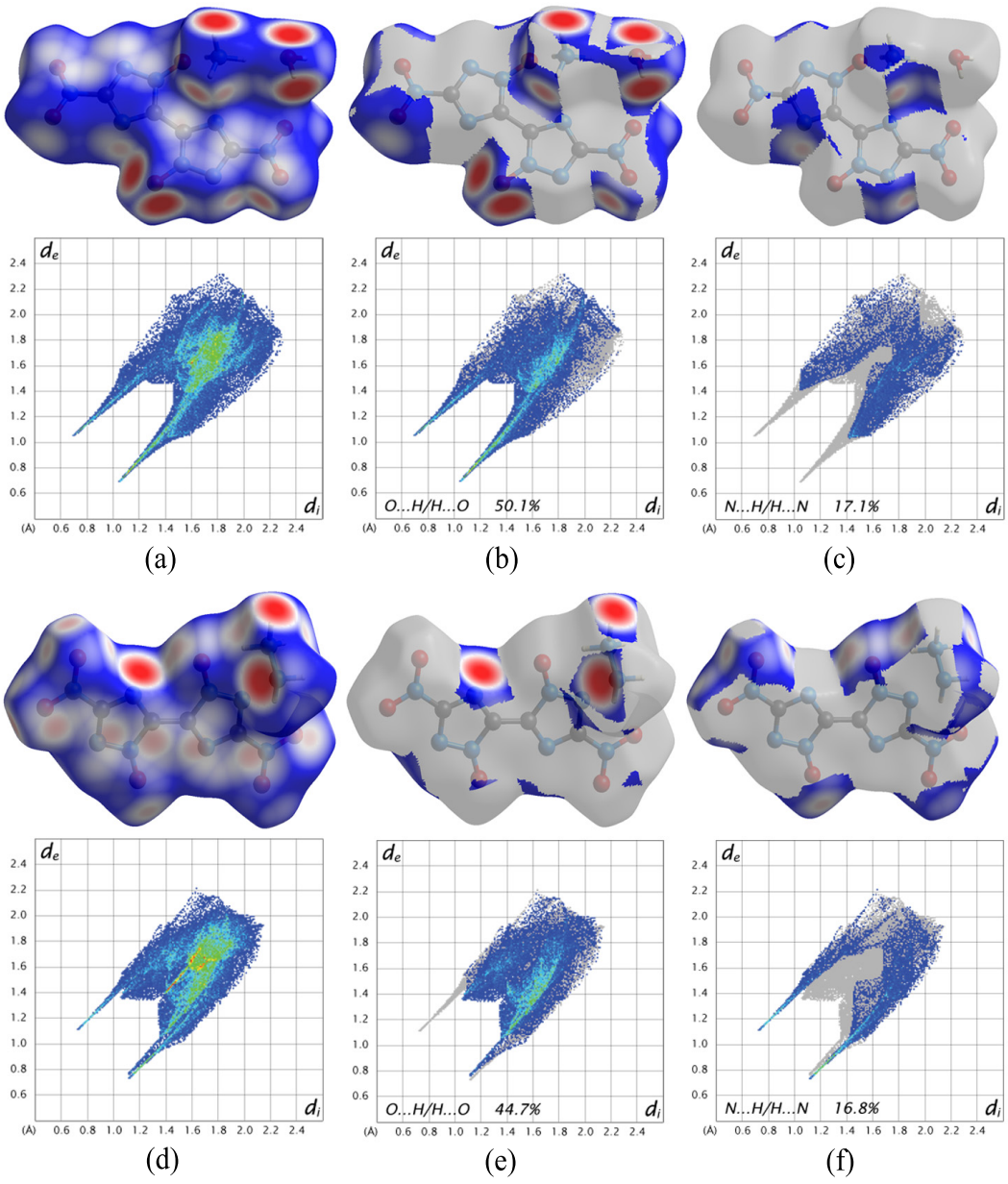

Figure 4.7: Hirshfeld surfaces mapped with d_{norm} and corresponding 2D fingerprint plots for (a-c) DA-DNBTO and (d-e) DH-DNBTO. d_i and d_e represents the closes internal and external distances from a given point on the Hirshfeld surface, respectively.

cording to US DOE standards [44, 60], these spikes indicate the significant features of insensitive energetic materials. The individual percentage contribution of O-H and N-H interactions (67.2%) of DA-DNBTO also confirmed the conclusion that the majority contributions are from intermolecular interactions. In case of DH-DNBTO, the red spots correspond to N-H...O and N-H...N hydrogen bonds. The O...H/H...O interactions appear as sharp spikes in the fingerprint spectra with a majority contribution of 44.7%. The N...H/H...N interactions are the second most abundant interaction in the structure with a proportion of 16.8%. The contribution of O-H and N-H interactions (61.5%) are comparatively smaller than that of DA-DNBTO energetic salt. In contrast, these N...H and O...H contributions are more evident in DNBTO salts than in common explosive crystals and energetic co-crystals because of high nitrogen percentage in the former. Further, the shorter $d_i + d_e$ value (1.75 Å) of DA-DNBTO represents the strength of hydrogen bonds. The $d_i + d_e$ value (1.83Å) of DH-DNBTO is larger than DA-DNBTO, representing the weak hydrogen bonds when compared with the latter. Another parameter that represents the sensitivity is the percentage contribution of O...O contacts [10]: higher the relative frequency of O...O interactions, greater the possibility of unexpected explosion. These O...O contacts that generally exist in most of the energetic materials [57, 58] do not show much impact in both the studied energetic salts due to long O...O distances and thus represents the insensitivity of the studied salts. According to these analyses, the strongest intermolecular interactions of DA-DNBTO represents its inferiority in molecular stability, which is in good agreement with the experimentally measured impact sensitivity (>40 J) and friction sensitivity (360 N) values and also explains why it has the highest stability compared to DH-DNBTO.

Figure 4.8 represent the populations of close intermolecular interactions for DA-DNBTO and DH-DNBTO energetic salts. As illustrated in the figure, the H...H interactions appear in the middle region of the fingerprint plots show a contribution of 4.8 % and 3.8% for DA-DNBTO and DH-DNBTO to the total

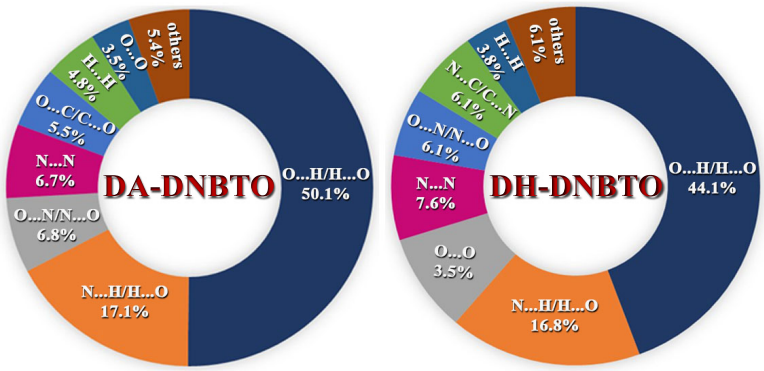

Figure 4.8: The percentage contributions to the Hirshfeld surface are for the various intermolecular interactions of (a) DA-DNBTO and (b) DH-DNBTO

Hirshfeld surface, respectively. It is noteworthy that the contribution of N...N interactions are higher than the DA-DNBTO, as a consequence of the higher proportion of nitrogen atoms in DH-DNBTO. Apart from these contacts, the minor contribution of O...O, O...N, O...C, N...C, C...C, C...H interactions were also observed in the studied energetic salts.

4.4 Conclusions

In summary, we have calculated the structural and vibrational properties of 3,3′-dinitro-5,5′-bis-1,2,4-triazole-1,1-diolate based EIS. The calculated ground state lattice constants, crystallographic angles and volumes using DFT-D2 method reproduces the experimental values. The spectrum of DA-DNBTO contains more number of peaks in the high frequency range (above 2850 cm-1) compared to DH-DNBTO. The Hirshfeld surface analysis reveals the presence of strongest intermolecular interactions in DA-DNBTO, representing its inferiority in molecular stability and also explains why it has the highest stability compared to DH-DNBTO. Further, the intermolecular O...H/H...O interactions show majority contribution to the crystal structure which visualized as bright red spots in the Hirshfeld surfaces. The N...H/H...N interactions are the second most abundant

interaction in both the studied energetic salts. Besides, we find that the O...O contacts that generally exist in most of the energetic materials do not show much impact in both the studied energetic salts. Therefore, combining the analyses of BTO and DNBTO based energetic salts, we re-verified that the intermolecular interactions are necessary for constructing high performance and low sensitive energetic materials. It confirms that the energetic ionic salts are indeed an effective way to enhance the performance with reasonable sensitivity due to the presence of improved intermolecular hydrogen bonding among the existing energetic molecules.

In combination with our earlier work, we have demonstrated the explosive sensitivity mechanism from the viewpoint of band gap criteria and intermolecular hydrogen bonding. Through this study, one can design a crystal structure of explosive molecules with desirable properties, such as minimized impact sensitivity and enhanced detonation performance.

References

[1] S. Zeman and M. Jungova, Propellants Explos. Pyrotech., **41**, 426 (2016).

[2] Y. Liu, C. He, Y. Tang, G. H. Imler, D. A. Parrishc and J. M. Shreeve, Dalton Trans., **47**, 16558 (2018).

[3] R. W. Millar, S. P. Philbin, R. P. Claridge and J. Hamid, Propellants Explos. Pyrotech., **29**, 81 (2004).

[4] P. Yin, Q. Zhang and J. M. Shreeve, Acc. Chem. Res., **49**, 4 (2016).

[5] P. Yin, D. A. Parrish and J. M. Shreeve, Angew. Chem. Int. Ed., **53**, 12889 (2014).

[6] H. Wei, J. Zhang, C. He and J. M. Shreeve, Chem. Eur. J., **21**, 8607 (2015).

[7] J. Zhang, S. Dharavath, L. A. Mitchell, D. A. Parrish and J. M. Shreeve, J. Am. Chem. Soc., **138**, 7500 (2016).

[8] A. A. Dippold and T. M. Klapotke, J. Am. Chem. Soc., 135, 9931 (2013).

[9] Y. Shang, B. Jin, R. Peng, Z. Guo, Q. Liu, J. Zhao and Q. Zhang, RSC Adv., **6**, 48590 (2016).

[10] J. H. Zhang, Q. H. Zhang, T. T. Vo, D. A. Parrish and J. M. Shreeve, J. Am. Chem. Soc. **137**, 1697 (2015).

[11] J. H. Zhang and J. M. Shreeve, J. Am. Chem. Soc., **136**, 4437 (2014).

[12] Z. B. Zhang, C. X. Xu, X. Yin and J. Guo, Dalton Trans., **45**, 19045 (2016).

[13] Q. Ma, Y. Chen, L. Liao, H. Lu, G. Fan and J. Huang, Dalton Trans., **46**, 7467 (2017).

[14] Y. Tang, C. He, H. Gao and J. M. Shreeve, J. Mater. Chem. A, **3**, 15576 (2015).

[15] D. Kumar, C. He, L. A. Mitchell, D. A. Parrish and J. M. Shreeve, J. Mater. Chem. A, **4**, 9220 (2016).

[16] P. Yin, C. He and J. M. Shreeve, J. Mater. Chem. A, **4**, 1514 (2016).

[17] Y. B. Zeldovich, J. Exp. Theor. Phys. (USSR), **10**, 542 (1940).

[18] J. von Neumann, *Office of Science Research and Development: Report No.* 549 (1942).

[19] W. Doring, Am. Phys., **43**, 421 (1943).

[20] K. Fucke and J. Steed, Water, **2(3)**, 333 (2010).

[21] I. Ortega, R. Escribano, D. Fernandez, V. Herrero, B. Mate, A. Medialdea and M. Moreno, Chem. Phys. Lett., **378**, 218 (2003).

[22] Y. Nishiyama, H. Chanzy, M. Wada, J. Sugiyama, K. Mazeau, T. Forsyth, C. Riekel, M. Muller, B. Rasmussen, and P. Langan, Adv. X-ray Anal., **45**, 385 (2002).

[23] A. D. Becke, J. Chem. Phys, **140**, 18A301 (2014).

[24] M. S. Miao, Z. A. Dreger, J. M. Winey and Y. M. Gupta, J. Phys. Chem. A, **112**, 12228 (2008).

[25] J. J. Zhao and H. Liu, Comput. Mater. Sci., **42**, 698 (2008).

[26] S. Appalakondaiah, G. Vaitheeswaran and S. Lebegue, J. Chem. Phys., **140**, 014105 (2014).

[27] E. F. C. Byrd and B. M. Rice, J. Phys. Chem. C, **111**, 2787 (2007).

[28] H. Liu, J. J. Zhao, J. G. Du, Z. Z. Gong, G. F. Ji and D. Q. Wei, Phys. Lett. A, **367**, 383 (2007).

[29] S. Appalakondaiah, G. Vaitheeswaran and S. Lebegue, J. Phys. Chem. A, **119**, 6574 (2015).

[30] E. F. C. Byrd, G. E. Scuseria and C. F. Chabalowski, J. Phys. Chem. B, **108**, 13100 (2004).

[31] A. Tkatchenko and M. Scheffler, Phys. Rev. Lett., **102**, 073005 (2009).

[32] S. Grimme, J. Comput. Chem., **27**, 1787 (2006).

[33] K. Lee, E. D. Murray, L. Kong, B. I. Lundqvist and D. C. Langreth, Phy. Rev. B, **82**, 081101 (2010).

[34] B. M. Abraham, V. D. Ghule and G. Vaitheeswaran, Phys. Chem. Chem. Phys., **20**, 29693 (2018).

[35] M. D. Segall, P. J. D. Lindan, M. J. Probert, C. J. Pickard, P. J. Hasnip, S. J. Clark and M. C. Payne, J. Phys: Condens. Matter, **14**, 2717 (2002).

[36] T. H. Fischer and Almlof, J. Phys. Chem., **96**, 9768 (1992).

[37] D. Vanderbilt, Phys. Rev. B., **41**, 7892 (1990).

[38] N. Troullier and J. L. Martins, Phys. Rev. B: Condens. Matter, **43**, 1993 (1991).

[39] J. P. Perdew, S. Burke and M. Ernzerhof, Phys. Rev. Lett., **77**, 3865 (1996).

[40] H. J. Monkhorst and J. D. Pack, Phys. Rev. B, **13**, 5188 (1976).

[41] M. A. Spackman and J. J. McKinnon, CrystEngComm, **4**, 378 (2002).

[42] B. M. Abraham, J. P. Kumar and G. Vaitheeswaran, ACS Omega, **3(8)**, 9388 (2018).

[43] Z. B. Zhang, T. Li, L. Yin, X. Yin and J. G. Zhang, RSC Adv., **6**, 76075 (2016).

[44] Y. Ma, A. Zhang, C. Zhang, D. Jiang, Y. Zhu and C. Zhang, Cryst. Growth. Des., **14**, 4703 (2014).

[45] Z. B. Zhang, C. X. Xu, X. Yin and J. G. Zhang, Dalton Trans., **45**, 19045 (2016).

[46] D. Hadzi and S. Bratos, *The Hydrogen Bond—Recent Developments in Theory and Experiments*, 565 (1976).

[47] H. Zhang, F. Cheung, F. Zhao and X. L. Cheng, Int. J. Quantum Chem., **109**, 1547 (2009).

[48] W. Zhu and H. Xiao, Struct. Chem., **21**, 847 (2010).

[49] C. Zhi, X. Cheng and F. Zhao, Propellants Explos. Pyrotech., **35**, 555 (2010).

[50] M. H. Keshavarz, M. Ghaffarzadeh, M. R. Omidkhah and K. Farhadi, Z. Anorg. Allg. Chem., **643**, 2158 (2017).

[51] C. F. Melius, J. Phys. Colloques, **48**, 341 (1984).

[52] C. Zhang, Propellants, Explos. Pyrotech., **33**, 139 (2008).

[53] C. Zhang, J. Hazard. Mater., **161**, 21 (2009).

[54] C. J. Wu and L. E. Fried, *Eleventh International Detonation Symposium, Snowmass, CO* (1998).

[55] M. M. Kuklja and S. N. Rashkeev, Appl. Phys. Lett., **90**, 151913 (2007).

[56] C. Zhang, X. Wang and H. Huang, J. Am. Chem. Soc., **130(26)**, 8359 (2008).

[57] Y. Ma, A. Zhang, X. Xue, D. Jiang, Y. Zhu and C. Zhang, Cryst. Growth Des., **14**, 6101 (2014).

[58] C. Zhang, X. Xue, Y. Cao, J. Zhou, A. Zhang, H. Li, Y. Zhou, R. Xu and T. Gao, CrystEngComm, **16**, 5905 (2014).

[59] C. Zhang, X. Xue, Y. Cao, Y. Zhou, H. Li, J. Zhou and T. Gao, CrystEngComm, **15**, 6837 (2013).

[60] Manual, *D. O. E. DOE Explosives Safety Manual*, **440**, 1-1A (2006).

Chapter 5

High pressure studies of hydrogen-bonded energetic solid 3,6-dihydrazino-s-tetrazine

In this chapter, by analysing the structural changes, IR spectra and Hirshfeld surfaces, the high pressure behavior of 3,6-dihydrazino-s-tetrazine (DHT) was investigated using dispersion corrected density functional theory in order to provide a clear description of hydrogen bonding interactions. In addition, detonation properties, namely, detonation pressures and velocities were calculated using Kamlet-Jacobs equations to determine the denotation characteristics of DHT.

B. Moses Abraham, J. Prathap Kumar and G. Vaitheeswaran, "High pressure studies of hydrogen bonded energetic material 3,6-dihydrazino-s-tetrazine using DFT", **ACS Omega**, **3(8)**, 9388 (2018).

5.1 Introduction

In the world of advanced technology, researchers are still digging deep down the track to achieve a reasonable balance between high performance and good molecular stability in order to develop high energy density materials. However, the major goal in the field of explosive materials is to design more powerful and insensitive explosives, propellants, oxidizers and pyrotechnics. To construct these types of energetic materials, many factors need to be addressed (eg: energy, safety, cost, etc.) before it is applied for practical applications [1]; one among such parameters is sensitivity, which is a major problem that has to be taken into account during storage, production and transportation of energetic materials. The best approach to improve the performance of an explosive without compromising safety is to choose the material that can form hydrogen bonding networks [2]. These noncovalent interactions, especially hydrogen bonding interactions show great influence on the chemical and physical properties of energetic materials giving rise to efficient packing in the crystal, which in turn enhances the density and stability of the material [3]. In addition, the low solubility in water is an extra advantage for strongly bonded energetic materials which can provide better sensitivity together with low toxicity [4]. Various hydrogen bonded energetic materials have been extensively studied in recent years to understand the nature of intermolecular interactions [5–8]. For instance, the recently synthesised eco-friendly energetic material hydrazine 5,5′-bitetrazole-1,1′-diolate (HA-BTO) exhibit high crystal density (ρ = 1.913 g/cm^3) [10] than 1,3,5-Trinitro-1,3,5-triazinane (RDX, ρ = 1.806 g/cm^3) [11] due to the influence of strong hydrogen bonding networks. The huge number of intermolecular hydrogen bonds not only play a crucial role in the formation of an interesting structure but also improve the stability of HA-BTO. Moreover, the strong hydrogen bonding networks in TATB not only enables the higher density (ρ = 1.937 g/cm^3) but also responsible for its insolubility in most of the common solvents [9]. Our previous results also have shown that

the presence of strong hydrogen bonding in Ammonium DiNitramide (ADN) is responsible for more hygroscopic nature over Ammonium Perchlorate (AP) [12].

Pressure on the scale of gigapascals can cause remarkable changes in the intermolecular interactions and reveals the hidden phenomena laying behind the extreme conditions [13–15]. Moreover, the influence of pressure on the crystal structure of energetic materials can facilitate efficient crystal packing and tune the non-covalent hydrogen bond interactions, thereby improving the detonation properties. These type of studies provide a better understanding about the nature of hydrogen bonding and structural stability of the energetic material under pressure. Li et al. carried out high pressure studies on energetic material acetamidinium nitrate [16] ($C_2N_2H_7^+ \cdot NO_3^-$) using diamond anvil cell. Their results show a deviation in the ideal hydrogen bonded arrays along with a small slippage between adjacent ion pairs, which is responsible for the fabrication of new high density material with better detonation performance. The pressure induced rearrangement of hydrogen bonded networks causes a phase transition in carbohydrazide (CON_4H_6) energetic material [17]. The reported high pressure phase with space group P1 exhibits almost 23.1% higher density than the ambient structure ($P2_1/n$). However, the application of pressure can change the direction of atoms and molecules in hydrogen bonded structures, allowing the explosive properties (such as sensitivity) to be modified. Therefore, it is of great interest to study the behavior of hydrogen bonded systems under pressure for exploring high energy density materials.

Nitrogen rich energetic materials, especially tetrazine based compounds have received special attention due to their better oxygen balance, high densities and higher positive heat of formation (HOF) [18]. As a component of gun and rocket propellant [19], eco-friendly smoke ingredient of pyrotechnic composition, 3,6-dihydrazino-s-tetrazine (DHT) is considered to be a nitrogen rich energetic material with a measured H_{50} and HOF value of 65 cm (2.5 kg, Type 12) and +536 kJ/mol, respectively [19]. It has been used to design a variety of other nitrogen

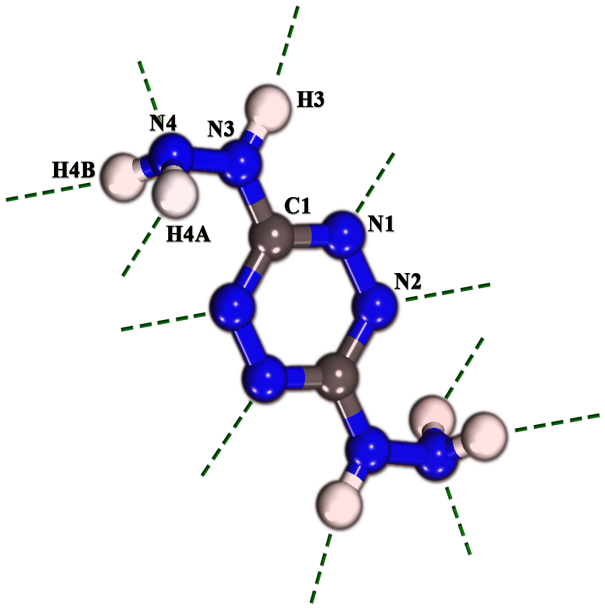

Figure 5.1: Molecular geometry of DHT. Green dashed lines represent hydrogen bonding.

rich energetic materials, such as 3,6-di-azido-1,2,4,5-tetrazine (DAT)[21]. The carbon free combustion and hot flames of DHT have made it an ideal for the new generation eco-friendly fireworks [20]. It can detonate with a rate of 7.54 km/s in the unconfined pressed pellets of 0.50 inches in diameter. DHT was first synthesized by Hiskey et. al. in the 1990's [22, 23] and later recognized by several experimental groups [24–29] but very few theoretical studies were reported [30–33]. Hu et. al. studied the intermolecular interactions of DHT using theoretical calculations and found that the strong intermolecular hydrogen bonding networks dominantly contributed to the dimers [33]. Consequently, the variations identified in microscopic level can also affect the macroscopic properties like density, which may further improve the performance of an explosive. Therefore, the increase in density of DHT as a function of pressure may greatly influence the detonation properties and corresponding applications. Herein, we report the high pressure investigation of structural and vibrational properties of DHT using first princi-

Table 5.1: Calculated lattice parameters (a, b ,c in Å), lattice angle (β, in ^{o}) and volume (V in Å^3) of DHT using PBE-GGA and dispersion corrected (TS, D2) functionals along with experimental data. The relative errors (in %) with respect to experiments are given in parenthesis, here '+' and '-' signs indicate overestimation and underestimation of the calculated values when compared with experiments.

	LDA	PBE	TS	D2	Expt [49]
a	3.996 (-1.18%)	4.798 (+18.64%)	4.178 (+3.31%)	4.036 (-0.17%)	4.043
b	5.364 (-4.97%)	5.340 (-5.39%)	5.506 (-2.45%)	5.541 (-1.83%)	5.644
c	11.532 (-4.92%)	12.501 (+3.06%)	11.984 (-1.19%)	11.855 (-2.25%)	12.129
β	101.23 (+2.12%)	88.9 (-10.31%)	98.22 (-0.9%)	99.9 (0.78%)	99.12
V	242.51 (-11.31%)	320.32 (17.37%)	272.95 (0.01%)	261.19 (4.29%)	272.91

ples calculations. Its axial and bond compressibilities and pressure-volume EOS have been calculated. In addition, the effect of pressure on NH/NH_2 stretching frequencies are crucial in understanding the behavior of hydrogen bonding. More information about the variations in packing patterns was obtained from Hirshfeld surfaces and the fingerprint plots. The present chapter explore the pressure induced changes in intermolecular interactions to provide valuable information about the stability of hydrogen bonded energetic materials.

5.2 Methodology of calculation

First-principles calculations were performed using plane wave the pseudo-potential method through CAmbridge Series of Total Energy Package (CASTEP) [34, 35]. The generalized gradient approximation (GGA) by Perdew-Burke-Ernzerhof (PBE) functional [36] is used to treat the exchange-correlation potentials. Broyden-Fletcher-Goldfarb-Shanno (BFGS) optimization method [37] is implemented to obtain the equilibrium crystal structure. The ultrasoft (USP) and norm-conserving pseudopotentials (NCP) have been utilized to calculate the structural properties and zone center IR spectra, respectively. For Brillouin zone integration, an $6 \times 5 \times 2$ Monkhorst-Pack grid [38] is used. The plane wave cut-off energy of 600 eV for USP, 950 eV for NCP were used to expand the wave functions. The

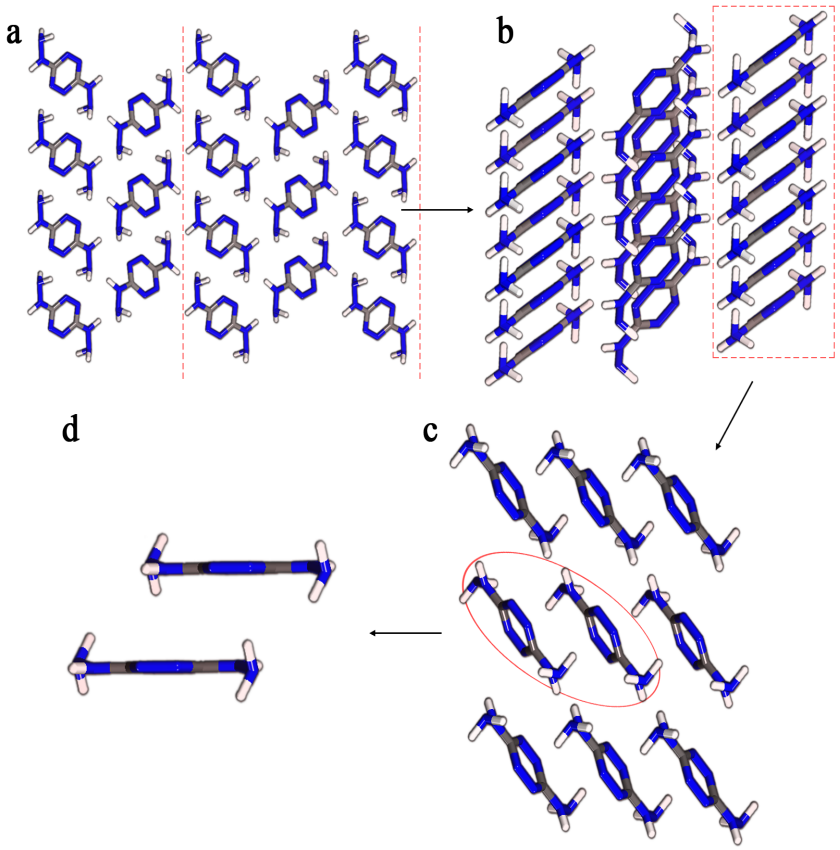

(a)

Figure 5.2: Crystal structure of DHT along (a) x-axis and (b) y-axis, (c and d) the significant H-π stacking interactions stacked in columns parallel to the c-axis.

maximum stress and self-consistent energy convergence criterion were set to 0.02 GPa and 5.0×10^{-6} eV/atom, respectively. The force per atom diminished to 0.01 eV/Å and the displacement is set to 5.0×10^{4} Å. The linear response method is used to calculate the vibrational spectra of DHT through density functional perturbation theory.

The accurate description of weak intermolecular interactions (eg: van der Waals (vdW) forces, hydrogen bonding) has been the subject of interest for many decades. Typically, the long range vdW forces are unable to capture accurately by conventional exchange-correlation functionals in DFT (eg: GGA, LDA). For example,

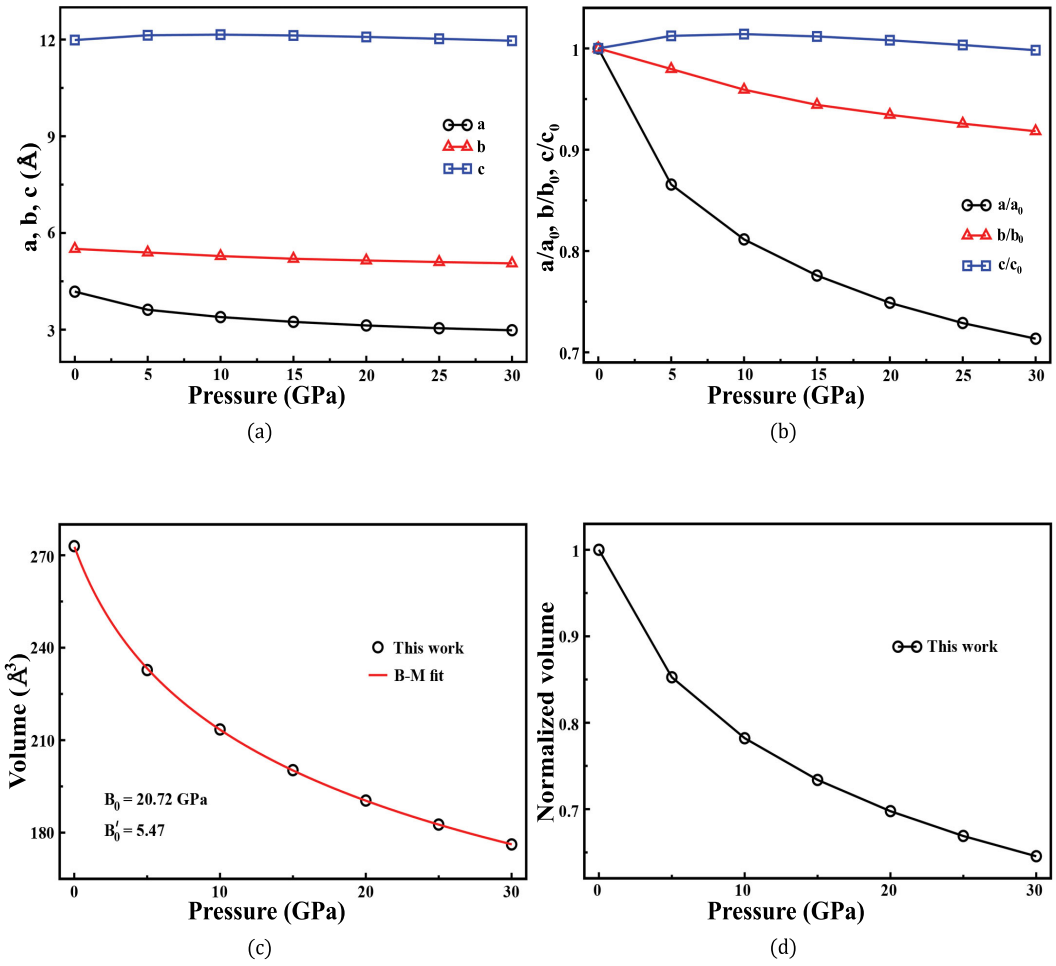

Figure 5.3: Calculated pressure dependence of (a) unit cell parameters (a, b, c), (b) normalized unit cell parameters (a/a_0, b/b_0, c/c_0), (c) volume (V) and (d) normalized volume (V/V_0) of DHT. The solid red line represents the compression data fit to the third order Birch Murnaghan equation of state.

GGA overestimates the volume by 10-15%, whereas LDA is underestimated by 7-30% for RDX [40], CL-20 [39], TNAD [45], FOX-7 [44], HMX [41], TATB [43] and PETN [42]. The inadequacies in predicting the intermolecular interactions not only affect the accurate description of crystal geometry but also lead to variations in the obtained properties including density, cohesive energy, elastic moduli and band gap. In order to include these types of weak dispersive forces, various developments were made to extend standard DFT. Particularly, the empirical vdW corrections such as the Tkatchenko and Scheffler (DFT-TS) [47] and Grimme (DFT-D2) [46] corrections to PBE are most successful methods. Within the DFT+D framework, the total energy including vdW correction is given by:

$$E_{DFT+D} = E_{DFT} + E_{disp}$$

E_{DFT} is the normal self-consistent Kohn-Sham energy and E_{disp} is the empirical dispersion correction expressed as:

$$E_{disp} = -s_6 \sum_{i<j} \frac{C_{ij}}{R_{ij}^6} f_{damp}(R_{ij}),$$

Where R_{ij} and C_{ij} denotes the interatomic distance and dispersion coefficient for the pair of i^{th} and j^{th} atoms, respectively. S_6 is a global scaling factor that only depends on the density functional used. In order to avoid divergence for small R_{ij}, the damping function $f_{damp} = \frac{1}{1+e^{-d(R_{ij}/R_0-1)}}$ is introduced.

The CrystalExplorer [48] is used to analyse the Hirshfeld surfaces, which is a most effective tool for understanding the behavior of intermolecular interactions within the crystal. The strength of the interactions can be described by d_{norm} (normalised contact distance):

$$d_{norm} = \frac{(d_i - r_i^{vdw})}{r_i^{vdw}} + \frac{(d_e - r_e^{vdw})}{r_e}$$

Where r_i and r_e denote the vdW radii of two atoms inside and outside to the Hirshfeld surfaces, d_i and d_e represent the internal and external separations from

the nearest atoms, respectively. The 3D d_{norm} surface is used to identify close intermolecular contacts, in which the positive and negative values denote the intermolecular contacts that are longer and shorter than the vdW separations, respectively. The graphical plots are mapped onto the Hirshfeld surfaces with d_{norm} using blue (longer intermolecular contacts), white (contacts around the vdW separation) and red (shorter intermolecular contacts) colours. In addition, the overall summary of intermolecular interaction in the molecule is provided by the associated 2D fingerprint plots.

5.3 Results and discussion

5.3.1 Crystal structure and equation of state.

The structure of DHT crystallize in the monoclinic space group P21/c with lattice parameters a = 4.043 Å, b = 5.644 Å, c = 12.129 Å, β = 99.124^o, and Z = 2 at 173 K [49]. The molecular geometry and crystal structure of DHT were shown in figures 5.1 and 5.2, where the tetrazine ring and the nitrogen atoms attached to hydrazino group are nearly coplanar with axial symmetry. Each molecule in the crystal structure connects with the neighbouring molecules to form three dimensional N-H...N hydrogen bonding networks in the form of herringbone like pattern. The presence of twelve hydrogen bonds in each molecule can strengthen the stability of the compound. The relaxed lattice parameters and the optimized volume obtained using various exchange-correlation functionals are presented in Table 5.1 along with the experimental values.

It is found that the calculated lattice parameters using generalized gradient approximation (GGA) are larger than the experimental results, while the local-density approximation (LDA) values are underestimated. The well known tendency of GGA/LDA calculations to overestimate/underestimate the lattice constants are precisely reflected in the obtained volumes (320.3/242.5) which fall above/below the experimentally measured volume of 272.9, respectively. In con-

trast, the correction to PBE functional (TS and D2) provide reasonable improvement with small deviations when compared with experimental unit cell parameters. Especially by TS method, the error in calculated volume is reduced to 0.01%, indicating the necessity of vdW interactions while studying the structure of DHT crystal.

In order to understand the response of DHT as a function of pressure, we carried out a detailed investigation of its crystal structure at different pressures up to 30 GPa in step size of 5 GPa at 0 K. Remarkably, the DHT exhibits an anisotropic behavior along three crystallographic directions under pressure (see figure 5.3a). The compressibility in the **a**- direction is markedly greater than **b**- and **c**- direction. At 30 GPa, the lattice parameter **a** and **b** is reduced by 28.6% and 8.17%, respectively, while **c** is first increased and then slightly reduced by 0.17% from its ambient pressure value. This indicates that the structure of DHT is much softer in the **a**- axis than in the **b**- and **c**- directions. Further, as pressure increases, the unit cell volume decreases monotonically and reaches to 85% of its ambient volume by 30 GPa (figure 5.3c), which in turn enhances the density from 2.7 to 3.1 g/cm^3. The resulting P-V data is used to calculate the bulk modulus (B_0) and its pressure derivatives (B_0') by fitting with third order Birch Murnaghan equation of state and is found to be 20.72 GPa and 5.47, respectively. The obtained results show that the DHT is more harder material than ADN and AP whose experimental bulk modulus value is reported as 16.4 GPa [50] and 15.2 GPa [51], respectively.

The application of pressure is not only responsible for the variations in the unit cell of DHT but also effect the molecular geometry like bond length and bond angles. More interestingly, there exist a strong N-H...N hydrogen bonding networks within the crystal structure between neighbouring molecules. Under ambient conditions, the bond lengths of N3-H3, N4-H4A and N4-H4B are 1.048 Å, 1.038 Å and 1.038 Å, respectively. The three N-H bonds of DHT molecule points to three neighbouring molecules. These intermolecular hydrogen bond distances

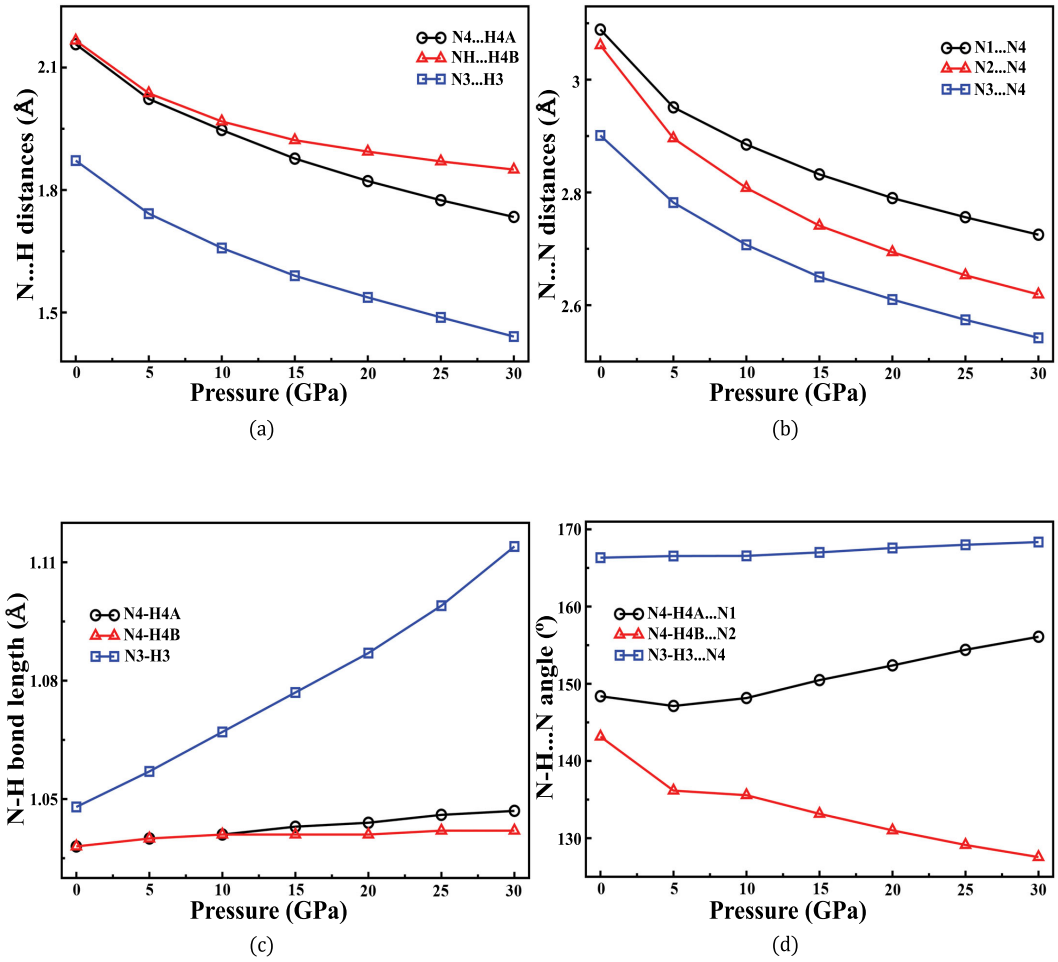

Figure 5.4: Calculated (a) intramolecular N-H (d_{N-H}) bond length, (b) intermolecular N...H ($d_{N...H}$) and (c) N...N ($d_{N...N}$) distance and (d) N-H...N ($\angle_{N-H...N}$) bond angle as a function of pressure in DHT.

can be measured using the N...H distance. For example, a DHT molecule connects with the neighbouring molecules in the direction of N1, N2 and N4 atoms and the N...H distances are 2.157 Å, 2.166 Å and 1.872 Å, respectively. The average distance of the intermolecular N...H pairs and N-H covalent bonds are 2.06 Å and 1.04 Å, respectively. These hydrogen bonds exhibit huge variations in the bond strength under compression. The calculated pressure dependence of intermolecular N...H ($d_{N...H}$) and N...N ($d_{N...N}$) distance, intramolecular N-H (d_{N-H}) bond length and N-H...N ($\angle_{N-H...N}$) bond angles are shown in the figure 5.4. The average distance between the intermolecular N...H contacts (see 5.4a) at 0 GPa (2.06 Å) and 30 GPa (1.97 Å) are found to be less than the sum of vdW radii of H and N (2.7), which supports the strengthening of hydrogen bond due to shortening of intermolecular N...H contact distance under pressure. Further, the calculated N-H bond lengths show anisotropic nature under pressure (see figure 5.4c), especially the covalent N3-H3 bond length is enlarged and increased from 1.044 Å at 0 GPa to 1.111 Å at 30 GPa. The increase of d_{N-H} bond length represents the weakening of covalent N-H bonds by facilitating the release of hydrogen atom. In general, the N-H covalent bond became larger under pressure, while H...N interaction shrinks due to reducing repulsive force, leading to a shortening of total N-N distance. The fundamental criteria to determine the weakening or/and strengthening of hydrogen bonding mainly depend on the above analyzed intermolecular distance and the frequency of their corresponding vibrational stretching modes and those of the donor hydrogen covalent bonds, which will be discussed in the next section.

5.3.2 IR spectra of DHT under pressure

Vibrational spectroscopic study of hydrogen bonded energetic materials as a function of pressure can tune the range of frequencies due to weak intermolecular interactions and explains the behavior of hydrogen bonding on the stability of crystal structure. Generally, the strengthening or weakening of hydrogen bonds

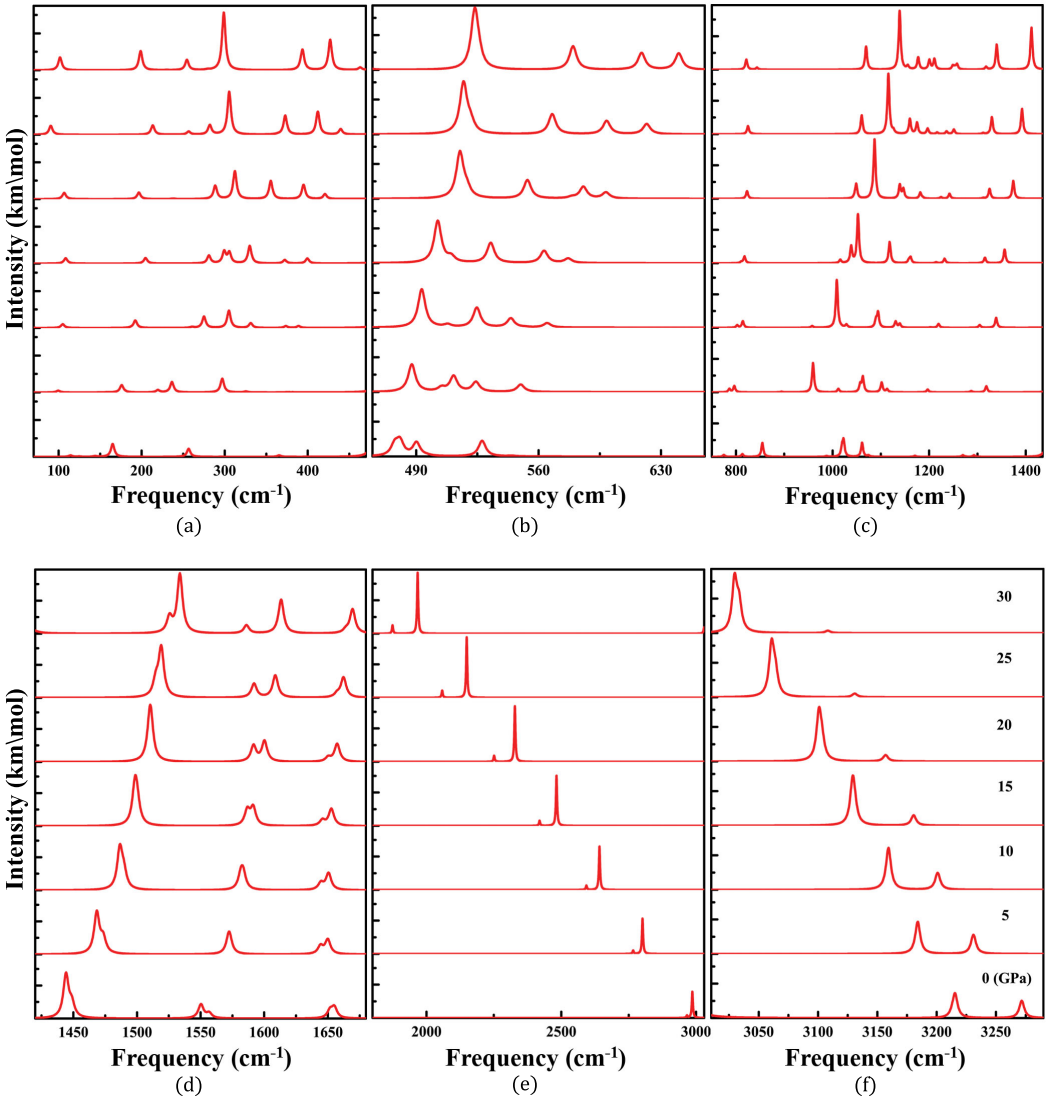

Figure 5.5: Calculated IR spectra (a) 70-470 cm^{-1}, (b) 465-655 cm^{-1}, (c) 750-1435 cm^{-1}, (d) 1420-1680 cm^{-1}, (e) 1800-3030 cm^{-1}, (f) 3010-3300 cm^{-1} of DHT as a function of pressure.

can be demonstrated based on the shift in the D-H vibrational frequency. For any material containing D-H...A hydrogen bonds, (A and D represent acceptor and donor, respectively), the IR spectra corresponding to a particular frequency shift towards lower energies with decreasing D-A distance. This can be explained in terms of electrostatic attraction between acceptor and proton atom. When the pressure is applied to the system, the distance between the acceptor and donor atom reduces, increasing the electrostatic attraction between H...A. This leads to elongation of D-H bond distance by decreasing the D-H stretching frequencies towards lower energies. This is in accord with the aforementioned N-H bond length, where the H...N distance reduces under compression that strengths the hydrogen bonding. As discussed in the above section, DHT crystallizes in the monoclinic structure containing 32 atoms in the primitive cell resulting in the 96 vibrational modes. From the group analysis of P21/c space group, the representation of symmetry decomposition is

$$\Gamma_{tot} = 24\mathrm{A}_u \oplus 24B_u \oplus 24A_g \oplus 24B_g$$

with 3 acoustic modes

$$\Gamma_{acoustic} = \mathrm{A}_u \oplus 2B_u$$

and 93 optical modes

$$\Gamma_{optical} = 23\mathrm{A}_u \oplus 22B_u \oplus 24A_g \oplus 24B_g$$

Group theoretical analysis of 93 optical modes show that the $23\mathrm{A}_u \oplus 22B_u$ are IR active modes and $24A_g \oplus 24B_g$ are Raman active modes. The obtained optical modes along with corresponding vibrational assignments are shown in Table 5.2. Out of these 93 optical modes, 18 were under the frequency range of 300 cm^{-1}. While, in the remaining 75 modes, 24 pairs of modes (48 modes) were under 10 cm^{-1} from each other (15 pairs of the 24 were below 5 cm^{-1} and 9 of the 24 were below 3 cm^{-1}). The pressure induced variations of IR spectra in the frequency range 70-470, 465-655, 750-1435, 1420-1680, 1800-3300 cm^{-1} are presented in the figure 5.5. The lattice modes between the vibrational frequency 58

and 322 cm^{-1} are mainly due to rotational and/or translational motion of NH_2 group and tetrazine ring. As a function of pressure, all the lattice modes shift monotonically towards higher frequencies due to the reduction of intermolecular separation, which demonstrates the strengthening of interactions between adjacent molecules [52, 53]. Figure 5.5b consists of tetrazine ring breathing and bending modes and NH_2 group rotation and bending vibrations, while NH (stretching, wagging, bending and rocking), NH_2 (twisting, wagging), N-N, C-N, C=N stretching and ring breathing modes are shown in the figure 5.5c. These modes show blue shift up to the studied pressure range. The most pronounced one is the significant splitting of NH bending mode (1550 cm^{-1}) into two distinguishable bands around 20 GPa (see figure 5.5d). One of these modes display positive pressure dependence while the other show a negative dependence.

The effect of pressure on N-H stretching vibrations can provide important information regarding the variations in hydrogen bonding networks. As shown in the figure 5.5e and f, the N-H stretching vibrations located between 2950 cm^{-1} to 3300 cm^{-1} are composed of three modes: The highest intensity peak at 2986 cm^{-1} corresponds to the stretching of NH group. While, the modes at 3215 cm^{-1} and 3271 cm^{-1} are assigned to symmetric and asymmetric stretching vibrations of NH_2 group (see figure 5.6), respectively. In contrast to other bands, the two lowest frequency modes situated at 2986 and 3215 cm^{-1} shift towards lower frequencies with increasing intensities as a function of pressure. The highest frequency mode found to reduce and eventually disappear at the maximum studied pressure range. The lowering of frequency is more pronounced in the NH and NH_2 symmetric stretching vibrations than in the NH_2 asymmetric stretching mode. The observed decreasing activity in NH/NH_2 vibrational modes corroborates with generalized rules of pressure induced strengthening of N-H...N hydrogen bonding in DHT crystal. As shown in figure 5.2, the nitrogen atoms in the tetrazene ring acts as proton acceptors and N-H groups of various molecules serve as a proton donors to form hydrogen bonding networks. The application of pressure will

Table 5.2: Calculated phonon frequencies along with the corresponding assignment of DHT at the DFT-TS equilibrium volume using NCP approach under ambient pressure.

Mode	Frequency (cm^{-1})	Assignment
M4-M22	58-322	lattice modes
M23,M24	364-365	ring lib
M25-M28	374-463	ring lib, NH_2 rot
M29	477	NH_2 rot
M30,M31	480-490	NH_2 wagg
M32-M34	496-526	NH_2 rot
M35	527	NH_2 bend, N-C=N wagg
M36	544	NH_2 rot
M37,M38	636-642	ring breath
M39,M40	665-686	ring bend, NH_2 wagg
M41-M44	763-802	NH wagg
M45	809	NH_2 wagg, NH str
M46	813	NH wagg
M47	845	ring breath
M48-M50	846-869	NH rock
M51-M58	987-1074	NH_2 wagg, C-N, C=N, N-N str
M59-M62	1157-1178	NH_2 wagg
M63,M64	1269-1274	N-C=N asy str, NH_2 twist
M65-M68	1284-1292	NH_2 twist
M69,M70	1330-1335	NH bend
M71,M72	1379.02-1379.77	C-N, C=N str, NH bend
M73-M80	1444-1557	NH bend
M81-M84	1648-1659	NH_2, NH scissor
M85-M88	2966-3064	NH str
M89-M92	3211-3215	NH_2 sym str
M93-M96	3271.49-3271.78	NH_2 asym str

decrease the separation between neighbouring molecules, leading to the reduction of N-H...N hydrogen bond lengths along hydrogen bonded chains. The observed variation trends of NH/NH_2 vibrational modes under pressure are quite similar to previous studies of hydrogen bonded energetic materials [54].

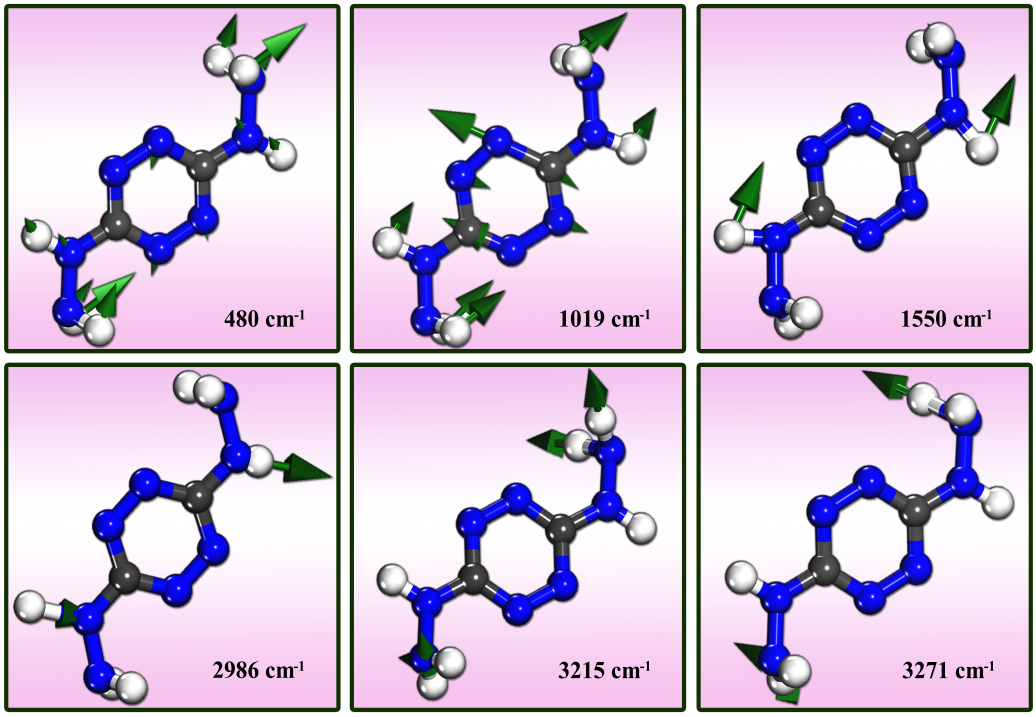

Figure 5.6: Few simulated vibrational modes of DHT crystal.

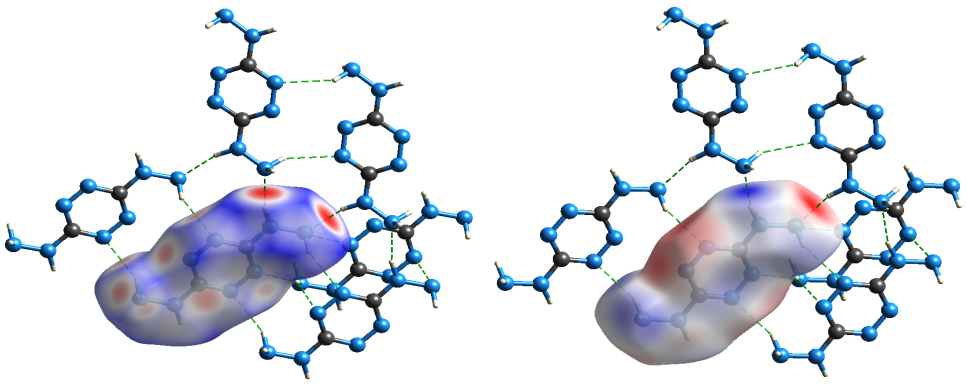

(a) (b)

Figure 5.7: (a) Hirshfeld surface of DHT crystal for visualizing the intermolecular interactions. (b) Electrostatic potential mapped on the Hirshfeld surface. The green dashed lines represents the hydrogen bonds.

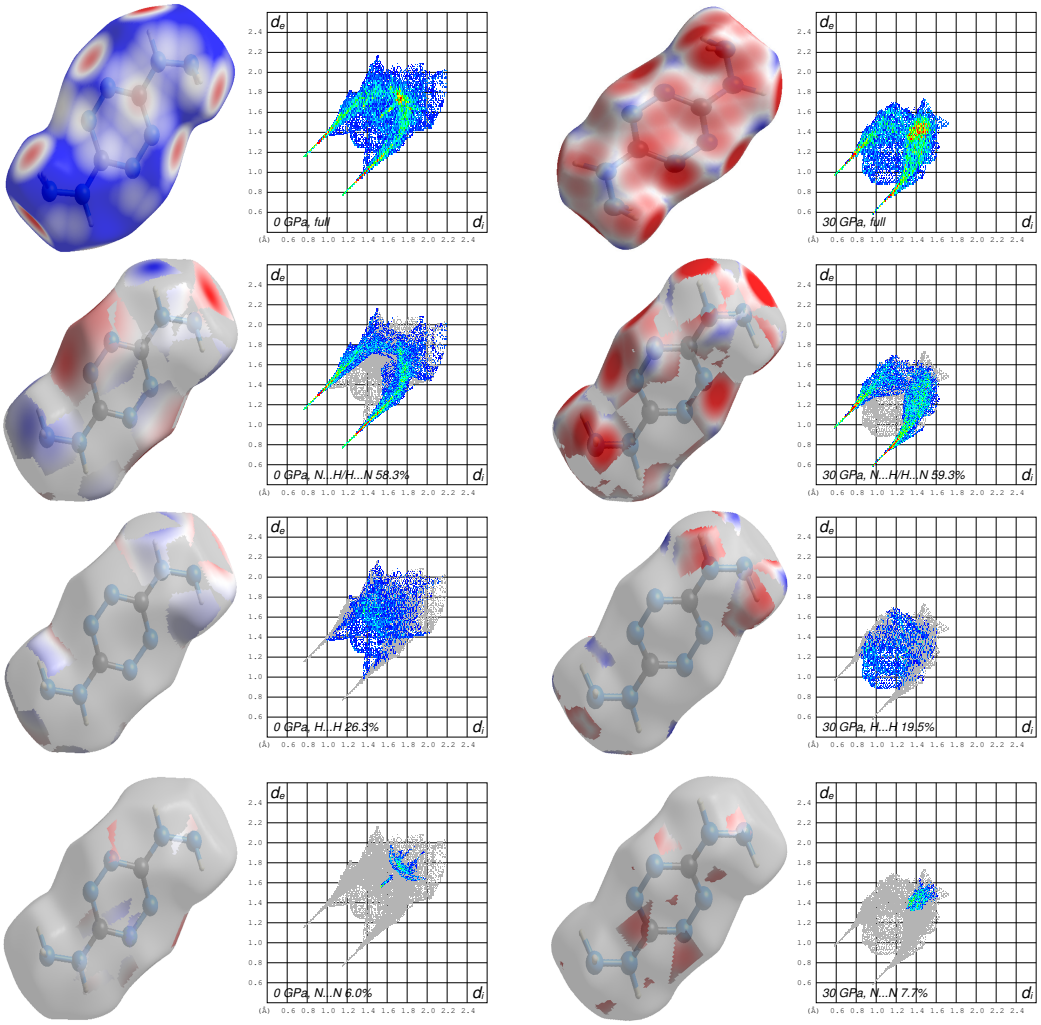

(a) (b) (c) (d)

Figure 5.8: (a and c) Hirshfeld surfaces, (b and d) 2D finger print plots of DHT crystal, showing the percentages of close intermolecular contacts contributing to the total Hirshfeld surface area at 0 GPa and 30 GPa, respectively. The graphical plots are mapped onto the Hirshfeld surfaces with d_{norm} using red (shorter intermolecular contacts), white (contacts around the vdW separation) and blue (longer intermolecular contacts) colours.

5.3.3 Hirshfeld analysis of DHT under pressure

The Hirshfeld surface analysis has made it possible to understand the behavior of intermolecular interactions that can provide direct insight into the molecular crystal. Recently, Ma et. al.[55] employed the Hirshfeld surface theory to analyze the intermolecular interactions of 10 existing impact sensitive high energetic materials (SHE) including HMX, CL-20, RDX and ONC. They observed that the low sensitive high energetic materials (LSHE) are governed by intermolecular hydrogen bonding, while covalent O...O interactions are predominant intermolecular interactions in SHE. The lack of planar big π-conjugated molecular geometric structures and intermolecular hydrogen bonding networks in SHE crystals are responsible for their low molecular stability when compared with that of LSHE. They also found that the intermolecular O...O interactions in impact sensitive high energetic materials can break more readily and thus sensitive compared to LSHE.

In order to provide a clear visualization of the molecule, the Hirshfeld surfaces were shown in transparent mode. The strong N-H...N hydrogen bonding networks between the respective acceptor and donor atoms are visualized as dark red spots on the Hirshfeld surfaces mapped over d_{norm} (see figure 5.7a) with adjacent molecules connected by N4-H4B...N2, N4-H4A...N1 and N3-H3...N4 hydrogen bonds. These observations are further confirmed by electrostatic potential (see figure 5.7b) mapped on Hirshfeld surfaces that clearly demonstrate the presence of strong negative electrostatic potential (red) surrounding the nitrogen atoms, while the electropositive (blue) region around hydrogen atoms. Further, the breakdown of fingerprint plots into specific atom types reveal that the participation of N...H/H...N contacts is about 58.3% of the total Hirshfeld surfaces and appear as a pair of distinct sharp spikes in the bottom right/left region of the 2D fingerprint plot, demonstrating the characteristics of strong hydrogen bonding. The contribution of H...H interactions are shown in the middle region of the fin-

gerprint plot with an overall 26.3% of the Hirshfeld surfaces (see figure 5.8a and b).

In general, the application of pressure can induce variations in the intermolecular interactions and will tend to bring the molecules together, enabling a denser molecular packing. As pressure increases, the red region spreads all over the Hirshfeld surfaces (see figure 5.8c and d). While, the blue region reduces and becomes almost invisible at 30 GPa, which indicates an increase in the number of closer contacts under pressure. Further, the structure of fingerprint has been compressed and drawn towards the origin due to shortening of longer intermolecular contacts, which is related to the decrease of d_e value at elevated pressures (0 GPa = 1.54 Å; 30 GPa = 1.26 Å). The red and orange points in the fingerprint plots of 30 GPa represents the closest contacts in this crystal structure. Overall, the effect of pressure decreases the contribution of H...H interactions while increases the N...H/H...N and N...N interactions to the total Hirshfeld surfaces (see figure 5.9).

5.3.4 Detonation properties of DHT

The explosive performance is strongly determined by the detonation characteristics: Higher the detonation pressure and velocity, greater will be the explosive performance. These detonation properties can be predicted using various methods through density and HOF. Foremost, the condensed phase HOF of $C_aH_bN_cO_d$ based energetic materials can be calculated by the following equation [57]:

$$\Delta_f H^\theta(c) = \Delta_f H^\theta_{EC} + 105.0\Delta_f H^\theta_{IEC} - 106.6\Delta_f H^\theta_{DEC} \tag{5.1}$$

$$\Delta_f H^\theta_{EC} = 32.33a - 39.49b + 92.41c - 63.85d \tag{5.2}$$

Where $\Delta_f H^\theta$ is the condensed phase HOF (kJ/mol); $\Delta_f H^\theta_{DEC}$ and $\Delta_f H^\theta_{IEC}$ are decreasing and increasing energy content parameters of an explosive, respectively.

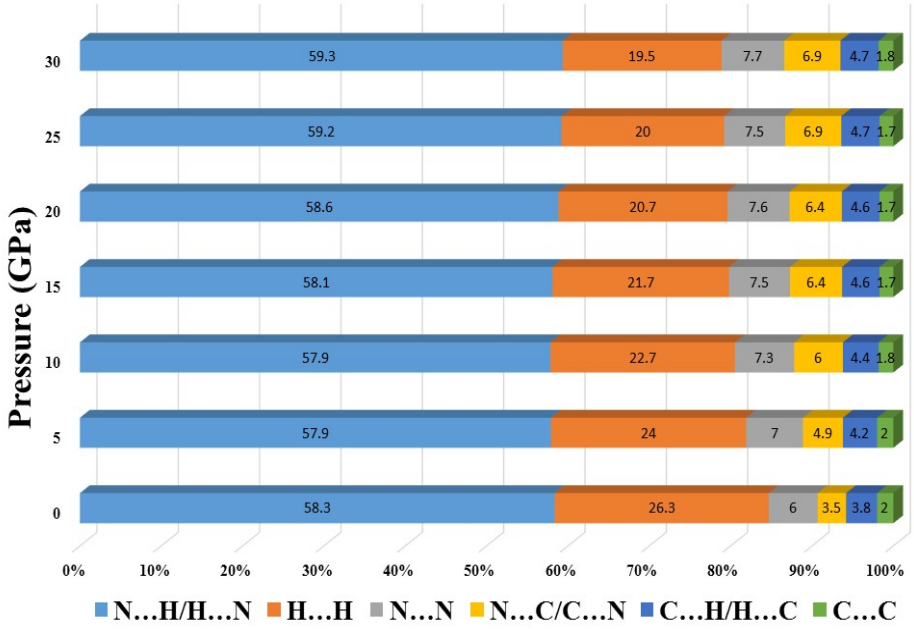

Figure 5.9: Pressure versus percentage contributions to the Hirshfeld surface area for the various intermolecular interaction of DHT crystal.

From Eqs (1) and (2), the $\Delta_f H^\theta$ value can be increased by reducing the oxygen and hydrogen number as well as by adding more number of nitrogen and carbon atoms. However, the obtained value of $\Delta_f H^\theta$ for DHT (+501.7 kJ/mol) is found to be higher than that of BNT (+336.1 kJ/mol) due to the absence of oxygen atoms in the former. Subsequently, the obtained HOF and crystal density were used to predict the detonation properties through Kamlet-Jacobs equations [58]:

$$D = 1.01(NM^{1/2}Q^{1/2})^{1/2}(1 + 1.30\rho) \tag{5.3}$$

$$P = 1.558NM^{1/2}Q^{1/2}\rho^2 \tag{5.4}$$

Where P and D are detonation pressure (GPa) and detonation velocity (km/s), respectively, which can be obtained by substituting ρ, the crystal density (g/cm^3); N, the moles of detonation gases products per gram of explosive; M, the average molecular weight of gaseous products (g/mol); and Q, the heat of detonation

Table 5.3: Calculated detonation properties of DHT were compared with the values of BNT [56].

	ρ (g/cm^3)	HOF (kJ/mol)	Q (cal/g)	D (km/s)	P (GPa)	OB (%)
DHT ($C_2H_6N_8$)	1.729	501.76 (536) [19]	1072.68	7.62 (7.54) [19]	25.19	-78.80
BNT ($C_4H_6N_10O_4$)	1.76 [56]	336.1	1165.61	7.90	27.36	-55.78

(cal/g) values according to the largest exothermic principle [59]. Further, the performance and sensitivity of an explosive can be roughly predicted by computing the oxygen balance (OB) using the formula [60]:

$$OB = \frac{-(2a + 0.5 \times b - c)}{M} \times 1600 \tag{5.5}$$

Where M represent the molecular weight; a, b and c are the number of C, H and O atoms, respectively. Typically, the higher oxygen balance leads to greater detonation velocity and pressure, and thus superior is the explosive performance [61]. At the same time, the negative OB can also be used to predict the shock sensitivity, where the explosives with zero oxygen balance are highly sensitive to shock [62]. The calculated HOF, P, Q, D and OB of DHT along with BNT are presented in Table 5.3. Moreover, the detonation properties of DHT (P = 25.19 GPa, D = 7.62 km/s) are smaller than BNT (P = 27.36 GPa, D = 7.9 km/s). This inadequacy in the explosive performance is due to a negative oxygen balance of DHT that may remarkably reduce the amount of pressure and velocity released during detonation. The negative OB also represents that DHT is less sensitive than BNT. It is worth noting that the heat of detonation (Q) for DHT is lower than that of BNT. The hydrogen bonded N-H...N intermolecular interactions which serve as stabilizing factor that reduces the heat of detonation, Q [63].

5.4 Conclusions

In summary, the structural and vibrational properties of hydrogen bonded energetic material 3,6-dihydrazino-s-tetrazine (DHT) as a function of pressure up to 30 GPa was systematically investigated using dispersion corrected DFT. The standard exchange correlation functionals (LDA/GGA) show drastic variations in the obtained ground state properties when compared with experiment values, whereas DFT-TS method provides an accurate description of the intermolecular interactions for the DHT crystal. The linear compressibility curves along the crystallographic a- and c- axes are shown to be most and least compressible, respectively. The obtained bulk modulus show that DHT is more harder than the well known energetic oxidizers Ammonium Perchlorate (AP) and Ammonium DiNitramide (ADN). The presence of strong hydrogen bonding networks in the high pressure region weakens the covalent N-H bond lengths, which is consistent with the decreasing activity of NH/NH_2 stretching vibrational modes. The 2D fingerprint plots reveal that the N...H/H...N interactions occupy the highest contribution with the proportion of 58.3% to the total Hirshfeld surfaces, indicating the importance of hydrogen bonds as a primary intermolecular interactions in DHT crystal. The calculated heat of formation (+501.7 kJ/mol) and detonation properties (P = 25.19 GPa, D = 7.62 km/s) of DHT are found to be higher and slightly smaller than the similar explosive BNT.

References

[1] H. Gao and J. M. Shreeve, Chem. Rev., **111**, 7377 (2011).

[2] U. Bemm and H. Stmark, Acta Crystallogr., Sect. C: Cryst. Struct. Commun., **54**, 1997 (1998).

[3] L. Meng, Z. Lu, Y. Ma, X. Xue, F. Nie and C. Zhang, Cryst. Growth Des., **16**, 7231 (2016).

[4] C. Ye and J. M Shreeve, J. Chem. Eng. Data, **53**, 520 (2008).

[5] Z. Su, X. Liu, Q. Yang, S. Zhang, Q. Wei, G. Xie, S. Chen and S. Gao, CrystEngComm, **16**, 4245 (2014).

[6] X. Zhang, H. Xiong, H. Yang and G. Cheng, ChemistryOpen, **6**, 447 (2017).

[7] P. Yin, L. A. Mitchell, D. A. Parrish and J. M. Shreeve, Chemistry - An Asian Journal, **12**, 378 (2017).

[8] J. Zhang, Q. Zhang, T. T. Vo, D. A. Parrish and J. M. Shreeve, J. Am. Chem. Soc., **137**, 1697 (2015).

[9] M. F. Foltz, D. L. Ornellas, P. F. Pagoria and A. R. Mitchell, J. Mater. Sci., **31**, 1893 (1996).

[10] Z. B. Zhang, C. X. Xu, X. Yin and J. G. Zhang, Dalton Trans., **45**, 19045 (2016).

[11] C. S. Choi and E. Prince, Acta Cryst., **B28**, 2857 (1972).

[12] N. Yedukondalu, D. G. Vikas and G. Vaitheeswaran, J. Chem. Phys., **145**, 064706 (2016)

[13] T. T. Yan, S. R. Li, K. Wang, X. Tan, Z. M. Jiang, K. Yang, B. B. Liu, G. T. Zou and B. Zou, J. Phys. Chem. B, **116**, 9796 (2012).

[14] C. Q. Sun, X. Zhang and W. Zheng, Chem. Sci., **3**, 1455 (2012).

[15] K. Roszak and A. Katrusiak, J. Phys. Chem. C, **121**, 778 (2017).

[16] S. Li, Q. Li, R. Li, J. Liu, K. Yang, B. Liu and B. Zou, J. Phys. Chem. C, **118**, 23443 (2014).

[17] T. Yan, K. Wang, X. Tan, J. Liu, B. Liu and B Zou, J. Phys. Chem. C, **118**, 22960 (2014).

[18] D. E. Chavez, M. A. Hiskey and R. D. Gilardi, Angew. Chem. Int. Ed., **39**, 1791 (2000).

[19] M. A. Hiskey, D. E. Chavez and D. L. Naud, Report LA-UR-01-1493, 1 (2001).

[20] V. LoPresti, *Versatile explosives, Los Alamos Res Q*, 4 (2003).

[21] X. T. Li, S. P. Pang, Y. Z. Yu and Y. Luo, J. Acta Chim. Sin., **65**, 971 (2007).

[22] D. E. Chavez and H. A. Hiskey, J. Energ. Mater., **17**, 357 (1999).

[23] D. E. Chavez and M. A. Hiskey, J. Heterocycl. Chem., **35**, 1329 (1998).

[24] J. C. Oxley, J. L. Smith and H. Chen, Thermochimica Acta, **384**, 91 (2002).

[25] S. Nurullah, Tetrahedron, **63**, 4199 (2007).

[26] P. F. Pagoria, G. S. Lee, A. R. Mitchell and R. D. Schmidt, Thermochimica Acta, **384**, 187 (2002).

[27] A. V. Sysoeva, Y. V. Moroshenkoa and D. I. Kolenoa, Procedia Chemistry, **10**, 467 (2014).

[28] V. P. Sinditskii, V. Y. Egorshev, G. F. Rudakov, A. V. Burzhava, S. A. Filatov and L. D. Sang, Thermochimica Acta, **535**, 48 (2012).

[29] M. B. Talawar, R. Sivabalan, N. Senthilkumar, G. Prabhu and S. N. Asthana, J. Harzad. Mater., **A113**, 11 (2004).

[30] M. Jaidann, S. Roy, H. A. Rachid and L. S. Lussier, J. Hazard. Mater., **176**, 165 (2010).

[31] S. Roy, M. Jaidann, S. Ringuette, L. S. Lussier and H. A. Rachid, Procedia Computer Science, **1**, 1203 (2012).

[32] L. Lu, K. Xu, H. Zhang, G. Wang, J. Huang, B. Wang and F. Zhao, Bull. Korean Chem. Soc., **33**, 2352 (2012).

[33] Y. Hu, H. X. Ma, J. F. Li, R. Gao and J. R. Song, Bull. Korean Chem. Soc., **31**, 2897 (2010).

[34] M. D. Segall, P. J. D. Lindon, M. J. Probert, C. J. Pickard, P. J. Hasnip, S. J. Clark and M. C. Payne, J. Phys: Condens. Matter, **14**, 2717 (2002).

[35] M. C. Payne, M. P. Teter, D. C. Allen, T. A. Arias and J. D. Joannopolous, Rev. Mod. Phys., **64**, 1045 (1992).

[36] J. P. Perdew, K. Burke and M. Ernzerhof, Phys. Rev. Lett., **77**, 3865 (1996).

[37] G. Kresse and J. Furthmuller, Phys. Rev. B., **54**, 11169 (1996).

[38] H. J. Monkhorst and J. Pack, Phys. Rev. B., **13**, 5188 (1976).

[39] E. F. C. Byrd and B. M. Rice, J. Phys. Chem. C, **111**, 2787 (2007).

[40] M. S. Miao, Z. A. Dreger, J. M. Winey and Y. M. Gupta, J. Phys. Chem. A, **112**, 12228 (2008).

[41] E. F. C. Byrd, G. E. Scuseria and C. F. Chabalowski, J. Phys. Chem. B, **108**, 13100 (2004).

[42] M. W. Conroy, I. I. Oleynik, S. V. Zybin and C. T. White, Phys. Rev. B, **77**, 094107 (2008).

[43] H. Liu, J. J. Zhao, J. G. Du, Z. Z. Gong, G. F. Ji and D. Q. Wei, Phys. Lett. A, **367**, 383 (2007).

[44] J. J. Zhao and H. Liu, Comput. Mater. Sci., **42**, 698 (2008).

[45] L. Qiu, H. M. Xiao, W. H. Zhu, J. J. Xiao and W. Zhu, J. Phys. Chem. B, **110**, 10651 (2006).

[46] S. Grimme, J. Comput. Chem., **27**, 1787 (2006).

[47] A. Tkatchenko and M. Scheffler, Phys. Rev. Lett., **102**, 073005 (2009).

[48] S. K. Wolff, D. J. Grimwood, J. J. McKinnon, M. J. Turner, D. Jayatilaka and M. A. Spackman, *CrystalExplorer 3.1, University of Western Australia, Australia* (2012).

[49] T. M. Klapotke, A. Preimesser and J. Stierstorfer, Z. Naturforsch, **68b**, 1310 (2013).

[50] C. R. Pulham, A. J. Davidson, I. D. H. Oswald, D. I. A. Millar, F. P. A. Fabbiani, D. J. Francis, W. G. Marshall, A. S. Cumming, D. R. Allan, A. R. Lennie and T. J. Prior, Acta Cryst., Sect. A, **63**, s44 (2007).

[51] S. M. Peiris, G. I. Pangilinan and T. P. Russell, J. Phys. Chem. A, **104**, 11188 (2000).

[52] A. F. Goncharov, M. R. Manaa, J. M. Zaug, R. H. Gee, L. E. Fried and W. B. Montgomery, Phys. Rev. Lett., **94**, 065505 (2005).

[53] J. A. Ciezak, T. A. Jenkins, Z. Liu and R. J. Hemley, J. Phys. Chem. A, **111**, 59 (2007).

[54] G. M. Borstad, I. G. Batyrev and J. A. C. Jenkins, J. Phys. Chem. A, **120**, 2712 (2016).

[55] Y. Ma, A. Zhang, X. Xue, D. Jiang, Y. Zhu and C. Zhang, Cryst. Growth Des., **14**, 6101 (2014).

[56] D. E. Chavez, M. A. Hiskey and R. D. Gilardi, Organic Letters, **6**, 2889 (2004).

[57] M. H. Keshavarz, J. Hazard. Mater., **190**, 330 (2011).

[58] M. J. Kamlet and S. T. Jacobs, J. Chem. Phys., **48**, 23 (**1968**,).

[59] G. Wang, X. Gong, Y. Liu and H. A. Xiao, Int. J. Quantum Chem., **110**, 1691 (2010).

[60] W. C. Lothrop and G. R. Handrick, Chemical Reviews, **44**, 419 (1949).

[61] Q. Wu, W. Zhu and H. A. Xiao, J. Mater. Chem. A, **2**, 13006 (2014).

[62] T. Jelena, S. Jonas and B. Svajone, J. Anal. Chem., **8**, 125 (2017).

[63] H. H. Cady, A. C. Larson, Acta Cryst., **18**, 485 (1965).

[64] R. Mayer, J. Kohler and A. Homburg, *Wiley-VCH, Weinheim, 5th ed.* (2002).

[65] T. N. Hall and J. R. Holden, *Navy Explosives Handbook, Explosion Effects and Properties – Part III, NSWC MP 88-116* (1988).

Chapter 6

Microscopic origin of pressure-induced phase-transitions in urea

In this chapter, the potential crystal structures and various properties (structural, vibrational, mechanical, electronic and optical) of urea polymorphs as a function of pressure were systematically investigated to understand the microscopic origin of pressure induced structural phase transitions. To predict accurate energy band gaps, the band structure calculations were performed using hybrid functional (Heyd, Scuseria and Ernzerhof, HSE), which includes a part of exact Fock-exchange. The geometry interpretation of intermolecular interactions were quantitatively visualized using Hirshfeld surface analysis. Overall, this chapter provides a complete picture of urea polymorphs as a function of pressure that lay the foundation for further understanding of structures and their applications.

B. Moses Abraham, B. Adivaiah and G. Vaitheeswaran, "Microscopic origin of pressure-induced phase-transitions in urea: a detailed investigation through first principles calculations", **Phys. Chem. Chem. Phys.**, **21**, 884 (2019).

6.1 Introduction

Urea (CH_4N_2O), the historical organic compound was initially synthesized in 1828 from inorganic materials by a German chemist F. Wohler [1]. Since then it is extensively investigated because of their fascinating applications in organocatalysis [5, 6], supramolecular chemistry [2–4] and triggered the development of new era in organic chemistry. The eco-friendly, non-flammable and odourless urea with 7.95 wt% of hydrogen content has a great advantage for safe hydrogen storage in transport applications [7]. Due to its high nitrogen content and quick conversion to ammonia in the soil, urea is considered as a major production of fertilizers and the starting material for manufacturing various drugs and plastics. The electric dipole moment of urea (4.56 D) is also significantly higher than the other amides and substituted ureas [10]. It consists of excellent nonlinear optical properties for second harmonic generation and sum frequency mixing in the ultraviolet region, with a nonlinear coefficient (1.4 pm/V) which is 2.5 times than that of well known ADP isomorphs [8, 9]. Urea enhances the solubility of hydrocarbons in water [11] and forms transition metal complexes [12]. In fact, urea can also be used as the basis for manufacturing improvised energetic materials. For example, urea nitrate ($(NH_2)_2COH^+ \cdot NO_3^-$), a highly powerful explosive designed through an aqueous solution of urea by adding nitric acid drop by drop [13]. Recently, a nitrogen rich energetic salt diuronium 1H,1′H-5,5′-bistetrazole-1,1′-diolate (DUBTO) was synthesized by Shang et. at. [14] through reacting urea with 1H,1′H-5,5′-bistetrazole-1,1′-diolate dihydrate. DUBTO is an insensitive energetic material with superior detonation velocity and pressure (D = 8267 m s^{-1} and P = 29.15 GPa) than that of 2-Methyl-1,3,5-trinitrobenzene, TNT (D = 6881 m s^{-1} and P = 19.50 GPa) [15].

The presence of hydrogen bonding in the crystal structure of urea also reflects its importance. Because of its facileness to fragmentation and reformation, hydrogen bonded materials can enable its directionality and reversibility to produce in-

teresting properties upon external stimuli. Especially, the application of pressure is an ideal strategy to transform crystal structure, where the geometry and bond strength may vary without any chemical adjustment. Consequently, the ability to understand the behavior of hydrogen bonding as a function of pressure leads to the design of various problems that can address the hydrogen storage in fuel cells, pharmaceutical industry, performance and sensitivity of explosives, and the attempt to stabilize polymerized materials. Thiourea ($SC(NH_2)_2$), a similar crystal structure to that of urea (O atom is replaced by S atom in thiourea) also exhibit interesting behavior under pressure. It undergoes pressure induced structural transition from phase V (orthorhombic Pbnm, Z = 4) to -VI with same space group (Z = 12) at 0.35 GPa [16, 17]. As pressure increases, three more additional phases VII, VIII and IX were identified at 1, 3, and 6.1 GPa, respectively [18]. However, these two molecules possess different chemical behavior [19]: Thiourea is found to release hydrogen sulphide to form either cyanamide or dicyandiamide (by spontaneous polymerization). While, Urea does not readily lose the water molecule, but it transforms into biuret/triuret by liberating one/two ammonia molecules per two/three urea molecules. Thus, urea lose NH_3 and thiourea release H_2S to form a chain like molecules. Two other similar structures Biurea and Biuret were also investigated extensively as a function of pressure. Biurea ($C_2H_6N_4O_2$, two urea molecules joined together via removal of two hydrogen atoms) show phase transition in the pressure range of 0.6-1.5 GPa from monoclinic C2/c structure to the proposed space group P2/n [20]. The rearrangement of N-H...O hydrogen bonds are the main driving force for this phase transition. The response of Biuret ($C_2H_5N_3O_2$, two urea molecules connected by removing one H and NH_2) to compression is also investigated by Raman spectroscopy and X-ray diffraction [21]. The vibrational modes related to N-H and C=O bonds show drastic variations in the pressure range 3-5, 8-12 and 16-20 GPa. These changes in Raman spectra are mainly related to the molecular distortions and modifications of hydrogen bonding networks. Even urea nitrate undergoes a phase transition from

monoclinic $P2_1/c$ symmetry to Pc space group around 9-15 GPa [22]. The proposed Pc phase show almost 11% smaller volume than the ambient phase due to transformation from 2D hydrogen bonded networks to 3D networks under pressure. These studies demonstrate that the application of pressure show drastic variations in hydrogen bonding networks, which play a crucial role in the structural stability of urea.

Under ambient condition, urea crystallizes in tetragonal $P\text{-}42_1m$ symmetry (Phase I) and then transforms to phase II at a temperature higher than 373 K and 0.60 GPa [23, 24]. At room temperature, the phase I transforms to orthorhombic Phase III ($P2_12_12_1$, Z = 4) above 0.48 GPa, followed by another transition to phase IV ($P2_12_12$, Z = 2) above 2.8 GPa [25, 26]. Subsequently, Phase V (Pmcn, Z = 4) is revealed using neutron-diffraction experiment at a pressure higher than 7.20 GPa [27]. Raman and x-ray scattering studies show different transition pressures: 5 GPa for III $\rightarrow$ IV and 8.0 GPa for IV $\rightarrow$ V transitions [28] and the obtained results demonstrate the co-existence of two crystal domains with discrete spectral characteristics. However, till date, neither unit cell parameters nor atomic positions of Phase II and V were reported. Gora et. al. [29] employed phenomenological approach to show a phase transition from $P\text{-}42_1m$ symmetry to space group $P2_12_12_1$ at 0.10 GPa followed by another transition at 1.20 GPa with space group $P2_12_12$. This phase transitions are in contrast with the experimental studies. Raphael et. al., [30] observed a monoclinic structure of urea ($P2_1/m$, Z = 2) at 535 GPa using self-consistent-charges density-functional tight-binding method (SCC-DFTB). The pressure induced ab-initio calculations were also performed on the ambient structure of urea using Ceperley-Alder local density correlation potential up to 10 GPa [31]. However, the accurate high pressure polymorphs of urea is under debate as shown in figure 6.1. Additionally, the electronic behavior of urea under compression remains unclear. Given aforementioned confusing experimental and theoretical results on the polymorphism of urea, our work clarifies the ambiguity regarding the high pressure phases of urea.

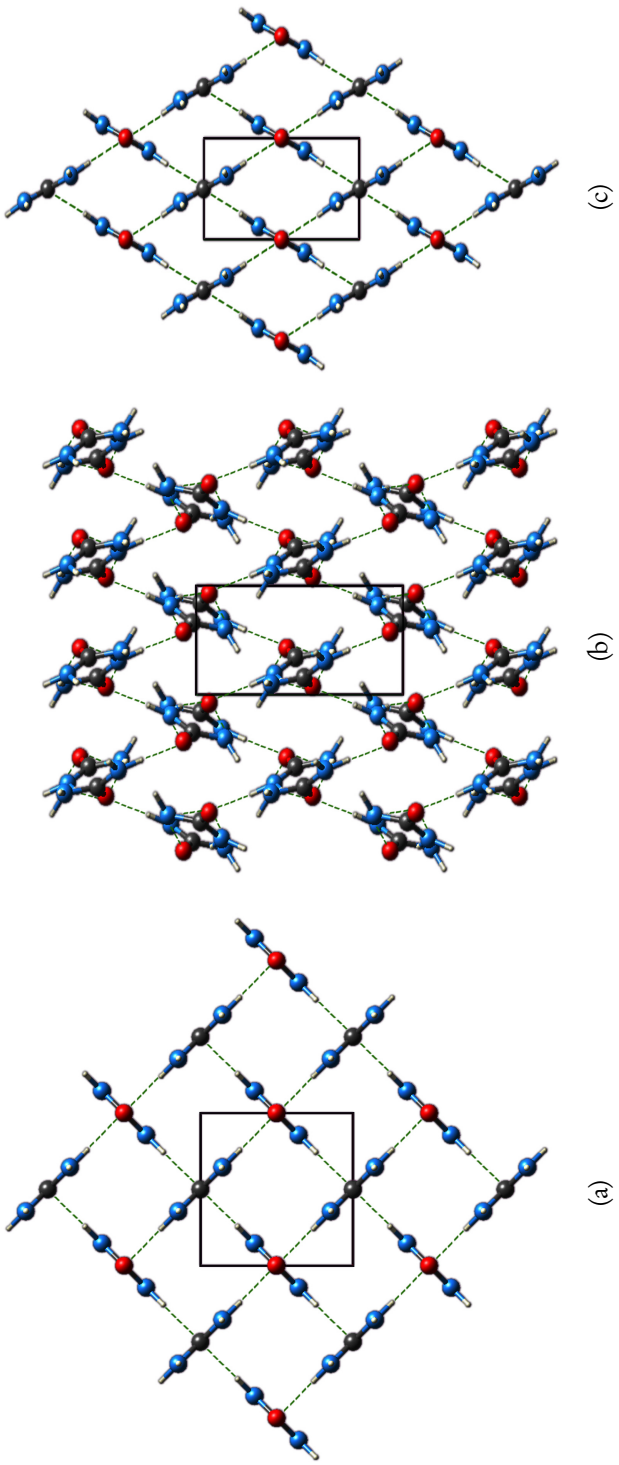

Figure 6.1: Crystal structures of urea polymorphs in (a) phase I ($P42_1m$), (b) phase III ($P2_12_12_1$), (c) phase IV ($P2_12_12$) viewed along [001] direction. Green dashed lines corresponds to hydrogen bonding. White, gray, blue and red color spheres represents H, C, N and O atoms.

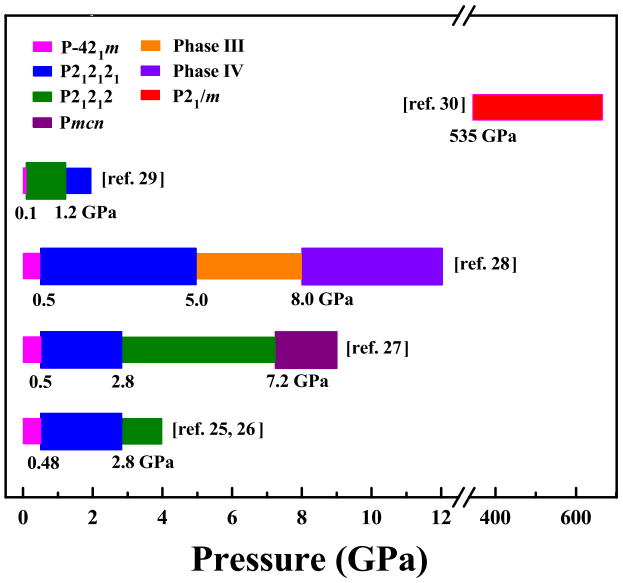

Figure 6.2: Pressure induced phase diagram of urea referred from various literatures [25–29].

6.2 Computational details

Ab-initio simulations were performed using Vienna Ab-Initio Simulation Package (VASP) [32, 33] via pseudopotential projector augmented-wave method [34]. The generalized gradient approximation (GGA) of Perdew, Burke and Ernzerhof (PBE) [35] was employed to treat the exchange-correlation functional. The kinetic energy cutoff of 470 eV is used to ensure high precision in our calculations. The Monkhorst-Pack k-point grids of $4 \times 4 \times 5, 7 \times 3 \times 3$ and $7 \times 3 \times 5$ for phase I, -III and -IV, respectively were used to discretize the Brillouin-zone integrations [36]. In relaxed equilibrium configuration, the Hellman-Feynman forces are less than 1 meV/Å. To ensure sufficient accuracy, the criteria for converging the electronic self-consistence simulations is set to be 10^{-6} eV . The band structure calculations were performed using more accurate Heyd-Scuseria-Ernzerhof (HSE) hybrid functional. It is obtained by mixing semi/local GGA/LDA exchange potential with an additional amount of non-local exact Hartree-Fock (HF) ex-

change energy. In order to avoid slowly decaying exchange interaction, Screened Coulomb potential is introduced. Thus, the exchange part is separated into Short Range (SR) and Long Range (LR) through coulomb kernel:

$$\frac{1}{r} = S_{\mu}(r) + L_{\mu}(r) = \frac{1 - erf(\mu r)}{r} + \frac{erf(\mu r)}{r} \tag{6.1}$$

Here, the range separation is defined by Screening parameter, μ. Thus, the expression for HSE screened hybrid functional is given by:

$$E_{XC}^{HSE} = \frac{1}{4}E_X^{HF,SR}(\mu) + \frac{3}{4}E_X^{PBE,SR}(\mu) + \frac{3}{4}E_X^{PBE,LR}(\mu) + E_C^{PBE} \tag{6.2}$$

where $E_X^{HF,SR}(\mu)$ is the short range HF exchange. $E_X^{PBE,SR}(\mu)$ and $E_X^{PBE,LR}(\mu)$ are the SR and LR components of the PBE exchange functional. This functional provides better numbers for semiconductors and insulators, particularly for the calculations of reliable band gaps. A more detailed description about the implementation of individual terms and parameters of HSE can be found in Refs. [37] and [38].

The vibrational and elastic properties were accomplished through CASTEP package [39] via plane wave pseudo-potential (PW-PP) method. To address the electron-ion interactions, the norm conserving [40] PW-PPs were implemented. The higher energy cut-off of 900 eV is used for the vibrational calculations. The linear response approach is considered with a q-vector grid spacing of 0.05 1/Å for the interpretation of phonon dispersion curves. Further, the intermolecular interactions were quantitatively addressed using Hirshfeld surface analysis as implemented in the software CrystalExplorer [41]. The d_{norm} values are mapped onto the Hirshfeld surface with a fixed colour scale of -0.5 (red) to 0.5 Å (blue).

6.3 Results and discussion

6.3.1 Pressure induced polymorphic phase transitions

Laborious verification was carried out to assert the reliability of the employed theoretical approach. Subsequently, the obtained lattice parameters for the three phases of urea using PBE-GGA method along with the experimental data are presented in Table 6.1. For tetragonal structure, the lattice constants a = b = 5.613 Å and c = 4.694 Å agrees well with the reference values of 5.638 Å and 4.714 Å within the errors of 0.44% and 0.42%, respectively. The crystal structures of various urea polymorphs are shown in the figure 6.2. Our calculated lattice parameters of phase III (a = 3.486 Å, b = 8.158 Å, and c = 8.635 Å) and phase IV (a = 3.531 Å, b = 7.097 Å, and c = 4.660 Å) also show good agreement with the numbers obtained from single crystal XRD data. Whereas, the calculated volume of phase I is underestimated by 1.33%, while phase III and -IV are overestimated by 0.40% and 0.94%, respectively. Overall, the average errors are less than 1% in all cases. Therefore, we accentuate that all calculations in the present work are performed without including dispersion corrections. Although appropriate treatment of dynamical correlations are important within the repulsive region of the interatomic potential, but transparently the utilization of oversimplified dispersion corrections is not an appreciable solution when pure DFT functionals produce comparably accurate values in the light of experimental data.

The pressure induced phase transition between these phases can be identified by enthalpy crossing. The lowest energy structure is considered as a stable phase and the complete profile of corresponding enthalpies as a function of pressure is shown in figure 6.3a. The tetragonal structure with $P42_1m$ symmetry is the most stable phase up to 0.66 GPa, which is further transformed to an orthorhombic $P2_12_12_1$ structure with lowest enthalpy between 0.66 to 3.09 GPa. As pressure increases above 3.09 GPa, another orthorhombic phase, $P2_12_12$, becomes the lowest enthalpy structure and remains as the most thermodynamically stable phase up

Table 6.1: Calculated high pressure crystal data of Urea Polymorphs -I, -III and -IV using PBE-GGA method is shown along with experimental values in parenthesis from Ref. [25].

Polymorph	I	III	IV
P (GPa)	0.15	2.75	2.96
CCDC [25]	1517197	1517204	1517205
C S	tetragonal	orthorhombic	orthorhombic
S G	$P42_1m$	$P2_12_12_1$	$P2_12_12$
a [Å]	5.632 (5.638)	3.486 (3.420)	3.531 (3.408)
b [Å]	5.632 (5.638)	8.158 (8.145)	7.097 (7.363)
c [Å]	4.699 (4.714)	8.635 (8.758)	4.660 (4.648)
Z	2	4	2
V [Å^3]	149.12 (149.8)	245.6 (243.9)	117.8 (116.7)
$\rho[gcm^{-3}]$	1.348 (1.331)	1.624 (1.635)	1.692 (1.710)

to the studied pressure range. Our calculated results are in good agreement with the previous experimental studies. However, one should note that the standard DFT calculations are performed at 0 K, hence the effect of temperature is not considered in this work, which can be incorporated through quasiharmonic approximation [42], for instance. Therefore, the obtained phase transition may vary slightly from the experimental observations.

The pressure (P) evolution of unit-cell volumes (V) along with the experimentally reported P-V data of urea structures were shown in the figure 6.3b. The computed unit-cell volumes of phase I is slightly lower compared to single crystal XRD data, whereas phase III and phase IV are slightly higher than the experimental values. During the transition from phase I $\rightarrow$ III, the unit-cell volume show a discontinuous jump representing a first order phase transition. This jump-wise decrease in the volume can be considered as the main driving force for the phase transition. At transition pressure, the unit-cell volume is lowered by 4.83 Å^3 at 0.66 GPa, which is underestimated by 1 Å^3 (ΔV = 5.83 Å^3 at 0.48 GPa) when compared with the single crystal data. At the same time, the carbonyl and amino groups were sightly twisted due to the distortion of N-H...O interactions, which

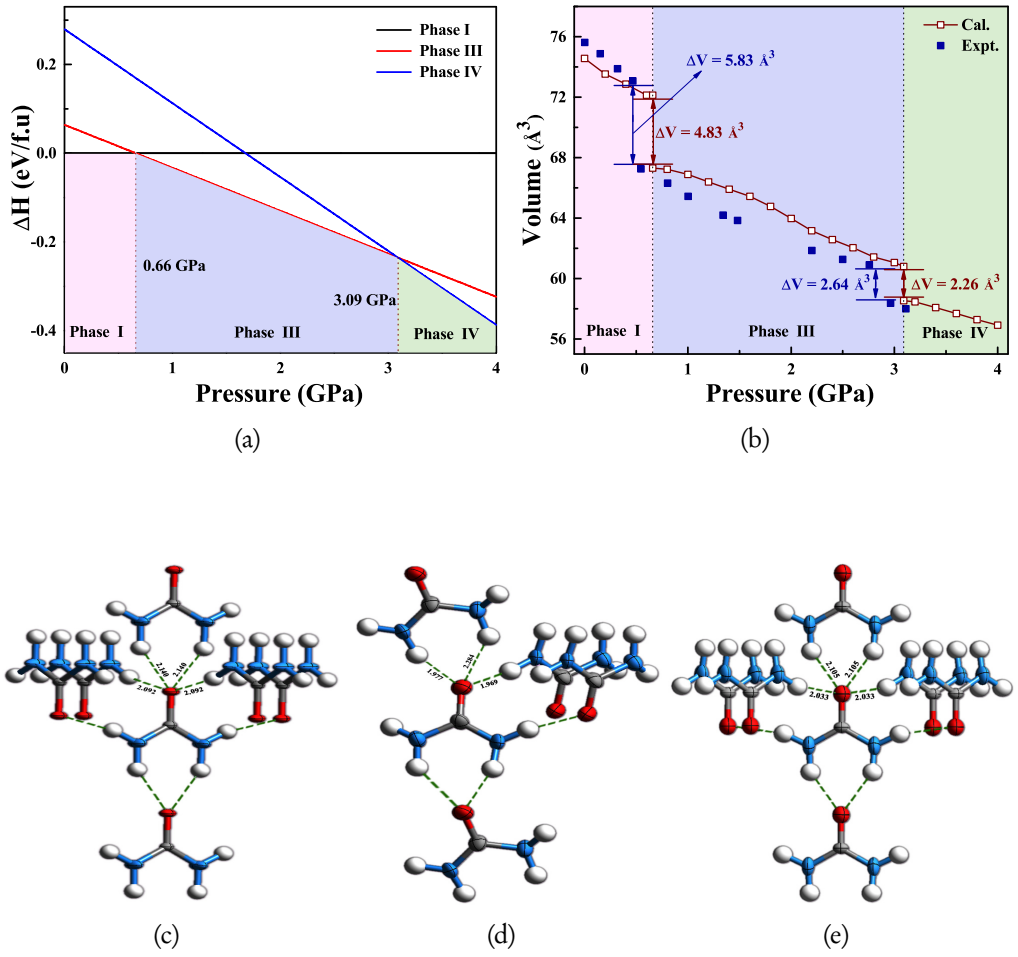

Figure 6.3: (a) Calculated enthalpies of urea polymorphs that are referenced by enthalpy of phase I as a function of pressure, (b) pressure-volume curve of urea structures showing the pressure induced phase transitions between phase I and -III and between phase III and -IV. Solid squares were taken from the ref. [25]. Intermolecular distances of (c) phase-I, (d) phase-III and (e) phase-IV of urea. The green dashed lines represents hydrogen bonding.

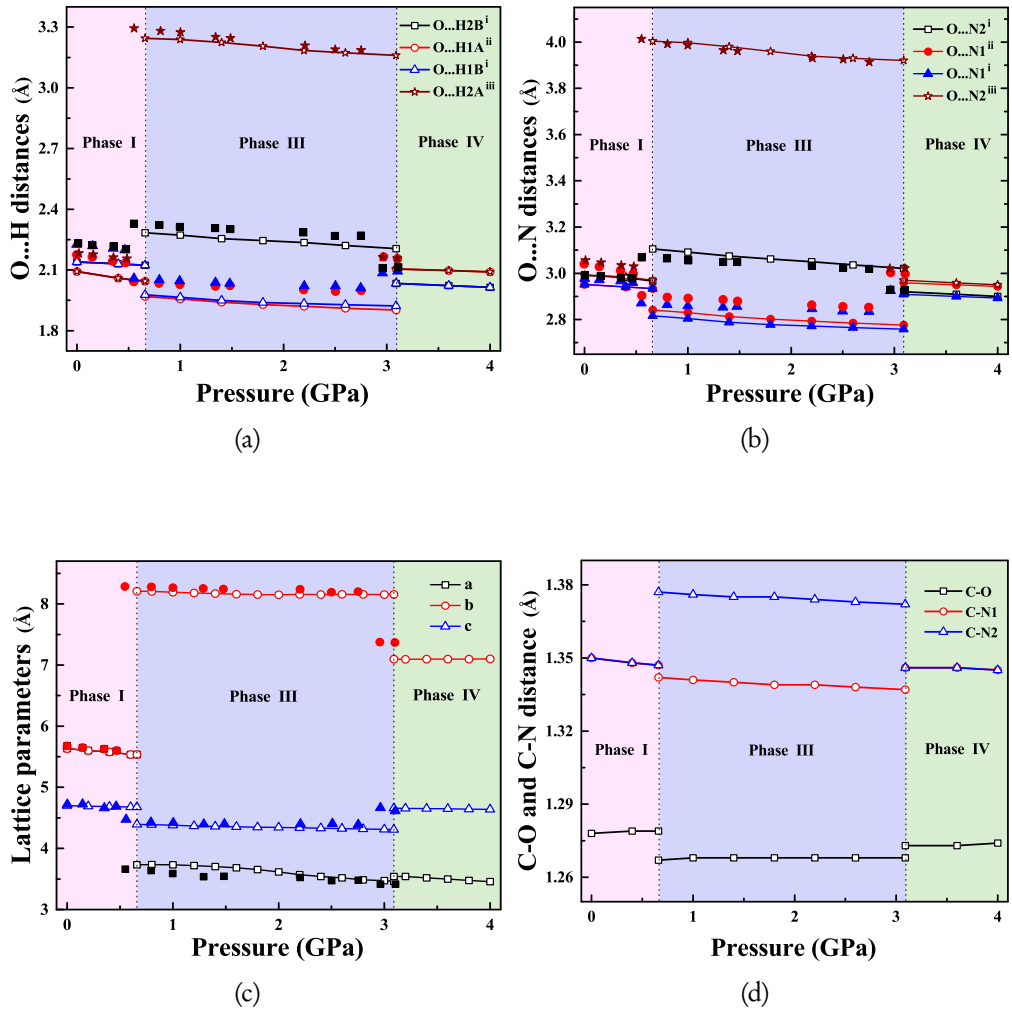

Figure 6.4: Calculated intermolecular (a) O...H and (b) O...N distances, (c) Pressure dependent unit cell parameters of urea crystal structures and (d) C-O and C-N distances. The filled symbols corresponds to the experimental values taken from ref. [25]. The vertical dotted lines represents the magnitudes of transition pressure between phases I/III and III/IV.

leads to considerable variations in the hydrogen bond pattern (see figure 6.3c-e). In phase I, Each molecule interacts with the four neighbouring molecules via each of four H-donor and H-acceptor N-H...O bonds to form four distinct hydrogen bonds. These hydrogen bonding networks look like square tunnels throughout the crystal structure. In phase III, one of the N-H...O bonds is broken and interacts with three other molecules to form three distinct hydrogen bonds. It is clearly observed that the effect of pressure in phase III has changed the directionality of hydrogen bonds. While, Phase IV is similar to phase I with four hydrogen bonds. However, if we look back into P-V plot, the unit cell volume at III $\rightarrow$ IV phase transition is lowered by 2.26 Å around 3.09 GPa. The obtained pressure induced phase transitions in the urea crystal agrees well with the ref. [25, 26]. Overall, the adoption of pressure leads to breaking and formation of N-H...O bonds in the crystal structure of urea, i.e., the H-acceptor capacitance of oxygen atom is varied between phase I/IV and phase III. The corresponding intermolecular O...H and O...N distances are shown in the figure 6.4a and b. The variations in these nearest molecular interactions are crucial in understanding its molecular and crystal stability. Since, an in-depth analysis in the geometry of urea molecules at the I $\rightarrow$ III and III $\rightarrow$ IV phase transitions were previously reported, only the effect of pressure on the bonds lengths were examined here. The computed intermolecular distances for all cases are slightly lower than the experimentally measured values. These distances in phase III show drastic variations compared to other phases. In phase I, the O...H (O...N) distances of two center bonds are shorter (longer) than the chelate H-bonds, whereas, in phase IV, these bonds show an opposite (same) trend. In phase III, one of the chelate bond distance drops drastically and the other becomes much larger. As a function of pressure, these interactions gradually decreases.

The compression behavior of lattice parameters also show a discontinuous jump at transition pressures (see figure 6.4c). This sudden discontinuity leads to contraction by 32.55% and 6.07% and expansion by 48.33% for the lattice pa-

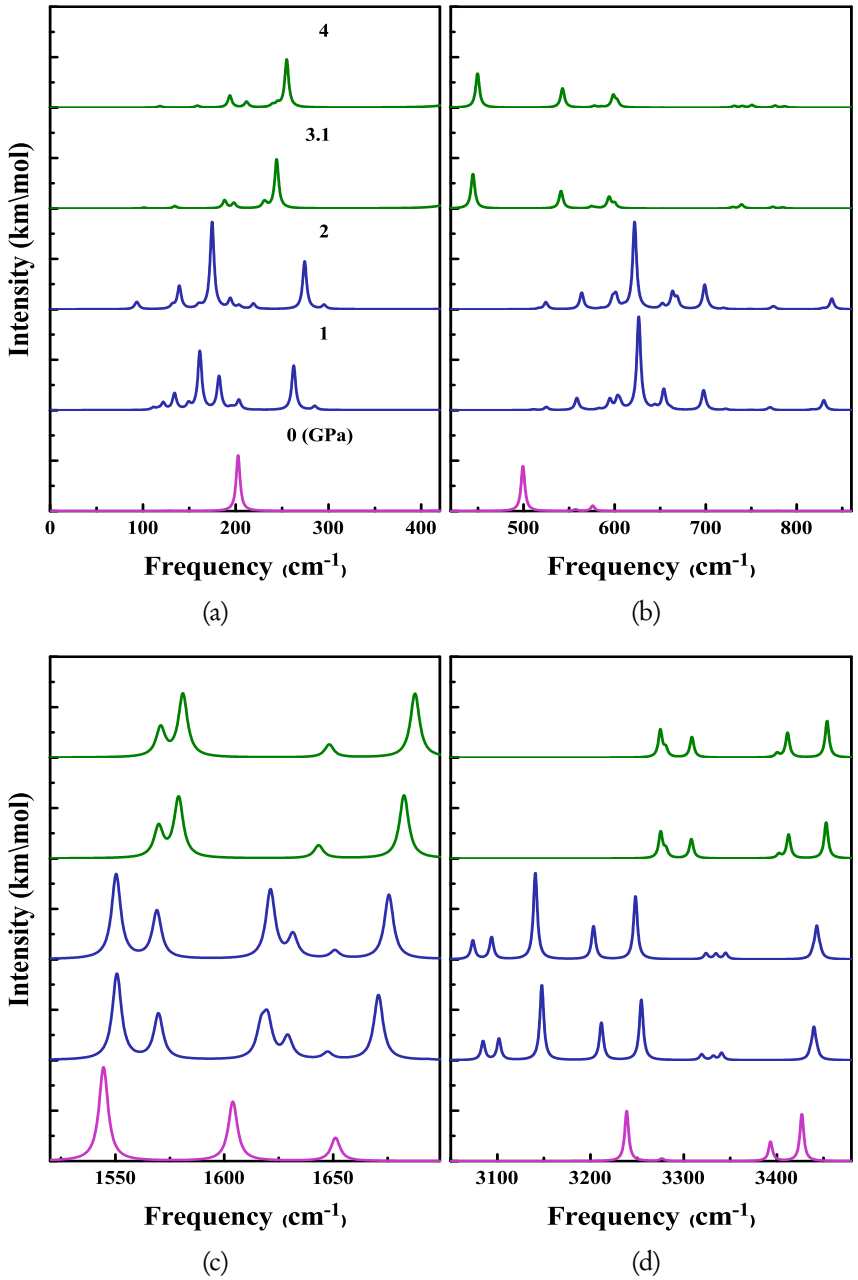

Figure 6.5: Calculated IR spectra of urea polymorphs in the frequency range (a) 0-420 cm^{-1}, (b) 420-860 cm^{-1}, (c) 1520-1699 cm^{-1}, (d) 3050-3480 cm^{-1} at selected pressures .

rameters a, c and b, respectively at 0.66 GPa. Whereas, for III to IV transition, the lattice parameters a and c expands by 2.37% and 7.96% and b contracts by 12.95 %. It is interesting to notice that the lattice parameters show opposite trend in compression behavior when two transitions are compared. Further, the intramolecular bond lengths of urea polymorphs were also investigated. As shown in figure 6.4d, the C=O and C-N bond lengths for the ambient structure are 1.278 Å and 1.350 Å, which is shorter than the normal C=O (1.28 Å) and C-N (1.47 Å) bonds, respectively. As pressure increases up to 0.66 GPa, these bond distances decrease rapidly and compress the crystal environment without any significant variation in the directionality of hydrogen bonds. After transition pressure, i.e., 0.66 GPa, the bonds become wider when compared to phase I. It is also interesting to mention that the bond length of C-N1 is systematically shorter than C-N2. This is due to the weakening of N-H...N bonds related to N2 atom. In general, for normal hydrogen bonds, the C-O/C-N distances expand as hydrogen bonds N-H...O shortens. But in all cases (expect C-O distance in phase III and C-N distance in phase IV), the lengths of C-O and C-N bonds decreases as a function of pressure.

6.3.2 Zone center IR spectra under pressure

The lattice vibration studies have become fundamental tools to explore the inherent nature of materials under ambient as well as extreme conditions. Especially, theis analysis help us to identify whether a phase transition occurs or not. From early fifties to till today, several articles were published on infrared (IR) spectrum of urea ambient structure using both experimental [43–53] and theoretical [54–66] techniques. Although a handful of work has been done on the ambient phase of urea, our vibrational analysis on high pressure phases will provide new insight into the structural changes during phase transitions. In this section, we examine the lattice dynamics of urea polymorphs by means of phonon frequencies. As mentioned earlier, the ambient tetragonal structure belong to $P42_1/m$ space group

(D2d point group symmetry) with two molecules per unit cell, which leads to 48 crystal lattice vibration modes. The corresponding irreducible representation is:

$$\Gamma_{P42_1/m} = 26\mathrm{E} \oplus 11B \oplus 11A$$

with 3 acoustic modes

$$\Gamma_{acoustic} = 2\mathrm{E} \oplus B$$

and 45 optical modes

$$\Gamma_{optical} = 24\mathrm{A} \oplus 10B \oplus 11A$$

Among 45 optical modes, there are 3 silent modes (B), 11 Raman active modes (A) and 31 infrared and Raman active modes (7B + 24E). For orthorhombic $P2_12_12_1$ structure, the obtained phonon modes are: $\Gamma_{P2_12_12_1} = 24B_1 \oplus 24B_2 \oplus 24B_3 \oplus 24A$. Here $1B_1$, $1B_2$ and $1B_3$ are acoustic modes, 24 are Raman (A) and 69 are infrared and Raman active modes ($23B_1$, $23B_2$ and $23B_3$). For $P2_12_12$ phase: $\Gamma_{P2_12_12} = 11B_1 \oplus 13B_2 \oplus 13B_3 \oplus 11A$, among these modes, 24 are Raman (A) and 69 are infrared and Raman active modes ($23B_1$, $23B_2$ and $23B_3$).

The vibrational spectra show drastic variations as a function of pressure due to molecular rearrangements in the crystal. Figure 6.5 represents the evolution of IR spectra for urea polymorphs in the frequency range 0-420, 420-860, 1520-1699, 3050-3480 cm^{-1} at selected pressures, respectively. The modes associated with low frequency region are the external vibrations, which consists of pure translational (T) and/or rotational lattice modes (RLM). Whereas, the high frequency region corresponds to the internal modes. The frequencies related to the external modes are shown in figure 6.5a. For phase I, there is only one intense peak in this region around 203 cm^{-1}, which corresponds to RLM. For phase III, we find several peaks along with the most pronounced TLM at 161 cm^{-1}. The IR spectra of phase IV also exhibit a set of broad absorption bands and the most intense peak in this region corresponds to RLM around 244 cm^{-1}. The computed optical modes as well as their vibrational assignments for Phase -I, -III and -IV, along with various experimental values [44, 48–51, 71, 81] are presented in Tables 6.2 and 6.3.

Table 6.2: Calculated infrared active modes of urea phase I (at ambient pressure) using NCP approach along with experimental data from Refs. [44, 48–51, 71, 81].

Phase-I									
Present work		Experimental data (cm^{-1})							
Mode	Frequency (cm^{-1})	Ref. [81]	Ref. [71]	Ref. [50]	Ref. [48]	Ref. [51]	Ref. [49]	Ref. [44]	Assignment
M04-M12	122-203								lattice modes
M13-M15	356-499								ωNH_2
M16	548	500							σNH_2, ωNH_2[81]
M17,M18	557,557	558	560						ρNH_2, δNCN[81], (δNCN + νCN)[71]
M19	577	575	574						σNH_2, δCO[81], δNCO[71]
M20,M21	588,646								τNH_2
M22-M24	670-750								ωNH_2 + ωCO, τNH_2[81]
M25,M26	779,779	785		770	786	790	786	788	τNH_2, ωCO[44], ωNH_2[48]
M27,M28	999,1003	1003	1005	1014	1000	1000	1000	1010	νCN + νCO, νCN [49, 81], (νCN + νCO)[71], νCN[50]
M29,M30	1069,1069				1055	1055	1050	1060	ρNH_2, ρNH_2,[49], (ωNH_2 or ρNH_2)[44]
M31,M32	1124,1165	1153	1157		1150	1155	1150	1160	ρNH_2 + νCO, ρNH_2[44, 49, 81], (ρNH_2 + νCO)[71]
M33,M34	1455,1455	1463	1467	1394	1457	1465	1464	1468	νCN, νCO[81],(νCN + δNCO + ρNH_2)[71], νCN[49, 50]
M35-M36	1476,1544	1615	1606	1605	1620	1627	1629	1625	νCO, (βNH_2 + νCO)[81], (νCO + νCN + ρNH_2)[71]
M37-M40	1604-1651	1678	1687	1734	1668	1687	1686	1680	βNH_2, (βNH_2 + νCO)[81], νCO[50], νCO[44, 49]
M41-M44	3238-3276	3352	3347	3440	3317	3265			$\nu_s NH_2$, $\nu_s NH_2$[48, 50, 71, 81]
M45-M48	3393-3427	3485	3449	3548	3404	3456			$\nu_a NH_2$, $\nu_a NH_2$[48, 50, 71, 81]

Table 6.3: Calculated infrared active modes of urea phase III (at 0.66 GPa) and phase IV (at 3.09 GPa) using NCP approach along with experimental data from Refs. [44, 48–51, 71, 81].

	Phase-III			Phase-IV			
Mode	Frequency (cm^{-1})	Assignment	Mode	Frequency (cm^{-1})	Assignment	Symbol	Description
M04-M24	98-285	lattice modes	M04-M12	105-244	lattice modes	$\nu_s NH_2$	NH_2 symmetric stretching
M25-M28	510-558	ρNH_2	M13,M14	402,428	ωNH_2	$\nu_a NH_2$	NH_2 asymmetric stretching
M29-M31	565-584	$\rho NH_2 + \rho CO$	M15-M17	541-577	ρNH_2	βNH_2	NH_2 bending
M32-M34	593-603	$\omega NH_2 + \omega CO$	M18,M19	579,594	$\rho NH_2 + \rho CO$	ρNH_2	NH_2 rocking
M35-M43	605-700	ωNH_2	M20-M23	598-739	τNH_2	ωNH_2	NH_2 wagging
M44-M48	721-771	$\omega NH_2 + \omega CO$	M24-M26	739-784	$\omega NH_2 + \omega CO$	τNH_2	NH_2 twisting
M49-M52	806-857	τNH_2	M27,M28	992,1019	$\nu CO + \nu CN$	σNH_2	NH_2 scissoring
M53-M56	983-991	$\nu CN + \nu CO$	M29,M30	1046,1089	ρNH_2	νCO	CO stretching
M57-M60	1087-1113	ρNH_2	M31,M32	1127,1143	$\rho NH_2 + \nu CO$	δCO	CO deformation
M61-M64	1186-1196	$\rho NH_2 + \nu CO$	M33-M35	1419-1532	$\beta NH_2 + \nu CN$	ρCO	CO rocking
M65-M68	1425-1466	νCN	M36-M38	1569-1627	βNH_2	ωCO	CO wagging
M69-M80	1514-1693	$\beta NH_2 + \nu CO$	M39,M40	1642-1681	$\beta NH_2 + \nu CN$	νCN	CN stretching
M81-M84	3084-3147	$\nu_s NH_2$	M41-M44	3275-3307	$\nu_s NH_2$	δNCO	NCO deformation
M85-M88	3206-3257	$\nu_a NH_2$	M45-M48	3402-3451	$\nu_a NH_2$	δNCN	NCN deformation
M89-M92	3306-3340	$\nu_s NH_2$					
M93-M96	3433-3442	$\nu_a NH_2$					

Figure 6.5c contains three major peaks in the region 1520-1700 cm^{-1}. A distinct sharp peak at 1544 cm^{-1} is assigned to both C=O stretching and NH_2 bending vibrations, while, the peaks at 1603 and 1651 cm^{-1} are associated with only NH_2 stretching modes. However, few articles [46, 67–69] demonstrate that the peak located at 1683 cm^{-1} as NH_2 symmetric vibrational motion and the peak at 1598 cm^{-1} as C-O stretching mode, whereas others [49, 70–72] assigned them in opposite order. Few simulated vibrational modes of the urea polymorphs at selected pressures are shown in figure 6.6. As mentioned earlier, our results support the former trend. Typically, the strength of the peak is based upon the number of components that are involved in a particular mode. For instance, the mode observed at 1544 cm^{-1} show marked variations during phase transition. Even though there is no much change in the peak position and intensity, but C=O stretching motion of a particular mode is found to diminish in the higher phases, which can be seen clearly from the animations. As a result, the intensity of the peak is slightly reduced in the high pressure phases compared to ambient structure. From figure 6.5d, it can be clearly seen that the modes in all cases above 3000 cm^{-1} originate from NH_2 stretching vibrations. A quick comparison of the whole spectrum reveals a separation between N-H high frequency stretching bands and the remaining vibrational modes. For ambient structure, the spectrum in this region is mainly composed of four vibrations modes: the peaks at 3238 and 3276 cm^{-1} corresponds to symmetric stretching, whereas, the other two highest frequency modes located at 3393 and 3427 cm^{-1} belong to asymmetric stretching vibrations. Most of the articles [49, 67, 68, 70, 71] reported two modes rather than four, except few [60, 65, 69]. These peaks show remarkable changes during I $\rightarrow$ III phase transition to represent the variations in hydrogen bonding networks and realignment in crystal packing. It is also noteworthy that phase III has the richest and broadest vibrational spectrum with a maximum number of peaks compared to other phases. There are two sets of absorption peaks in this region: The first half is composed of N-H symmetric (3084, 3101 and 3147 cm^{-1}) and asymmet-

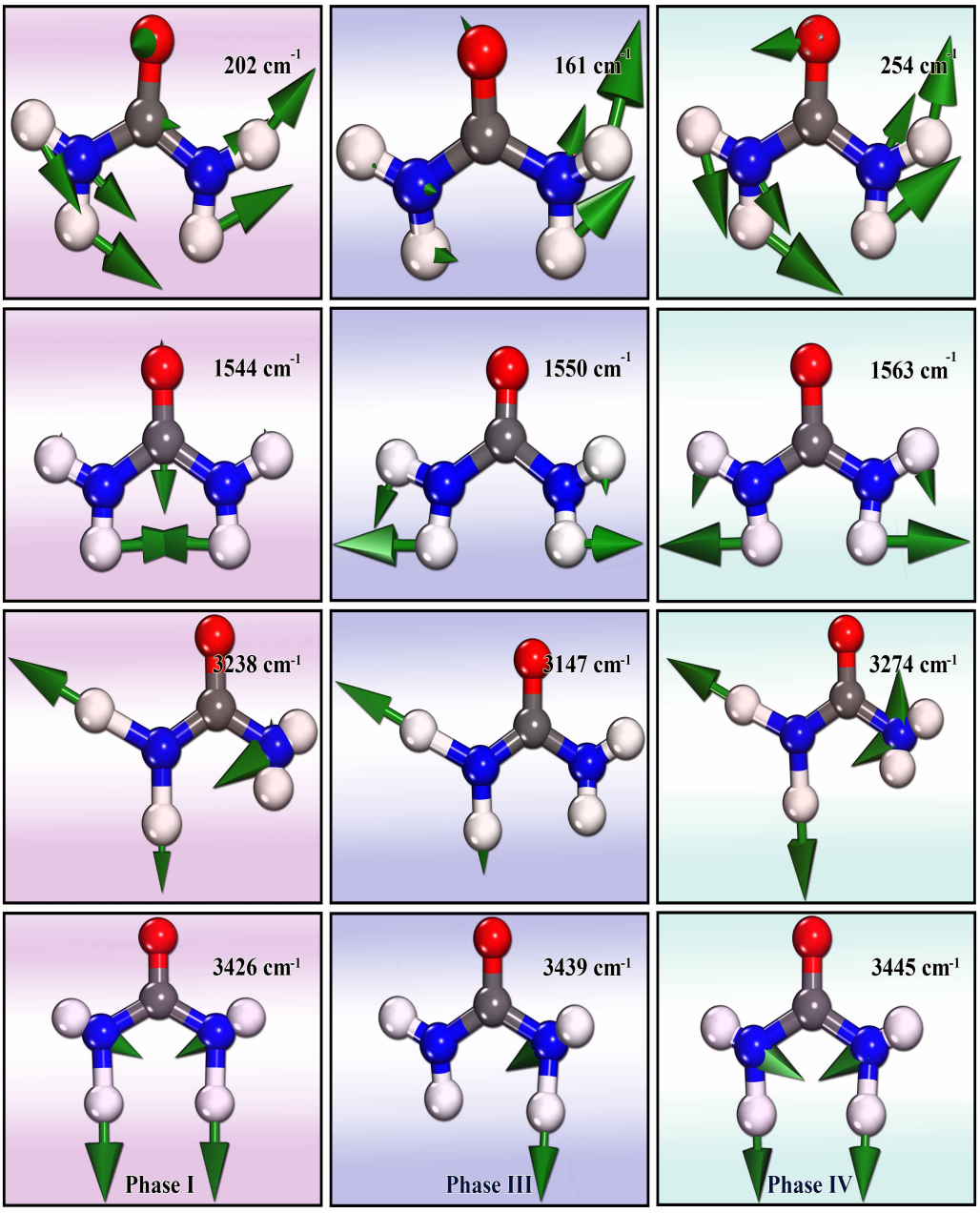

Figure 6.6: Few simulated vibrational modes of urea polymorphs at selected pressures.

ric (3211 and 3254 cm^{-1}) stretching modes. The other half contains only N-H symmetric stretching vibrations (3319, 3313 and 3340 cm^{-1}), in agreement with experimental results. For phase IV, the peaks at 3275 and 3280 cm^{-1} belong to N-H symmetric stretching modes followed by two other asymmetric stretching modes (3412 and 345 cm^{-1})

The phonon spectrum plays a crucial role in determining the dynamical stability, phase transitions and phase stability of crystalline materials. The soft phonon frequencies with imaginary modes indicate the dynamical instability of a crystal. The phonon dispersion spectrum of urea phases along high symmetry directions of the Brillouin zone at selected pressures are shown in the figure 6.7. The nonexistence of imaginary modes in the entire Brillouin zone indicates the inherent dynamical stability of urea polymorphs. Further, the low frequency modes are separated from the high frequency optical modes by a gap of 5.3, 6.6 and 5.2 THz for phase-I, -III and -IV, respectively. Additionally, in phase III, the low frequency acoustic mode show a deep dip along the high symmetry U-R direction. Clearly, the presence of soft mode along the aforementioned high symmetry direction is expected to paly a significant role under external pressure.

To illustrate the phase transition from $P42_1m \rightarrow P2_12_12_1$ and $P2_12_12_1 \rightarrow P2_12_12$ more clearly, we also calculated the phonon dispersion spectrum at transition pressures (see figure 6.8). For phase I, at transition pressure (i.e.,0.66 GPa), the acoustic mode with a steep slope along Γ-X direction is found to soften and becomes negative, which induces a high symmetry loss along Γ-X direction. The softening of phonon mode at this specific short wavelength exhibit the strongest dependence on pressure, indicating the dynamical instability and drives the pressure induced structural phase transition from $P42_1m$ to $P2_12_12_1$ structure. For phase III, the vibrational mode with a deep dip located along U-R direction becomes imaginary at transition pressure. This reflects and confirms that the $P2_12_12_1$ phase is energetically unstable and transforms to $P2_12_12$ structure. The pressure induced symmetry breaking lifts the phonon degeneracy by changing the phonon

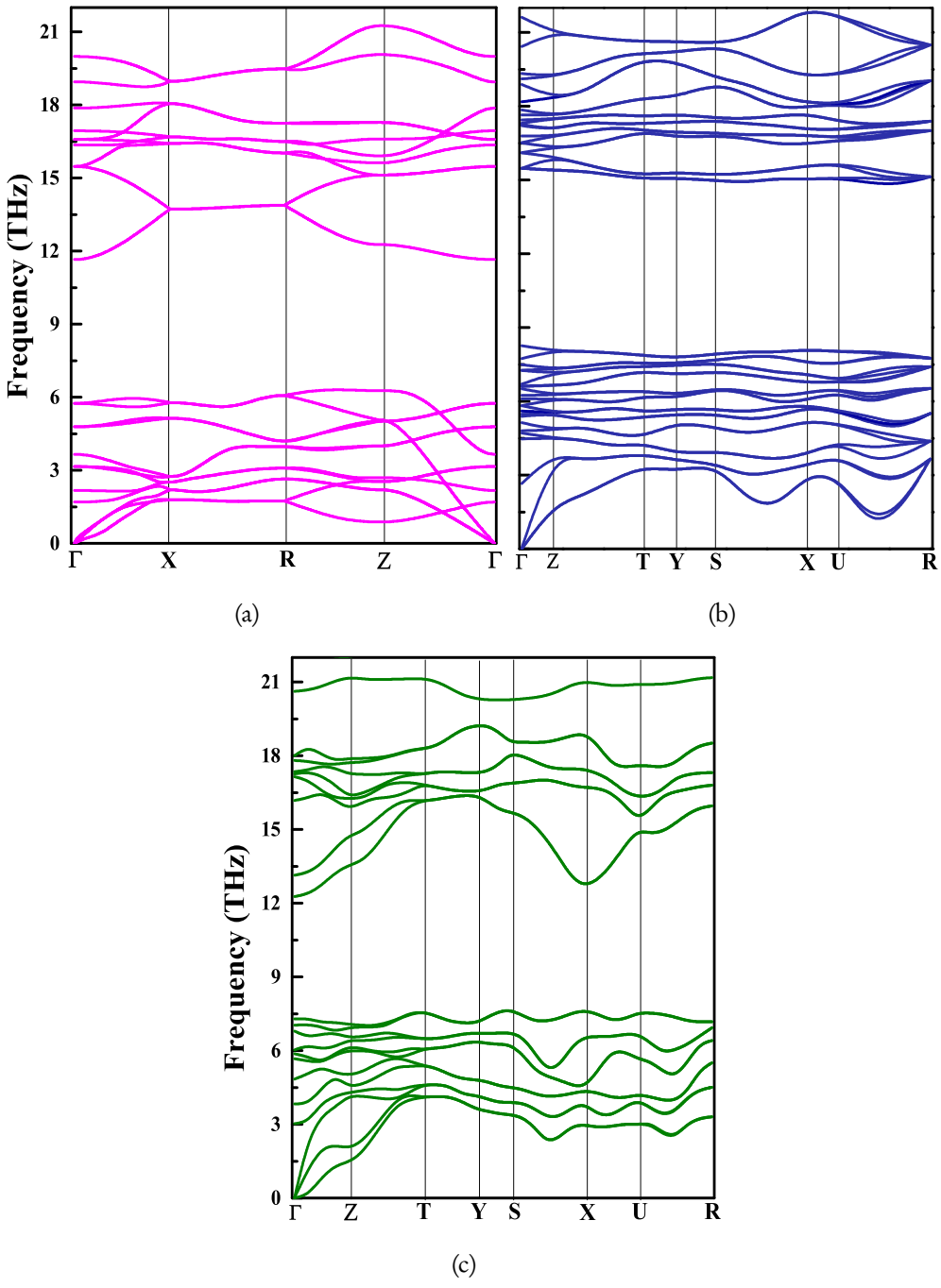

Figure 6.7: Calculated phonon dispersion spectrum for a) phase I (at 0 GPa), (b) phase III (at 0.66 GPa) and (c) phase IV (at 3.09 GPa) of urea polymorphs along the high symmetry direction of the Brillouin zone.

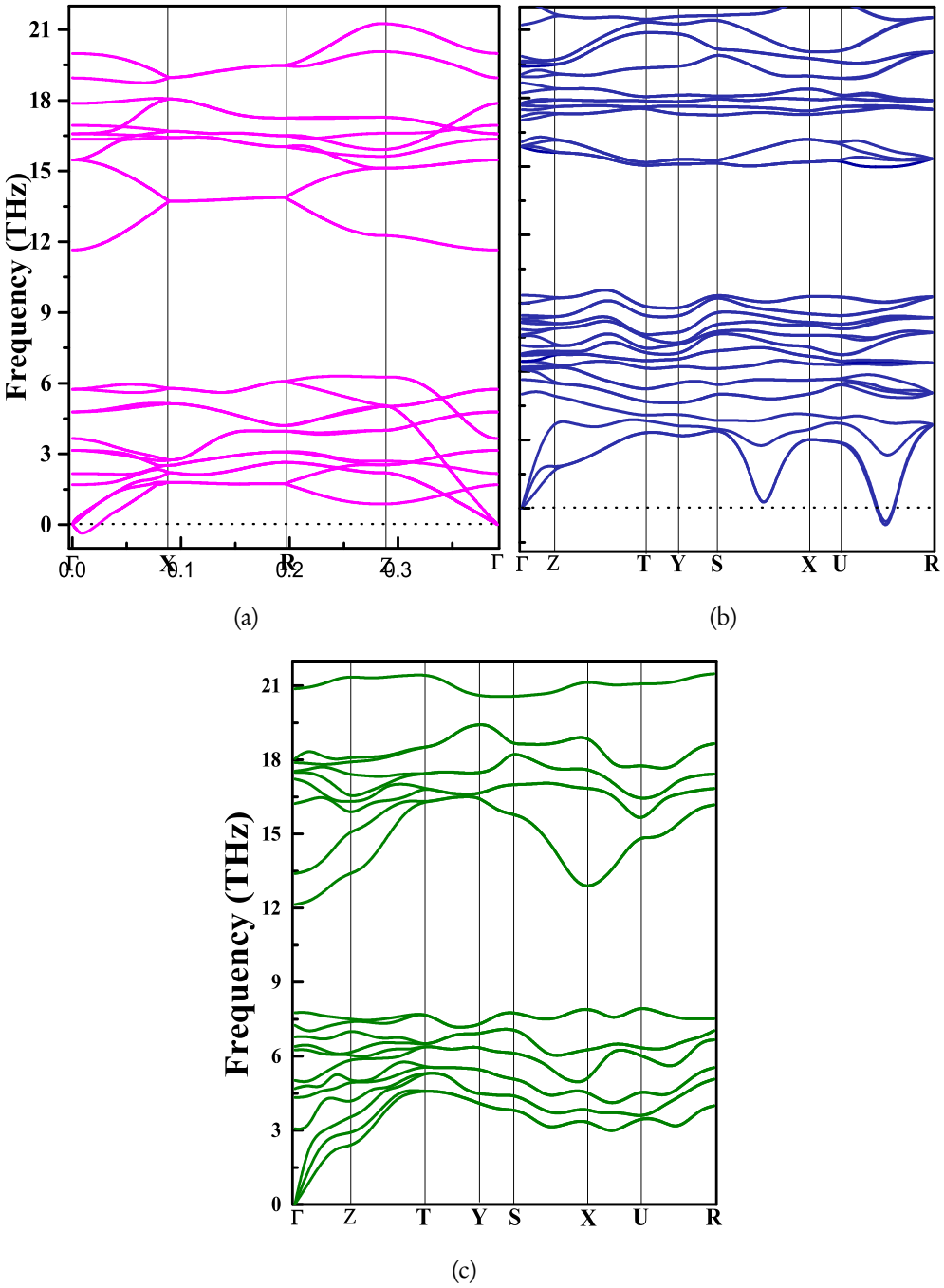

Figure 6.8: Calculated phonon dispersion spectrum for (a) phase I (at 0.66 GPa), (b) phase III (at 3.09 GPa) and (c) phase IV (at 4 GPa) of urea polymorphs.

frequencies differently for different vibrations. Overall, these results indicate that the presence of soft phonon modes are responsible for the pressure induced phase transitions among urea polymorphs.

6.3.3 Mechanical properties of urea polymorphs

The knowledge of elastic constants C_{ij} is crucial for accommodating link between dynamical and mechanical behavior of a system and provides vital information about the nature of forces operating the crystals. To determine the elastic constants, various types of deformations are chosen for different phases depending upon the space group symmetry through CASTEP code. Accordingly, there are six and nine independent elastic constants for tetragonal and orthorhombic structures, respectively. The computed elastic constants at selected pressures for the three phases of urea along with other theoretical [73] and experimental data [74–76] are presented in Table 6.4. In order to assure the mechanical stability, the system should possess a positive strain energy. This means the Born-Huang stability criteria [77] should be obeyed by the elastic constants. The general criteria for mechanical stability [78] of tetragonal systems are as follows:

$$C_{ii} > 0 \ (i = 1, 2, 3, 4, 5, 6) \quad C_{11}\text{-}C_{12} > 0 \quad C_{11} + C_{33}\text{-}2C_{13} > 0$$
$$2C_{11} + C_{33} + 2C_{12} + 4C_{13} > 0$$

The corresponding mechanical stability criterion for the orthorhombic phases is given by:

$$C_{ii} > 0 \ (i = 1, 2, 3, 4, 5, 6) \quad C_{11} + C_{22} + C_{33} + 2(C_{12} + C_{13} + C_{23}) > 0$$
$$C_{11} + C_{22}\text{-}2C_{12} > 0 \quad C_{11} + C_{33}\text{-}2C_{13} > 0 \quad C_{22} + C_{33}\text{-}2C_{33} > 0$$

The elastic constants satisfy all the above criteria at 0, 0.66 and 3.09 for phase -I, -III and -IV, respectively, indicating the mechanical stability of the studied urea polymorphs. Ab initio quantum mechanical calculations have previously been used to calculate the elastic constants of urea $P42_1m$ phase at 0 K and at room

Table 6.4: The calculated elastic constants C_{ij} (in GPa) of Urea phase -I, -III and -IV at selected pressures using PBE-GGA method along with other theoretical[73] and experimental data[74–76]

	C_{11}	C_{22}	C_{33}	C_{44}	C_{55}	C_{66}	C_{12}	C_{13}	C_{23}
0 GPa	16.4		70.7	10.1		24.5	16.1	9.0	
PBE-D3[73]0 K	16.7		73.2	9.9		22.0	17.5	10.9	
Exp.[74]298 K	23.5		51.0	6.2		0.5	-0.5	7.5	
Exp.[75]298 K	21.7		53.2	6.3		0.5	8.9	24.0	
Exp.[76]293 K	11.7		54.0	6.2		10.6	10.7	9.2	
0.66 GPa	22.6		78.6	11.3		28.5	22.4	14.0	
0.66 GPa	17.2	44.7	46.7	16.2	5.1	5.9	12.1	9.0	33.2
3.09 GPa	35.0	57.6	37.1	17.5	7.4	-3.6	20.0	20.5	61.8
3.09 GPa	39.9	76.4	109.1	32.5	4.1	25.1	31.4	18.7	44.2
4.0 GPa	48.0	84.4	130.0	37.4	5.1	30.2	34.4	20.4	47.9

temperature using -D3 corrected functionals [73]. Our calculated elastic constants show excellent agreement with their values obtained using PBE-D3 method at 0 K. These results once again confirm that the standard PBE-GGA functional for urea structure can produce appropriate values comparable to that of dispersion corrections. However, the computed elastic constants show a large deviation from the experimental data. It is quite interesting that the reported experimental C_{12} and C_{13} values differ from each other. The elastic stiffness constants C_{11} or C_{33} can be used to measure the resistance along **x-** and **z**- direction. The greater value of C_{33} (70.7 GPa) than C_{11} (16.4 GPa) indicates that the bonding strength along **z**-direction is stronger than that of the bonding in **x**- and **y**- direction. Further, the smaller value of C_{44} (10.1 GPa) than C_{66} (24.5 GPa) represents that the (010)[100] shear is more difficult than the (001)[100] shear (where (ijk) and [ijk] corresponds to symmetry plane and axis, respectively). For phase 1, at 0.66 GPa, all the lattice constants are found to increase with pressure, as shown in the Table 6.4. The constant C_{33} is largely sensitive to pressure than the other constants. For orthorhombic $P2_12_12_1$ structure, at 3.09 GPa, the elastic constants show anisotropic nature. As a function of pressure, all the elastic constants tend to increase except C_{33} and C_{66}: the constant C_{33} falls drastically to 37.1 GPa, while the value of C_{66} becomes

negative (-3.6 GPa). The softening of C_{66} demonstrates that the $P2_12_12_1$ structure is mechanically unstable against the shear deformation along the direction of the C_{66} elastic tensor. For phase IV, at 4.0 GPa, all the elastic constants increase and the C_{33} remains highly sensitive to pressure. This indicates that the $P2_12_12$ phase is mechanically stable up to the studied pressure range. To our knowledge, this is the first report of pressure dependent elastic constants for urea polymorphs.

6.3.4 Electronic structure and chemical bonding

The qualitative investigation of electronic band structure enable us to understand various properties, especially the optical behavior of a system. Since, the most dramatic failure of precise band gap prediction using common exchange - correlation functionals (eg: LDA, GGA) suppresses the inherent promising features. In order to overcome these stumbling blocks, the electronic as well as optical properties in the below section were addressed using the Heyd-Scuseria-Ernzerhof (HSE 06) hybrid functional rather than the scissors operator for pure DFT functional. The finite variations in the crystal geometries of various phases have a strong impact on the electronic band structures. In order to understand the energy band behavior of urea polymorphs, we calculated the electronic properties using hybrid functionals. The ambient phase of urea is found to be insulator with a direct band gap, i.e., the conduction band minimum (CBM) and valence band maximum (VBM) is along Γ-point, while the local maxima in other directions are slightly off the Γ-point. The Bravais lattices show that the urea polymorphs has a direct band gap at Γ of 6.21, 6.85 and 6.99 eV for phase I, phase III and phase IV (see figure 6.9), respectively. We note that phase III has a larger band gap compared to the low pressure phases. More interestingly, the band structures of phase I and IV are found to be identical due to their similar geometric structures. The HOMO-LUMO gap of urea in its liquid environment is found to be 6.75 eV [79]. Further, the highest valence band at Γ-point decreases its energy when going towards F- and Z- directions. We also notice that the two local maxima of the highest valence

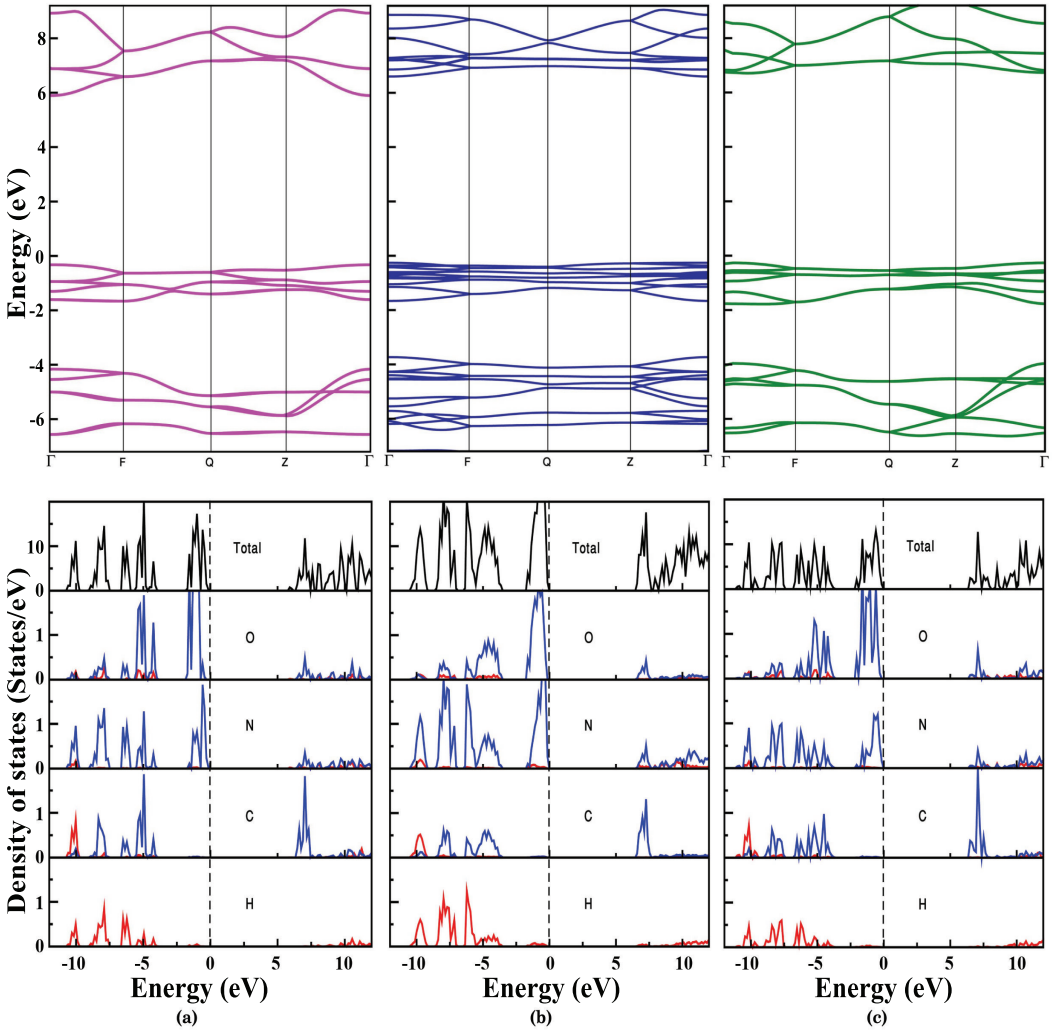

Figure 6.9: Calculated band structures and partial density of states using HSE functional for (a) phase I, (b) phase III and (c) phase IV with corresponding at 0, 0.66 and 3.09 GPa, respectively.

band along Γ-F and Γ-Z show similar energies.

In phase I and IV, the top of the valance bands are dominated by 2p states of nitrogen atoms as well as a minor contribution from the same states of oxygen atoms. When compared with phase III, the p states of oxygen atoms contribute largely to the valence states along with nitrogen atoms. Whereas, in all three cases, the bottom of the conduction bands are mainly dominated by 2p states of carbon, nitrogen and oxygen atoms. The predominant behavior of hybridization for H 1s orbital and 2p orbital of C, N and O atoms is observed in the energy region of -9 to -5 eV. In the lower end of the valence band near -10 eV, the C states possess s-character. These states are mixed with p-states of O and N as well as with s-states of H atoms.

6.3.5 Optical properties under pressure

The accurate prediction of optical spectroscopic results are very crucial to understand the nature of electronic band structure, as it is directly related to the complex dielectric function. The optical response of urea polymorphs were calculated through complex dielectric function, $\epsilon(\omega) = \epsilon_1(\omega) + i\epsilon_2(\omega)$. The real $\epsilon_1(\omega)$ and imaginary $\epsilon_2(\omega)$ parts of the dielectric function corresponds to the dispersion of incident photons and energy absorbed by the material, respectively. The dielectric functions of phase I contains two components $\epsilon_{xx}(\omega)$ and $\epsilon_{yy}(\omega)$, whereas, phase III and -IV contains three components $\epsilon_{xx}(\omega)$, $\epsilon_{yy}(\omega)$ and $\epsilon_{zz}(\omega)$, which are related to the polarization along x, y and z directions, respectively. The calculated HSE curves of dielectric function (the real $\epsilon_1(\omega)$ and imaginary $\epsilon_2(\omega)$ parts), absorption coefficient and refractive index as functions of photon energy for urea polymorphs at selected pressures are shown in the figure 6.10. In all cases, we have compared the results along x-direction and the complete profile is presented in the Table 6.4.

The electronic polarizability of a material can be analyzed thoroughly from the real part $\epsilon_1(\omega)$ of dielectric function. From first row of figure 6.10, the real

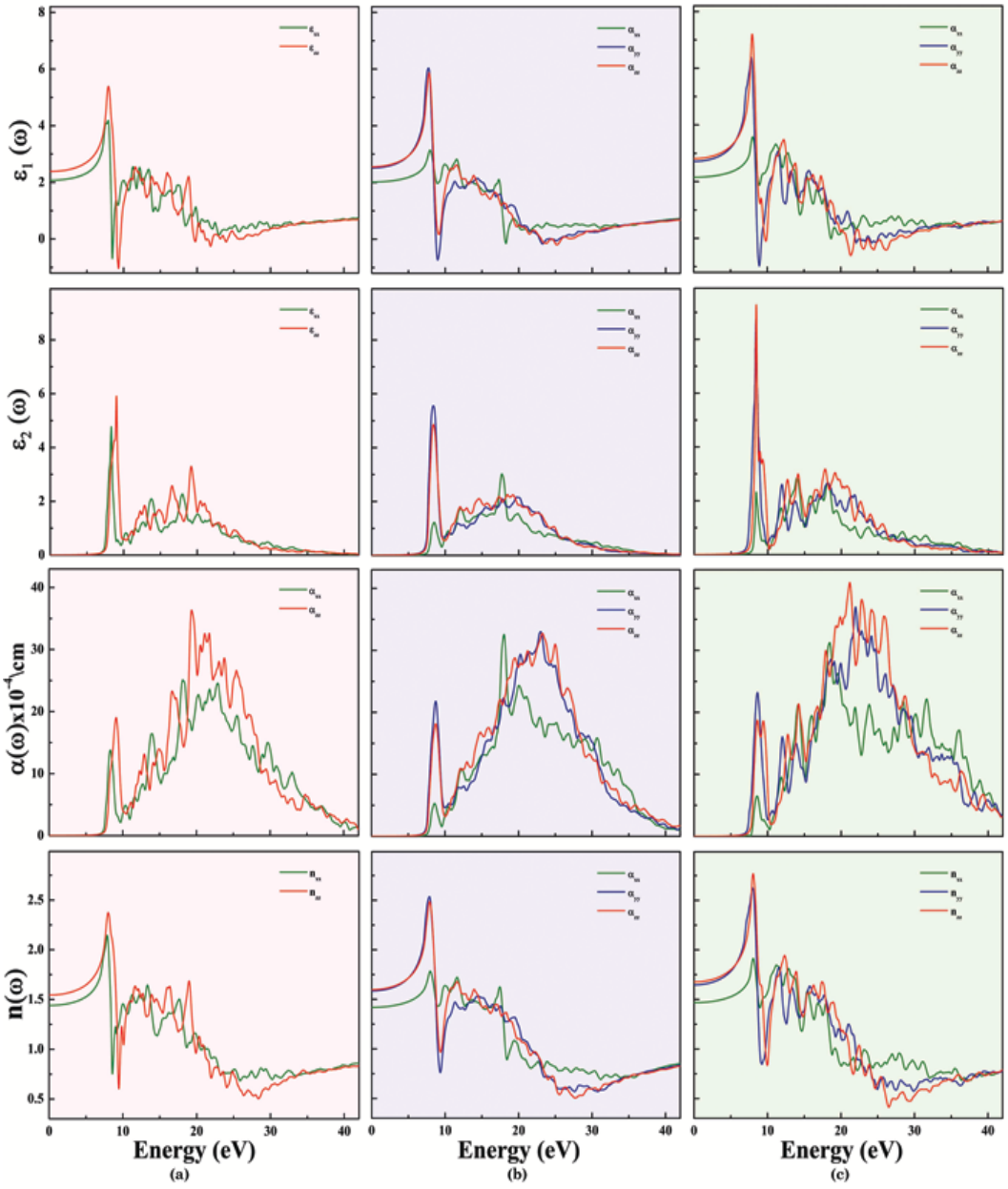

Figure 6.10: Optical spectra (dielectric functions (real ($\epsilon_1(\omega)$) and imaginary ($\epsilon_2(\omega)$) parts), absorption spectra and refractive index of urea polymorphs as a function of photon energy calculated using HSE method for (a) phase I, (b) phase III and (c) phase IV at 0, 0.66 and 3.09 GPa, respectively.

Table 6.5: The real part of dielectric function $\epsilon_1(0)$ and refractive indices n(0) computed using HSE method for phase I, -III and IV, respectively.

Polymorph	I	III	IV
$\epsilon_{1xx}(0)$	2.07	2.01	2.15
$\epsilon_{1yy}(0)$	2.07	2.51	2.71
$\epsilon_{1zz}(0)$	2.38	2.55	2.81
$n_{xx}(0)$	1.44	1.41	1.46
$n_{yy}(0)$	1.44	1.58	1.64
$n_{zz}(0)$	1.54	1.59	1.67

part $\epsilon_1(\omega)$ interacts the vertical axis at 2.07 (phase I), which represents the value of static dielectric constant and this value is nearly same for other phases (2.01 in phase III and 2.15 in phase IV) using HSE method. The pronounced peaks in the real part obtained using HSE functional are located at 7.87, 7.88 and 7.98 eV for Phase I, -III and -IV, respectively. These energy numbers belong to the ultraviolet region. However, the amplitude of the most pronounced peak in the spectrum of phase IV becomes larger compared to other phases. The real part also contains negative values around 9 eV, which indicates a complete reflection of incident photons in these regions. The $\epsilon_2(\omega)$ of dielectric function (second row of figure 6.10) represents that urea is anisotropic and the fundamental absorption edge using HSE functional is located at 6.2, 6.75 and 6.83 eV for phase I, -III and -IV, respectively, which is in good agreement with the calculated energy band gaps. This also confirms the direct optical transition between VBM and CBM along Γ-point. Typically, the materials with energy band gaps of this range absorb electromagnetic radiations in the ultraviolet (UV) region of the spectrum. The optical properties of ambient structure of urea are also derived from pure DFT functionals by S. J. Luo and co-workers, which show an underestimation in the E_g value. However, the adoption of scissor energy corrected the E_g value and produced very similar curves of real and imaginary parts of dielectric function when compared to our results.

The absorption coefficient elucidates the decay of light intensity that travels

through unit distance in a substance. The calculated absorption coefficient is zero when the energy is below 6.2, 6.75 and 6.83 eV for phase I, -III, and -IV, respectively. Subsequently, the absorption coefficient increases, which represents the occurrence of absorption at particular photon energy. The maximum absorption peaks are located at 19.30, 23.27 and 21.19 eV for phase I, -III and -IV, respectively. The strongest absorption peaks for all cases appear in the ultraviolet region. It is noteworthy that the major peaks of α_{zz} are higher than that of α_{xx} and α_{yy}, which indicates that the absorption along z-direction is greater than along the x- or y-directions. A significantly strong absorption spectrum is observed in the case of Phase IV, especially in ultraviolet ranges as compared to other phases. Refractive index n(ω) is also an important parameter with respect to optical and electronic properties. The computed HSE values of refractive index are 1.44, 1.41 and 1.46 for phase I, -III and -IV, respectively. The strong peaks in the spectrum of refractive index are due to excitonic transitions near the band gap edge. The real part of the dielectric function can also be used to obtain the value of static refractive index: $n(0) = \epsilon_1(0)^{\frac{1}{2}} = \sqrt{2.07} = 1.43$, which is similar to that obtained from phase I. Overall, these analyses of dielectric functions confirm the conclusion that the urea polymorphs will have strong absorption in the UV region of electromagnetic spectrum.

6.3.6 Hirshfeld analysis of urea polymorphs

Polymorphs with different chemical and physical properties may change the quality of products, especially in drug industry. Even the sensitivity and detonation performance of explosives may vary with the polymorphs. For example, CL-20 is a well known powerful energetic material with four polymorphic phases, among them only ϵ-CL-20 is preferred due to its high density, lower sensitivity and exceptionally high detonation performance compared to other polymorphs [80]. Therefore, a thorough investigation regarding the behavior of various polymorphic forms will guide the commercial companies to manufacture the products

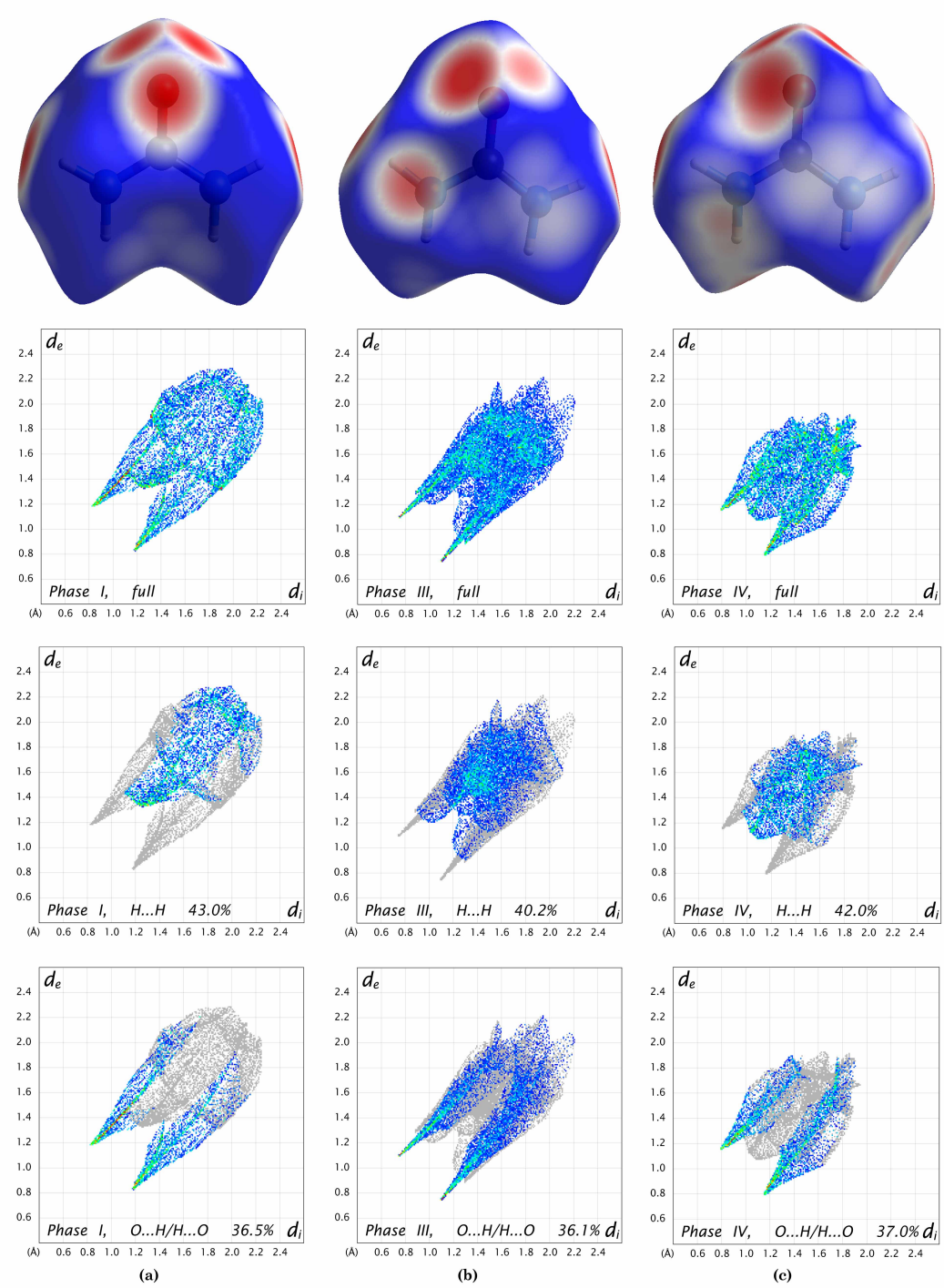

Figure 6.11: The Hirshfeld surfaces and 2D fingerprint plots of urea structure at (a) phase I, (b) phase III and phase (IV). The white color represents the contacts nearer to sum of the vdW radii, while red and blue color indicates shorter and longer contacts.

with suitable applications. In the simplest possible scenario, for any crystal structure, the Hirshfeld surfaces and the corresponding 2D fingerprint maps are different and subsequently for any polymorph, which may allow us to compare and elucidate the common features and to understand the intermolecular interactions involved within the crystal. The 3D d_{norm} surfaces were quantitatively analyzed to identify the close intermolecular contacts. The negative or positive value of d_{norm} depends on whether the intermolecular interactions are shorter or longer than the vdW radii, r^{vdW}, respectively. The influence of pressure upon the d_{norm} Hirshfeld surfaces of urea polymorphs were shown in the figure 6.11. It can be seen clearly from the Hirshfeld surfaces that the blue region reduces slowly from ambient structure to high pressure phases, which usually denotes the shortening of longer contacts. This general behavior was previously observed in various studies that the application of pressure reduces the size of voids when compared with that of ambient structure. The intermolecular O...H/H...O interactions are seen as large red circular depressions on the Hirsfeld surfaces. These vdW interactions provide a significant contribution to the tight packing arrangement of urea molecules. In all cases, the fingerprint plots belonging to signature O...H/H...O interactions are the shortest contacts with an average $d_i + d_e$ 1.9 Å and are depicted as symmetrical spikes in the bottom area. The upper (lower) spike corresponds to the hydrogen bond donor, $d_e > d_i$ (acceptor, $d_i > d_e$). However, the spikes in phase III are shorter than other phases, representing a larger hydrogen bonds. Besides, the N...H/H...N interactions are characterised by an average $d_i + d_e$ 2.3 Å, usually longer than that of the O...H/H...O interactions. The scattered points in the middle region of the fingerprint maps belong to dihydrogen bond (H...H) interaction. Further, the fingerprint of phase IV is more squashed than the other phases because of large reduction in the intermolecular contact distances.

From 2D fingerprint plots, the majority contribution to the total Hirshfeld surfaces is due to H...H interactions with a proportion of 43.0, 40.2 and 42.0% for Phase I, -III and -IV, respectively (see figure 6.12. The O...H/H...O inter-

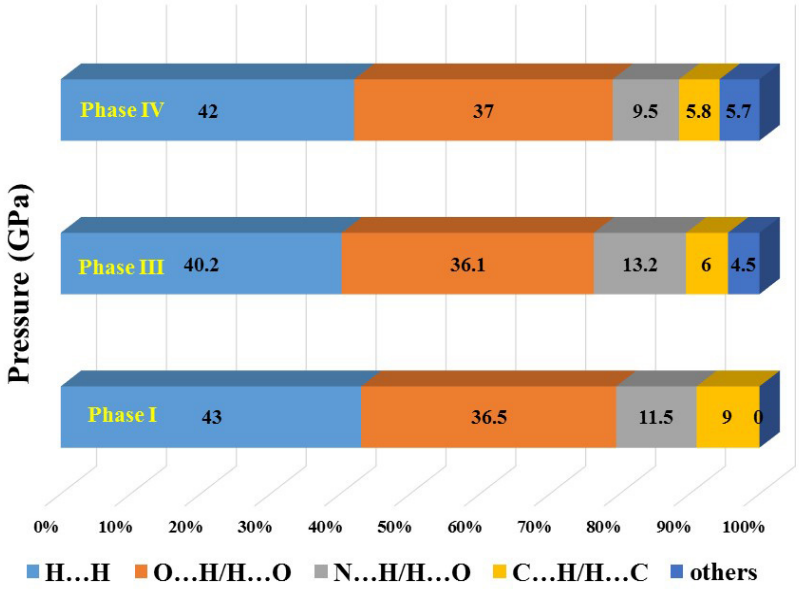

Figure 6.12: Pressure versus percentage contributions to the Hirshfeld surface area for the various intermolecular interaction of urea polymorphs.

actions make similar contribution for all the phases with an average value of 36.5%. In phase III, the minor quantitative contributions of C...N/N...C, C...C and N....N interactions are higher than other phases. In phase I, the contribution of N...H/H...N interactions are higher than phase III and -IV, the same facts occur for C...H/H...C interactions. The most striking feature in fingerprint plots are the expansion of scattered area towards higher d_i and d_e values in phase III. Typically these regions represent voids within the molecular structure and the effect of pressure would expect to decrease the size of voids towards lower d_i and d_e values. In contrast, longer contacts still exist in phase III. From figure 6.3c-e, the oxygen atoms of phase I are surrounded by hydrogen atoms to form four distinct hydrogen bonds, while at phase transition, one of the two-centre hydrogen bonds is broken and the strain is released in one of those bonds, which allow longer contacts to be observed at higher d_i and d_e values.

6.4 Conclusions

In summary, various properties (structural, vibrational, mechanical, electronic and optical) of urea polymorphs were quantitatively analyzed as a function of pressure to provide a comprehensive characterization of the nature and a detailed explanation about the pressure induced structural phase transitions of urea. A transition from $P42_1m$ type phase to an orthorhombic phase (space group $P2_12_12_1$, $Z = 4$) is identified from enthalpy calculations with a volume collapse of 4.83%, driven by softening of acoustic mode in the phonon dispersion along Γ-X direction. Another phase transition from $P2_12_12_1 \rightarrow P2_12_12$ structure is observed at 3.09 GPa. The softening of accosting mode in U-R direction along with the violation of Born stability criteria in $P2_12_12_1$ structure is responsible for the pressure induced phase transition. The corresponding volume collapses as a function of pressure are 4.83% and 2.26%, indicating the first order phase transition. Further, the influence of pressure leads to the breaking and formation of N-H...O bonds in the crystal structure of urea during phase transitions. The vibrational spectra of urea polymorphs show huge variations in transition pressures due to molecular reorientations. The variation in hydrogen bond dimensions and molecular rearrangements in urea polymorphs demonstrate the importance of directionality and angular dimensions of hydrogen bonds for polymorphism and phase transitions. The electronic band structure calculations using HSE functional show that the urea polymorphs are wide band gap insulators with a band width of 6.21, 6.85 and 6.99 eV for phase -I, -III and -IV, respectively. The analysis of dielectric functions confirm that the urea polymorphs will have strong absorption in the UV region of the electromagnetic spectrum. Hirshfeld surfaces and the corresponding 2D fingerprint plots were quantitatively analyzed to understand the variations in intermolecular interaction of urea polymorphs.

References

[1] F. Wohler, Ann. Phys., **12**, 253 (1828).

[2] P. Dydio, D. Lichosyt and J. Jurczak, Chem. Soc. Rev., **40**, 2971 (2011).

[3] J. W. Steed, Chem. Soc. Rev., **39**, 3686 (2010).

[4] R. Custelcean, Chem. Commun., **0**, 295 (2008).

[5] T. J. Auvil, A. G. Schafer and A. E. Mattson, Eur. J. Org. Chem., 2633 (2014).

[6] Z. Zhang and P. R. Schreiner, Chem. Soc. Rev., **38**, 1187 (2009).

[7] S. Satyapal, J. Petrovic, C. Read, G. Thomas and G. Ordaz, Catal. Today, **120**, 246 (2007).

[8] J. M. Halbout, S. Blit, W. Donaldson and C. L. Tang, IEEE J. Quantum Electron., **15**, 1176 (1979).

[9] S. K. Kurtz and T. T. Perry, J. Appl. Phys., **39**, 3798 (1968).

[10] W. D. Kumler and G. M. Fohlen, J. Am. Chem. soc., **64**, 1944 (1942).

[11] D. B. Wetlaufer, S. K. Malik, L. Stoller and R. I. Coffin, J. Am. Chem. Soc., **86**, 508 (1964).

[12] T. Theophanides and P. D. Harvey, Coord. Chem. Rev., **76**, 237 (1987).

[13] J. E. Worsham and W. R. Busing, Acta Crystallogr., **B25**, 572 (1969).

[14] Y. Shang, B. Jin, Q. Liu, R. Peng, Z. Guo and Q. Zhang, J. Mol. Struct., **1133**, 519 (2017).

[15] R. H. Wang, H. Y. Xu, Y. Guo, R. J. Sa and J. M. Shreeve, J. Am. Chem. Soc., **132**, 11904 (2010).

[16] H. Orihara, T. Ishidate, A. Sawada and Y. Ishibashi, J. Phys. Soc. Jpn., **51**, 1216 (1982).

[17] T. Asahi, K. Hasebe and A. Onodera, J. Phys. Soc. Jpn., **69**, 2895 (2000).

[18] A. Banerji and S. K. Deb, J. Phys. Chem. B, **111**, 10915 (2007).

[19] R. C. Haworth and F. G. Mann, J. Chem. Soc., 0, 603 (1943).

[20] T. Yan, K. Wang, X. Tan, K. Yan, B. Liu and B. Zou, J. Phys. Chem. C., **118**, 15162 (2014).

[21] G. M. Borstad and J. A. C. Jenkins, J. Phys. Chem. A, **121**, 762 (2017).

[22] S. Li, Q. Li, K. Wang, M. Zhou, X. Huang, J. Liu, K. Yang, B. Liu, T. Cui, G. Zou and B. Zou, J. Phys. Chem. C, **117**, 152 (2013).

[23] P. W. Bridgman, Am. Acad. Arts Sci., **52**, 91 (1916).

[24] P. W. Bridgman, Am. Acad. Arts Sci., **52**, 57 (1916).

[25] K. Roszak and A. Katrusiak, J. Phys. Chem. C, **121 (1)**, 778 (2017).

[26] A. Olejniczak, K. Ostrowska and A. Katrusiak, J. Phys. Chem. C, **113**, 15761 (2009).

[27] H. P. Weber, W. G. Marshall and V. Dmitriev, Acta Crystallogr., **A58**, 174 (2002).

[28] F. J. Lamelas, Z. A. Dreger and Y. M. Guta, J. Phys. Chem. B, **109**, 8206 (2005).

[29] D. Gora and K. Parlinski, J. Chem. Phys., **316**, 8138 (2000).

[30] M. Raphael, D. Arnaud and K. D. M. Harris, J. Phys. Chem. B, **111**, 3960 (2007).

[31] M. S. Miao, V. E. Van Doren, R. Keuleers, H. O. Desseyn, C. Van Alsenoy and J. L. Martins, Chem. Phys. Lett., **316**, 297 (2000).

[32] G. Kresse and J. Furthmuller, Phys. Rev. B, **54**, 11169 (1996).

[33] G. Kresse and J. Hafner, Phys. Rev. B, **48**, 13115 (1993).

[34] G. Kresse and D. Joubert, Phys. Rev. B, **59**, 1758 (1999).

[35] J. P. Perdew, K. Burke and M. Ernzerhof, Phys. Rev. Lett., **77**, 3865 (1996).

[36] H. J. Monkhorst and J. D. Pack, Phys. Rev. B, **13**, 5188 (1976).

[37] J. Heyd, G. E. Scuseria and M. Ernzerhof, J. Chem. Phys., **118**, 8207 (2003).

[38] J. Heyd and G. E. Scuseria, J. Chem. Phys, **120**, 7274 (2004).

[39] M. C. Payne, M. P. Teter, D. C. Allen, T. A. Arias and J. D. Joannopoulos, Rev. Mod. Phys., **64**, 1045 (1992).

[40] N. Troullier and J. L. Martins, Phys. Rev. B, **43**, 1993 (1991).

[41] S. K. Wolff, D. J. Grimwood, J. J. McKinnon, M. J. Turner, D. Jayatilaka and M. A. Spackman, *CrystalExplorer (Version 3.0), Uni. West. Aust.* (2012).

[42] S. Baroni, S. D. Gironcoli, A. D. Corso and P. Giannozzi, Rev. Mod. Phys., **73**, 515 (2001).

[43] W. Kutzelnigg and R. Mecke, Chem. Ber., **94**, 1706 (1961).

[44] H. J. Becher, *Chem. Ber.*, **89**, 1951 (1956).

[45] R. B. Penland, S. Mizushima, C. Curran and J. V. Quagliano, J. Am. Chem. Soc., **79(7)**, 1575 (1957).

[46] A. Yamaguchi, T. Miyazawa, T. Shimanouchi and S. Mizushima, Spectrochim. Acta., **10**, 170 (1957).

[47] A. A. V. Stuart, Rec. Trav. Chim., **75**, 906 (1956).

[48] G. B. Barlow and P. J. Corish, J. Chem. Soc., 1706 (1959).

[49] J. E. Stewart, J. Chem. Phys., **26**, 248 (1957).

[50] S. T. King, Spectrochim. Acta, Part A, **28**, 165 (1972).

[51] Z. Piasek and T. Urbanski, Organic Chemistry, **3**, 113 (1962).

[52] R. J. Meier and B. Coussens, J. Mol. Struct. (THEOCHEM), **253**, 25 (1992).

[53] K. Dziubek, M, Citroni, S. Fanetti, A. B. Cairns and R. Bini, J. Phys. Chem. C, **121**, 2380 (2017).

[54] C. V. Alsenoy, J. O. Williams and L. Schafer, J. Mol. Struct. (THEOCHEM), **76**, 179 (1981).

[55] T. K. Ha and C. Puebla, Chem. Phys., **181**, 47 (1994).

[56] S. T. Elbert and E. R. Davidson, Int. J. Quantum Chem., **8**, 857 (1974).

[57] P. D. Godfrey, R. D. Brown and A. N. Hunter, J. Mol. Struct., **405**, 413 (1997).

[58] R. J. Meier, J. R. Maple, M. J. Hwang and A. T. Hagler, J. Phys. Chem., **99(15)**, 5445 (1995).

[59] M. Koizumi, A. Tachibana and T. Yamabe, J. Mol. Struct. (THEOCHEM), **164**, 37 (1988).

[60] A. Vijay and D. N. Sathyanarayana, J. Mol. Struct., **295**, 245 (1993).

[61] F. Ramondo, L. Bencivenni, V. Rossi and R. Caminiti, J. Mol. Struct. (THEOCHEM), **277**, 185 (1992).

[62] D. A. Dixon and N. Matsuzawa, J. Phys. Chem., **98(15)**, 3967 (1994).

[63] M. Spoliti, A. Pieretti, L. Bencivenni and N. Sanna, Electron. J. Theor. Chem., **2**, 149 (1997).

[64] C. Gatti, V. R. Saunders and C. Roetti, J. Chem. Phys., **101**, 10686 (1994).

[65] B. Rousseau, R. Keuleers, H. O. Desseyn and C. V. Alsenoy, J. Phys. Chem. A, **102**, 6540 (1998).

[66] J. George, R. Wang, U. Englert and R. Dronskowski, J. Chem. Phys., **147**, 074112 (2017).

[67] I. Laulicht, S. Pinchas, E. Petreanu and D. Samuel, Spectrochim. Acta, **21**, 1487 (1965).

[68] J. Arenas and R. Parellada, J. Mol. Struct., **10**, 253 (1971).

[69] J. L. Duncan, Spectrochim. Acta A, **27**, 1197 (1971).

[70] T. Rajalakshmi, R. S. Q. Fareed, R. Dhanasekaran, P. Ramasamy, J. Thomas and K. Srinivasan, Mater. Sci. Eng. B, **39**, 111 (1996).

[71] D. Hadzi, J. Kidric, Z. V. Knezevic and B. Barlic, Spectrochim. Acta A, **32**, 693 (1976).

[72] K. Liapis, U. A. Jayasooriya, S. F. A. Kettle, J. Eckert, J. A. Goldstone and A. D. Taylor, J. Phys. Chem., **89(21)**, 4560 (1985).

[73] A. Erba, J. Maul and B. Civalleri, Chem. Commun, **52**, 1820 (2016).

[74] A. Yoshihara and E. R. Bernstein, J. Chem. Phys., **77**, 5319 (1982).

[75] G. Fischer and A. Zarembowitch, C. R. Seances Acad. Sci., Ser. B, **270**, 852 (1970).

[76] S. Haussuhl, Z. Kristallogr., **216**, 339 (2001).

[77] M. Born and K. Huang, *Clarendon Press* (1954).

[78] Nye, J. F, *Oxford University Press, Oxford* (1985).

[79] M. F. Tesch, R. Golnak, F. Ehrhard, D. Schon, J. Xiao, K. Atak, A. Bande and E. F. Aziz, Chem. Eur. J., **22**, 12040 (2016).

[80] M. Ghosh, S. Banerjee, M. A. S. Khan, N. Sikdera and A. K. Sikder, Phys. Chem. Chem. Phys., **18**, 23554 (2016).

[81] Y. Saito, K. Machida and T. Uno, Spectrochim. Acta, Part A, **27**, 991 (1971).

Chapter 7

Summary & Future scope

The science of energetic materials face tremendous challenges in predicting the precise correlation between performance and sensitivity characteristics with high fidelity. As the more chemical energy stored in the molecules should largely weaken the chemical bonds, leading to lower molecular stability and an enhanced sensitivity. Numerous attempts have been made to obtain fine balance between energy and safety for various kinds of energetic materials. This thesis mainly focused on how the non-covalent interactions, especially hydrogen bonding influence the macroscopic properties to enhance the energetic performance with reasonable sensitivity. Also, the effect of hydrostatic pressure was systematically investigated to understand the remarkable variations in the intermolecular interactions for the construction of high energy density materials. Various physicochemical and detonation properties for several energetic materials at ambient as well as at high pressures have been studied using DFT-based *ab initio* calculations. The specific conclusions drawn for each of these energetic materials were already described at the end of the corresponding chapter. Therefore, it is now time to summarise the crucial outcomes of the entire thesis and open up with new ideas and future scope, leading to further exploration of hydrogen bonded energetic materials.

7.1 Summary

A series of energetic ionic salts namely, ABTOX, DMA-BTO, DU-BTO, HA-BTO, M_2BTO and TKX-50 were thoroughly investigated to understand the structure -property-performance interrelationship. The strong intermolecular hydro-

gen bonding environment between various cations and the BTO^{2-} anion are mainly responsible for the enhanced molecular stability and prominent detonation performance. The detonation characteristics demonstrate these energetic salts as potential explosive candidates, especially, HA-BTO and TKX-50 provide superior detonation velocities (9.94 and 9.91 km/s) and detonation pressure (38.85 and 40.23 GPa) owing to their high positive HOFs and densities. Our results highlight the importance of hydrogen bonding interactions in designing energetic salts for next-generation explosives, propellants, and pyrotechnics. As a continuation for the search of precise correlation between performance and sensitivity of high energy density materials, a similar energetic ionic salts are chosen based on 3,3 -dinitro-5,5 -bis-1,2,4-triazole-1,1 -diolate anion with ammonium (DA-DNBTO) and hydrazinium (DH-DNBTO) cations. The geometry optimization highlights the significance of van der Waals correction when studying the structure and properties of EIS, and highlights the importance of DFT-D2 method proposed by Grimme in reproducing the experimental crystal structures of energetic salts. Especially, the electronic band gap of DNBTO salts obtained using the HSE06 hybrid functional are reduced to 50% when compared with that of BTO based energetic salts due to NO_2 group attached to the DNBTO anion. The Hirshfeld surface analysis reveal the presence of strong intermolecular interactions in DA-DNBTO, representing its inferiority in molecular stability and also explains why it has highest stability compared to DH-DNBTO. Besides, we find that the O...O contacts that generally exist in most of the energetic materials do not show much impact in both the studied energetic salts. Therefore, by combining the analyses of BTO and DNBTO materials, we confirmed that the energetic ionic salts are indeed an effective way to enhance the performance with reasonable sensitivity due to the presence of improved intermolecular hydrogen bonding among the existing energetic molecules.

The pressure dependent structural changes, IR spectra and the Hirshfeld surfaces of 3,6-dihydrazino-s-tetrazine (DHT) were investigated to understand the importance of hydrogen bonding interactions. The intermolecular interactions in DHT crystal lead to a more compact and stable structure that can increase the density but diminishes the heat of detonation, Q. The obtained bulk modulus

show that DHT is more harder than the well known energetic oxidizers Ammonium Perchlorate (AP) and Ammonium DiNitramide (ADN). The presence of strong hydrogen bonding networks in the high pressure region weakens the covalent N-H bond lengths, which is consistent with the decreasing activity of NH/NH_2 stretching vibrational modes. Overall, the crystallographic and spectroscopic results along with Hirshfeld surface analysis as a function of pressure reveal the presence of strong hydrogen bonding networks in the crystal structure of DHT. The long standing ambiguity in the high pressure phases of urea has been resolved with convincing conclusions through enthalpy-pressure behavior as well as mechanical and dynamical stabilities. The enthalpy-pressure behavior show that urea undergoes pressure induced structural phase transition from $P42_1m$ (phase I) $\rightarrow$ $P2_12_12_1$ (phase III) at 0.66 GPa with a volume collapse of 4.83%, driven by softening of acoustic mode along Γ-X direction. Another phase transition from $P2_12_12_1 \rightarrow P2_12_12$ structure is identified at 3.09 GPa. The softening of acoustic mode in U-R direction along with the violation of Born stability criteria in $P2_12_12_1$ structure is responsible for the pressure induced phase transition. Further, the adoption of pressure leads to breaking and formation of N-H...O bonds in the crystal structure of urea during phase transition, i.e., the H-acceptor capacitance of oxygen atom is varied between phase I/IV and -III. The analysis of dielectric functions confirm that the urea polymorphs will have strong absorption in the UV region of electromagnetic spectrum. Our results provide a complete picture on various properties of urea polymorphs that lay the foundation for further understanding of structures and their applications.

To put an end to this thesis, it should be remarked that the presence of strong intermolecular interactions, especially hydrogen bonding can have a tremendous capability to tune the performance and stability of energetic materials. Through this study, one can design crystal structure of explosive molecules with desirable properties, such as minimized impact sensitivity and enhanced detonation performance.

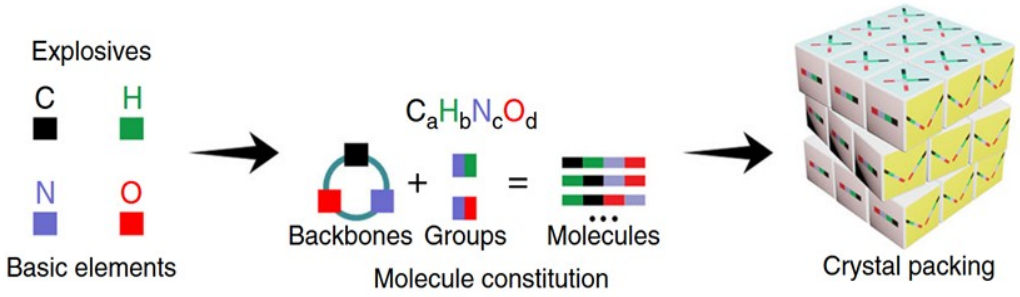

Figure 7.1: Illustration of various crystal packing structures for organic explosives formed by the self-assembly of extensive intermolecular interactions - Taken from Ref. [1].

7.2 Future scope

The results presented in the thesis represent a step towards understanding the challenges in predicting the precise correlation between performance and sensitivity characteristics through structure-property-performance interrelationship. For developing revolutionary advances in the next-generation high energy density materials, further studies should focus on the combination of chemistry, crystallography and physics to prepare high-level energy sources. Generally, most of the energetic materials are composed of four basic elements, namely carbon, hydrogen, nitrogen and oxygen. The permutation and combination of these elements decide the original molecular constitution. For a given molecular constitution, various molecules of high energy density materials can be developed by rational combination of molecular backbones and functional groups. As discussed in section 1, the energy-safety contradiction can largely be alleviated at the higher level of crystal, i.e., to facilitate reduced sensitivity by improving crystal packing. In the simplest possible scenario, one can design molecules with various crystal packing structure by the self-assembly of extensive intermolecular interactions (e.g., $\pi - \pi$ stacking and hydrogen bonds). Moreover, the energetic materials with a packing structure of ready shear sliding facilitate low impact sensitivity, in combination with a high molecular stability. Therefore, the basic element constitution, molecular structure, and crystal packing manners (see figure 7.1) together determine the mechanical sensitivities and energetic performance of high energy

density materials.

References

[1] Y. Wang, Y. Liu, S. Song, Z. Yang, X. Qi, K. Wang, Y. Liu, Q. Zhang and Y. Tian, Nat. Commun., **9, 2444 (2018)**

List of Publications

Publications included in the thesis

[1] **B. Moses Abraham** and G. Vaitheeswaran, "From van der Waals Interactions to Structures and Properties of 3,3′-Dinitro-5,5′-Bis-1,2,4-Triazole-1,1′-Diolate Based Energetic Materials" *Mat. Chem. Phys.*, **240**, 122175 (2020).

[2] **B. Moses Abraham**, B. Adivaiah and G. Vaitheeswaran, "Microscopic origin of pressure-induced phase-transitions in urea: a detailed investigation through first principles calculations", *Phys. Chem. Chem. Phys.*, **21**, 884 (2019).

[3] **B. Moses Abraham**, Vikas D. Ghule and G. Vaitheeswaran, "A comparative study of the structure, stability and energetic performance of 5,5′-bitetrazole-1,1′-diolate based energetic ionic salts: future high energy density materials", *Phys. Chem. Chem. Phys.*, **20**, 29693 (2018).

[4] **B. Moses Abraham**, J. Prathap Kumar and G. Vaitheeswaran, "High pressure studies of hydrogen bonded energetic material 3,6-dihydrazino-s-tetrazine using DFT", *ACS Omega*, **3(8)**, 9388 (2018).

Publications not included in the thesis

[1] **B. Moses Abraham** and G. Vaitheeswaran, "First Principles study of pressure induced polymorphic phase transition in trimethylamine", *AIP Conf. Proc.*, **1942**, 030006 (2018).

[2] **B. Moses Abraham** and G. Vaitheeswaran, "Structural and electronic properties of 5,5′-hydrazinebistetrazole under high pressure: A DFT study", *IOP Conf. Ser.: Mater. Sci. Eng.*, **377**, 012107 (2018).

[3] **B. Moses Abraham**, N. Yedukondalu and G. Vaitheeswaran, "Structural, electronic and lattice dynamical properties of perovskite $CaZrO_3$ under high pressure", *AIP Conf. Proc.*, **1832**, 090042 (2017).

[4] G. Vaitheeswaran, N. Yedukondalu and **B. Moses Abraham**, "Structural, vibrational and bonding properties of hydronitrogen solids under high pressure: an abinitio study", *J. Chem. Sci.*, **128**, 1631 (2016).

[5] **B. Moses Abraham**and G. Vaitheeswaran, "Electronic properties and Hirshfeld surface analysis of Dihydroxylammonium 5,5-bistetrazole-1,1-diolate under pressure", *Materials Today: Proceedings* (accepted).

[6] **B. Moses Abraham** and G. Vaitheeswaran, "An innovative explosive detection designed from a sensitive g-C_3N_4 nanostructure: insights from DFT computations", *Submitted to journal*.

[7] **B. Moses Abraham**, N Yeduondalu and G. Vaitheeswaran, "High pressure structural and electronic properties of potassium based green primary explosives", *Submitted to journal*.

Scientific Activities

Oral presentations

- Structure-properties-performance interrelationship of energetic ionic salts: A comparative study,
  at "Dr. K.V. RAO's 19th Annual Research Award", Hyderabad, March (2019)

- An innovative explosive detection designed from a sensitive g-C_3N_4 nanostructure: Insights from DFT computations,
  "5th International Conference on Nanoscience and Nanotechnology (ICONN 2019)", SRM Institute of Science and Technology, Kottankulathur, January (2019)

- Structural and electronic properties of 5,5′-hydrazinebistetrazole under high pressure: A DFT study,
  "1st International Conference on Mechanical, Materials and Renewable Energy", Organized by Sikkim Manipal Institute of Technology, Sikkim, December (2017)

- Structural and vibrational behavior of 3,6-dihydrazino-s-tetrazine under pressure,
  "International Conference on Electronics, Physics and Chemistry", Jyothi Nivas College, Bangalore, February (2017)

Poster presentations

❖ Structure-property-performance interrelationship of 5,5′-bitetrazole-1,1′-diolate based energetic ionic salts: A comparative study,
"International Conference on Materials Chemistry (MC14)", Aston University, United Kingdom, July (2019)

❖ Structure-property-performance interrelationship of 5,5′-bitetrazole-1,1′-diolate based energetic ionic salts: A comparative study,
"European Materials Research Society 2019 Spring Meeting (EMRS-2019)", Nice, France, May (2019)

❖ Microscopic origin of pressure-induced phase-transitions in urea: A detailed investigation through first principles calculations,
"International winter school 2018 on frontiers in materials science", at JNCASR, Bangalore, December (2018)

❖ Electronic properties and Hirshfeld surface analysis of Dihydroxylammonium 5,5-bistetrazole-1,1-diolate under pressure,
"Advances in Materials and Manufacturing Applications (IconAMMA 2018)", at AMRITA University, Bangaluru, August (2018)

❖ First Principles study of pressure induced polymorphic phase transition in trimethylamine,
"62nd DAE solid state physics symposium", at Bhabha Atomic Research Centre, Mumbai, December (2017)

❖ High pressure study of structural and electronic properties of potassium based green primary explosives,
"Recent trends in condensed matter physics", at Bose Institue, Kolkata, November (2017)

- Structural, electronic and lattice dynamical properties of perovsite $CaZrO_3$ under high pressure,
  "61st DAE solid state physics symposium", at KIIT University, Bhubaneswar, December (2016)

Workshops

- *International winter school 2018 on "frontiers in materials science"* JNCASR, Bangalore during 03rd - 07th December, 2018
- *Workshop on "Functional Magnetic Materials"* organized by UGC Networking Resource Centre, School of Physics, University of Hyderabad during 26th February – 3rd March, 2018
- *Sorbonne-JNCASR School on "Advanced Computational Material Science"* jointly organized by Sorbonne University, Paris and JNCASR, Bangalore during 29 th Jan - 02nd Feb, 2018
- *Workshop on "Modeling and Simulations of Nanomaterials using VASP"* organized by Centre for Clean Energy & Nanoconvergence, Hindustan University, Chennai during 20 - 21st February, 2017

List of Publications

Publications included in the thesis

[1] **B. Moses Abraham** and G. Vaitheeswaran, "From van der Waals Interactions to Structures and Properties of 3,3′-Dinitro-5,5′-Bis-1,2,4-Triazole-1,1′-Diolate Based Energetic Materials" *Mat. Chem. Phys.*, **240**, 122175 (2020).

[2] **B. Moses Abraham**, B. Adivaiah and G. Vaitheeswaran, "Microscopic origin of pressure-induced phase-transitions in urea: a detailed investigation through first principles calculations", *Phys. Chem. Chem. Phys.*, **21**, 884 (2019).

[3] **B. Moses Abraham**, Vikas D. Ghule and G. Vaitheeswaran, "A comparative study of the structure, stability and energetic performance of 5,5′-bitetrazole-1,1′-diolate based energetic ionic salts: future high energy density materials", *Phys. Chem. Chem. Phys.*, **20**, 29693 (2018).

[4] **B. Moses Abraham**, J. Prathap Kumar and G. Vaitheeswaran, "High pressure studies of hydrogen bonded energetic material 3,6-dihydrazino-s-tetrazine using DFT", *ACS Omega*, **3(8)**, 9388 (2018).

Publications not included in the thesis

[1] **B. Moses Abraham** and G. Vaitheeswaran, "First Principles study of pressure induced polymorphic phase transition in trimethylamine", *AIP Conf. Proc.*, **1942**, 030006 (2018).

[2] **B. Moses Abraham** and G. Vaitheeswaran, "Structural and electronic properties of 5,5′-hydrazinebistetrazole under high pressure: A DFT study", *IOP Conf. Ser.: Mater. Sci. Eng.*, **377**, 012107 (2018).

[3] **B. Moses Abraham**, N. Yedukondalu and G. Vaitheeswaran, "Structural, electronic and lattice dynamical properties of perovskite $CaZrO_3$ under high pressure", *AIP Conf. Proc.*, **1832**, 090042 (2017).

[4] G. Vaitheeswaran, N. Yedukondalu and **B. Moses Abraham**, "Structural, vibrational and bonding properties of hydronitrogen solids under high pressure: an abinitio study", *J. Chem. Sci.*, **128**, 1631 (2016).

[5] **B. Moses Abraham**and G. Vaitheeswaran, "Electronic properties and Hirshfeld surface analysis of Dihydroxylammonium 5,5-bistetrazole-1,1-diolate under pressure", *Materials Today: Proceedings* (accepted).

[6] **B. Moses Abraham** and G. Vaitheeswaran, "An innovative explosive detection designed from a sensitive g-C_3N_4 nanostructure: insights from DFT computations", *Submitted to journal*.

[7] **B. Moses Abraham**, N Yeduondalu and G. Vaitheeswaran, "High pressure structural and electronic properties of potassium based green primary explosives", *Submitted to journal*.

Scientific Activities

Oral presentations

- Structure-properties-performance interrelationship of energetic ionic salts: A comparative study,
  at "Dr. K.V. RAO's 19th Annual Research Award", Hyderabad, March (2019)

- An innovative explosive detection designed from a sensitive g-C_3N_4 nanostructure: Insights from DFT computations,
  "5th International Conference on Nanoscience and Nanotechnology (ICONN 2019)", SRM Institute of Science and Technology, Kottankulathur, January (2019)

- Structural and electronic properties of 5,5′-hydrazinebistetrazole under high pressure: A DFT study,
  "1st International Conference on Mechanical, Materials and Renewable Energy", Organized by Sikkim Manipal Institute of Technology, Sikkim, December (2017)

- Structural and vibrational behavior of 3,6-dihydrazino-s-tetrazine under pressure,
  "International Conference on Electronics, Physics and Chemistry", Jyothi Nivas College, Bangalore, February (2017)

Poster presentations

❖ Structure-property-performance interrelationship of 5,5′-bitetrazole-1,1′-diolate based energetic ionic salts: A comparative study,
"International Conference on Materials Chemistry (MC14)", Aston University, United Kingdom, July (2019)

❖ Structure-property-performance interrelationship of 5,5′-bitetrazole-1,1′-diolate based energetic ionic salts: A comparative study,
"European Materials Research Society 2019 Spring Meeting (EMRS-2019)", Nice, France, May (2019)

❖ Microscopic origin of pressure-induced phase-transitions in urea: A detailed investigation through first principles calculations,
"International winter school 2018 on frontiers in materials science", at JNCASR, Bangalore, December (2018)

❖ Electronic properties and Hirshfeld surface analysis of Dihydroxylammonium 5,5-bistetrazole-1,1-diolate under pressure,
"Advances in Materials and Manufacturing Applications (IconAMMA 2018)", at AMRITA University, Bangaluru, August (2018)

❖ First Principles study of pressure induced polymorphic phase transition in trimethylamine,
"62nd DAE solid state physics symposium", at Bhabha Atomic Research Centre, Mumbai, December (2017)

❖ High pressure study of structural and electronic properties of potassium based green primary explosives,
"Recent trends in condensed matter physics", at Bose Institue, Kolkata, November (2017)

- Structural, electronic and lattice dynamical properties of perovsite $CaZrO_3$ under high pressure,
  "61st DAE solid state physics symposium", at KIIT University, Bhubaneswar, December (2016)

Workshops

- *International winter school 2018 on "frontiers in materials science"* JNCASR, Bangalore during 03rd - 07th December, 2018
- *Workshop on "Functional Magnetic Materials"* organized by UGC Networking Resource Centre, School of Physics, University of Hyderabad during 26th February – 3rd March, 2018
- *Sorbonne-JNCASR School on "Advanced Computational Material Science"* jointly organized by Sorbonne University, Paris and JNCASR, Bangalore during 29 th Jan - 02nd Feb, 2018
- *Workshop on "Modeling and Simulations of Nanomaterials using VASP"* organized by Centre for Clean Energy & Nanoconvergence, Hindustan University, Chennai during 20 - 21st February, 2017

Computational Study of Hydrogen Bonded Energetic Materials

by Moses Abraham Bokinala

Computational Study of Hydrogen Bonded Energetic Materials

ORIGINALITY REPORT

55%	9%	54%	8%
SIMILARITY INDEX	INTERNET SOURCES	PUBLICATIONS	STUDENT PAPERS

PRIMARY SOURCES

1	B. Moses Abraham, G. Vaitheeswaran. " From van der Waals interactions to structures and properties of 3, -dinitro-5, -bis-1,2,4-triazole-1, -diolate based energetic materials ", Materials Chemistry and Physics, 2020 Publication	18%
2	B. Moses Abraham, B. Adivaiah, G. Vaitheeswaran. "Microscopic origin of pressure-induced phase-transitions in urea: a detailed investigation through first principles calculations", Physical Chemistry Chemical Physics, 2019 Publication	14%
3	B. Moses Abraham, Vikas D. Ghule, G. Vaitheeswaran. "A comparative study of the structure, stability and energetic performance of 5,5′-bitetrazole-1,1′-diolate based energetic ionic salts: future high energy density materials", Physical Chemistry Chemical Physics, 2018 Publication	11%
	B. Moses Abraham, J. Prathap Kumar, G.	

4	Vaitheeswaran. " High-Pressure Studies of Hydrogen-Bonded Energetic Material 3,6-Dihydrazino- -tetrazine Using DFT ", ACS Omega, 2018 Publication	7%
5	Submitted to University of Hyderabad, Hyderabad Student Paper	1%
6	www.ncbi.nlm.nih.gov Internet Source	1%
7	refubium.fu-berlin.de Internet Source	<1%
8	elib.uni-stuttgart.de Internet Source	<1%
9	dcwww.camd.dtu.dk Internet Source	<1%
10	Yi Wang, Yuji Liu, Siwei Song, Zhijian Yang, Xiujuan Qi, Kangcai Wang, Yu Liu, Qinghua Zhang, Yong Tian. "Accelerating the discovery of insensitive high-energy-density materials by a materials genome approach", Nature Communications, 2018 Publication	<1%
11	Submitted to Sardar Patel University, Vallabh Vidyanagar Student Paper	<1%